

Broadband Millimeter-Wave Spectroscopy with Z-Spec: An Unbiased Molecular-Line Survey of the Starburst Galaxy M82

Thesis by
Bret J. Naylor

In Partial Fulfillment of the Requirements
for the Degree of
Doctor of Philosophy



California Institute of Technology
Pasadena, California

2008
(Defended August 21, 2007)

© 2008

Bret J. Naylor

All Rights Reserved

I would like to dedicate this thesis to my loving wife, Michelle,
for her patience and generous support throughout this long process.

Acknowledgments

First and foremost, I would like to thank my advisor, Jonas Zmuidzinas, for his deep understanding of fundamental physics and excellent ability and strong desire to share that knowledge. He has been a wonderful guide to the world of millimeter-wave astrophysics.

I would also like to thank the fabulous team who worked so hard to get Z-Spec up and running. Thanks to Matt Bradford for teaching and guiding me through the process of designing, building, testing, and deploying a scientific instrument. Thanks to Lieko Earle who was ready and eager to take over day-to-day lab operations of the cryostat when it was time for me to start writing my thesis. I thank James Aguirre for his guidance of the software-development effort and his willingness to answer my silly data-analysis questions. Thanks to Jason Glenn for supporting this effort with both his time and resources. Thanks to Hien Nguyen for his assistance with the cryogenic integration effort and his positive and supportive attitude. And thanks to Jamie Bock for providing the detectors that turned two hunks of cold metal into an actual spectrometer.

I owe a debt of gratitude to the collaborators who provided several key components of Z-Spec. First, I would like to thank Hideo Matsuhara and his group at ISAS for delivering our sturdy and reliable cryostat. I thank Peter Ade and his group for providing our filter stack. Thanks to Mark Dragovan for allowing us to extract the magnet and salt pill from an old experiment of his. Thank you to Lionel Duband for designing and delivering a fabulous $^3\text{He}/^4\text{He}$ fridge that worked well beyond our expectations. Thanks to Ben Cain and Peter Timbie for growing a new salt pill for us.

I would like to thank Tom Phillips and the CSO for supporting my research and for being willing to send me to Scotland on a week's notice because we had just demonstrated that the spectrometer actually worked.

I am thankful that Peter Siegel and his group at JPL were willing to let Matt and me attach a large hunk of metal to their delicate waveguide parts for our initial grating tests. Thanks also to Frank Rice for trusting us with his expensive and custom-made millimeter wave source for our first cryogenic grating tests.

Thank you to my brother Jason for his assistance in the editing process. Thanks to my son Brandon for lighting up my life with his laughs. And finally I would like to thank my parents, Doreen and Bill, for fostering a love of learning that has proved invaluable to me during this adventure.

Abstract

Z-Spec is a broadband, millimeter-wave, direct-detection spectrometer based on a novel waveguide grating architecture. It is designed to fully cover the wide one-millimeter atmospheric window with a frequency range of 186 to 307 GHz at a resolution of ~ 250 . The design goal is the detection of rotational and fine structure lines from the distant population of galaxies that make up the far-infrared background. Its large instantaneous bandwidth enables detection of multiple transitions of carbon monoxide and a relatively rapid determination of redshift. The grating design is based on the Rowland architecture but is much more compact because of the use of a parallel-plate waveguide propagation medium. Z-Spec uses 160 silicon nitride micromesh bolometers and is cooled to less than 100 mK to achieve background-limited performance. Moreover, Z-Spec serves as a technology demonstration of a technique that is uniquely suited to far-infrared extragalactic spectroscopy from space.

Z-Spec's capabilities enable wide-coverage, unbiased line surveys of nearby galaxies. Searches for molecular lines outside our own galaxy have typically been targeted at specific transitions of particular molecules. The brightest sources of extra-galactic molecular lines come from galaxies with physical conditions very different from those found in the Milky Way. Unbiased searches for spectral lines can discover transitions and molecules that are unexpected. A three-pointing study of the prototypical starburst galaxy M82 was performed with Z-Spec at the Caltech Submillimeter Observatory. The survey detected eleven bright lines in the center of the Z-Spec band, of which four had not been previously detected. Two of the new detections are for molecules that had been detected at lower frequencies (HNC 3 - 2 and C₂H 3 - 2) and the other two are potentially transitions of SO₂, for which only upper limits on lower frequency transitions were previously available. Several detected molecules are analyzed using a large-velocity-gradient (LVG) radiative-transfer model and indicate significant regions of high-density molecular gas along the major axis of M82.

Contents

| | |
|--|-------------|
| Acknowledgments | v |
| Abstract | vii |
| List of Figures | xiii |
| List of Tables | xv |
| 1 Science Goals and Design Choices | 1 |
| 1.1 Submillimeter Galaxies | 1 |
| 1.2 Instrument Background and Design | 4 |
| 1.2.1 Measurement Approach | 4 |
| 1.2.2 Spectrometer Architecture Comparison | 6 |
| 1.2.3 Design Overview | 6 |
| 2 Spectrometer Design and Operation | 9 |
| 2.1 Grating Operation | 9 |
| 2.1.1 Rowland Design | 9 |
| 2.1.2 Facet Optimization | 9 |
| 2.1.3 Prototype Testing | 12 |
| 2.1.4 Science Grating | 14 |
| 2.2 Input Coupling Structures | 14 |
| 2.2.1 Dewar Window | 14 |
| 2.2.2 Filter Stack | 14 |
| 2.2.3 Waveguide Input Components | 16 |
| 2.2.3.1 Corrugated Input Horn | 16 |
| 2.2.3.2 Waveguide Coupler | 17 |
| 2.2.3.3 Grating Input Horn | 17 |
| 2.3 Output Couplers | 18 |
| 2.3.1 Design Considerations | 18 |

| | | |
|----------|---|-----------|
| 2.3.2 | Curved Bend Blocks | 18 |
| 2.4 | Cryogenic Grating Tests | 20 |
| 3 | Cryogenic System: Design, Integration, and Performance | 25 |
| 3.1 | System Overview | 25 |
| 3.2 | Thermal Loading | 25 |
| 3.3 | System Components | 29 |
| 3.3.1 | Cryostat | 29 |
| 3.3.2 | Adiabatic Demagnetization Refrigerator | 30 |
| 3.3.3 | Helium-3/Helium-4 Sorption Cooler | 31 |
| 3.3.4 | Gas-Gap Heat Switches | 32 |
| 3.3.5 | Thermal Mounts | 32 |
| 3.4 | System Operation | 33 |
| 3.4.1 | Cycling Procedure | 33 |
| 3.4.2 | Cycle Performance | 34 |
| 4 | Bolometer Readout and Signal Sensitivity | 41 |
| 4.1 | Bolometer Operation | 41 |
| 4.2 | Bolometer Readout Electronics | 43 |
| 4.3 | Photon Noise and Z-Spec Sensitivity | 45 |
| 4.4 | Noise Measurements | 47 |
| 5 | Unbiased Line Survey of M82 | 51 |
| 5.1 | Emission from M82 | 51 |
| 5.2 | Description of Observations | 53 |
| 5.2.1 | Measured Spectra | 55 |
| 5.2.2 | Continuum Results | 55 |
| 5.3 | Spectral Line Results | 59 |
| 5.3.1 | Spectral Fitting | 59 |
| 5.3.2 | CO and its Isotopologues | 62 |
| 5.3.3 | CN and C ₂ H | 62 |
| 5.4 | Radiative Transfer Modeling | 62 |
| 5.4.1 | HCO ⁺ and HCN | 66 |
| 5.4.2 | HNC | 73 |
| 5.4.3 | CS | 73 |
| 5.4.4 | SO ₂ | 77 |
| 5.5 | Multiple Species Model | 81 |

| | | |
|----------|--|------------|
| 5.6 | Summary Discussion | 89 |
| 6 | Future of Waveguide Spectrometers | 93 |
| A | Propagation of Guided Waves | 95 |
| A.1 | Electromagnetic Plane Waves | 95 |
| A.1.1 | Maxwell's Equations | 95 |
| A.1.2 | Solving the Wave Equation | 95 |
| A.1.3 | Wave Definitions and Constraints | 96 |
| A.2 | Wave Propagation in Media | 96 |
| A.2.1 | Auxiliary Fields | 96 |
| A.2.2 | Conducting Media | 97 |
| A.3 | Guided Waves | 98 |
| A.3.1 | Waveguide Basics | 98 |
| A.3.2 | Parallel-Plate Waveguide | 99 |
| A.3.2.1 | TE Modes | 99 |
| A.3.2.2 | TM and TEM Modes | 100 |
| A.3.3 | Rectangular Waveguide | 101 |
| A.4 | Waveguide Power Flow and Loss | 102 |
| A.5 | Waveguide Horns | 106 |
| A.5.1 | 2D Scalar Field Representation | 107 |
| A.5.2 | Waveguide Horn Beam Pattern | 107 |
| A.5.3 | Scattering Matrix Theory | 109 |
| A.5.4 | 2D Friis Transmission Formula | 110 |
| B | Thermometry Monitoring and Control | 113 |
| B.1 | LabVIEW Programming | 113 |
| B.2 | Readout Program | 115 |
| B.3 | Cycling and Control Programs | 115 |
| B.3.1 | Automated Cycles | 115 |
| B.3.2 | Cryogenic Controls | 116 |
| B.4 | SubVI Reference | 117 |
| B.4.1 | Instrument Interface Functions | 119 |
| B.4.1.1 | Power Supplies | 119 |
| B.4.1.2 | Resistance Bridge | 120 |
| B.4.1.3 | Temperature Monitors | 122 |
| B.4.1.4 | Other Instruments | 122 |

| | | |
|----------|--|------------|
| B.4.2 | Helium-3/Helium-4 Sorption Cooler Controls | 123 |
| B.4.3 | ADR Controls | 125 |
| B.4.4 | File I/O | 127 |
| B.4.5 | Sensor Calibration | 128 |
| B.4.6 | Miscellaneous | 130 |
| B.4.7 | Global Variables | 133 |
| C | Bolometer Readout Roll Off | 137 |
| C.1 | Circuit Model | 137 |
| C.2 | Parameter Fitting | 139 |
| D | Data Reduction Pipeline | 143 |
| E | Warm Optics for the Caltech Submillimeter Observatory | 149 |
| | Bibliography | 151 |

List of Figures

| | | |
|-----|---|----|
| 1.1 | Followup observations of Bolocam Lockman Hole survey | 2 |
| 1.2 | Radio-preselected submillimeter galaxy redshift distribution | 3 |
| 1.3 | CO detectability with broadband spectrometer at CSO | 5 |
| 2.1 | 2D Rowland grating schematic | 10 |
| 2.2 | Prototype grating picture | 13 |
| 2.3 | Prototype grating performance | 13 |
| 2.4 | Picture of science grating | 15 |
| 2.5 | Bend block design | 19 |
| 2.6 | Installation of all bend blocks | 20 |
| 2.7 | Cryogenic grating tests – first light | 21 |
| 2.8 | FTS-measured bolometer response profiles | 22 |
| 2.9 | FTS-measured bandwidth and resolution | 23 |
| 3.1 | Thermal noise from grating | 26 |
| 3.2 | Cryogenic system schematic | 27 |
| 3.3 | Cryostat photographs | 29 |
| 3.4 | Pictures of adiabatic demagnetization refrigerator | 30 |
| 3.5 | Helium-3/Helium-4 sorption cooler | 36 |
| 3.6 | Thermal mounting modules | 37 |
| 3.7 | Cryogenic cycle with unpumped baths | 38 |
| 3.8 | Cryogenic cycle with pumped helium bath | 39 |
| 4.1 | Bolometer mesh and detector key pictures | 42 |
| 4.2 | Signal flow diagram – from bolometer to data acquisition computer | 44 |
| 4.3 | Bolometer noise spectra | 48 |
| 4.4 | Sensitivity and optical efficiency | 49 |
| 5.1 | Composite image of M82 | 52 |
| 5.2 | Pointings observed in M82 | 54 |

| | | |
|------|--|-----|
| 5.3 | Spectra of NE pointing | 56 |
| 5.4 | Spectra of CEN pointing | 57 |
| 5.5 | Spectra of SW pointing | 58 |
| 5.6 | Detected line intensities chart | 61 |
| 5.7 | HCO ⁺ radiative transfer likelihood distributions | 67 |
| 5.8 | HCO ⁺ radiative transfer two-dimensional likelihood distributions | 68 |
| 5.9 | HCN radiative transfer likelihood distributions | 70 |
| 5.10 | HCN radiative transfer two-dimensional likelihood distributions | 71 |
| 5.11 | HNC radiative transfer likelihood distributions | 74 |
| 5.12 | HNC radiative transfer two-dimensional likelihood distributions | 75 |
| 5.13 | CS radiative transfer likelihood distributions | 78 |
| 5.14 | CS radiative transfer two-dimensional likelihood distributions | 79 |
| 5.15 | Multiple species model distributions for NE pointing – primary parameters | 82 |
| 5.16 | Multiple species model distributions for NE pointing – projected parameters | 83 |
| 5.17 | Multiple species model distributions for CEN pointing | 84 |
| 5.18 | Multiple species model distributions for SW pointing | 85 |
| 5.19 | Multiple species model derived abundances | 88 |
| 5.20 | Estimated total mass versus density in M82 | 90 |
| A.1 | Z-Spec parallel-plate waveguide loss | 105 |
| B.1 | Front panel of Z-Spec thermometry readout | 114 |
| B.2 | Automated cycling interface | 116 |
| B.3 | Cryogenic controls | 117 |
| B.4 | Thermometry software hierarchy | 118 |
| C.1 | Bolometer readout circuit | 138 |
| C.2 | Roll off parameter fits | 140 |
| D.1 | Data reduction schematic | 144 |
| E.1 | Z-Spec CSO relay optics | 150 |

List of Tables

| | | |
|------|--|-----|
| 5.1 | M82 pointing details | 55 |
| 5.2 | M82 continuum fit results | 55 |
| 5.3 | M82 line fit results | 60 |
| 5.4 | HCO ⁺ and HCN transition data | 66 |
| 5.5 | HCO ⁺ radiative transfer results | 69 |
| 5.6 | HCN radiative transfer results | 72 |
| 5.7 | HNC transition data | 73 |
| 5.8 | HNC radiative transfer results | 76 |
| 5.9 | CS transition data | 77 |
| 5.10 | CS radiative transfer results | 80 |
| 5.11 | Multiple species modeling results | 86 |
| 5.12 | Selected molecular abundance ratios for M82 | 87 |
| A.1 | Rectangular waveguide fields | 101 |
| A.2 | Power transmitted and conduction losses in waveguide | 104 |

Chapter 1

Science Goals and Design Choices

1.1 Submillimeter Galaxies

Understanding the origins of the far-infrared, extra-galactic background is one of the important problems in astrophysics today. Detected by the COBE satellite [Puget et al. 1996] and shown to account for a significant fraction of the radiant energy we receive from outside our galaxy [Hauser et al. 1998; Fixsen et al. 1998], the far-infrared background has been partially resolved by long integrations with ground-based, large-format bolometer array cameras such as SCUBA [Holland et al. 1999], MAMBO [Bertoldi et al. 2000] and Bolocam [Laurent et al. 2005]. These cameras have captured deep images of small patches of the sky to reveal several sources that are bright at millimeter and submillimeter wavelengths. More recently, deep integrations with the MIPS camera on the Spitzer Space Telescope have resolved many sources that contribute to the far-infrared background [Papovich et al. 2004; Dole et al. 2004]. These sources provide strong evidence of evolution of the star formation rate with a peak occurring somewhere in the redshift range $z \sim 1$ to 3.

Efforts to understand the redshift distribution of these objects have been hampered by instrumental limitations [Blain et al. 2002]. The angular resolution of ground-based millimeter and submillimeter telescopes is lower than that of their optical counterparts, so identifying candidates for follow-up observations can be difficult. At times, several candidate objects fall within the submillimeter beam, while in other cases the source has so much dust extinction that no optical counterpart can be identified. Examples of followup observations of several sources from the survey of the Lockman Hole region using the Bolocam instrument at the Caltech Submillimeter Observatory (CSO) [Laurent et al. 2005, 2006] are shown in figure 1.1. These images indicate the limited resolution of the bolometer cameras in the millimeter and submillimeter bands and the challenges involved in identifying appropriate counterparts in other wavebands.

Spectroscopic investigation with millimeter and submillimeter instruments is difficult because of the strong negative K-correction present in the submillimeter bands. The intrinsic spectrum of a galaxy rises rapidly through the far-infrared, fast enough to counteract the reduction in intensity due

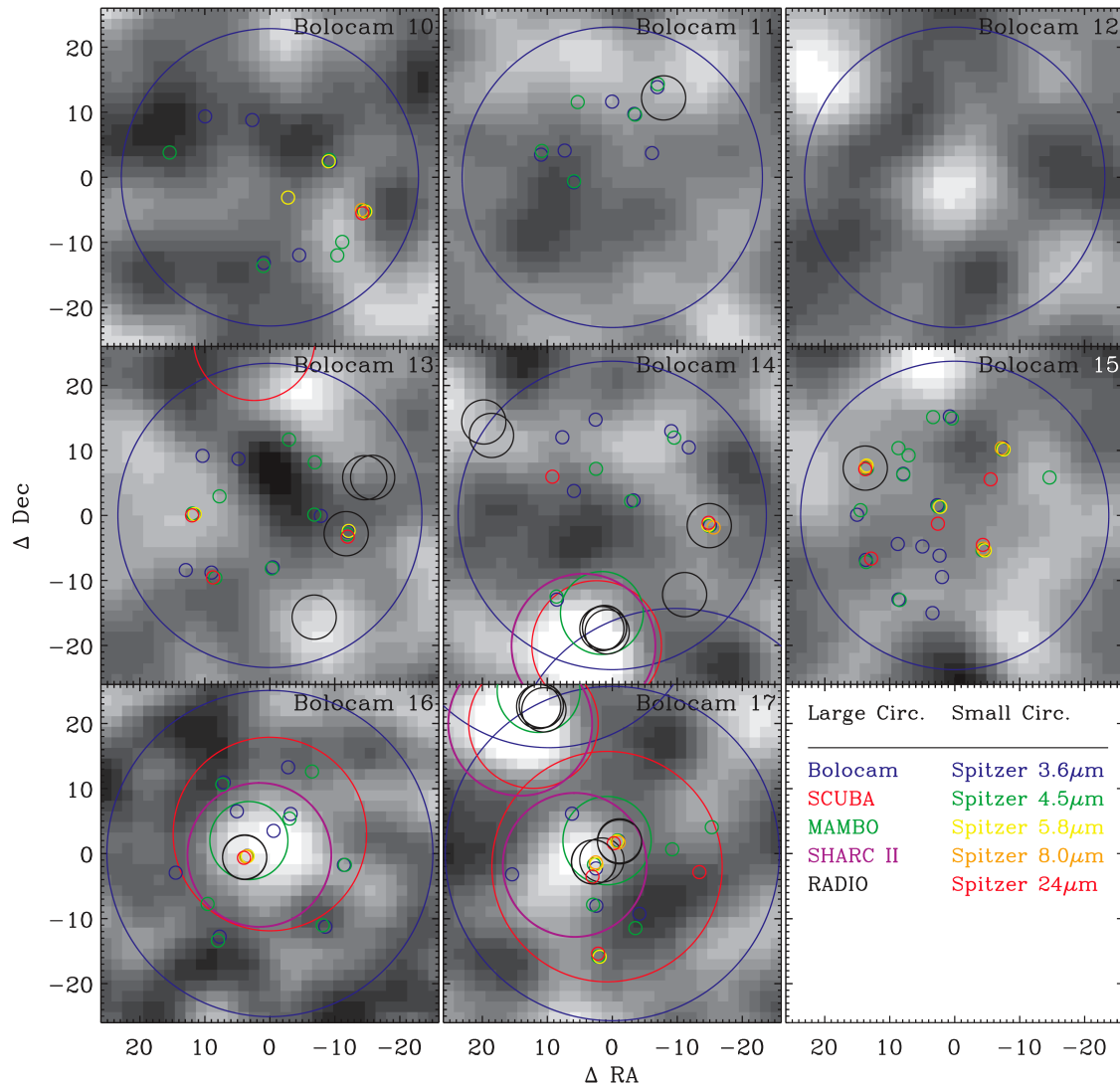


Figure 1.1. This set of images from Laurent et al. [2006], used with permission, is based on observations with the SHARC II submillimeter camera at the CSO of sources originally detected using the Bolocam instrument at the same observatory. The grayscale backgrounds show images from the SHARC II fields centered on the Bolocam source. The large circles indicate point sources detected by Bolocam (1.1 mm), SCUBA (850 μ m), MAMBO (1.2 mm), SHARC II (350 μ m) and in the radio by the VLA (6 and 20 cm) while the small circles identify point sources seen by the IRAC (3.6, 4.5, 5.8 and 8.0 μ m) and MIPS (24 μ m) instruments on the Spitzer Space Telescope. Bolocam 14, 16 and 17 are all detected by SCUBA, MAMBO, SHARC II, and the VLA with Bolocam 16 and 17 also seen in several Spitzer bands. The lack of millimeter and submillimeter confirmation of the other sources (10-13 and 15) suggests that they are not submillimeter galaxies and may be false detections which are expected to account for about one-third of the sources in the Bolocam survey.

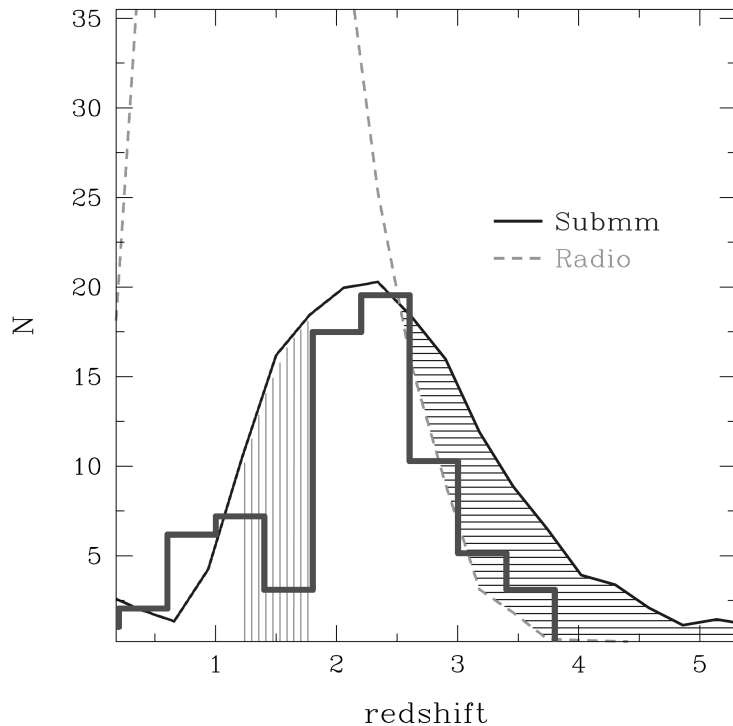


Figure 1.2. This figure from Chapman et al. [2005], used with permission, shows the redshift distribution of the 73 submillimeter galaxies found using their radio preselection method. Deep radio maps with very accurate pointing information are used to direct both submillimeter imaging and optical spectroscopy. This method indicated that the submillimeter galaxy population was very distant with a median redshift of 2.2. The two shaded areas indicates regions in redshift space that are not accessible with this method.

to increased distance between the source and the observer. A source of fixed luminosity at redshifts from $z \sim 1$ to 10 produces a roughly constant flux density as seen by a submillimeter camera. This creates an intrinsically large uncertainty in the redshift of an object seen by such an instrument and difficulty in developing photometric redshift estimators. A large fractional bandwidth of order unity must be covered to measure the unknown redshift of a submillimeter galaxy. Most long-wavelength spectrometers are much more constrained in their bandwidth, limited by the currently available technology for heterodyne spectrometer backends. These backend systems can cover up to 4 to 8 GHz, or about 2 to 3% fractional bandwidth at 250 GHz. A dual side band receiver would double the coverage of its backend, but that would still be much less than is desired for this type of measurement.

Some progress has been made in measuring the redshift distribution of optically-faint, submillimeter-bright objects via radio preselection [Chapman et al. 2005]. This method has discovered over seventy submillimeter galaxies with a median redshift of 2.2; the histogram of detections versus redshift is shown in figure 1.2. This method has far surpassed the efforts to measure redshifts of submillime-

ter galaxies using long wavelength spectrometers but its sample is limited by two selection effects. Since the method uses optical spectroscopy to measure the redshift, the spectroscopic desert in the rest-frame ultraviolet emission from these sources implies that no redshifts can be measured in a range from about 1.3 to 1.8. Furthermore, the radio images limit the high redshift tail that can be seen using this method due to the flux limit of the radio maps.

Understanding the nature of submillimeter galaxies is a challenge of modern astronomy. Extensive modeling of the evolution of a universe filled with cold dark matter and with a nonzero cosmological constant has been able to match the observed source counts of submillimeter galaxies and other types of high redshift sources [Baugh et al. 2005]. This modeling uses the density perturbations indicated by the cosmic microwave background and evolves these perturbations through gravitational collapse and galaxy mergers. The modeling supports the idea that submillimeter galaxies are high-redshift analogues of the local population of ultra-luminous infrared galaxies (ULIRG) [Sanders et al. 2003] and are associated with mergers and high rates of star formation. However, in order for the modeling to match the submillimeter source counts, the modeled mergers must occur more frequently and produce stars more efficiently than originally expected.

1.2 Instrument Background and Design

1.2.1 Measurement Approach

A more direct method of measuring the redshift of submillimeter galaxies would be to use the ladder of carbon monoxide (CO) rotational lines. CO is a very common species in molecular gas and its rotational transitions have a simple spectrum. The lowest level transition occurs at 115 GHz, and the spacing between transitions is also 115 GHz. As the ladder of CO lines is redshifted, the frequencies and the spacings are reduced. By measuring the frequencies and spacing between two CO lines, the redshift can be determined uniquely.

Observing at least two CO transitions from a distant galaxy of unknown redshift requires an instrument that can quickly cover a large bandwidth with good sensitivity. High spectral resolution is not as important because the doppler-broadened linewidths are a few hundred megahertz at 250 GHz, though higher resolution does reduce the background noise limit up until the line is resolved. These general design requirements are very different than what is desirable for millimeter-wave spectral observations within our own galaxy, where linewidths are at least a factor of 10 narrower than for extra-galactic sources and spectral resolution is paramount. However, for a CO-ladder redshift instrument, the bandwidth coverage is most crucial. A plot of the detectability of CO lines using a broadband spectrometer at the Caltech Submillimeter Observatory (CSO) is shown in figure 1.3.

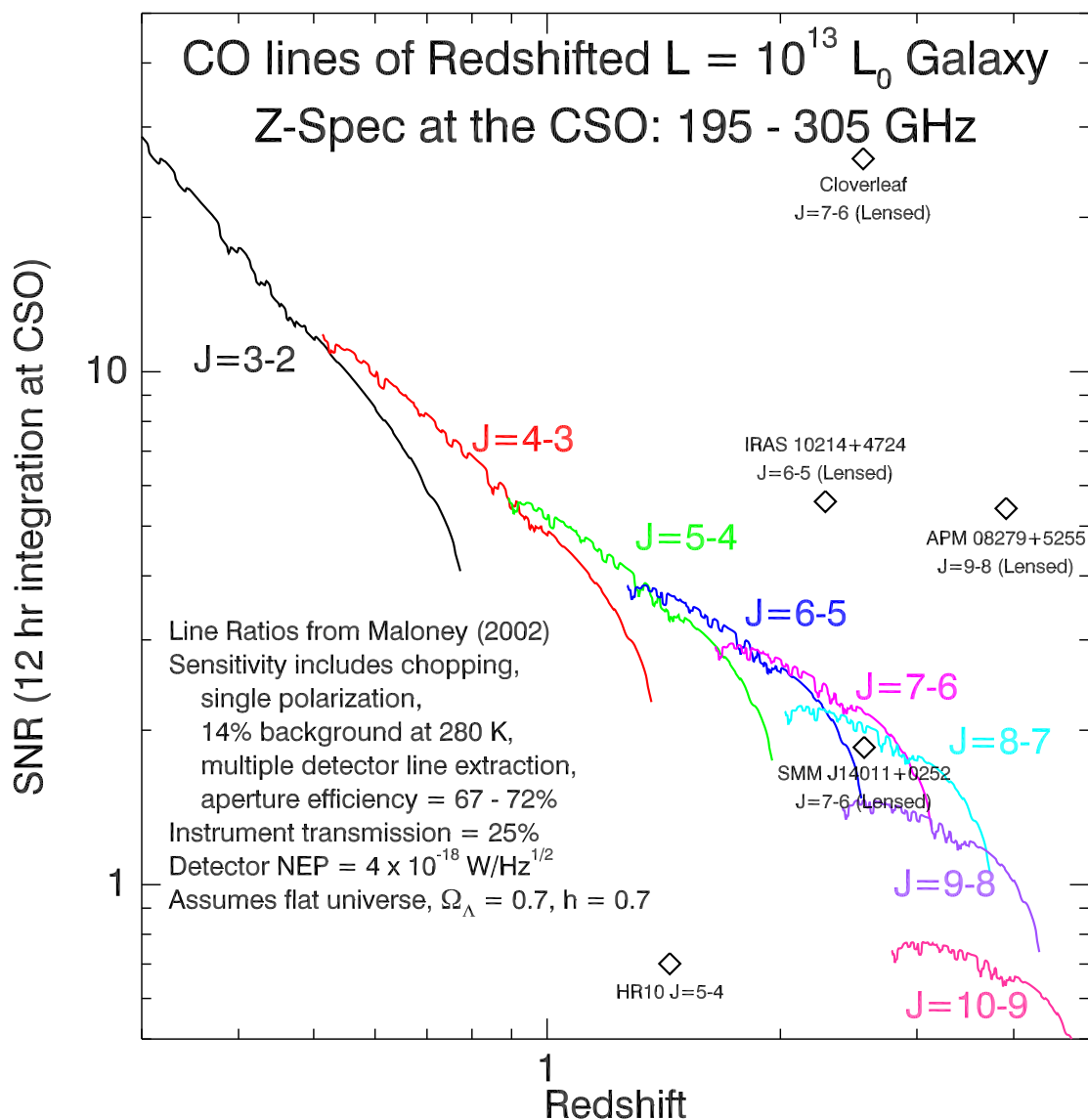


Figure 1.3. This plot shows the signal-to-noise ratio for the ladder of CO transitions of a bright ULIRG using a broadband spectrometer at the CSO. This spectrometer has 110 GHz of instantaneous bandwidth and 25% optical efficiency and is limited by the optical background from the telescope, though the calculation includes a detector noise term. The instrument is capable of measuring two CO lines from a redshift of 0.5 to 3, with a small gap from 0.75 to 0.9. Some high-redshift CO detections are also shown for comparison (Cloverleaf: Alloin et al. [1997], IRAS 10214+4724: Solomon, Downes, and Radford [1992], APM 08279+5255: Downes et al. [1999], SMM J14011+0252: Downes and Solomon [2003], HR10: Andreani et al. [2000]).

1.2.2 Spectrometer Architecture Comparison

Nearly all millimeter-wave spectrometers built have been based on heterodyne spectroscopy and have been limited in the instantaneous bandwidth coverage. This technology can be extended and improved to increase the bandwidth by about an order of magnitude to perhaps 24 GHz (see Rice et al. [2003] for an example) but that is still about a factor of 4 to 5 smaller than ideal. Heterodyne spectrometers take the astronomical signal and mix it with a locally-generated signal (LO) to create radiation at a frequency given by the difference between the sky signal and the LO. This process adds both quantum and receiver noise to the signal; however, once the signal is downconverted, it is much easier to amplify and process than the high-frequency signal from the sky.

A direct-detection spectrometer would not suffer from quantum noise and could potentially be more sensitive depending on the architecture and choice of detectors. Bolometers are very sensitive detectors in the millimeter-wave region with intrinsically broadband response. One way to make a spectrometer using bolometers is using a tunable Fabry-Perot filter. A Fabry-Perot spectrometer can be both quite sensitive and offer high resolution but suffers from a scanning penalty when covering a large bandwidth. Another common optical architecture is the Fourier Transform Spectrometer (FTS) which can be designed to cover a broad band quickly, but is much less sensitive because all of the background power within that broad band falls on the detectors. A third optical arrangement for direct detection spectroscopy is a grating. Gratings do not need to be scanned and can cover large bandwidths if operated in a low order. Also, the background power from the sky seen by an individual detector is reduced by the resolution of the grating. Of all the direct-detection spectrometer architectures, a first-order grating can provide the widest spectral coverage and highest sensitivity for a given resolution, which is why it was chosen for Z-Spec. A description of some of Z-Spec's design details is given in the next section.

1.2.3 Design Overview

Z-Spec's novel two-dimensional optical system uses a grating with 480 facets, each about 1 mm in size. The grating operates in first order and provides frequency coverage from 186 to 307 GHz at moderate resolutions of $R \equiv \nu/\Delta\nu \sim 250$ across the band. The light is detected by 160 Si_3N_4 micromesh bolometers which are read out in parallel without the use of multiplexing. The readout system uses cryogenic J-FET source-follower amplifiers and a custom-designed room temperature readout electronics system (RTE) which provides J-FET and bolometer bias power along with a digital lock-in amplifier for each bolometer. The detectors and grating are cooled to <100 mK by a combination of an adiabatic demagnetization refrigerator (ADR) and closed-cycle sorption cooler encased in a liquid He–liquid N_2 cryostat. Light from the telescope passes through a window in the cryostat and several low-pass filters before entering a corrugated feedhorn which tapers down

to a single-mode rectangular waveguide. That waveguide defines the low-frequency cutoff for the system and restricts the photon propagation to a single spatial and polarization mode. The intended observing strategy involves chopping and nodding on and off the source.

The optical system components are described in chapter 2. Details of the cryogenic system are discussed in chapter 3. Chapter 4 describes the bolometer readout system and sensitivity analysis. Results from the astronomical observations of the starburst galaxy M82 are covered in chapter 5, and some remarks on the future of waveguide spectrometers are given in chapter 6.

Chapter 2

Spectrometer Design and Operation

2.1 Grating Operation

2.1.1 Rowland Design

The size of the grating element in a direct-detection spectrometer relative to the wavelength of operation determines the approximate resolution such an instrument can achieve. A standard planar grating is designed to receive and reflect plane waves and thus requires additional optical elements to collimate and focus the input and output beams. A curved grating can be designed to focus as well as disperse incident waves. Such a design was used in the late 19th century [Rowland 1883] for optical spectroscopy. A Rowland grating's facets lie on a circle of radius $2R$ and the grating will disperse and focus white light from a point source on a circle tangent to the grating circle with half the radius. The locus of points where output frequencies are focused also lies on this smaller circle, called the Rowland circle. The point of tangency between the grating arc and the input/output circle is called the grating pole. The geometry of a Rowland grating is shown in figure 2.1

Since the Rowland grating does all the required work, its size dictates the size of the spectrometer. Therefore, a very compact design for a given resolution gives the Rowland geometry a primary advantage for a cryogenic optical system. Further space savings can be obtained by using a two-dimensional propagation medium such as parallel-plate waveguide. The performance of a two-dimensional grating based on the Rowland design can be modeled using the techniques discussed in McGreer [1995].

2.1.2 Facet Optimization

The Rowland grating's facets are equally spaced along a circular arc; however, better performance can be obtained by allowing these parameters to vary [Marz and Cremer 1992]. In a two-dimensional

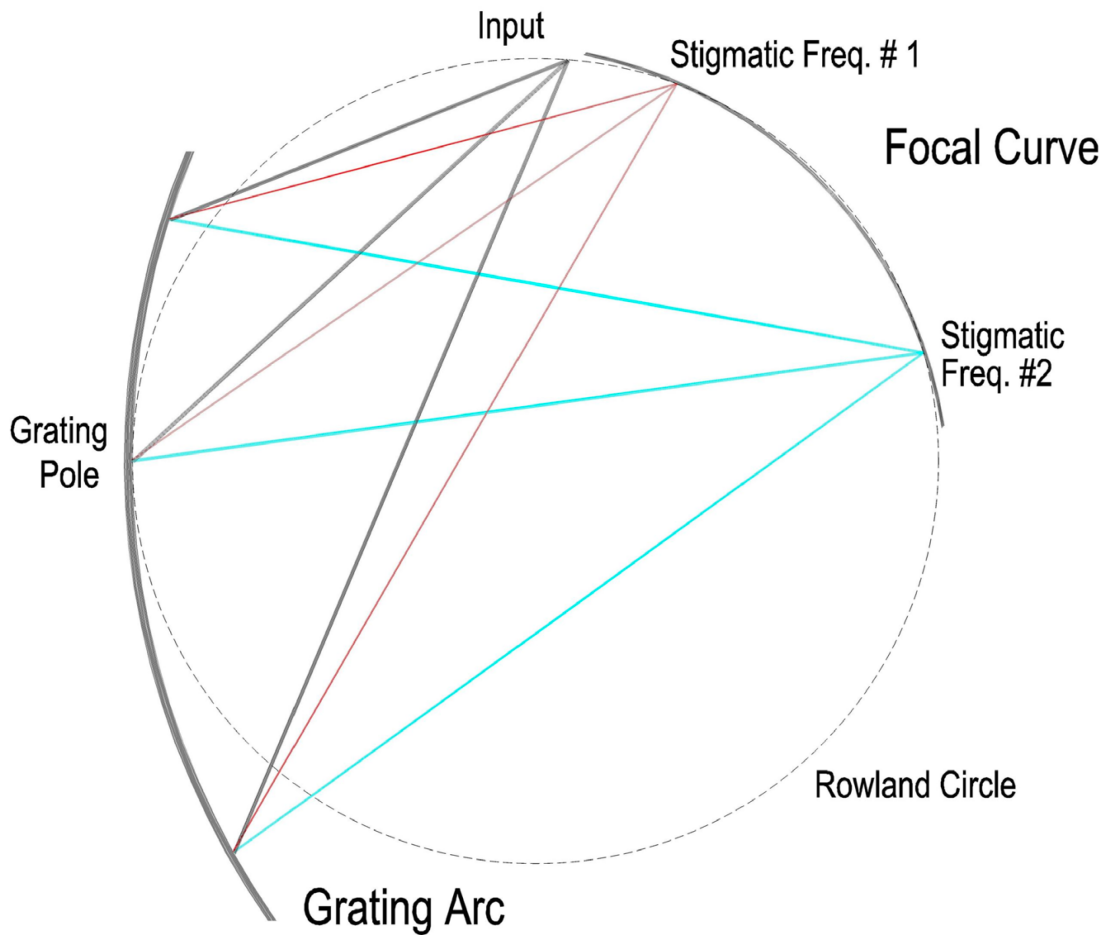


Figure 2.1. This diagram indicates the geometry of the Rowland grating. Light diverges from a focus at the input and reflects off the facets of the grating on the left. The grating disperses and focuses different colors onto the focal arc on the right, where two stigmatic frequencies are indicated in red and cyan. The input and outputs lie on the Rowland circle that is tangent to the grating arc at the grating pole. The radius of the grating arc is twice that of the Rowland circle. In a two-dimensional architecture, the facet locations can be optimized to give perfect performance at the two stigmatic frequencies. After the grating facets are optimized, the locations of the best focus for the output frequency range of the design can be calculated from the fields produced by light waves propagating from the input, bouncing off the grating facets and propagating to the focal arc. It is clear that the ideal focus locations do not exactly lie on the Rowland circle; for frequencies between the two stigmatic points, they are somewhat closer, while on the edges of the band they are somewhat farther away. This figure also indicates the angle between the normal of the focal arc and the direction of propagation as the light is focused by the grating. This is only a few degrees at stigmatic frequency #2 but 20° - 30° at #1.

medium, two constraints must be established to uniquely determine a facet's location. By selecting two stigmatic output frequencies, the position constraints can be written in terms of the i -th facet center position (x_i, y_i) ,

$$\begin{aligned} 0 &= \epsilon_{i,1}(x_i, y_i) = R_{in,i}(x_i, y_i) + R_{i,1}(x_i, y_i) + i\lambda_1 - R_{in} - R_1, \\ 0 &= \epsilon_{i,2}(x_i, y_i) = R_{in,i}(x_i, y_i) + R_{i,2}(x_i, y_i) + i\lambda_2 - R_{in} - R_2. \end{aligned}$$

These two equations require that each facet be positioned such that for the two stigmatic frequencies (defined by their wavelengths λ_1 and λ_2) the change in path length from one facet to the next results in a phase shift of exactly 2π . R_{in} , R_1 and R_2 are constants relating to the distance from the input horn, stigmatic output 1 and stigmatic output 2, respectively, to the facet at the grating pole; these are determined by the initial design choices. $R_{in,i}(x_i, y_i)$ is the distance from the input to the i -th facet while $R_{i,1}(x_i, y_i)$ and $R_{i,2}(x_i, y_i)$ are the distances from that facet to the two stigmatic points. The derivatives of $\epsilon_{i,1}$ and $\epsilon_{i,2}$ with respect to x_i and y_i can be computed analytically, so Newton's method can be used to find the optimum facet locations numerically using the Rowland geometry as a starting point.

After the optimum facet locations are calculated, the performance of the grating can be modeled using a simple 2D scalar approximation of the fields inside the parallel-plate waveguide. If the fields in the planar waveguide are excited in the lowest-order mode, then they can be described in terms of a scalar field ψ introduced in section A.5.1. The beam pattern of a rectangular waveguide horn with aperture w has a beam pattern in a parallel-plate waveguide given in equation (A.47). This beam pattern gives the field intercepted by each facet in terms of $\theta_{in,i}$, the angle from the horn to the facet with respect to the horn axis,

$$\phi_i = \phi_0 \frac{w}{\sqrt{\lambda_g R_{in,i}}} e^{2\pi j R_{in,i}/\lambda_g} \cos \theta_{in,i} \operatorname{sinc} \left[\frac{\pi w \sin \theta_{in,i}}{\lambda_g} \right],$$

where ϕ_0 is the input amplitude at the mouth of the horn and λ_g is the reduced wavelength in the guide. The small phase factor has been dropped under the assumption that the grating facets are many wavelengths away from the aperture of the horn. Each facet will reradiate these fields in much the same way such that the field at the output surface is the sum of the contributions from all facets,

$$\phi_{out} = \sum_i \phi_i \frac{w_i}{\sqrt{\lambda_g R_{i,out}}} e^{2\pi j R_{i,out}/\lambda_g} \eta_{\text{blaze}}(\lambda_g, i, \theta_{in,i}, \theta_{i,out}).$$

η_{blaze} is the blaze efficiency that depends on the wavelength, facet spacing and the input and output angles. $\theta_{i,out}$ is the angle between the local grating normal at facet i to a point on the output surface. ϕ_i is assumed to have negligible variation across the width of a facet, w_i , which is calculated based

on the angular size as seen from the input. Therefore $w_i = R_{in,i}\delta\theta_i$ and the output field is

$$\phi_{out} = \phi_0 \frac{w}{\lambda_g} \sum_i \delta\theta_i \sqrt{\frac{R_{in,i}}{R_{i,out}}} e^{2\pi j(R_{in,i}+R_{i,out})/\lambda_g} \cos \theta_{in,i} \operatorname{sinc} \left[\frac{\pi w \sin \theta_{in,i}}{\lambda_g} \right] \eta_{\text{blaze}}(\lambda_g, i, \theta_{in,i}, \theta_{i,out}). \quad (2.1)$$

This output field can be used to calculate the power flow across the focal curve using the Poynting vector formula from equation (A.44). This enables calculation of the spectral profiles of the system at various frequencies. These spectral profiles provide feedback to drive the selection of the initial design parameters: Rowland circle radius, input horn location and width, and the two stigmatic frequencies.

Our model assumed unit blaze efficiency even though it can be calculated using a scalar model. A scalar model has generally been shown to be inaccurate for planar, free-space gratings and thus is unlikely to be sufficient for our situation. Instead, we used a vector-based electromagnetic calculation method from Loewen and Popov [1997] that is implemented in a commercial software package. These calculations were for infinite, planar gratings in free space. The fields in the parallel-plate waveguide are similar to the S-polarization in standard grating terminology. A 29° blaze angle was chosen to give good performance across our band.

2.1.3 Prototype Testing

Initial testing of this concept was performed on a prototype grating with 400 facets. This prototype was not intended for cryogenic use and was based on two 1 cm thick plates of aluminum separated by spacers 2.5 mm thick. The plates were machined with an end mill on the edges and each was polished to a mirror surface on one side. The length of the longest edge was about a half meter. The calculated resolution using an illuminating horn with a 3.2 mm aperture was about 200. The input and output horns were also directly machined and were attached to the edges of the thick plates. A photograph of the grating and one of the (unpolished) plates is shown in figure 2.2.

The prototype was tested using a backward-wave oscillator source, provided by Peter Siegel at the Jet Propulsion Laboratory, and a diode detector. The diode detector was mounted in a single-mode rectangular waveguide and was attached to a waveguide horn in order to match the parallel-plate separation. Two output horns were tested: one with an aperture roughly equal to the spot size of the grating and the other with a much more narrow aperture. The first horn was used to measure the total throughput of the system while the narrower horn with its broad beam was used to measure the spectral profile.

Both horns were designed to attach anywhere along the focal curve, which is essentially a circular arc. The horns are oriented radially with respect to this arc which is not the ideal orientation, particularly for the larger aperture horn. For low output frequencies that focus near the input,

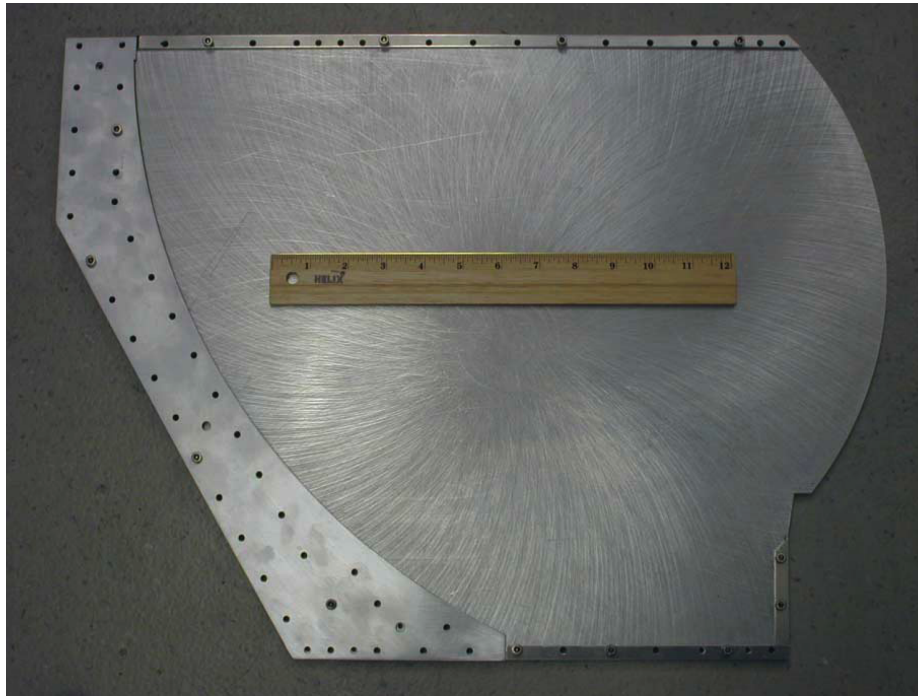


Figure 2.2. This photograph of the prototype grating shows the grating piece on the left, the focal arc on the right, spacers on the top and bottom, and the input area on the bottom right. There is a 12-inch ruler in the middle on top of one of the unpolished plates for scale. After this picture was taken, the plates were polished to a mirror finish by hand.

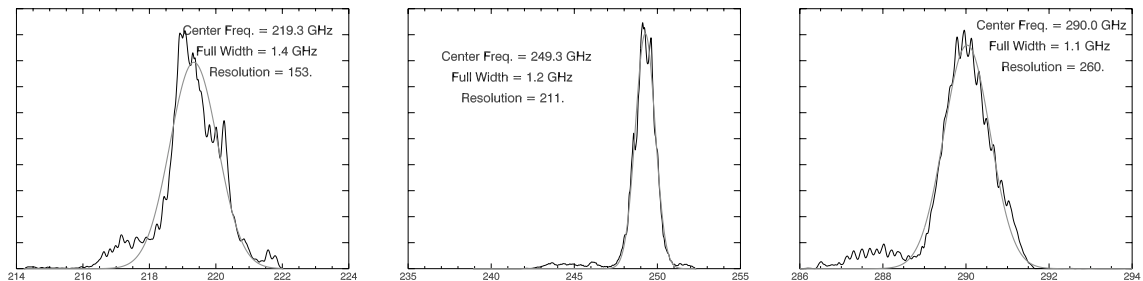


Figure 2.3. These three plots show the spectral performance of the prototype grating at three different frequencies across the band. The measurements were made using a backward-wave oscillator as a millimeter wave source and a single mode diode detector. The amplitude is arbitrary and this measurement method has two important limitations in terms of its ability to measure the grating throughput. The single-mode detector rejects some of the focused power because of mode mismatch and the radially-oriented output horn does not match the angle of the incident radiation, potentially rejecting a large fraction of the incident power. In spite of these limitations, the measured resolution of the grating agreed well with the modeled performance.

a horn pointed in the radial direction does not see much of the grating and thus the total power collected by such a horn is much less than the true throughput of the grating. A correction factor for this beam pattern mismatch can be calculated from the integral of the product of two rectangular waveguide beam patterns, equation (A.47), where one beam pattern's angular coordinate has an additional offset, $\theta \rightarrow (\theta - \theta_0)$. We measured this prototype grating at several frequencies across the band and found that it performed according to our specifications (see figure 2.3).

2.1.4 Science Grating

The success of the prototype grating tests convinced us to proceed with the scientific instrument (shown in 2.4). This version used 480 facets with a smaller aperture input horn (1.8 mm) to broaden the illumination pattern and increase the resolution. The largest dimension is about 61 cm and the parallel plates are lightweighted to reduce the heat capacity. The science grating was also tested using the backward-wave oscillator and diode detector and similar agreement between the modeled and measured performance was found. The mismatch between the radial direction and the propagation direction of the lower frequency spots from the grating is handled by a system of bend blocks described in section 2.3.2.

2.2 Input Coupling Structures

2.2.1 Dewar Window

Light enters the dewar through a millimeter-wave transparent, vacuum tight material called Zotefoam composed of closed-cell puffed polyethylene. It has excellent transmission in our band and is strong enough to withstand the large pressure differential. Our window is made from an 80 cm diameter disk of ~ 35 cm thick foam. Due to the pressure forces present on the foam when one side is under vacuum, it must be secured along the sides as well as the back. A holder was designed to seal to an O-ring on the dewar and allow for good adhesion between the aluminum window holder and the Zotefoam disk.

2.2.2 Filter Stack

The initial filter design called for capacitive mesh filters on the nitrogen, helium and ^3He radiation shields, and on the corrugated input horn. All these low-pass filters were designed by Peter Ade at the University of Wales, Cardiff. The cutoffs for each filter are 13 cm^{-1} , 12 cm^{-1} , 11 cm^{-1} and 10.3 cm^{-1} , respectively. The lower frequency edge of Z-Spec's band is set by the output waveguide cutoff of the corrugated feed horn discussed in the next section. The spectral performance of each filter was measured on an FTS, showing that they give several orders of magnitude of rejection of the

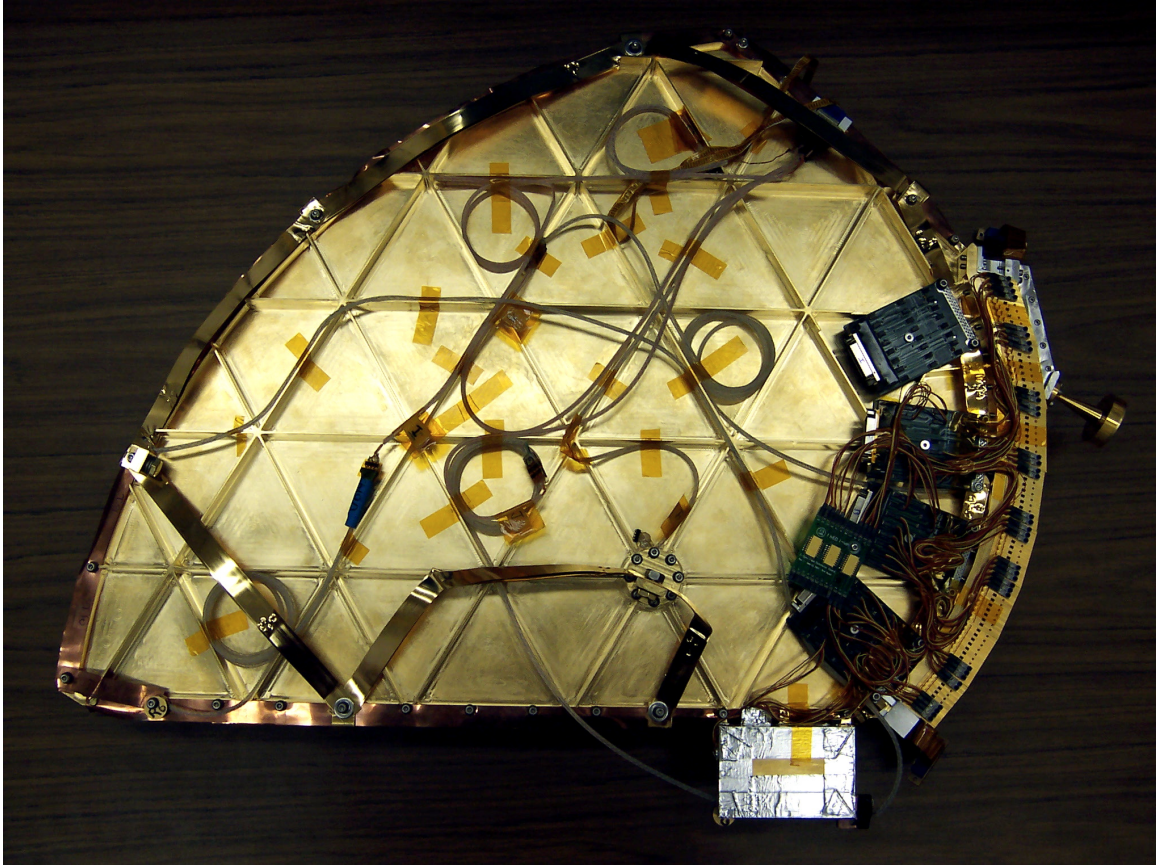


Figure 2.4. This photograph shows the exterior of the science grating with the input and output horns attached. The grating plates are lightweighted in a triangular pattern and gold plated. The faceted spacer extends along the arc from the top middle to the bottom left. The corrugated input horn, waveguide coupler and grating input horn can be seen in the upper-right corner. The bend blocks are installed on the right side. The grating has copper strapping attached around the edge and has some housekeeping wiring shown. Four fanout boards which collect the signals from the bolometers onto a few large cables can be seen mounted on the grating plates near the bend blocks. The rectangular box in the bottom right is a dark box designed for performing dark bolometer tests even when the grating can see out of the cryostat.

room-temperature infrared emission when cascaded together while providing excellent transmission within the bandpass of the spectrometer. The filter holders were designed to squeeze around the rims of the filters to maintain good thermal contact and also block any light that might scatter out of the thin edges of the filter disks.

During the course of lab testing, we found that while the out-of-band power reaching the detectors through the grating was sufficiently small, there were cryogenically significant optical loads present when using only the metal-mesh filters. The FTS measurements of these filters do not extend to the frequencies of the peaks of the blackbody spectra they are trying to block, so the nature of the optical loads we observed is unclear. The excess loads were particularly problematic to the ^3He stage of the sorption cooler (see section 3.3.3) which is connected to a large radiation shield surrounding the grating. This stage is capable of absorbing 12 J of energy which was used up in less than 12 hours when the original filter stack was installed.

The solution to this problem was to install four layers of thin fluorogold sheets along with the metal-mesh filter on the helium shield. Fluorogold is a dielectric glass-fiber-loaded teflon material, whose transmission spectrum through a length l of material is $T(\nu) = \exp(-\alpha(\nu)l)$. The absorption coefficient α can be described by a power law in frequency ($\alpha(\nu) = a\nu^b$). The exponent of that power law controls how strongly it can cut off higher frequencies while the overall constant determines how well it will transmit at low frequencies. Fluorogold has a large exponent and small constant factor (see Halpern et al. [1986]) and its moderate index of refraction makes it a useful infrared blocker. After installing these 4 sheets of fluorogold (3.27 mm total thickness), the radiation load on the ^3He shield was significantly reduced, achieving a ^3He hold time of almost 48 hours without significantly reducing the in-band transmission.

2.2.3 Waveguide Input Components

2.2.3.1 Corrugated Input Horn

Our corrugated input feedhorn was designed and built by Custom Microwave in Longmont, CO. We specified the dimensions of the rectangular waveguide output, the circular aperture of the horn and the overall length of the part. We also had a reflection loss requirement across the Z-Spec band. Custom Microwave took our specifications and simulated a design based on the prescription outlined in Zhang [1993] and their own expertise. Based on their simulations and subsequent measurements the feedhorn is known to have good performance across the Z-Spec band.

A key feature of the corrugated feedhorn is that the size of its rectangular waveguide output determines the low frequency edge of Z-Spec bandpass. The size of the guide is $0.0358'' \times 0.0179'' \pm 0.0005''$. The lowest-order waveguide mode (see section A.3.3) has a cutoff frequency of 164.8 GHz which is the lowest frequency that will be accepted by the corrugated feedhorn and propagate into

the grating. The next waveguide modes will start to propagate at twice this frequency. The size of this guide was chosen such that frequencies that could propagate in the rectangular guide in multiple modes would be attenuated by the filter stack before reaching the feedhorn.

2.2.3.2 Waveguide Coupler

The cryostat window and the input to the grating do not line up. This is because we wanted to fit as large a grating as possible inside the cryogenic volume and thus did not want to constrain the location of the grating input horn. This required the design and manufacture of a coupling piece from the single-mode rectangular waveguide output of the corrugated horn and the single-mode rectangular waveguide input of the grating horn. The coupling piece is several centimeters long and therefore could not remain in single-mode waveguide for its entire length; the conduction losses would be too large in standard guide. Furthermore, the coupling piece needed two $\sim 90^\circ$ bends to join the orientations and locations of the corrugated horn and grating horn.

Electromagnetic simulations of certain components of the coupler design using Ansoft Corporation's High Frequency Structure Simulator (HFSS) steered the overall design. Waveguide bends can be designed in a large variety of ways. The best style of bend from a broadband, power transmission point-of-view is a curved bend with a radius of curvature several wavelengths long. A $\sim 90^\circ$ bend would clearly be several wavelengths long and could produce significant conduction losses if it remained at standard single-mode dimensions. The HFSS simulations showed that the waveguide dimension perpendicular to the curved walls could be extended without significantly impacting the transmission. In this case, the long side (or a) of the rectangular cross section can be extended, strongly reducing the conduction loss in the waveguide (see table A.2). The waveguide coupler has two curved bends with gradually tapered long dimensions connected by three straight sections: one long section that is highly oversized and two gradual tapers in the short dimension to match the profiles coming out of the bends. The overall piece is too large to simulate in HFSS, but simulations of the various sections indicate that it should not significantly affect the overall instrument transmission.

2.2.3.3 Grating Input Horn

The grating input horn connects the waveguide coupler described in the previous section and the parallel-plate waveguide. This rectangular waveguide horn has a standard size single-mode input and tapers in height to match the separation of the parallel-plate waveguide and tapers in width to properly illuminate the facets of the grating. The single-mode input is necessary to control the mode structure that is excited in the parallel-plate waveguide. Since different modes have different dispersion relationships, our grating is designed to work for only one particular mode. Power that is excited into another mode will not be focused properly by the grating. A single-mode interface

ensures that all the power that makes it into the grating input horn will have the appropriate field profiles to excite the desired parallel-plate waveguide mode.

2.3 Output Couplers

2.3.1 Design Considerations

The output of the grating is a focal curve where a continuous range of frequencies is focused along a nearly circular arc. We did not want to include any cryogenic mechanism to move the grating thereby shifting the mapping of focus position and frequency. However, this required some method to map the entire focal curve to the active areas of our 160 detectors without any gaps. The required frame around the individually mounted bolometers meant that simply mounting the devices directly on the parallel-plate output would not suffice. A network of horns would be necessary to properly couple the focal curve to the detectors.

Unfortunately, tapered horns would not work because they would reject some of the power focused by the grating. A single mode horn of a certain width has a well-defined beam pattern. A similar analysis can be applied to higher order modes and in the limit of highly overmoded waveguide, the aggregate beam pattern is nearly isotropic. A taper that cuts off certain modes is equivalent to rejecting certain angles from the parallel-plate region. This was deemed unacceptable.

The solution to this problem was to use waveguide bends to route adjacent frequencies above and below the parallel-plate waveguide such that physically adjacent detectors are separated by two frequency channels. The channels vary in width across the band but the bolometer separation is never less than 3 mm. This enabled use of a single bolometer design for the entire focal plane (see chapter 4) so that the detectors could be mass-produced.

2.3.2 Curved Bend Blocks

The curved waveguide bends which route the 160 frequency channels above and below the plane off the parallel-plate waveguide are grouped into sets of 20 waveguides. These sets are called bend blocks and were designed to be somewhat mass produced. They apply the technique of split-block waveguide manufacture whereby a desired planar waveguide structure is split lengthwise in half along a symmetry plane and the two halves are machined out of two pieces of metal. Registration pins are used to align the blocks to each other for the final assembly.

Each bend block is a stack of 20 rectangular waveguides. These guides join together to form a parallel-plate region along part of the bend and then split up or down as seen in figure 2.5. If each of these guides is split down the middle, the curved bend block can be directly machined from a stack of 21 sheets. Two of those sheets are end caps and are unique, but the 19 interior slices, which

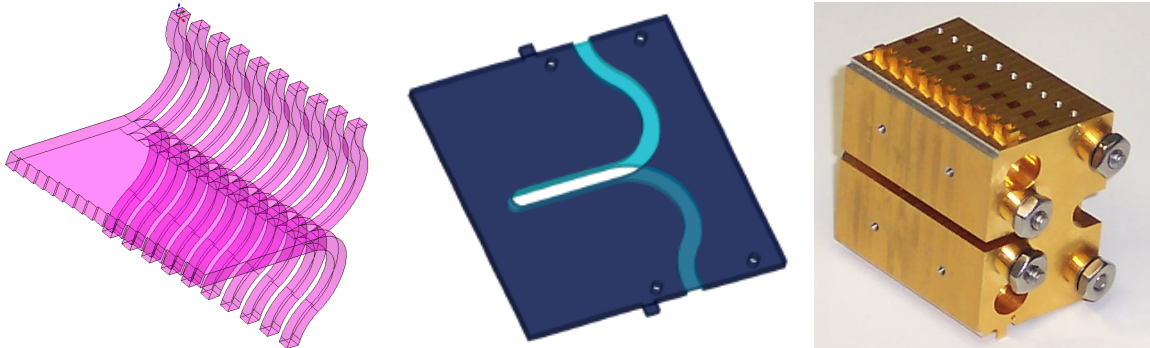


Figure 2.5. These images demonstrate some of the features of the bend block design. The rendering on the left shows the stacked waveguide bends that make up the interior of the bend block. The curved rectangular waveguides bend alternately up or down out of the plane of the parallel-plate guide which is created by the adjoining rectangular guides. The adjacent guides are shifted with respect to each other thus aligning the guides to the incoming radiation.

The middle image shows one of the 21 sheets that make up the bend block. A half-depth waveguide channel is cut by an end mill in the cyan region. The sheet is then flipped over and machined halfway through again. These two steps remove all the material along a portion of the center line of the sheet. There are four pin holes shown that align the adjacent slices; two are used for the slice above and two for the slice below. The two small tabs that stick up from the top and bottom plates are used to align the detector keys on the bend block.

The photograph on the right shows one of the completed blocks. After the slices are stacked up, additional machining steps are necessary to cut off the front of the block and cut clearance holes on the sides so that adjacent blocks can fit next to each other. The bolts that hold the stack together are shoulder bolts so that the shaft of the bolt fits snugly through its clearance hole. This provides alignment reinforcement for the bend block and is used because the pins aligning one slice to the next are fairly short and small in diameter.

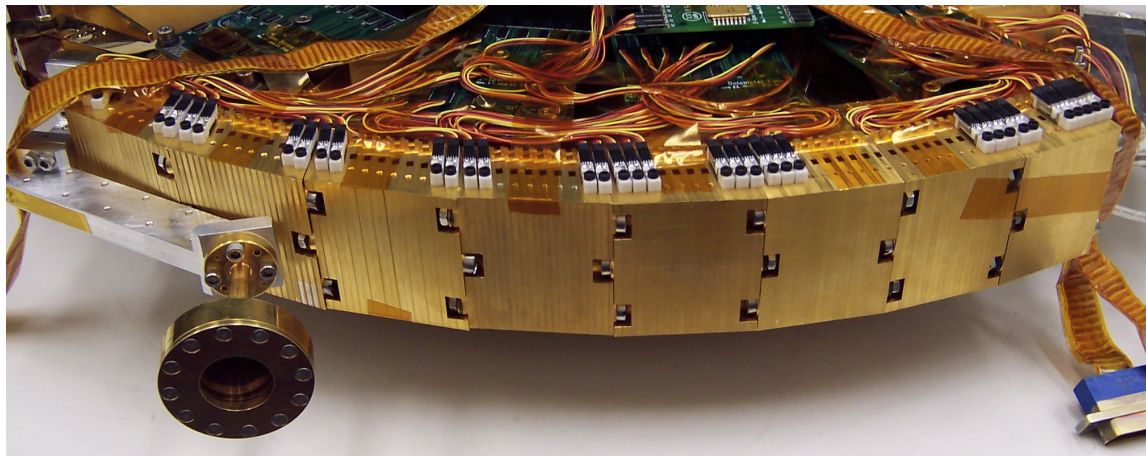


Figure 2.6. This photograph shows how all eight bend blocks fit onto the grating plates. The screws holding the bend blocks together alternate between two patterns: one style has two screws near the back while the other has only one screw. Several detectors are installed on the bend blocks, though the array is not fully populated in the photograph. The gold-plated corrugated input horn with its metal-mesh filter attached can also be seen on the left. The unplated aluminum piece connected to the input horn is the waveguide coupler described in section 2.2.3.2. Its other end is connected to the grating input horn that is also unplated aluminum and is barely visible in this image.

are one waveguide width thick, can be made from two slightly different designs. Ten up slices, nine down slices plus a bottom and a top slice are used to manufacture a single bend block. Each of these slices has short pins which align with the adjacent slices and are squeezed together using shoulder bolts which provide some overall alignment. The stack of slices is further machined as a single unit to allow each bend block to mate with the spectrometer plates and adjacent bend blocks.

The waveguides in the bend blocks are highly overmoded, ranging in cross-section from about 1.6×2.5 mm to 2.0×2.5 mm, capable of supporting thirty or more waveguide modes for frequencies in the Z-Spec band. This is fairly large compared to typical machining tolerance and thus would seem to indicate that the bend blocks would not be that difficult to machine. However, there were some challenges found in the manufacturing process, and after the first block was made, some design changes were necessary. The end caps of the blocks proved particularly difficult and flaws could be seen even in the second-generation versions. Unfortunately, there was no way to separately test the bend block performance independent of the entire grating. The installed bend blocks can be seen in figure 2.6. The next section discusses the lab tests performed on the science grating.

2.4 Cryogenic Grating Tests

The science grating and input and output coupling structures were installed into the cryostat and integrated with the cryogenic system. When the system could be maintained below 100 mK for

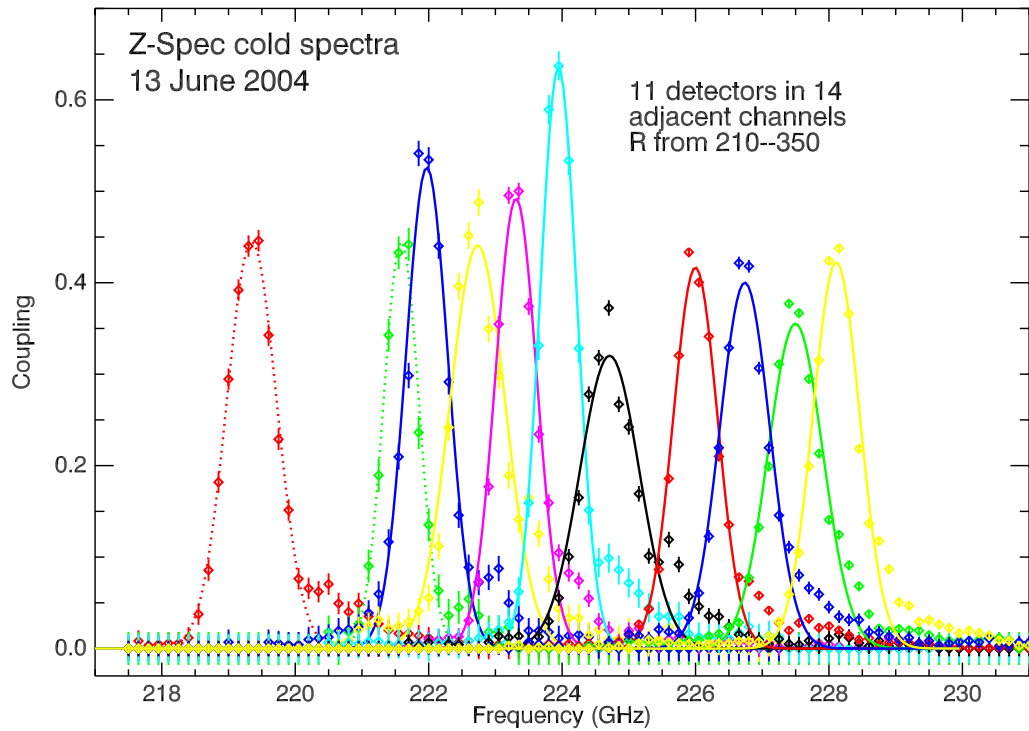


Figure 2.7. This plot shows eleven measured spectrometer profiles, the results from the first full system tests. The source was a chopped microwave multiplier chain whose output frequency was controlled by a microwave generator. The bolometer response for these eleven channels was measured with DC bias using an external lock-in amplifier. The height of each trace is based on a measurement of the total coupling by comparing bolometer load curves with room temperature and 77 K loads in front of the dewar window. The coupling is quite good, though the measurement is somewhat flawed due to the presence of excess in-band loading; the resolution matches well with expectation, within the accuracy of the measurement. The diamonds are the measurements while the curves are single-peak Gaussian fits to the data points for each channel.

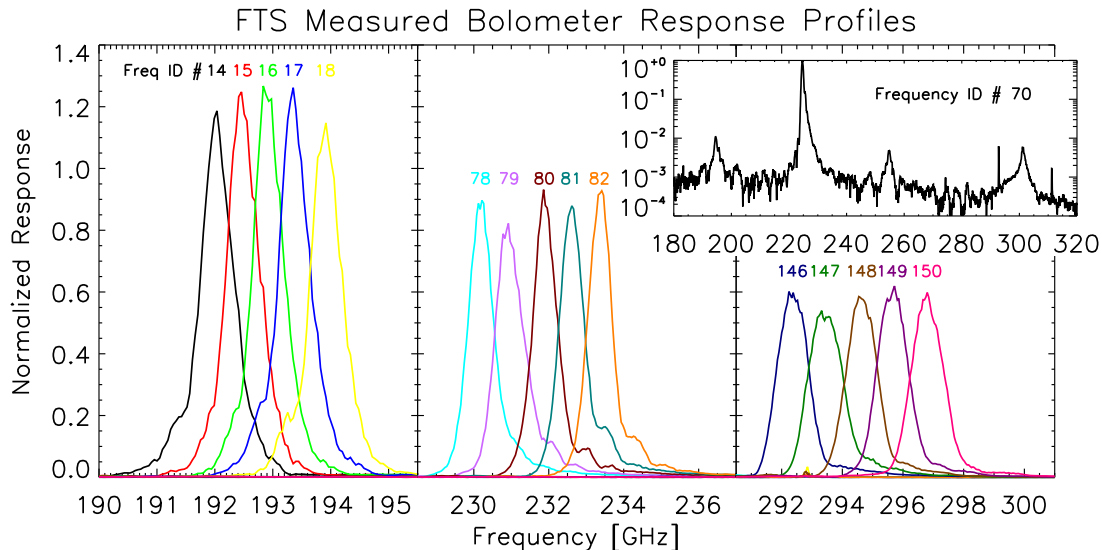


Figure 2.8. These plots show several bolometer spectral response profiles as measured by an FTS. The profiles are labeled by the frequency ID number which orders the bolometers from lowest (freq ID # 0) to highest (freq ID # 159) frequency. The profiles are normalized to have unit integral, which gives the narrower, low-frequency channels on the left a larger peak amplitude than the wider, high-frequency channels on the right. The inset plot shows the profile for frequency ID # 70 over the full range of the instrument. The main lobe at 225 GHz is about two orders of magnitude taller than the tallest sidelobes. The three sidelobes seen in this channel’s spectrum are typical of all channels. There are two “Rowland Ghosts” 30 GHz to the left and the right of the main lobe which arise from periodic manufacturing defects in the grating and do represent actual off-peak response. These two lobes move with the main lobe but the other sidelobe at about 300 GHz actually moves to lower frequencies as the frequency ID increases. This sidelobe is actually the main lobe response to light that has traveled twice through the arms of the FTS. The center frequency of this side lobe is twice that of the main lobe aliased down by the FTS Nyquist frequency at 375 GHz.

several hours, we performed various tests to evaluate the performance of the grating system. The backward-wave oscillator source was too difficult to use for the cryogenic tests, so we borrowed a frequency-multiplier source from a receiver developed for the CSO described in Rice et al. [2003]. An electronically-controlled microwave synthesizer drove the multiplier chain which could generate ample millimeter wave power at a well-defined and tunable frequency. By chopping this source and using a lock-in amplifier on the bolometer readout, we could measure the spectral profiles for various channels of the instrument. The results of those measurements can be seen in figure 2.7. We measured profiles that had resolutions similar to what our modeling predicted and indicated that the various coupling structures did not degrade the intrinsic performance of the grating.

Additional cryogenic tests were performed by placing room temperature and cold loads in front of the cryostat window. A load of known temperature T that fills the beam generates $k_b T \Delta\nu$ power per mode in the Rayleigh–Jeans limit. Since Z-Spec operates in a single mode, the difference in measured power from the hot and cold loads gives a very simple measure of the optical efficiency

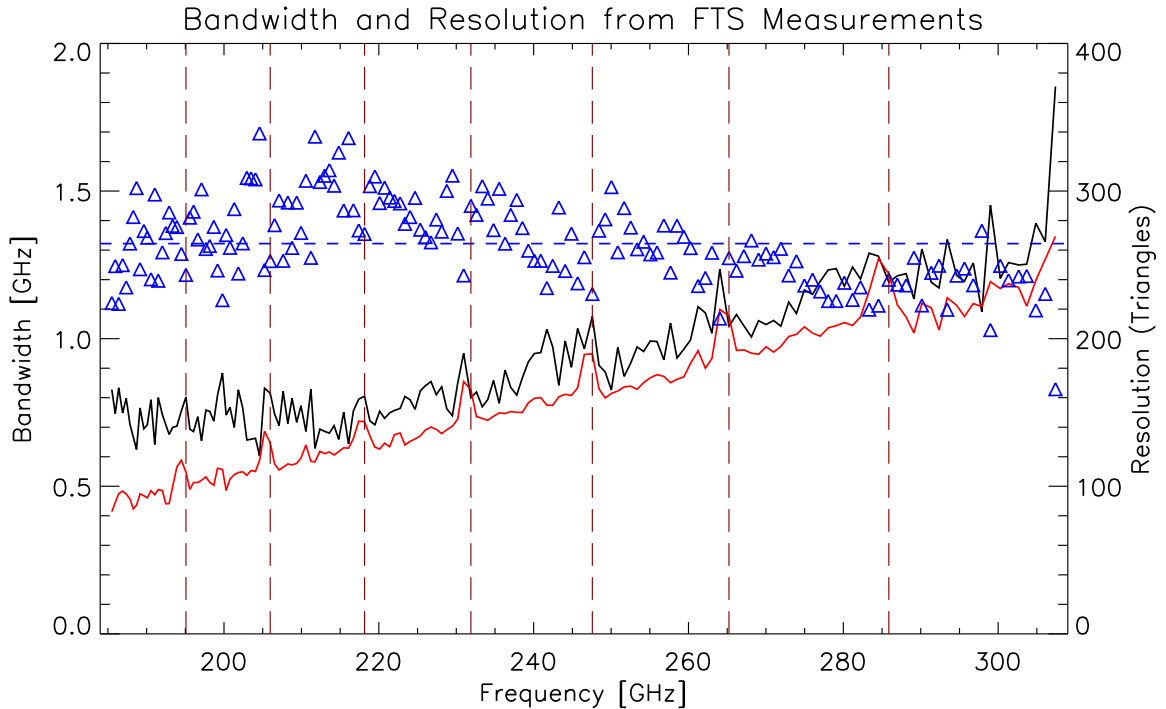


Figure 2.9. This plot shows the bandwidth of each channel measured in two ways: the black line is the full-width, half-maximum (FWHM) value obtained from Gaussian fits to the main lobe peak in the FTS spectra while the red curve is the difference between the center frequencies of adjacent channels. The red curve clearly shows increased bandwidth at the bend block edges, indicated by the dashed vertical lines. This increase is also present in the gaussian measured bandwidths. The resolution for each channel is plotted with the triangle symbols and is calculated from the ratio of the center frequency and the gaussian FWHM. The median resolution indicated by the dashed horizontal line is about 265.

of the instrument as long as $\Delta\nu$, the bandwidth seen by a particular detector, is well determined. The fixed-source measurements described above enabled precise determination of the bandpass for individual detectors; tests with a thick-grille filter indicated less than one part in 300 high-frequency leakage power coming through the filter stack at frequencies above 325 GHz. These optical efficiency measurements indicated about 25% overall coupling for the channels we tested.

As more detectors were installed into the system, bandpass testing with the multiplier chain and lock-in amplifier system became impractical. We used a Fourier Transform Spectrometer (FTS) to measure the bandpasses of all channels simultaneously. The first FTS we used slowly advanced the moveable arm of the interferometer in the typical way. This first test was limited by the number of working channels and also by our incomplete knowledge of the position of the mirror. Another FTS system was used after all channels were functional. This instrument operated in a rapid-scan mode and the profiles obtained served a crucial role in extracting spectral information from observational data. Some plots of the FTS profiles, band centers and bandwidths are shown in figures 2.8 and 2.9.

Chapter 3

Cryogenic System: Design, Integration, and Performance

3.1 System Overview

The cooling requirements for the Z-Spec instrument are dominated by the noise budget and the expected load on the bolometers. As shown in chapter 4, it is necessary to cool the detectors to less than 100 mK to achieve background-limited performance. Furthermore, a comparison between the background photon noise from the telescope and the broadband noise due to the self-radiation of the grating indicates that the grating must be cooled to less than a few hundred mK (see figure 3.1). While it was not necessary to cool the entire grating along with the bolometers, we decided this would be easier than designing a thermal break between the grating and the bolometers.

Cooling four kilograms of aluminum to less than 100 mK is challenging and requires a variety of cryogenic technologies. The design is constrained to use an unpumped 4.2 K He bath and to have a 48-hour hold time. The base temperature is achieved by an adiabatic demagnetization refrigerator (ADR), which uses a strong magnetic field and quantum mechanical system of isolated spins to reach very low levels of entropy and thus temperature. The ADR is backed by an integrated, closed-cycle $^3\text{He}/^4\text{He}$ sorption cooler. The ^3He and ^4He stages work by condensing stored gas into liquid, then pumping away the gas that boils off the liquid, which cools the liquid. Included with the sorption cooler are four gas-gap heat switches which are used to thermally connect or isolate various components of the cryogenic system. A schematic of the system is shown in figure 3.2.

3.2 Thermal Loading

There are two primary forms of thermal loading to consider when designing a cryogenic system: conductive and radiative loading. Conductive heat flow comes from the presence of a temperature gradient along the length of some material. It is parameterized in terms of the thermal conductivity

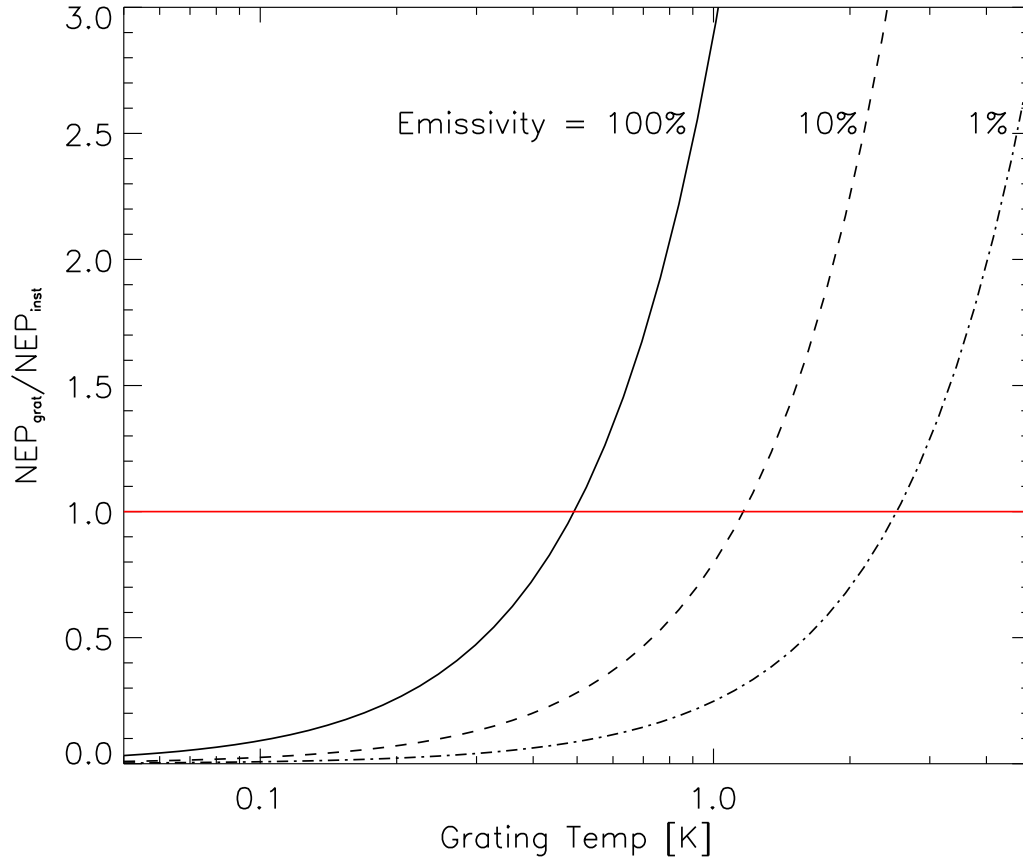


Figure 3.1. This plot shows the temperature dependence of the ratio between the noise due to the radiation of the grating and the instrumental noise determined by the atmospheric loading and intrinsic detector noise. The grating noise is broadband and comes from the blackbody radiation of the grating itself coupled through the bend block feedhorns to the bolometers. Both noises are calculated using the formalism developed in Zmuidzinas [2003]; the instrument noise calculation is described in section 4.3. For unit emissivity, which is clearly an overestimate, cooling the grating to 300 mK would be sufficient from a noise perspective. However, we chose to cool the grating with the bolometers down to less than 100 mK to avoid the difficulty in designing a thermal break between the bolometers and the grating module.

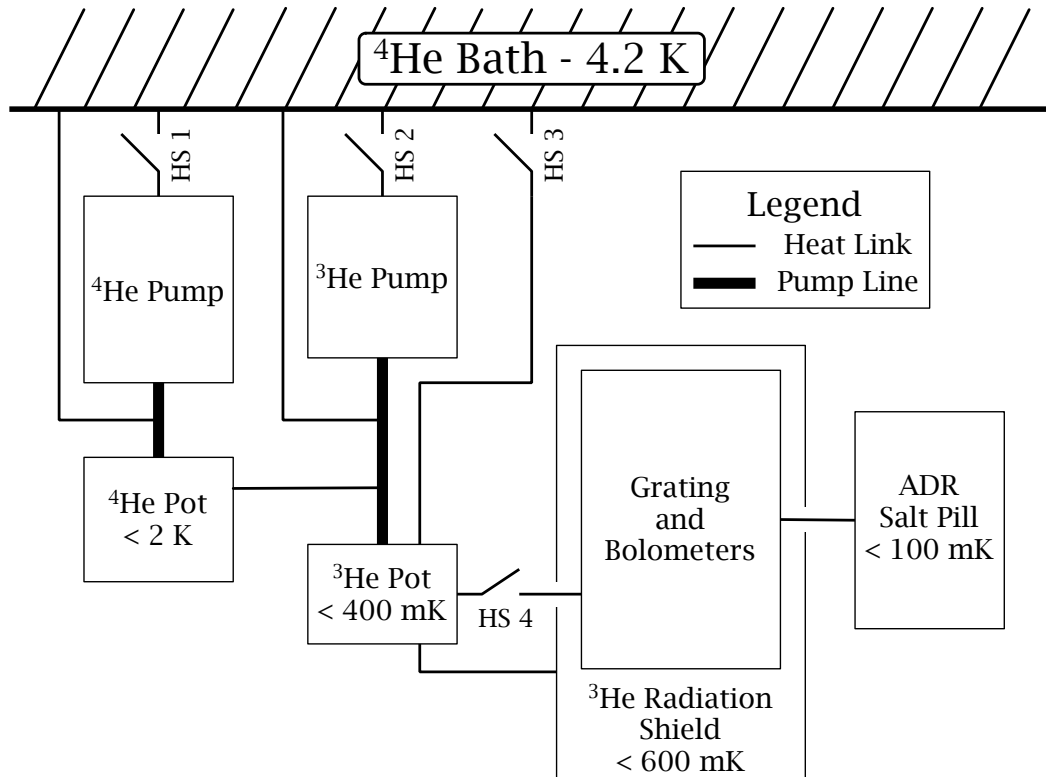


Figure 3.2. This figure is a schematic representation of the cryogenic system. The grating and bolometers are first cooled by the $^3\text{He}/^4\text{He}$ sorption cooler and then by the ADR. The heat of magnetization of the ADR salt pill is extracted through the grating and HS 3 and 4. The grating and bolometers are surrounded by a radiation shield sunk to the ^3He pot. The shield is made of thin aluminum sheet metal and has relatively poor thermal conductivity. It does not get as cold as the ^3He pot, but it is cold enough to guard the ADR from radiative and conductive loads from the 4.2 K helium bath. The system is designed to stay cold for 48 hours and the cycle time is about 7–8 hours. All the heat switches are the gas-gap type described in section 3.3.4. HS 1 and HS 2 are filled with ^4He gas but HS 3 and HS 4 are filled with ^3He so that they will operate well below 4.2 K.

σ which is defined by

$$\dot{Q} = -\sigma(T)A \frac{\partial T}{\partial l}, \quad (3.1)$$

where \dot{Q} is the heat flow, A is the cross-sectional area and the negative sign indicates that heat flows from higher to lower temperature. The thermal conductivity typically has a strong temperature dependence so extending this definition to describe heat flow created by a macroscopic temperature difference is nontrivial. It is shown in Garwin [1956] that using the thermal potential,

$$\Sigma(T) = \int_0^T \sigma(T')dT', \quad (3.2)$$

is an easy way to calculate macroscopic heat flow through a homogenous material. The heat flow through a material from one end at T_1 to the other at T_2 is

$$\dot{Q}_{cond} = G [\Sigma(T_1) - \Sigma(T_2)], \quad (3.3)$$

where the factor G is determined by the geometry, such that

$$\frac{1}{G} = \int_{x_1}^{x_2} \frac{dx}{A(x)}. \quad (3.4)$$

$A(x)$ is the possibly position-dependent cross-sectional area and x_1 and x_2 are the positions from and to which the heat flow is calculated. If the cross section is constant and $L = x_2 - x_1$, then $G = A/L$.

Thermal loading due to radiation is caused by the fact that anything with a temperature above absolute zero will radiate energy with a black-body spectrum determined by that object's temperature and scaled by the object's emissivity. The total power radiated, P_{rad} , by a blackbody at temperature T is given by the Stefan–Boltzmann law,

$$P_{rad} = \epsilon \sigma A T^4, \quad (3.5)$$

where ϵ is the body's emissivity which, for simplicity, is assumed to be constant over all frequencies, A is its surface area, and σ is the Stefan–Boltzmann constant which in SI units is

$$\sigma = \frac{2\pi^5 k_b^4}{15c^2 h^3} = 5.67 \times 10^{-8} \text{ W m}^{-2} \text{ K}^{-4}, \quad (3.6)$$

where k_b is the Boltzmann constant, c is the speed of light and h is Planck's constant. A perfect blackbody has $\epsilon = 1$ whereas objects with high reflectivity can have very low emissivity.

A typical application of the Stefan–Boltzmann law in cryogenics is to calculate the power delivered to a cold stage by a surrounding warmer stage. Let the cold stage have surface area A_c and be in thermal equilibrium with a thermal bath at temperature T_c . If it is completely surrounded by a warmer stage maintained at temperature T_w , then the net heat flow to the cold stage via radiation is given by

$$\dot{Q}_{rad} = \left(\frac{\epsilon_c \epsilon_w}{\epsilon_c + \epsilon_w - \epsilon_c \epsilon_w} \right) \sigma A_c (\kappa T_w^4 - T_c^4), \quad (3.7)$$

where ϵ_c and ϵ_w are the emissivities of the cold and warm stages, respectively, and κ is a geometrical factor determined by the relative sizes of the two stages that ranges from 0.5 to 1. Kirchoff's law of thermal radiation, which states that the emissivity of a surface equals the absorptivity of that surface, has also been applied. Since $T_w/T_c \approx 2$ to 5, the cold-stage radiation term is much smaller than the warm-stage term and is generally ignored.

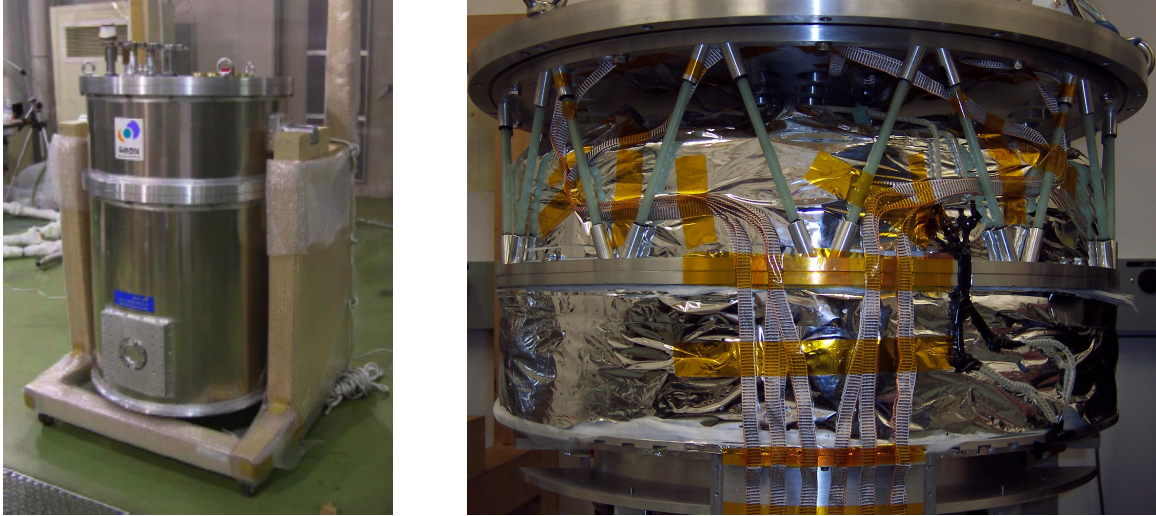


Figure 3.3. Two pictures of the cryostat, one shortly after delivery from Japan, the other after cryogenic cabling installation. The photo on the left shows the whole cryostat; the blanked-off window can be seen near the bottom and the fill ports are on the top left. The picture on the right shows the exposed nitrogen tank, wrapped in shiny MLI. The light-green G10 rods, in a drum-head configuration, mechanically support and thermally isolate the tank from the room-temperature vacuum jacket. One of the vacuum sealing surfaces is seen at the top of this picture, though the O-ring has been removed from the groove. Though it cannot be seen in this picture, the helium tank is supported by a similar series of G10 rods around the inner surface of the toroidal nitrogen tank. Each cryogenic cable has 48 to 50 three mil diameter manganin wires woven together with thin string. These cables attach to the cryostat with orange kapton tape. In addition, the black structure to the right of center is a 77 K heat sink for the ADR magnet leads. The black epoxy is stycast which electrically isolates while providing good thermal conductivity.

3.3 System Components

3.3.1 Cryostat

The Z-Spec cryostat is a typical cylindrical shape, about 1.2 meters tall and 0.8 meters in diameter. It was designed by Johannes Gromke while he was a postdoc at Caltech and built by the Japanese company SAAN, who were contracted for the work by our Japanese collaborators, led by Hideo Matsuhara of ISAS. It is a standard wet cryostat with liquid He and liquid N₂ tanks and a side-looking window. Z-Spec's cryogen tanks are fairly large, about 20 liters for nitrogen and 30 liters for helium to achieve the 48-hour hold time requirement. These large tanks and the desire for a large volume inside the helium radiation shield led the design to an unusual configuration. Instead of having the cryogen tanks stacked on top of one another inside the vacuum jacket, they are mounted concentrically such that the cylindrical He tank is surrounded by a toroidal N₂ tank. The two tanks are mounted around their outer circumference with G10 rods in a drumhead pattern.

Cold plates are attached to both tanks at approximately the same level inside the cryostat. The nitrogen work surface is a small segment of the circular cross section inside the vacuum jacket. The

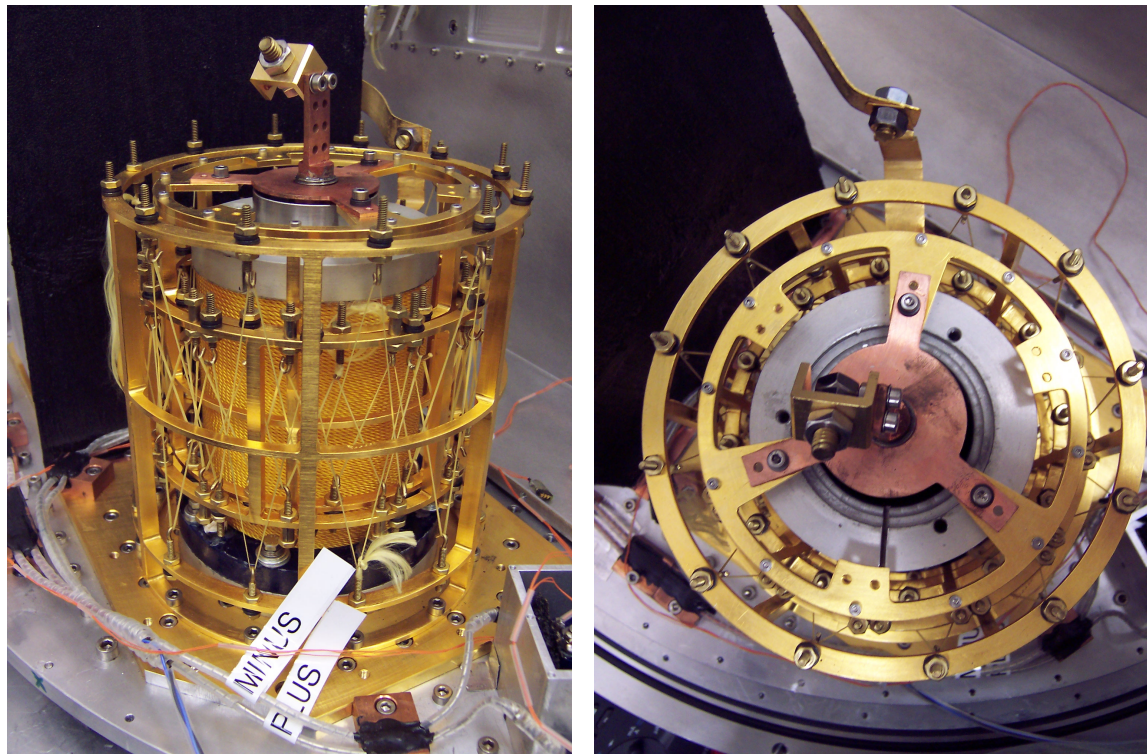


Figure 3.4. These pictures show a side and top view of the ADR and the kevlar suspension system for the salt pill with the enclosing radiation shield removed. The suspension system uses three open columns of gold-plated aluminum connected to various temperature stages. The outer column along with the magnet and radiation shield are mounted to a gold-plated copper interface plate on the helium work surface. Suspended from the outer column is an intermediate support stage whose strap to the ^3He pot can be seen extending up the top of the image on the right. The interior column, suspended from the intermediate stage, supports the cylindrical salt pill in the center bore of the magnet. The salt pill has a copper finger extending above for thermal linking to the grating. On the bottom of the left side image, the superconducting magnet leads are seen stycasted into several copper heat sinks. The radiation shield around the persistence switch can be seen in the lower right-hand corners of both images.

internal J-FET followers sit on the nitrogen work surface and self-heat up to 140K, their optimal operating temperature. The helium work surface covers much of the rest of the interior cross section and thus its radiation shield is a partial cylinder with a planar face parallel to the cylinder's axis. This is well suited to the planar geometry of the grating design. The grating mounts on the planar face bisecting the cryostat. Both the radiation shields are wrapped on the outside in multilayer insulation (MLI) which is very reflective thereby reducing the radiative load from the vacuum shield at 293 K to the 77 K nitrogen shield and from the nitrogen shield to the 4.2 K helium shield.

3.3.2 Adiabatic Demagnetization Refrigerator

The base temperature for operating Z-Spec is established by an adiabatic demagnetization refrigerator (ADR) which is capable of cooling the entire grating system to less than 100 mK. We use a

sealed ferric ammonium alum (FAA) salt pill for which the entropy is entirely magnetic below about 1.5 K. After aligning the isolated spins in the FAA pill by applying a magnetic field, extracting the heat of magnetization and slowly decreasing the applied field, the entropy available is approximately $\ln(6)$ times the ideal gas constant (R) per mole of salt. Our pill contains about one-half of a mole of FAA, so its 7 J/K cooling capacity is sufficient to cool the whole grating, which has about 0.5 J/K of entropy at 1.5 K. A thermal break between the detectors and the grating is not necessary; however, the radiative and conduction loads from the 4.2 K He bath would quickly overwhelm the ADR. That power must be intercepted at an intermediate temperature.

3.3.3 Helium-3/Helium-4 Sorption Cooler

The sorption cooler [Duband 2000] and gas-gap heat switches were provided to the project by Lionel Duband and his team at Service des Basses Températures in Grenoble, France. Both stages of the cooler use the principle that the boiling point of a liquid depends on the pressure of the gas above it. Normal helium with two protons and two neutrons in the nucleus boils at 4.2 K at STP, but that boiling point can be reduced to less than 2 K by pumping away the gas as it boils off. ^3He with only one neutron in its nucleus condenses below 3.2 K and can be pumped down below 400 mK. The pumps are made from porous charcoal. A metal cylinder packed with charcoal can store large amounts of helium gas if kept below 15–20 K. Heating a charcoal reservoir filled with He above those temperatures will force the gas out. The gas comes out of the charcoal (or pump) heated but can be condensed if it contacts a bath at temperatures below its triple point. The ^4He system uses the cryostat helium bath to induce its condensation. The condensed liquid drips into a pot and then the pump is cooled off. The 4.2 K pump draws the gas off the condensed liquid which lowers the liquid's temperature. The pumped ^4He stage can then be used to condense the ^3He gas. These stages work together to extract the heat of magnetization of the FAA salt pill in the ADR, precool the grating and protect the ADR from the 4.2 K wiring and radiation loads. The cycling details will be discussed in section 3.4.1.

With a pumped ^3He liquid bath as a thermal guard, the hold time of the half-mole salt pill should be many days. Therefore the 48-hour hold time goal is dependent on the hold time of the ^3He stage of the sorption cooler. It was designed to absorb a continuous $50 \mu\text{W}$ load for two days, or a total of 8.6 J. The dominant loads delivered to the ^3He stage are the conduction load from the bolometer readout wires and the 4.2 K radiation load on the ^3He radiation shield surrounding the grating. The 400+ readout wires are made of 3 mil diameter manganin alloy, which has good electrical but modest thermal conductivity. If the cables are assumed to be sunk at about 5 K, then the conduction load through the 20 cm length of wires is about $15 \mu\text{W}$. In addition, the ^3He radiation shield has almost a square meter of surface area and is cooled to well below 1 K by the ^3He pot. The radiation load it receives from the enclosing ~ 5 K ^4He bath shield is almost $35 \mu\text{W}$

assuming both shields have unit emissivity. In addition, there are loads on the ^3He pot from its pump line and one of the heat switches, but both of these are delivered via ~ 1 cm diameter stainless steel tubes with 3 mil thick walls. Stainless steel has even less thermal conductivity than manganin so these contributions are negligible.

3.3.4 Gas-Gap Heat Switches

The gas-gap heat switches use principles similar to the sorption cooler stages and are essential components to the efficient heating and cooling of the pumps. Gas-gap heat switches have high on-state conduction which is crucial to effective cooling of the large grating mass, from both room to cryogenic temperature, and from 4.2 K to demagnetization temperature. The two ends of the switch are supported mechanically by a sealed thin-walled stainless steel tube. Within the stainless steel tube are concentric copper tubes extending from both ends but only connected to one (or the other) end. One copper tube has a slightly smaller diameter than the other and the smaller inserts into the larger; they are separated by about 3 mils. In addition, there is a small piece of charcoal in a sealed can with a heater and a thin capillary tube that connects to the sealed chamber within the stainless steel tube. This chamber is filled with helium gas which provides thermal conductivity between the two copper fingers when it is heated out of its charcoal pot. This creates a simple electrical control between the on and off states of the heat switch. The heat switch's conductivity can be turned on quickly by applying current to the heater on the charcoal pump. It turns off more gradually because the charcoal takes a few minutes to cool off after the current applied to its heater is shut down. The off-state conductivity through the stainless steel tube depends on the temperature of the two ends of the switch, but this is orders of magnitude less than the on-state conduction from conductivity through the gas. Gas-gap heat switches were chosen because strong on-state conductivity was more important than minimizing off-state conduction.

3.3.5 Thermal Mounts

The mechanical support of the ^3He radiation shield and the grating is based on a thermally isolating, mechanically rigid module that was designed by Lieko Earle of the University of Colorado, Boulder, inspired by a design by Peter Hargrave. They use braided kevlar string for mechanical support which has extremely low thermal conductivity; almost an order of magnitude less than G10 at 1 K. The kevlar is strung in a drumhead pattern between two concentric cylindrical structures which do not touch each other. The two ends of the interior structure are supported by a stack of spring washers in order to absorb the expansion of the kevlar string as it cools. The interior and exterior cylindrical structures have mechanical attachment points and are strongly thermally isolated. The modules are used in parallel and the primary load is in the radial direction. Each module can support about 10

N of force (1 kg at 1 G) radially and several tens of N in the (obviously) stronger axial direction. Z-Spec uses seven modules to support the grating from the ^3He radiation shield, and that assembly is supported by eight additional modules mounted at 4.2 K. Close-up pictures of the modules and the integrated mounting structures can be seen in figure 3.6.

3.4 System Operation

3.4.1 Cycling Procedure

In the previous section, the basic operating procedures for the various components of the cryogenic system were outlined. The integrated method for reliably cycling all of the components was developed through many iterations. The procedure starts by turning on HS 3 and 4 and turning off HS 1 and 2. Then, current is driven into the superconducting magnet which aligns the spins in and heats up the FAA salt pill. The current is ramped up to 20 amps in about a half an hour. The heat of magnetization travels through the grating and the two activated heat switches and is dumped to the helium bath at the base of the sorption cooler. As magnetization begins and the pump heat switches turn off, current is applied to the pump heaters, warming the ^3He and ^4He pumps to 40 K and 45 K, respectively. These temperatures are maintained via software regulation which adjusts the voltage applied to the pump heaters based on the value and derivative of the pump temperature. After several tens of minutes at maximum heating voltage, the pumps reach their set temperatures and the applied voltages reduce to about 6 to 8 volts for each pump.

The current in the magnet must be maintained until the salt pill is cold enough for demagnetization; less than about 2 K. Z-Spec's superconducting magnet includes a persistence switch which simplifies achieving this requirement. The persistence switch is a small piece of superconductor that has a heater attached and is wired in parallel with the magnet. The superconductor has zero resistance at 4.2 K, but goes normal above about 10 K. Applying current to the heater controls the switch. An external power supply is used to control the current in the magnet, but it can only apply this control when the persistence switch is heated into the normal conducting state. Both the magnet and the persistence switch have zero resistance to DC currents at 4.2 K, but the magnet has AC impedance from its inductance. To ramp up the current in the magnet, the persistence switch is heated and then the power supply ramps up the applied current. Then the persistence switch heater current is turned off and it returns to the superconducting state. Changing the applied current from the external power supply now has no effect on the current in the magnet, so the applied current can be quickly ramped down to zero.

After baking the ^4He pump for 60 to 75 minutes, most of the ^4He gas has condensed and dripped into its pot. With the ^4He condensed and the ^3He gas forced out of its pump, it is time to start pumping on the ^4He liquid to cool it below 3.2 K and allow the ^3He to condense. A few minutes

before ^4He baking ends, HS 3 is turned off. It is no longer necessary to have this supplemental link to the helium bath because the heat of magnetization has already dissipated. When HS 1 is closed, pumping on the ^4He liquid begins and it slowly cools. The charcoal is an effective pump, but the ^4He pot is cooling the ^3He gas, the ^3He radiation shield, the grating and the salt pill. Pumping on the ^4He continues until the liquid runs out or the salt pill gets below a certain threshold temperature, below which demagnetization will yield a good base temperature. If the ^4He liquid runs out before this threshold temperature is achieved, then pumping begins on the now condensed ^3He liquid to achieve additional pre-cooling of the salt pill and grating.

Once the salt pill temperature threshold is achieved, HS 4 is turned off, isolating the grating and salt pill system. The ^3He guard must be in place once the demagnetization process is complete to protect the salt pill from the 4.2 K loads. ^3He pumping is activated by turning off the current to that pump's heater and switching on HS 2, which occurs either when demagnetization starts or when the ^4He liquid runs out and additional salt pill pre-cooling is necessary. The demagnetization process begins by quickly ramping the external applied current up to the current that was established in the magnet during the magnetization phase. Then the persistence switch heater current is switched on and the persistence switch becomes a normal conductor. The applied current can be slowly ramped down, pulling the magnet current with it. The temperature of the salt pill drops at a rate proportional to the rate of change of the magnet current, though if this rate is too high, eddy current heating will reduce the cooling rate of the salt pill. For a typical cycle, the 20 amps of magnet current is drawn out over about one hour.

When the magnet current reaches zero and the persistence switch heater current is switched off, the cycle is complete, though it takes an additional hour for the temperatures of the salt pill and grating to equilibrate. Both pumps are drawing gas off the liquid in the pots. Since the ^4He pot is only used to condense the ^3He and cool the salt pill/grating assembly, there is no effect when the ^4He liquid runs out. However, once the ^3He liquid runs out it will warm up quickly and cease to effectively guard the ADR, which rapidly warms up in response. The system is ready to be cycled again.

3.4.2 Cycle Performance

Several cycles of cooling down and warming up the cryostat were used to test the cryogenic system before the grating was installed. First the $^3\text{He}/^4\text{He}$ sorption cooler was tested by itself. Initial testing demonstrated the crucial importance of the temperature and thermal conductivity to the helium bath of the cooler base. Mounting the angle bracket directly to the aluminum cold plate was insufficient, probably due to the way the cold plate extends beyond the diameter of the helium tank. A large, high-purity copper plate was firmly attached to the cold plate and the angle bracket to this copper plate. This enabled sufficient conductivity at the base of the cooler.

This conductivity is crucial because the sorption cooler can fail in two ways if the conductivity is insufficient. When the pumps are first heated, they force hot gas into the pump lines and pots. Along both pump lines, there is a heat tap to the cooler base. This heat tap must get below 5.2 K, the triple point of ^4He , to condense that gas into liquid. If this does not occur, then there will be no ^4He liquid to condense the ^3He gas. Furthermore, if the sorption cooler base conductivity is poor when the hot pump's heat switches are turned off, they dump their energy into the base, heating it up dramatically. If this energy is not quickly delivered to the helium bath, it can leak into the condensed liquid, boiling it away very rapidly.

Once the sorption cooler base conductivity was high enough, the cooler's load handling capabilities were assessed. By pumping the ^4He to exhaustion before starting to pump on the ^3He , the cooler beat the 50 μW load for 48 hours specification by almost 40%. The ^3He pot could absorb over 12 J before running out of liquid.

Integrating the ADR system was fairly involved but straightforward. However, initial tests showed that the original salt pill we used, which was almost 10 years old, had lost a significant amount of capacity. It seemed to contain less than one eighth of a mole of operable FAA rather than the half mole we needed. A freshly made pill worked very well. As expected, the hold time was determined by the ^3He stage of the sorption cooler, which was fairly short until some hot radiation leaks through the filters were sealed (see discussion in section 2.2.2).

Because of the unexpected filter leakage, the hold time of the ^3He stage is somewhat less than 48 hours and more importantly, the salt pill warms up too much over this time. Therefore, the system is cycled every 24 hours to keep the bolometers cold enough. The salt pill warms up more slowly at lower temperatures, so the key to a good cycle is getting a low final temperature. This is not strongly correlated to the temperature of the salt pill when the demagnetization begins. However, the demagnetization rate does have a significant impact on the final temperature, presumably due to reduced eddy current heating. A cycle takes about 5 to 6 hours and the salt pill bottoms out around 60 mK, though a slower demagnetization rate can get the salt pill just under 50 mK. At the end of a night of observing, the salt pill is up to 80 to 90 mK which is still sufficiently cold. Typical cycles at the Caltech Submillimeter Observatory are shown in figures 3.7 and 3.8.



Figure 3.5. This photo shows one side of the sorption cooler installed in the cryostat. It is upside down relative to the operating configuration. The ^3He pot is seen at the top in the center. To its left is HS 4 from figure 3.2 which connects to the grating and salt pill. There is a strap extending down diagonally to the right of the pot which connects to HS 3 which connects to the helium bath. The ^4He pot is below this diagonal strap. The pump tubes extend down below both pots and wrap around the bottom to the pumps on the other side of the aluminum plate. Neither the pumps nor the pump heat switches (HS 1 and 2) can be seen in this picture. The cooler is mounted to the cold plate via a copper right-angle bracket and a gold-plated copper interface plate. The helium work surface, made of aluminum, extends near the edge of the cryostat, but the helium tank has a much smaller diameter; thus there is a lip of aluminum around the perimeter of the work surface that does not have direct coupling to the liquid helium tank. The copper interface plate improves the thermal conductivity of the sorption cooler base to the helium bath which is vitally important for its operation.

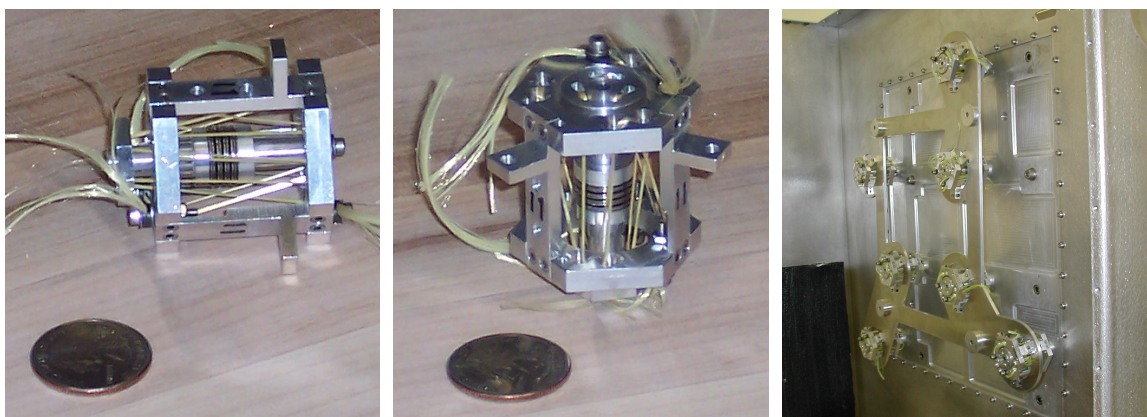


Figure 3.6. The left and center photographs depict an individual mounting module and a quarter to indicate the scale. The outer support is a hollow hexagonal prism with three tabs extending radially for mechanical attachment. The yellow kevlar string threads between the outer support and the two-piece internal column. The dark lines in the middle of the internal column indicate the stack of belleville spring washers that are compressed by the tight kevlar at room temperature. As the mount cools and the kevlar stretches out, the washers expand to keep the kevlar under tension. There is a tapped hole on one end of the internal column for mechanical attachment.

The photograph on the right shows how several thermal modules are integrated to support the weight of the grating. Most of the frame is filled by the ^3He radiation shield which is supported by eight unseen modules attached to a plate that extends perpendicularly from the helium cold plate. Seven modules connected to an adapter plate are attached inside the ^3He shield. The grating attaches to the four squat posts extending from the adapter plate.

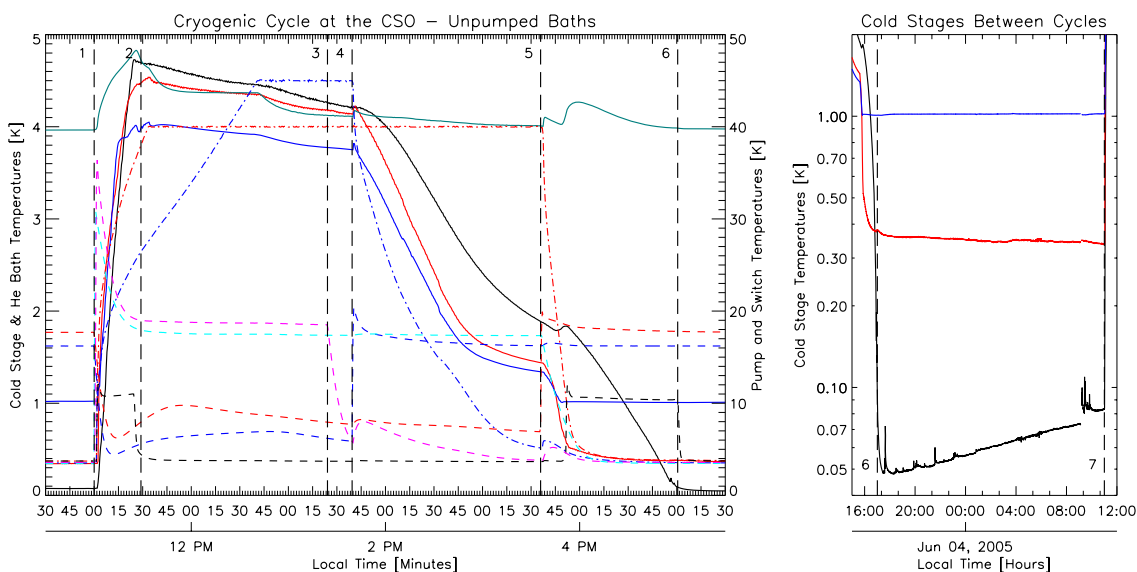


Figure 3.7. These two plots show the cycling process and performance for a typical cycle at the Caltech Submillimeter Observatory. The helium and nitrogen baths are in contact with the local atmospheric pressure which makes for slightly cooler baths than at sea level (the ^4He bath is slightly below 4.0 K). The plot on the left shows various temperature stages over the course of a 6-hour cycle which starts at 11 AM on Jun 3, 2005. All the solid lines use the scale on the left while the dashed and dash-dotted lines use the ten-times-larger scale on the right. The salt pill is shown in solid black, the ^3He pot, pump and pump heat switch (HS 2) in blue, the ^4He components in red, the ^4He bath in dark green, HS 3 in purple, HS 4 in cyan and the persistence switch in dashed black. All the switches' temperatures are drawn with dashed lines while the pumps are drawn with dash-dotted lines. The vertical lines indicate certain cycle events. Line number 1 is the start of the cycle. Line 2 marks the end of the magnetization phase. At line 3, HS 3 is switched off in preparation of pumping on the ^4He at line 4. The salt pill reaches the 2.0 K trigger temperature by line 5 and ^3He pumping begins as HS 4 is closed. The demagnetization phase starts when HS 4 is cold enough and ends at line 6.

The plot on the right shows the cold-stage temperatures during the course of that night's observing, using the same colors as the plot on the left. The scaling for this plot is logarithmic which highlights the rise in temperature of the salt pill over the course of the evening. After the cycle is complete at line 6, the salt pill temperature falls for another hour as it and the grating come into equilibrium. The temperature glitches in the salt pill reading are likely due to mechanical effects. The grating is very thermally sensitive to vibration and this cycle occurred early in the engineering run. It is possible that people walking around the cryostat caused the grating to vibrate and warm up. This cycle bottomed out at just under 50 mK, which is the calibration limit of the sensor on the salt pill and rose to 85 mK when the next cycle ran at line 7 at 11 AM the following morning. The 1.0 K ^4He pot reading is also the limit of that sensor's calibration and so it might be somewhat colder. In this case it indicates that ^4He liquid remains in the pot. Some other features of this cycle will be discussed in comparison to the cycle shown in figure 3.8.

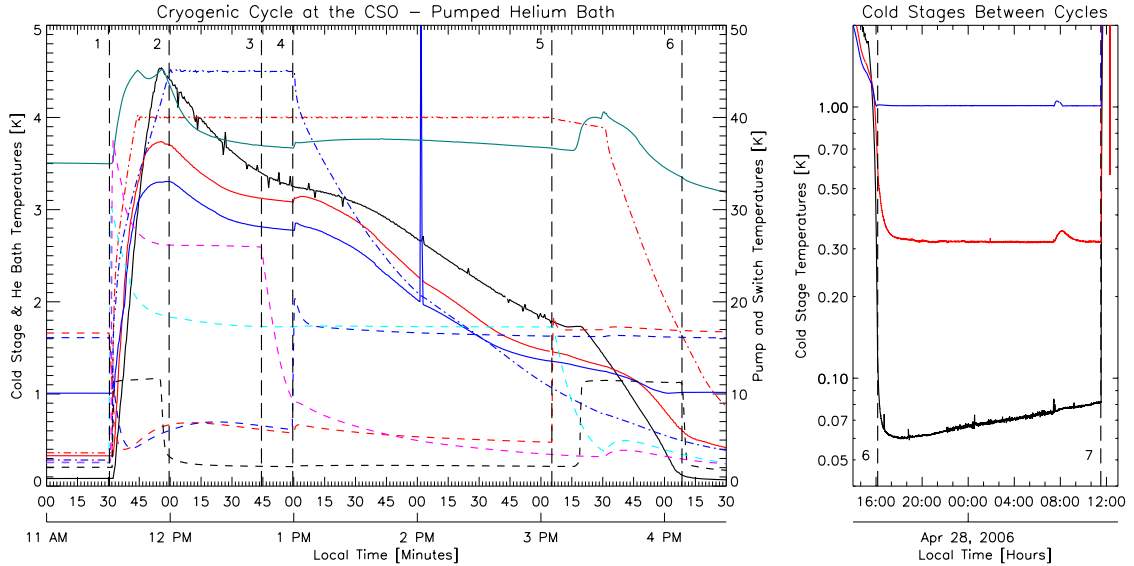


Figure 3.8. These two plots show a typical cycle from the first observing run, specifically from Apr 27, 2006. The helium bath is on the pump for this cycle which explains why most of the temperatures are lower than in the cycle shown in figure 3.7. These plots use the same legend as described in the previous figure's caption.

Other than the pumped bath, there are several other differences to highlight. The glitches in the salt pill reading and the large glitch at 2 PM in the ^3He reading can be ignored. Both pumps heat up to their set temperatures much more quickly because stronger power supplies are driving their heaters. These power supplies are capable of applying 36 volts to the 400 ohm heaters plus 200 ohms of leads as opposed to the 25 volt maximum for the power supplies used in June 2005. The pumps cool more slowly as well because more flexible, lower conductivity straps were installed between June 2005 and April 2006. Furthermore, the ^3He pump does not immediately start to cool off when its heat switch is closed at line 5 as the ^4He pump does at line 4. The delay between applying voltage to a heat-switch heater and the commencement of thermal conduction 30–45 minutes later is sometimes seen in HS 3 and HS 4. The solution to this delay is to apply a larger initial voltage to spike the heat-switch temperature well above the desired 15–20 K. A possible cause for this delay is that the gas ejected from the charcoal in the heat switch condenses before it can provide conductivity between the two concentric copper tubes.

The demagnetization phase is faster for this cycle which achieves a base temperature of 60 mK. The thermal loading on the grating is reduced compared to the 2005 cycle and so the salt pill warms to only 80 mK by the time the next cycle runs. The faster pump heating and demagnetization generate a shorter cycle time of 4.5 hours.

Chapter 4

Bolometer Readout and Signal Sensitivity

4.1 Bolometer Operation

Bolometers are thermal detectors which detect light by absorbing photons, warming up and detecting the increased temperature with some kind of thermometer, typically a thermistor. The changing resistance of the thermistor can be read out using a simple electrical circuit and the reading from the electrical circuit can be used to measure the power of the incident radiation. Bolometers are subject to a fundamental noise limit based on phonon fluctuations that can be characterized in terms of a noise equivalent power (NEP), which is the amount of incident optical power necessary to produce a signal-to-noise ratio of unity. The NEP of a bolometer is related to the operating temperature T and its thermal conductance G by the formula $\text{NEP}_{\text{bolo}} \sim \sqrt{4kT^2G}$. This formula is derived in Richards [1994] and is clearly related to the formula for Johnson noise in a resistor. The thermal conductance cannot be made arbitrarily small without slowing down the response of the detector, which has a time constant given by C/G , where C is the heat capacity of the absorber. Both of these quantities must be lowered to reduce thermal noise and produce a useful detector.

Si_3N_4 micromesh bolometers [Mauskopf et al. 1997] can be designed to effectively absorb millimeter-wave photons using very small volumes and thus can have very small heat capacities. The thermal conductance of the absorbing layer of the bolometer is independent of geometry and simply proportional to temperature [Turner et al. 2001]. The dark-noise requirement for the bolometers is set so that the dominant noise comes from fluctuations in the photon background (see section 4.3). We chose a dark-noise level of $\sim 4 \times 10^{-18} \text{ W Hz}^{-1/2}$, including readout noise, which requires operating the bolometers at 100 mK and gives a thermal conductance of $\sim 15 \text{ pW/K}$. The heat capacity is determined by the volume of the different components that make up the bolometer design and the corresponding volumetric specific heat of those components. The largest contribution to the heat capacity comes from the neutron-transmutation-doped Ge thermistor and the overall heat capacity

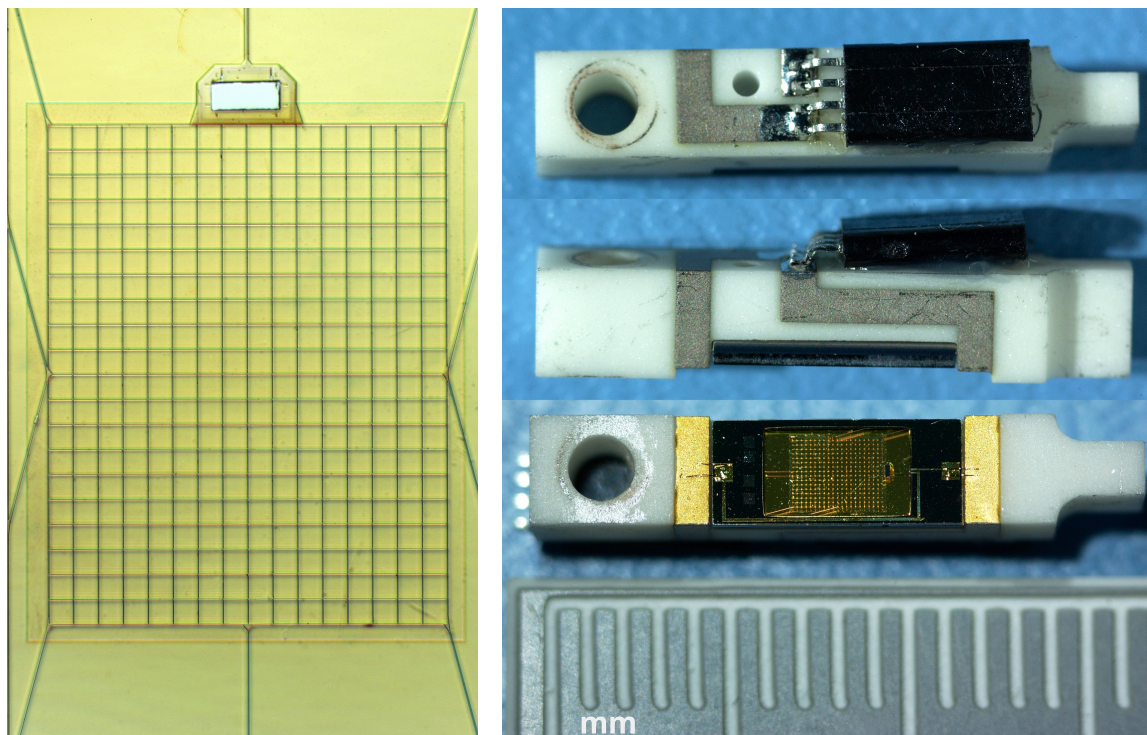


Figure 4.1. The photograph on the left shows the mesh of a Z-Spec bolometer. The active area is 2.5×2.0 mm. The thermistor is the silver rectangle above the mesh. The pictures on the right show three sides of a detector key and a millimeter scale ruler. The small black connector on the back side has four pins (wired in pairs) and mates to a short cable that carries the bolometer signal away.

is designed to give a time constant of ~ 15 ms. Each detector chip, which measures $7 \text{ mm} \times 3 \text{ mm}$ is glued to a backshort chip of the same size. A quarter-wave backshort can improve absorption efficiency significantly. While a quarter-wave backshort works best on resonance, the resonance is fairly broad and we found that two backshort distances would work to effectively cover the Z-Spec frequency range.

The detector chip and backshort assembly is glued to a mounting device called a detector key. It is made from the ceramic material alumina and has traces painted on it. On one side of the key the traces are wire bond pads for establishing an electrical connection to the bolometer chip. The two traces then route down one side of the key and onto the back side where a connector is soldered to the traces and glued to the key. This assembled key has a tight fit screw hole and a narrowed section that fits between two alignment tabs on the output sides of the bend blocks. Since the keys are modular, they can be replaced easily in case a detector fails. After several iterations, 100% spectral coverage can be obtained. A fully assembled key can be seen in figure 4.1.

4.2 Bolometer Readout Electronics

The fundamental goal of bolometer readout is to measure the resistance of the thermistor. The simplest way to do this is to current bias the bolometer and measure the voltage drop across the device. This is complicated by the fact that the bolometer resistance can be very large (a few $\text{M}\Omega$) if the optical loading is small and the base temperature is low. This requires a larger load resistance to convert a voltage source into a current bias for the bolometer. For our readout circuit, we use a symmetric bias setup with a pair of $30 \text{ M}\Omega$ load resistors in series with the bolometer (see figure C.1).

The voltage signal across the bolometer is delivered to cryogenic J-FET amplifiers wired in a source-follower configuration. A matched pair of J-FETs is used to transform the source impedance of both ends of the bolometer signal. Due to the high source impedance of the signal prior to the J-FET transformation, the signal is very susceptible to RF and microphonic pickup. To block the RF signal, we designed a box for the J-FETs that encloses them and seals to the nitrogen radiation shield, which serves as the RF cage. To minimize microphonic pickup, we worked hard to bundle the cryogenic cables together, using stiffening members to help drive up the resonant frequencies.

The signals are carried out of the cryostat into the room temperature electronics (RTE) system which was custom designed for Z-Spec and a few other instruments. In addition to the readout functionality, the RTE produces bias for the bolometers and the J-FETs. The bolometers can be biased in AC or DC mode: DC mode is useful for making load curves which allow measurement of bolometer loading and bolometer parameters while AC mode is used for astronomical observing. A diagram showing the flow of signals from the bolometers to the components of the RTE to the data

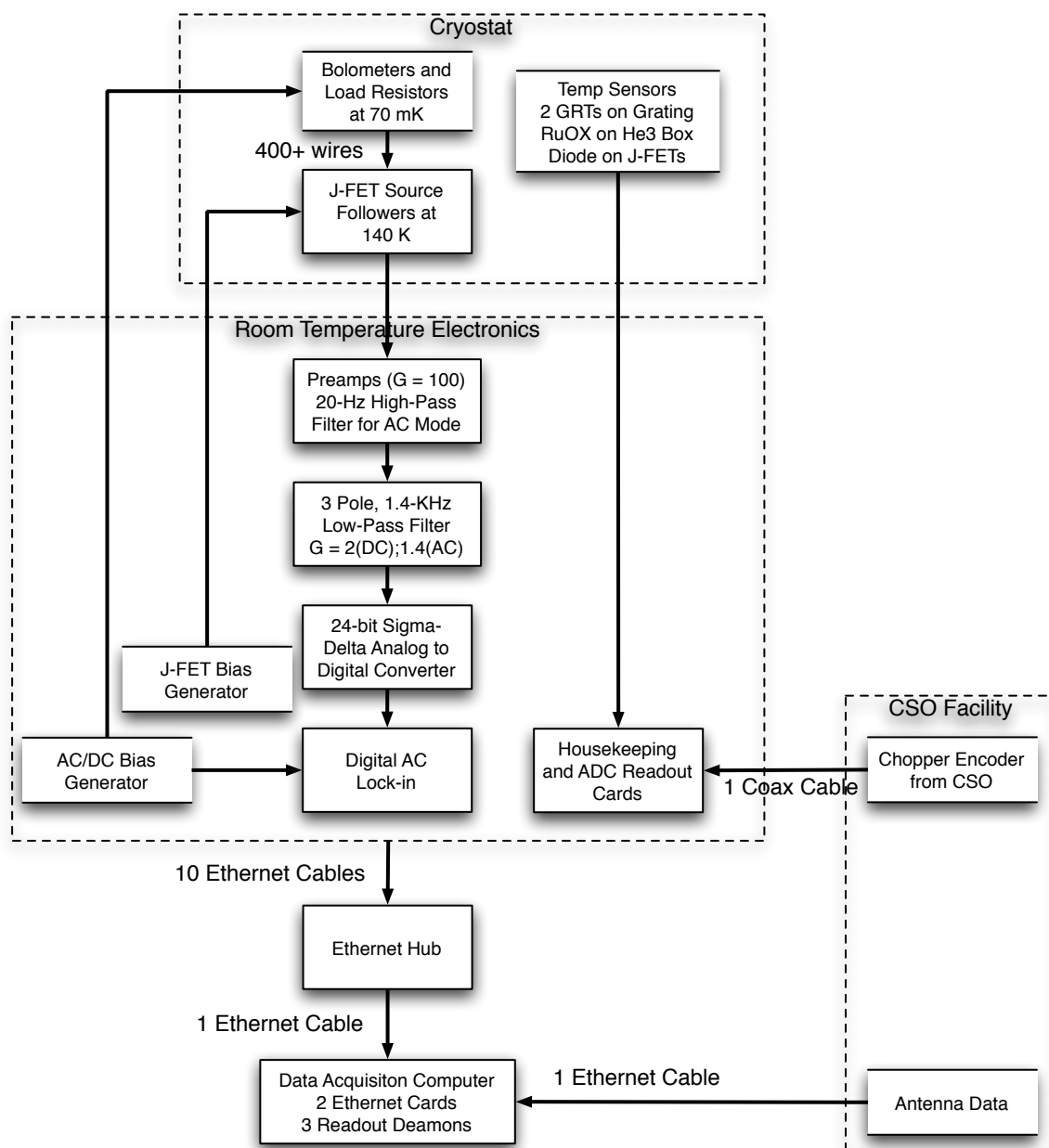


Figure 4.2. This diagram indicates the flow of signals from the bolometers through the readout electronics and onto the data acquisition computer, including the connections to the CSO facility resources used by Z-Spec. A full description of the components of this system can be found in the text.

acquisition computer is shown in figure 4.2.

The readout system can handle both AC and DC modes. There is a differential instrumentation amplifier with gain $G = 100$ and an optional 20-Hz high-pass filter for AC coupling on the input. Following that is an anti-aliasing, three-pole low-pass filter with a knee at 1.4 kHz and a factor of 2 or $\sqrt{2}$ gain for DC or AC mode, respectively. This signal is digitized by a 24-bit sigma-delta analog-to-digital converter sampling at 32 times the bias frequency; programmable logic performs the AC lock-in function digitally. Both quadrature phases (X and Y) of the lock-in product are averaged over 64 samples by a programmable low-pass filter and reported to a controller card once every two bias periods. The bias frequency is adjustable and is typically set to 70-100 Hz. The data are collected and organized into ethernet packets for transmission to a host computer which records the data to disk. The host computer can also issue commands to the electronics to control the bias parameters and to switch between AC and DC modes. The RTE also include a few speciality cards for digitizing some cryostat housekeeping and telescope signals, particularly the chopper encoder.

The lock-in amplifier (LIA) provides both phases of the lock-in signal, which correspond to the real and imaginary parts of the bolometer signal at the input to the RTE; $Z = X + jY$. The ideal readout scenario would be to adjust the phase of the lock-in reference signal in order to drive all of the signal into only one of these components, such that the perpendicular component could be ignored. A more typical procedure would be to take the quadrature sum of the two components, $\sqrt{X^2 + Y^2}$, but this may reduce the signal-to-noise ratio.

There is a further complication in using the quadrature sum of the two lock-in components due to the presence of reactive elements in the readout circuit. The cryogenic cables inside the cryostat have some intrinsic capacitance and the J-FETs have input capacitance, both of which can roll off the high-impedance bolometer signal before the impedance transformation in the J-FETs. This causes the two quadrature components from the LIA to diverge from a linear trajectory in the complex plane as a function of the bolometer resistance, $Z(R_b)$. The effect is strongest when the bolometer impedance is largest or when the loading is smallest.

The ideal signal extraction method for a given operating point would be to select the tangent dZ/dR_b of the roll-off curve and project the two LIA components onto that vector. This technique avoids the S/N degradation that can occur when using the quadrature sum. A simple electrical model is derived in appendix C which can be used to fit the necessary roll off parameters and apply the optimal projection.

4.3 Photon Noise and Z-Spec Sensitivity

Several noise sources effect Z-Spec's performance. Some can be controlled by design choices: for example, the bolometer noise or RTE noise. Other noise sources, like microphonic noise, can be

controlled by careful assembly. However, the fundamental noise source that cannot be reduced or eliminated by careful design is photon background noise which comes from statistical fluctuations in the number of photons incident on the detectors [Hanbury Brown and Twiss 1956; Benford et al. 1998; Zmuidzinas 2003].

The astronomical power detected by Z-Spec is many orders of magnitude smaller than the power received from the atmosphere, telescope and from ground scattering, etc. This sky and telescope loading must be cancelled using a chopping scheme in order to detect the astronomical signal, but the loading dominates the photon noise. Blackbody radiation at a temperature T can be characterized by the Planck distribution of photon occupation number which describes how many photons occupy a single spatial-polarization mode at a particular energy (or equivalently, frequency, ν).

$$n_{phot} = \frac{1}{e^{\frac{h\nu}{kT}} - 1}, \quad (4.1)$$

where h is Planck's constant and k is Boltzmann's constant. The NEP due to this distribution is given by $NEP_{phot} = h\nu \sqrt{2\Delta\nu n_{phot}(n_{phot} + 1)}$, where $\Delta\nu$ is the detector bandwidth.

The photon occupation number distribution that lands on a detector is modified from the standard formula by two important considerations. First, the optical efficiency of the instrument only allows a fraction of the photon distribution to get into the spectrometer. Second, the atmosphere is mostly transparent at our frequencies, and thus the background emissivity is reduced from unity. Using the same temperature for the atmospheric and ground loading, the proper photon distribution \bar{n} to use in the equation for photon NEP is

$$\bar{n} = \eta [1 - \xi T_{atm}(\nu : \tau_{225})] n_{phot}, \quad (4.2)$$

where η is the optical efficiency of the instrument including the detector absorption efficiency and ξ is the forward efficiency of the telescope (about 0.9 at the CSO). T_{atm} is the transmission of the atmosphere, which is a function of frequency ν and the observing conditions characterized by τ_{225} , the atmospheric optical depth at 225 GHz. For typical observing conditions at the CSO ($\tau_{225} = 0.1$, observing at a zenith angle of 35°) and assuming 20% instrument transmission, this works out to be $\sim 5-10 \times 10^{-18} \text{ W Hz}^{-1/2}$ using the measured detector bandwidth shown in figure 2.9. This is combined in quadrature with the detector and electronics noise given above to give the total noise at the detector, NEP_{tot} .

A more interesting sensitivity measure is the noise equivalent flux density (NEFD) which describes the sensitivity to a given flux at the top of the atmosphere. The NEFD is a straightforward

scaling of the NEP_{tot} given above,

$$\text{NEFD} = 2 \times 2 \times \frac{1}{\eta \zeta T_{atm}} \times \frac{1}{\nu A_{tel} 10^{-26}} \times \frac{\text{NEP}_{tot}}{\sqrt{2}} \quad \text{Jy} \sqrt{\text{sec}}. \quad (4.3)$$

The two initial factors of two come from chopping and polarization. Chopping increases the NEFD by two factors of $\sqrt{2}$: one because half the integration time is spent looking off source and the other because two measurements with roughly equal noise are subtracted from each other. Since Z-Spec is a single polarization instrument and the polarization of the light from the galaxy is random, we need twice as much power at the top of the atmosphere to generate a given signal at the detectors. An additional factor of $\sqrt{1.6}$ should be included when calculating the line sensitivity because, on average, 1.6 detectors will be needed for a detection. The next set of factors comes from the transmission efficiency of the instrument, η , the Ruze-corrected aperture efficiency of the telescope, $\zeta = \zeta_0 \exp(-4\pi\sigma/\lambda)$, and the transmission through the atmosphere, T_{atm} . The final set of factors converts from units of power to units of Jy ($10^{-26} \text{ W m}^{-2} \text{ Hz}^{-1}$), where $A_{tel} = \pi D^2/4$, the area of the CSO ($D = 10.4 \text{ m}$). The final $\sqrt{2}$ converts the $1/\text{Hz}^{1/2}$ to $\text{sec}^{1/2}$ because one second of integration time corresponds to 0.5 Hz of bandwidth. The aperture efficiency of the CSO is about 75% with a surface quality $\sigma = 25 \mu\text{m}$ which gives a predicted flux sensitivity of about $0.4 \text{ Jy} \sqrt{\text{sec}}$.

4.4 Noise Measurements

The timestreams coming from the readout electronics contain signals at many frequencies. The strongest signal should be the chopper-modulated signal from the telescope. The rest of the spectral content will be noise and harmonics of the chopper. The noise spectrum has several components: a white-noise floor, $1/f$ noise rising above the noise floor at low frequencies and microphonic noise at high frequencies. The contributions of these noise sources determine how well the chopper-modulated sky signal can be extracted. Plots of typical noise spectra can be seen in figure 4.3.

One method for analyzing the spectral content of a timestream is via the discrete Fourier transform (DFT) which can be used to convert from the time domain to the frequency domain for a sampled waveform. We are free when using the DFT to choose a suitable normalization. One such normalization developed in Aguirre [2003] deliberately links the components in the power spectral density (PSD), the squared magnitude of the complex DFT, and the statistical characterization of fluctuations in a time series, namely the variance. With this normalization, conversion from PSD amplitude to sample variance simply requires dividing by the total integration time being evaluated. When this is combined with the calibration scheme outlined in appendix D, a direct comparison with the predicted NEFD from the previous section can be made.

Using the observations of M82 described in chapter 5, we find that the measured sensitivity

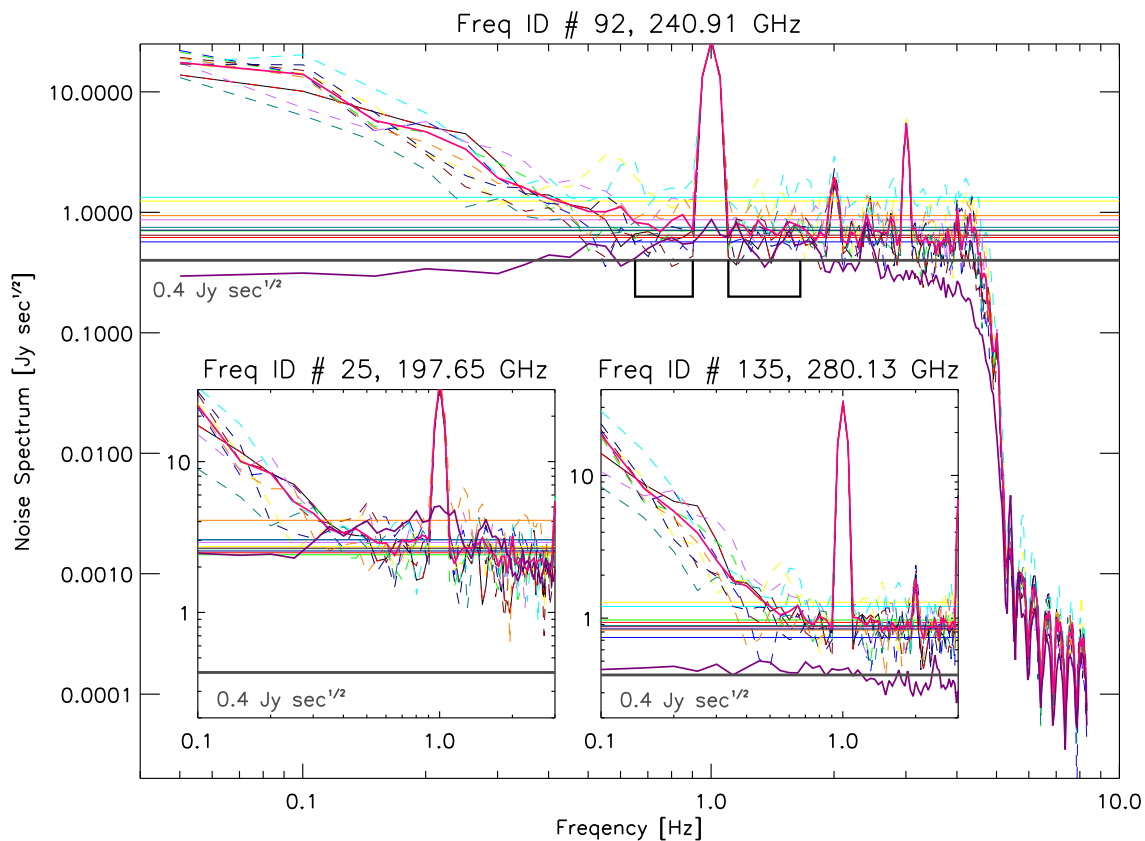


Figure 4.3. This figure shows noise spectra for three different channels taken from the NW pointing of the M82 observations (see table 5.1). The main panel shows several spectra for a channel in the center of the band in units of $\text{Jy}\sqrt{\text{sec}}$ while the two inset plots show spectra for channels closer to the edges of the band. The solid magenta curve is the average optimum signal projection noise spectrum. This is the average of the ten spectra plotted with dashed lines, each of which is averaged over four nod positions. The colored horizontal lines indicate the estimated white-noise level near the chop frequency (1 Hz) for each nod's spectrum. This average takes the points that lie in the range indicated by the black lines from about 0.6 to 1.7 Hz, not including the 1 Hz point and its nearest neighbors. The purple spectrum is the nod and nod position averaged spectrum for the perpendicular timestream projection which should indicate the electronics noise level. The thick gray line indicates a rough sensitivity estimate of $0.4 \text{ Jy}\sqrt{\text{sec}}$. The data-processing pipeline filters the bolometer timestreams with a 4.5 Hz low-pass filter, which explains the high frequency rolloff. The $1/f$ rises above the white noise level below the chop frequency so it does not affect the noise at 1 Hz.

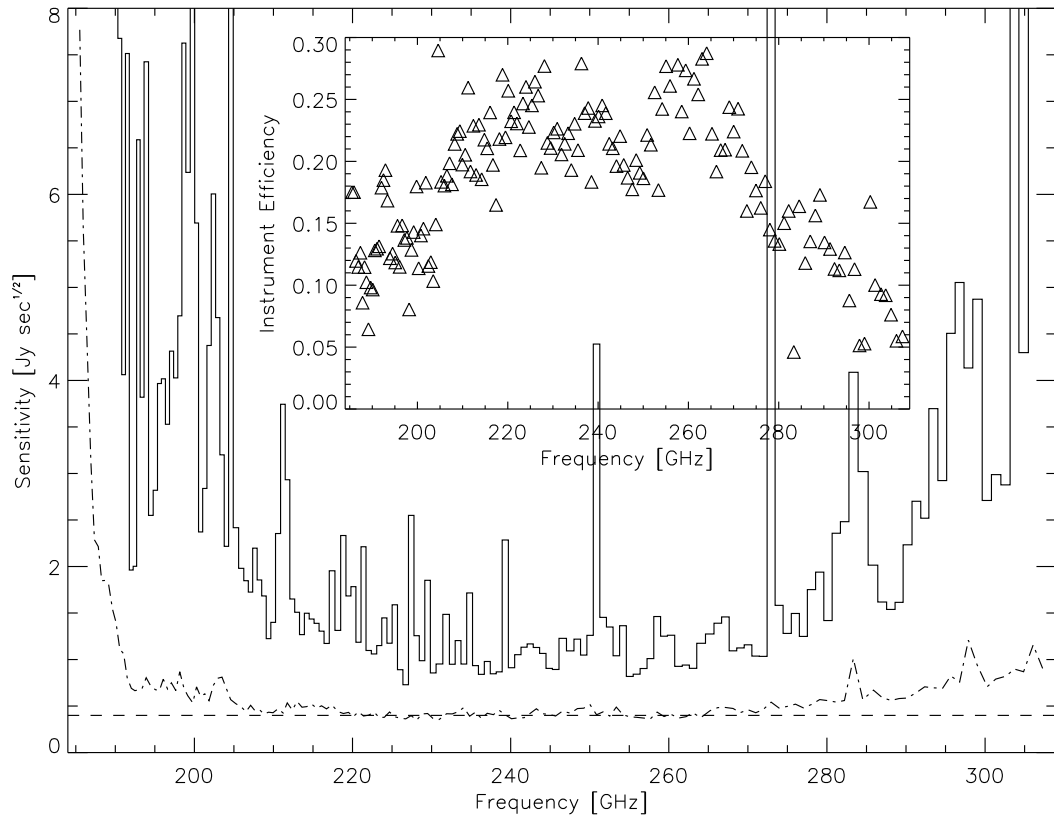


Figure 4.4. This plot compares the sensitivity model with the measured sensitivity from the NW pointing of the M82 observations (see table 5.1). The modeled sensitivity (dash-dot line) is well below the measured sensitivity (solid line). Because M82 is a bright source, the noise is dominated by systematics and does not represent the ultimate instrument performance. The optical efficiency of the instrument, indicated by the triangles in the inset plot, was measured by comparing the detected power when beam-filling room temperature and 77 K blackbodies were placed in front of the cryostat window. The structure seen in the optical efficiency has been significantly reduced by instrument improvements that are outside the scope of this thesis.

does not meet the predicted $0.3 \text{ Jy}\sqrt{\text{sec}}$ background limit. The best channels in the center of the band get within a factor of 3 of this prediction (see figure 4.4). The primary causes for this reduced sensitivity are smaller than expected instrument transmission, excess internal loading and warm-optics performance problems. The instrument transmission ranges from about 10% to 20%, though at 10% transmission, the expected sensitivity would be $0.5 \text{ Jy}\sqrt{\text{sec}}$. The methods used to improve the instrument transmission, excess loading and optical alignment are outside the focus of this dissertation and will be discussed in L. Earle's Ph.D. dissertation.

Chapter 5

Unbiased Line Survey of M82

5.1 Emission from M82

M82 is the brightest infrared galaxy in the sky due to its proximity (3.9 Mpc from Sakai and Madore [1999]) and fairly large infrared luminosity $L = 5.9 \times 10^{10} L_{\odot}$ [Sanders et al. 2003]. It is considered to be a prototypical starburst galaxy and an ideal candidate for investigating physical conditions present in galaxies with large quantities of dust and molecular gas and undergoing rapid star formation. The high star formation rate creates a far-ultraviolet radiation field several orders of magnitude larger than the local value [Colbert et al. 1999]. This extreme nuclear starburst is believed to have been triggered by an encounter with M81 100 million years ago, indicated by the atomic hydrogen bridges seen by Yun, Ho, and Lo [1994] between the two Messier objects and a third galaxy, NGC 3077. The current star formation rate is unsustainable and is predicted to consume the reserves of molecular gas in another 200 million years [Lord et al. 1996]. M82 is an edge-on irregular galaxy with two primary lobes of activity to the northeast and southwest of the dynamical center. A composite image from three space observatories is described in figure 5.1.

There are two categories of bright millimeter-wave emission from M82: line and continuum. The broadband continuum emission comes from thermal radiation of dust [Thuma et al. 2000] and from free-free radiation of scattering electrons in large ionized HII regions [Carlstrom and Kronberg 1991]. The thermal dust emission of the entire galaxy was modeled by Hughes, Gear, and Robson [1994] and was found to be well described by a single temperature graybody function,

$$F_{\text{T}}(\nu) = \Omega B_{\nu}(T) \left\{ 1 - \exp \left[- \left(\frac{\lambda_0}{\lambda} \right)^{\beta} \right] \right\}, \quad (5.1)$$

where $B_{\nu} = (2h\nu^3/c^2)/(e^{h\nu/kT} - 1)$ is the Planck function. The results from a fit to a collection of observations from 3.3 mm to 40 μm are $\Omega = 1.34 \times 10^{-8}$ steradian, $T = 48.1$ K, $\beta = 1.3$ and $\lambda_0 = 7.9$ microns. The spectral dependence of optically thin free-free emission from the hot ionized



Figure 5.1. This picture is a composite of observations of M82 with the Hubble Space Telescope (courtesy of NASA, ESA, and The Hubble Heritage Team (STScI/AURA)), Chandra X-Ray Observatory (courtesy of NASA/CXC/JHU/D.Strickland), and Spitzer Space Telescope (courtesy of NASA/JPL-Caltech/C. Engelbracht (University of Arizona)). Visible blue light appears in yellow-green and H α emission in orange. The X-ray data is mapped to blue while the infrared observations are shown in red. The field is about 8 arcminutes across and north is approximately 50° to the left of vertical. The major axis of the galaxy extends from the lower-left to the upper-right with the nuclear starburst region not clearly indicated in this composite image. The extended emission above and below the plane of the galaxy is the result of the evolution of extremely massive stars forming in the central regions of the galaxy. These massive stars lose large amounts of material before they explode as supernovas. The energy generated by these explosions drives the gas out of the galaxy at millions of miles per hour. In addition to the super-heated gas in blue and ionized hydrogen in orange, there is cooler dust shown in red that is rich in polycyclic aromatic hydrocarbons seen in the ejected material.

gas surrounding high mass stars is given by a simple power law,

$$F_{\text{ff}}(\nu) = F_0 \left(\frac{\nu}{\nu_0} \right)^{-0.1}, \quad (5.2)$$

where F_0 is the free-free flux at ν_0 . Analysis of a map of M82 at 92 GHz found that the emission at that frequency is dominated by free-free emission. Carlstrom and Kronberg [1991] show that the free-free flux density $F_{\text{ff}}(92 \text{ GHz}) = 0.5 \pm 0.1 \text{ Jy}$, which is 60 %–100 % of the total emission detected. At 250 GHz, the free-free emission contributes about a quarter of the total flux density.

In addition to the continuum sources in M82, line emission contributes about 15% to the broadband flux around one millimeter [Thuma et al. 2000]. Line emission comes from rotational transitions of molecules in the interstellar medium that are excited by collisions with molecular hydrogen. The strongest line feature is from carbon monoxide (CO) which has a simple ladder of rotational states; if J is the upper level total angular momentum quantum number, then the frequency of the transition to the $J - 1$ state is $J \times 115 \text{ GHz}$. There are several other molecules with similar ladders of transitions that have been studied in M82 [Wild et al. 1992].

Molecules and transitions are typically detected using targeted searches, where the species and transition are chosen first and then observations attempt to find them [Huettemeister et al. 1995; Petuchowski and Bennett 1992]. An alternative strategy is an unbiased spectral line survey which attempts to cover a certain range in frequencies to discover all the lines in that range. This has been done for several sources within our galaxy at millimeter wavelengths, such as the Orion molecular cloud [Sutton et al. 1985; Blake et al. 1986; Greaves and White 1991] and the galactic center [Nummelin et al. 1998]. The first molecular line survey of a source outside the galaxy observed a starburst galaxy NGC 253 at 2 mm [Martín et al. 2006].

5.2 Description of Observations

Z-Spec’s first trip to the Caltech Submillimeter Observatory (CSO) was in June 2005. The focal plane was not fully populated with functional detectors and there were some problems with the data acquisition software. It was clear, however, that the instrument worked as a spectrometer. Z-Spec returned to the CSO in April 2006 for a second run. Its focal plane was fully operational and improvements were made to the acquisition software so that scientific observations could begin.

The observations of M82 were made on April 14, 2006 and again on April 16, 2006. Three pointings along the major axis were observed. These pointings are plotted and summarized in figure 5.2 and table 5.1. In addition to the observations of M82, calibration observations of Mars were made on both the 14th and the 16th. The data were reduced using the demodulation and differencing method described in appendix D.

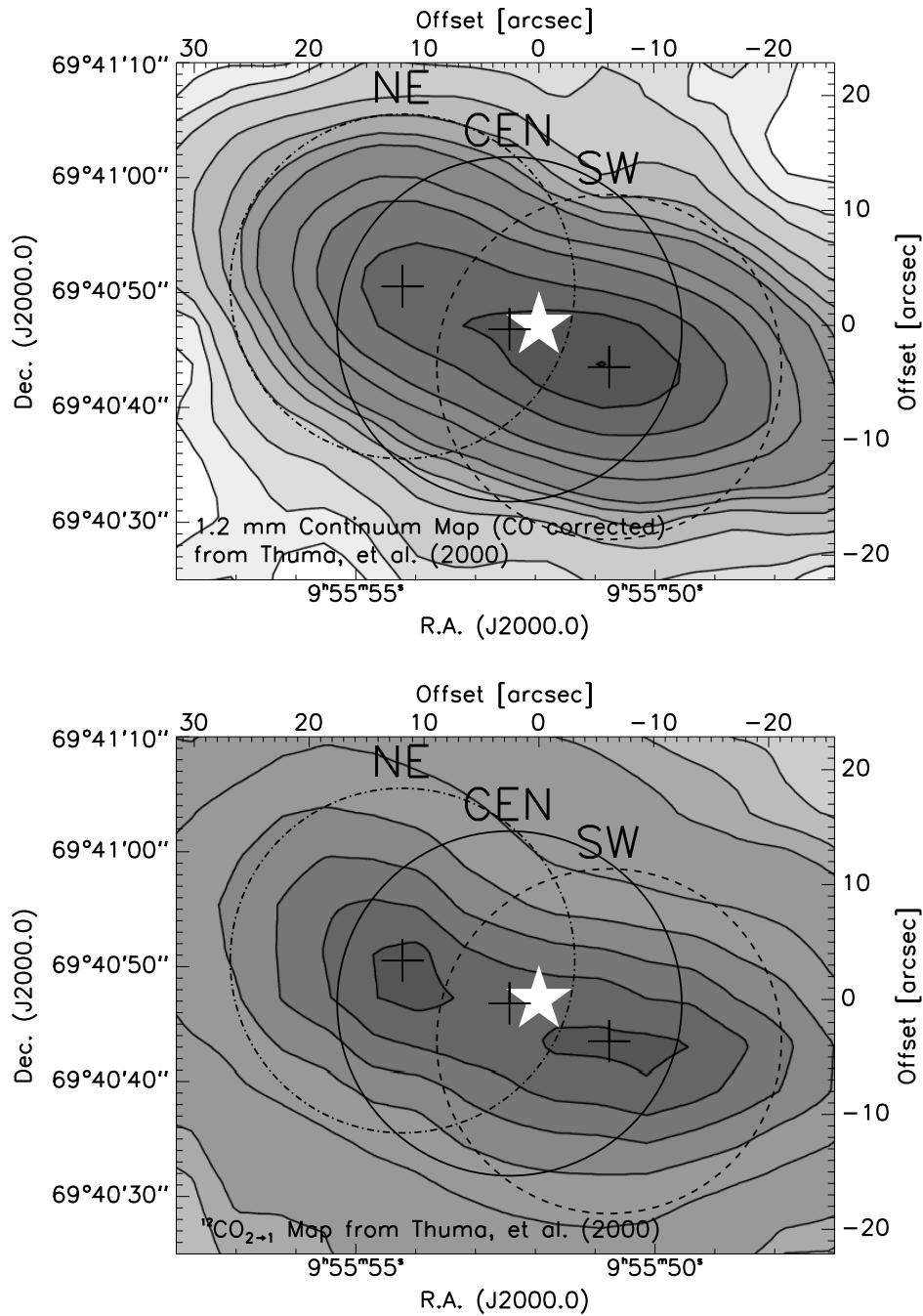


Figure 5.2. These pointing maps show Z-Spec’s 30" beam (FWHM at 240 GHz) for the observed pointings of M82 plotted over single dish measurements of the 1.2 mm continuum and a ¹²CO 2-1 map both from Thuma et al. [2000]. The white star marks the 2.2 μm peak at $\alpha_{J2000.0} = 9^h55^m51.9^s$, $\delta_{J2000.0} = 69^\circ40'47.1''$ which is the adopted center for the observations. The offsets relative to the center, observation dates and integration times are given in table 5.1. All three pointings use a 60" symmetric azimuthal chop throw.

Table 5.1. M82 pointing details

| Pointing Name | R. A. Offset [arcsec] | Dec. Offset [arcsec] | Int. Time [min] | Obs. Date | DC Level Change | Pointing Notes |
|---------------|-----------------------|----------------------|-----------------|---------------------|-----------------|--|
| NE | +11.9 | +3.4 | 26.6 | 4/14/06 | 3.6% | northeast CO peak |
| CEN | +2.6 | -0.3 | 79.1 | 4/14/06 and 4/16/06 | 4.5% | center of galaxy |
| SW | -6.1 | -3.6 | 39.9 | 4/14/06 | 1.9% | 1 mm continuum peak; southwest CO peak |

Note. — This table provides information regarding the observed pointings of M82. The R. A. and Dec. offsets are relative to $\alpha_{J2000.0} = 9^h55^m51.9^s$, $\delta_{J2000.0} = 69^\circ40'47.1''$. The integration time is the total demodulated time; on-source time is half of that. The fractional change in DC level compares the DC bolometer voltage of the M82 observations to the Mars calibration observation. Twice this number yields a rough estimate of the calibration uncertainty based on an advanced calibration model that is under development.

5.2.1 Measured Spectra

Spectra for the NE, CEN and SW pointings are shown in figures 5.3, 5.4 and 5.5. The general features agree with the 1.2-mm continuum and CO 2–1 maps shown in 5.2. Continuum emission from the NE pointing is somewhat weaker than the CEN and SW positions while the CO 2–1 intensity is mostly constant for all three. Furthermore, the spectral features shift from pointing to pointing due to the rotation of the galaxy. Their line widths are significantly broadened by the limited resolution of the instrument. In addition to the continuum and spectral-line features described in the following sections, we see a broad unexplained feature on the high frequency side of the HCO⁺ 3-2 line at 267.5 GHz.

5.2.2 Continuum Results

The continuum emission component of the spectra shown in figures 5.3, 5.4 and 5.5 are fitted with a simple power law of the form $F(\nu) = A(\nu/240\text{GHz})^B$. Best-fit parameters are given in table 5.2.

Table 5.2. M82 continuum fit results

| Pointing | A [Jy] | B | Reduced χ^2 |
|----------|-------------------|-----------------|------------------|
| NE | 0.447 ± 0.005 | 1.19 ± 0.14 | 2.9 |
| CEN | 0.593 ± 0.002 | 1.18 ± 0.05 | 6.1 |
| SW | 0.572 ± 0.004 | 1.47 ± 0.09 | 3.1 |

Note. — This table gives the parameters of a simple power law fit to the continuum level of the three measured spectra of M82. The reduced χ^2 values are for the line and continuum fits and are calculated based solely on statistical errors, not including errors due to calibration. The fits use 72 data points in the center of the band and has 54 degrees of freedom.

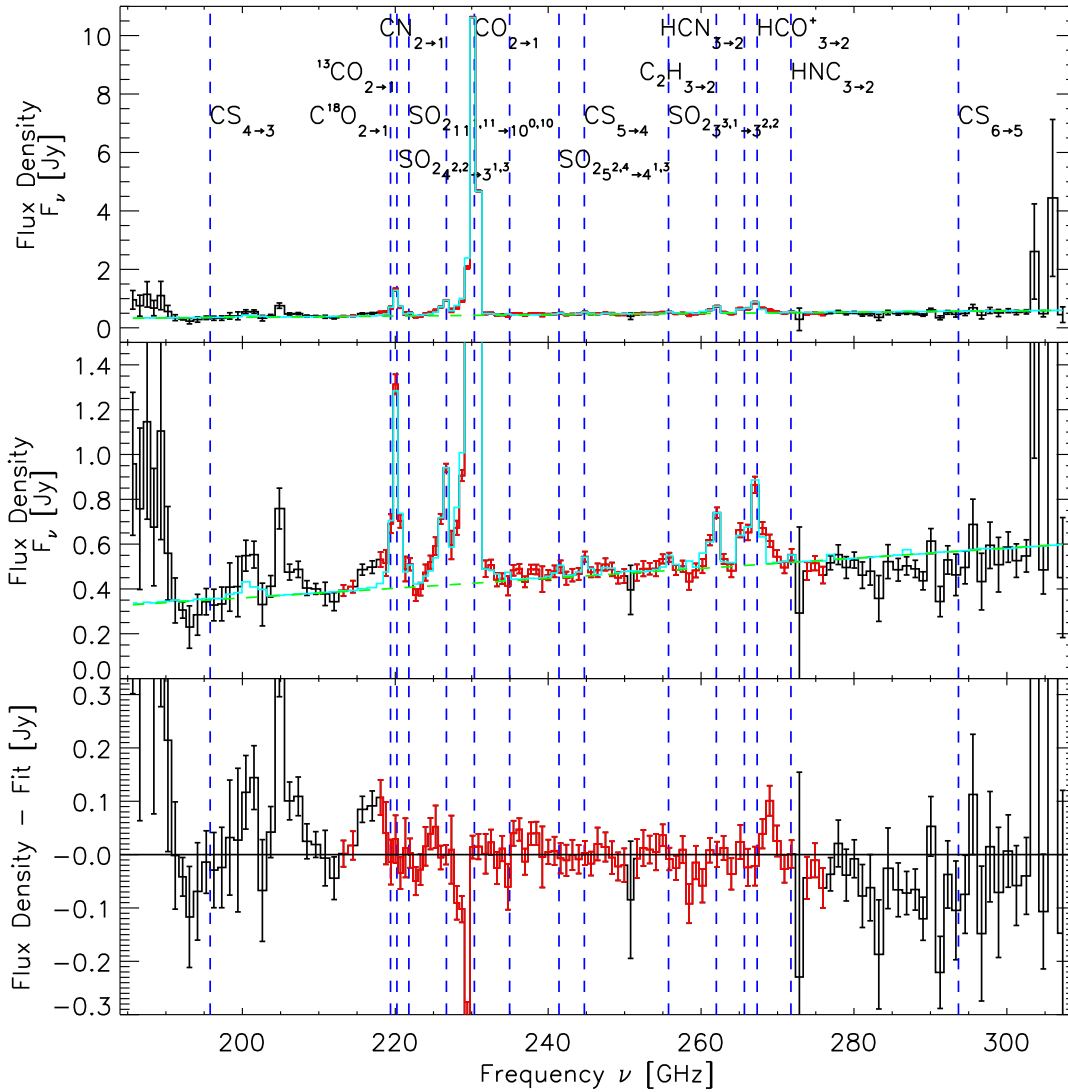


Figure 5.3. This three-panel plot shows the spectrum measured for the NE pointing: the upper panel shows the full range which is dominated by the CO line at 230.538 GHz, the middle panel zooms in to show the other lines and the continuum level and the bottom panel shows the fit residuals. The 11 fitted lines plus two additional CS transitions are identified by the dashed blue vertical lines. Only the fraction of points plotted in red are included for the fit and the lowest 60 frequency channels, below 218 GHz, are binned together in pairs. Two noisy channels in the fit range from 213 to 276 GHz are excluded from the fitting. The line and continuum fit is plotted in the cyan histogram and the fitted continuum spectrum appears in dashed green. The parameters of the fits are given in tables 5.2 and 5.3.

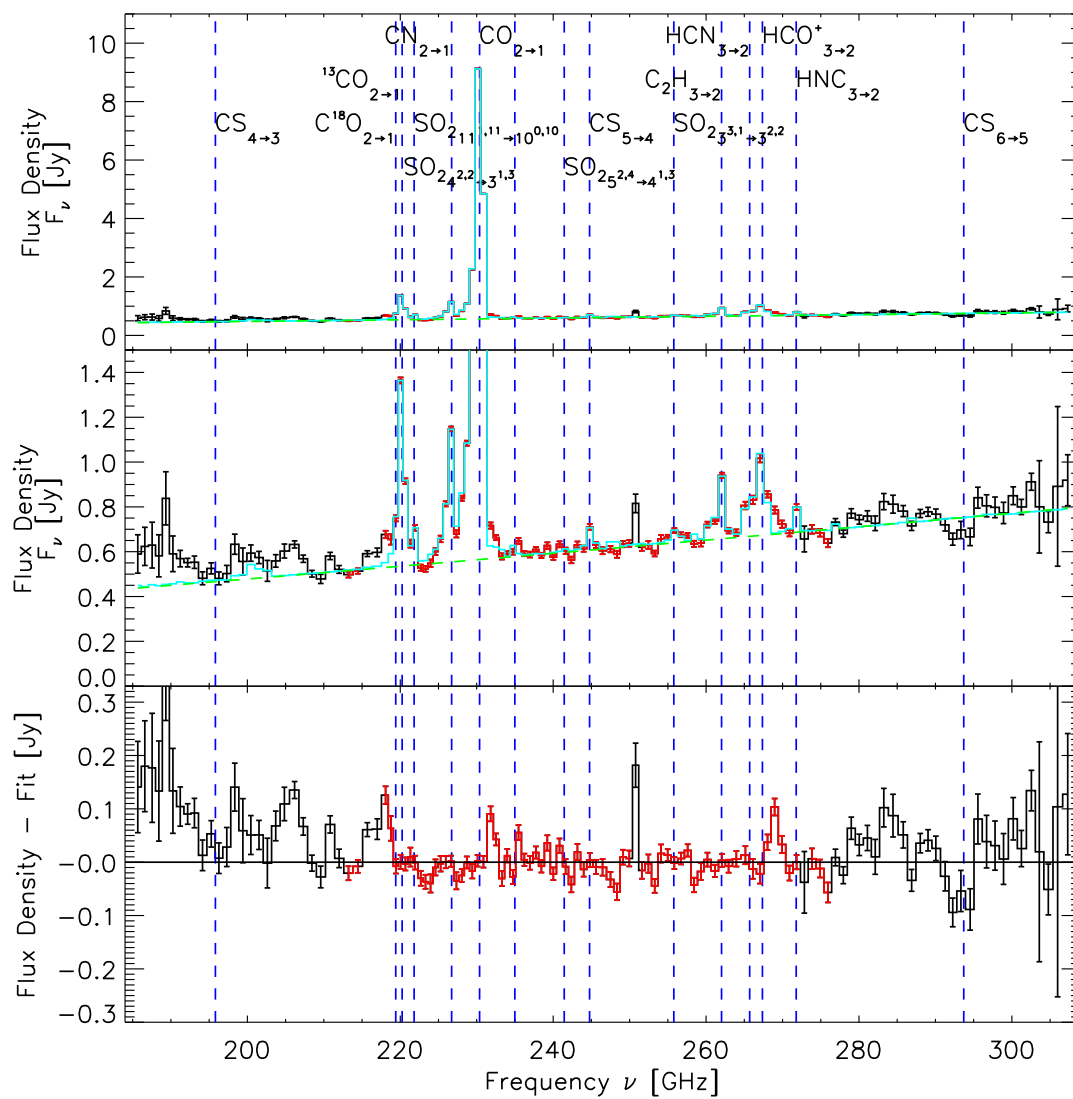


Figure 5.4. This is the measured spectrum for the CEN pointing. See figure 5.3 for a detailed description.

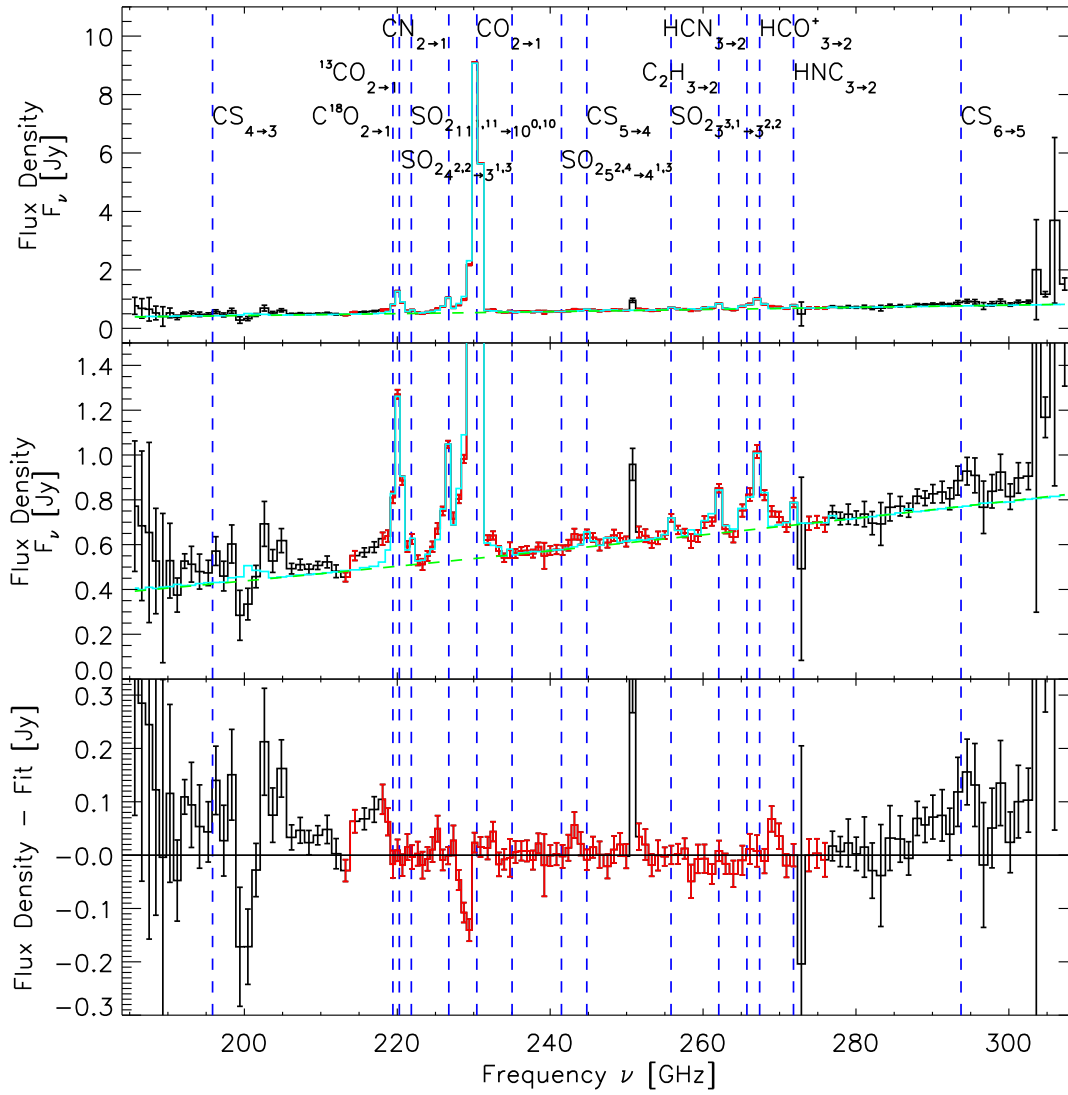


Figure 5.5. This is the measured spectrum for the SW pointing. See figure 5.3 for more information.

A more sophisticated fitting method based on the flux density models of the thermal and free-free emission can be applied to provide insight regarding the range and variation in spectral index from pointing to pointing. This method is described below but does not affect the fitted line intensities nor the reduced χ^2 of the fits.

Radiation from a hot graybody point source would have a spectral index of $2 + \beta$, which is the spectral dependence of equation (5.1) for $h\nu/kT \ll 1$. The dust in M82 is not hot enough to fall completely in this regime; $h\nu/kT$ ranges from 0.2 to 0.3 from 200 to 300 GHz. Furthermore, it is clear that the emission from M82 is not fully captured in our beam and thus cannot be considered a point source. Assuming the thermal and free-free components have the same spatial distribution, the continuum spectrum can be fit to the function

$$F(\nu) = \mathcal{A} \left(\frac{\nu}{240\text{GHz}} \right)^{\mathcal{B}-2} [F_{\text{T}}(\nu) + F_{\text{ff}}(\nu)]. \quad (5.3)$$

This method correctly compensates for the spectral dependence from the spatial distribution. If M82 filled our beam at all frequencies, we would expect $\mathcal{B} = 0$, while $\mathcal{B} = 2$ would be the prediction for a point source. The best-fit values range from 0.9 to 1.2, which roughly agrees with the fact that M82 is observed edge-on. It is essentially extended in one dimension while roughly pointlike in the other, relative to our $30''$ beam. Fixing $\mathcal{B} = 1$ in the above equation and refitting does not significantly increase the reduced chi-squared value, indicating that our data are consistent with the measured models and no additional components (e.g., colder dust, dust emissivity variation) are indicated.

5.3 Spectral Line Results

5.3.1 Spectral Fitting

The limited resolution of Z-Spec smears out the line features of M82 which have an intrinsic line width of 100-250 km/s. The line fitting method employed starts with an assumed Gaussian line profile of a certain center and width. This Gaussian profile is multiplied by a channel's measured FTS profile (shown in figure 2.8) and integrated over the whole frequency range of the instrument to estimate the response of that channel to the modeled line. This process is repeated for several channels to create a template response profile. The parameters of the original line profile and amplitude of the template are adjusted to fit the identified spectral features.

This fitting procedure demonstrated that while the instrument is very insensitive to the line width, it is reasonably sensitive to the center frequency of the Gaussian line profile. This enabled centroid measurements of line features that did not have an obvious identification accurate to about 100 to 200 km/s. The fitting method also helped identify possible ghosting effects whereby bright

Table 5.3. M82 line fit results

| Species & Transition | Freq. [GHz] | E_{upper} [K] | Beam Size $1.2 \times \lambda/D$ | Integrated Line Intensity [K km/s] | | |
|---------------------------------------|-------------|------------------------|----------------------------------|------------------------------------|-----------------|-----------------|
| | | | | NE | CEN | SW |
| CO 2-1 | 230.538 | 16.60 | 30.9'' | 552.7 ± 1.2 | 495.5 ± 0.6 | 528.9 ± 1.2 |
| ^{13}CO 2-1 | 220.399 | 15.87 | 32.4'' | 40.2 ± 2.0 | 40.2 ± 0.7 | 37.7 ± 1.1 |
| C^{18}O 2-1 | 219.560 | 15.81 | 32.5'' | 4.9 ± 1.7 | 1.8 ± 0.6 | 6.5 ± 1.1 |
| CN 2-1 | 226.6 | 16.3 | 31.5'' | 24.9 ± 1.1 | 25.9 ± 0.5 | 21.9 ± 0.8 |
| CS 5-4 | 244.936 | 35.27 | 29.1'' | 3.8 ± 1.0 | 4.4 ± 0.6 | 3.0 ± 0.9 |
| HCO^+ 3-2 | 267.558 | 25.68 | 26.7'' | 21.9 ± 2.0 | 22.1 ± 1.0 | 21.5 ± 1.7 |
| C_2H 3-2 | 262.1 | 25.2 | 27.2'' | 12.9 ± 1.3 | 13.4 ± 0.6 | 9.2 ± 1.0 |
| HCN 3-2 | 265.886 | 25.52 | 26.8'' | 9.2 ± 2.0 | 8.7 ± 1.1 | 6.4 ± 1.6 |
| HNC 3-2 | 271.981 | 26.11 | 26.2'' | 1.5 ± 1.2 | 5.0 ± 0.6 | 4.4 ± 1.0 |
| SO_2^* $11_{1,11}-10_{0,10}$ | 221.965 | 60.36 | 32.1'' | 2.9 ± 1.3 | 5.8 ± 0.6 | 3.5 ± 1.0 |
| SO_2^* $3_{3,1}-3_{2,2}$ | 255.958 | 27.62 | 27.9'' | 2.8 ± 1.0 | 2.3 ± 0.5 | 3.9 ± 0.8 |
| SO_2^* $4_{2,2}-3_{1,3}$ | 235.152 | 19.04 | 30.4'' | 0.1 ± 1.9 | 0.9 ± 0.7 | -0.7 ± 1.6 |
| SO_2^* $5_{2,4}-4_{1,3}$ | 241.616 | 23.60 | 29.5'' | 3.1 ± 1.5 | 0.7 ± 0.8 | -0.2 ± 1.1 |

Note. — This table lists the measured line intensities and their estimated error for the eleven identified lines and two SO_2 non-detections for all three pointings. The line width for all lines in all pointings is 250 km/s which is probably an overestimate for most of the detections. However, nearly halving or doubling the line width does not significantly change the line intensities nor affect the reduced χ^2 value. The errors are based on the statistical errors in the spectral data and do not include any uncertainty due to calibration. Intensities of the C^{18}O line should be considered rough estimates due to the proximity of the much brighter ^{13}CO line (see text for additional discussion). Hyperfine splitting in the CN and C_2H lines are not accessible at Z-Spec's resolution.

* All SO_2 transitions are tentative identifications. The $3_{3,1}-3_{2,2}$ transition may be blended with nearby transitions at 255.553 and 256.247 GHz.

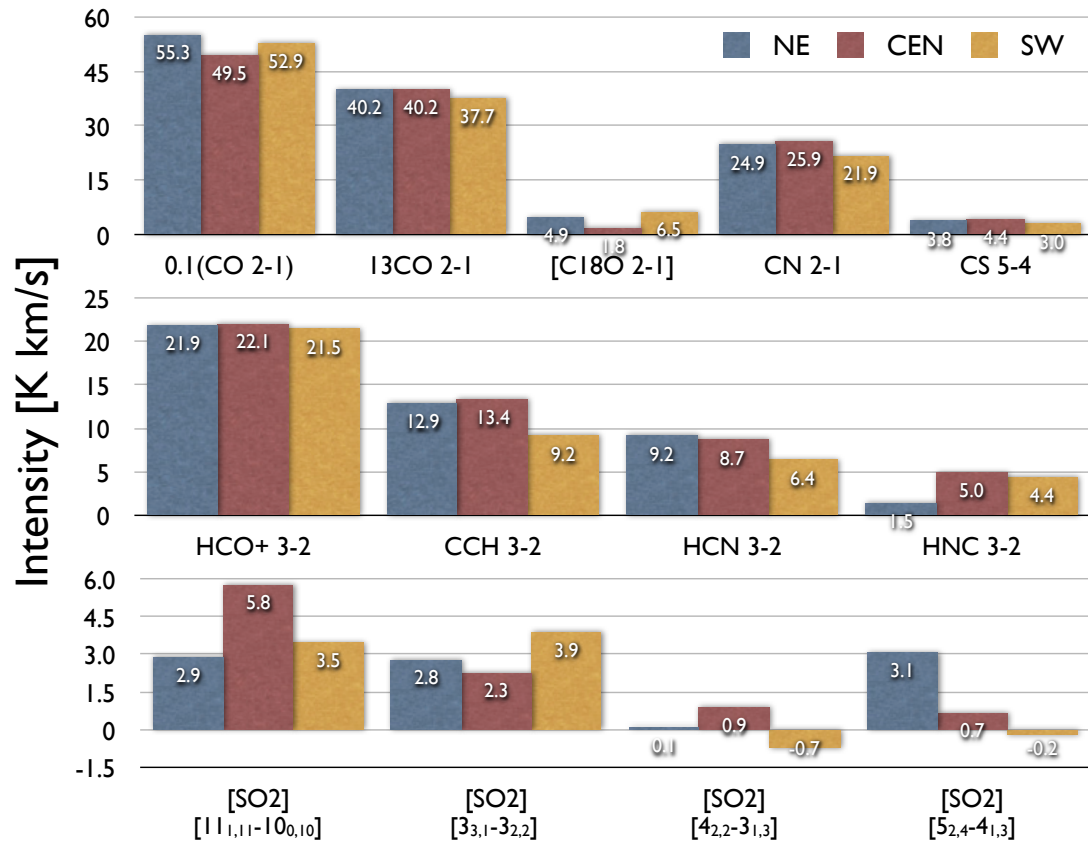


Figure 5.6. These bar charts show the line intensities obtained for the identified transitions in the three pointings of M82. The CO intensity is divided by 10 to match the scale of the other two-species molecules plotted. See table 5.3 for more details. Square brackets indicate tentative results.

line features leak into other spectrally distant channels and look like a separate line. There is some ghosting of the CO 2–1 line at 200 and 260 GHz from the Rowland ghosts discussed in figure 2.8, but they did not have a significant impact on the identified lines. The fitted line intensities are given in table 5.3 and plotted in figure 5.6.

5.3.2 CO and its Isotopologues

The CO, ^{13}CO and C^{18}O 2–1 transitions have been extensively studied and mapped by previous experiments [Mao et al. 2000; Weiß et al. 2001]. Direct comparison with published intensities is limited by beam size mismatch. Wild et al. [1992] quotes integrated main-beam intensities nearly double what we measured in a $13''$ beam for the CO 2–1 transition. This line traces the bulk of the molecular gas and has fairly extended emission consistent with the weak dependence of line intensity on beam size. Our intensities for the ^{13}CO 2–1 line are about 67% of the intensities given in Mao et al. [2000] which are quoted for a $22''$ beam. This beam scaling is somewhat stronger than for ^{12}CO , but is still reasonable. Wild et al. [1992] reports intensities for the C^{18}O transition in a $13''$ beam that do not agree very well with our results. This indicates a limitation of Z-Spec because the two isotopologues of CO we identify are strongly blended together. The intensity of the C^{18}O line is estimated at almost an order of magnitude fainter than ^{13}CO . Since these two spectral features are smeared together, it is difficult to recover information about the weaker line.

5.3.3 CN and C_2H

We strongly detect both the CN 2–1 and C_2H 3–2 transitions in all pointings. The primary rotational energy levels of both of these molecules are split slightly by spin-orbit and spin-spin couplings, giving spectra that have both fine and hyperfine structure which is inaccessible to Z-Spec. The intensities quoted in table 5.3 are obtained by fitting a single Gaussian profile but likely represent the total integrated intensity for all splittings combined. These species have been detected before in M82 by Henkel, Schilke, and Mauersberger [1988] and Fuente et al. [2005], though the C_2H 3–2 is a newly-detected transition. Neither of these papers quote the intensity seen in all fine-structure components, making a direct comparison with our results difficult. Collisional rate coefficients are not available for these molecules which precluded them from the analysis method described in the next section.

5.4 Radiative Transfer Modeling

Molecular line emission comes from photons radiated by compounds in an excited state transitioning to a lower state. In the millimeter region of the electromagnetic spectrum, typical excitations occur in rotational (and sometimes vibrational) modes. The separation between energy levels determines

the frequency of light emitted. A molecule can be boosted into an excited state when a collision occurs: generally with H_2 or He, which are the two most abundant species in a molecular gas cloud. Collisions can also cause downward transitions from higher to lower energy states. The rate of collision-induced transitions from an upper level u to the lower level l is given by

$$C_{ul} = n_{\text{col}}\gamma_{ul}, \quad (5.4)$$

where n_{col} is the density of the collision partner in cm^{-3} and γ_{ul} is the collisional rate coefficient for the upper to lower transition in $\text{cm}^3 \text{sec}^{-1}$.

In addition to the collisional rates, the rates of spontaneous emission, stimulated emission and stimulated absorption, given by the Einstein coefficients A_{ul} , B_{ul} , and B_{lu} , respectively, affect the strength of line emission. These three coefficients are connected by the Einstein relations such that only one needs to be measured or calculated. The balance between collisional and radiative excitation and de-excitation is a function of density and can be characterized by critical density, n_{crit} , i.e. the density at which the downward collisional rate, C_{ul} , equals the spontaneous emission rate, A_{ul} , or

$$n_{\text{crit}} = \frac{A_{ul}}{\gamma_{ul}}. \quad (5.5)$$

For a simple two-level system, the radiation intensity is proportional to the volume number density n when $n < n_{\text{crit}}$ and independent of n when it is above the critical density. For multi-level systems, the situation is more complicated; however, the critical density remains a useful rule-of-thumb for understanding the typical densities that will give rise to particular transitions.

The occupation of the available states plays a crucial role in determining the radiation intensity. In local thermodynamic equilibrium, the level populations are determined by a Boltzmann distribution with a characteristic temperature T_{ex} . In the optically-thin limit, where the column density of the species is small enough such that an emitted photon generally escapes the region where it is created, the line intensity is proportional to the occupation of the upper level state. The level occupation is determined by the Boltzmann factor, $e^{-E_u/kT_{\text{ex}}}$, where E_u is the energy of the upper state and k is Boltzmann's constant. For sufficiently high excitation temperatures, where $E_u < kT_{\text{ex}}$, the radiation intensity will be independent of temperature.

Clearly, the radiation intensity will be related to the column density, or the number of molecules (or, more generally, radiators) along the line of sight. The intensity will be directly proportional to the column density in the optically-thin limit. For optically-thick transitions, the intensity is independent of column density because additional radiators along the line of sight do not result in any net increase in the number of photons along the line of sight. For a source with a known volume density distribution of a reference molecule, the column density of a particular species can be calculated using the relative abundance ratio of the species with respect to the reference molecule.

This direct relationship between column density and abundance ratio means that, in the optically-thin limit, a species with twice the abundance compared to another species will radiate with twice the intensity assuming all other factors are equal.

Molecular abundances can be calculated using chemical modeling of the interstellar medium. Both gas-phase chemical networks and dust grain surface chemistry are important [van Dishoeck and Blake 1998]. Furthermore, the chemistry present in photodissociation regions [Hollenbach and Tielens 1997] and in shocked gas clouds [Scalo and Elmegreen 2004] can differ significantly from that found in more quiescent portions of the interstellar medium. Interpreting measurements of line emission for several species and transitions can assist in understanding the chemical modeling results.

Radiative transfer is a calculation method used to estimate observed line intensities based on the balance between excitation and de-excitation mechanisms, including both collisional and radiative. A freely available code for performing the calculations is described in van der Tak et al. [2007]. The program is called RADEX and it can solve for line intensities of atomic and molecular transitions for which radiative and collisional rate coefficients are available. The necessary data for five of the eleven species we detect in our spectra of M82 are available from the online database outlined in Schöier et al. [2005]. The line intensities for these five species have been simulated over a wide range of physical conditions in the galaxy.

The primary inputs to RADEX are the choice of molecule, the kinetic temperature of the molecular gas T_{kin} , the density of molecular hydrogen n_{H_2} in cm^{-3} and the column density of the species N_{mol} in cm^{-2} . The radiative transfer calculation depends on $N_{\text{mol}}/\Delta v$, where Δv is the velocity width of the line. Z-Spec cannot measure the linewidth, so $\Delta v = 250 \text{ km/s}$ is used throughout the radiative transfer modeling to be consistent with the linewidth used for the spectral fits. RADEX does not assume local thermal equilibrium, but uses an escape probability formalism that connects the optical depth to the chance an emitted photon escapes the source cloud. Several different physical models for this escape probability have been derived. I use the expanding spherical shell model, also called the Sobolev or large velocity gradient (LVG) approximation. Starting with an initial guess for the level population distribution, the code solves for the optical depths of all the molecules' transitions, from which a new level population distribution can be calculated. This process repeats until a self-consistent solution is achieved such that the optical depth changes by less than a default tolerance from one iteration to the next.

Once the line intensities have been calculated, they must be compared to the measurements of the detected transitions of the chosen molecule. An additional parameter must be included in the model because the clumps of gas producing the radiation do not necessarily completely fill the beam. The area filling factor Φ_{A} scales down the line intensities from RADEX so that they can be directly related to the measurements. When Φ_{A} is less than 1, N_{mol} represents the column density

of an individual radiating clump while the product $\Phi_A N_{\text{mol}}$ is the beam-averaged column density, $\langle N_{\text{mol}} \rangle$. $\Phi_A > 1$ implies more than one clump along the line of sight which must be modeled using a larger column density.

The line-intensity measurements are inherently uncertain and the physical interpretation using models should reflect that. A Bayesian method for calculating likelihood distributions for various physical quantities of interest can be used to address this measurement uncertainty [Ward 2002; Ward et al. 2003]. The method constructs the probability distribution of obtaining the given measurements with their associated errors based on a given set of physical parameters, assuming the measurements are independent and the errors are Gaussian distributed. Using a prior-probability density function for the range of physical parameters, the probability distribution of the measurements given the physical parameters can be inverted into a likelihood distribution for the physical parameters given the measurement results.

Bayes' Postulate says that the prior probability density function should be uniform for all cases in the absence of prior knowledge. The prior probability distributions used for this analysis are assumed to be logarithmically uniform in all four model parameters, T_{kin} , n_{H_2} , N_{mol} and Φ_A . However, this prior probability is used to exclude certain non-physical situations relating to large column densities and small molecular hydrogen densities. Both constraints require knowledge of the molecular abundance ratio, $X_{\text{mol}} \equiv n_{\text{mol}}/n_{\text{H}_2}$. These constraints limit the total molecular mass contained in the telescope beam to less than half of the dynamical mass of the galaxy and limit the column length, equal to the column density divided by the total density, to less than the length of the bright molecular emission. These constraints are also described in Ward et al. [2003]. In addition, models with optical depths larger than 100 in any transition are excluded because very large optical depths are not appropriate for the species under consideration and RADEX is not accurate when the optical depth is this large.

One difficulty with this method is that it requires appropriately scaling the published transition measurements with beam size so that all the line fluxes represent the integrated intensity seen in a particular size beam. The naive limits of beam scaling are θ^0 for a source that is much larger than the observing beam and θ^{-2} for a source much smaller than the beam. M82 is in an intermediate range with respect to the 25'' to 35'' beam size of Z-Spec; it is neither fully pointlike nor beam filling. Furthermore, different species will have different spatial distributions, which may be more or less point-like. For each molecule below, the likelihood plots for the kinetic temperature, molecular hydrogen density, species column density and filling factor are given for three values of the beam scaling exponent and the indications from the likelihood distributions are discussed.

Table 5.4. HCO⁺ and HCN transition data

| Transition | Freq. [GHz] | E _{upper} [K] | Beam Size | NE Flux | CEN Flux | SW Flux |
|------------------|-------------|------------------------|-----------|------------|------------|------------|
| HCO ⁺ | | | | | | |
| 1-0 | 89.118 | 4.28 | 23'' | 35.0 | 38.3 | 37.2 |
| 3-2 | 267.557 | 25.68 | 27'' | 21.9 ± 2.0 | 22.1 ± 1.0 | 21.5 ± 1.7 |
| 4-3 | 356.734 | 42.80 | 23'' | 20.4 ± 2.0 | 15.3 ± 1.5 | 19.0 ± 1.9 |
| HCN | | | | | | |
| 1-0 | 88.631 | 4.25 | 23'' | 21.8 | 18.5 | 23.7 |
| 3-2 | 265.886 | 25.52 | 27'' | 9.2 ± 2.0 | 8.7 ± 1.1 | 6.4 ± 1.6 |
| 4-3 | 354.505 | 42.53 | 23'' | 3.0 ± 0.6 | 4.2 ± 0.8 | 3.5 ± 0.7 |

Note. — This table lists the data that were used to analyze the radiative transfer models of HCO⁺ and HCN. All line intensities are given in units of K km/s. The 1-0 line data for both molecules from Nguyen-Q-Rieu, Nakai, and Jackson [1989] do not quote errors, so a fixed 2 K km/s was used, corresponding to approximately 5% and 10% errors, respectively, for the HCO⁺ and HCN likelihood calculations. They are rescaled from the published T_A^* units into T_{mb} by dividing by the 60% main beam efficiency. The 4-3 lines, mapped at a resolution of 14'' by Seaquist and Frayer [2000] were downsampled at the center pointing to the 23'' resolution given in this table. The ratio between the measured line flux at the center and the downsampled value was used to scale the other pointings to the 23'' resolution.

5.4.1 HCO⁺ and HCN

HCO⁺ and HCN have simple ladders of rotational transitions starting at 89.118 and 88.631 GHz, respectively. The 1-0, 3-2 and 4-3 transitions for both species have been previously detected by Nguyen-Q-Rieu, Nakai, and Jackson [1989], Wild et al. [1992] and Seaquist and Frayer [2000]. The 3-2 lines are strongly detected by Z-Spec in all three pointings with intensities given in table 5.4. The 1-0 observations were made with a 23'' beam, close to the 27'' beam of Z-Spec at 267 GHz. The 4-3 data were mapped with a 14'' beam, but the center pointing was downsampled to a 23'' beam to match the 1-0 measurements.

With only three measurements and four free parameters, it is not surprising that the HCO⁺ data do not completely constrain the radiative transfer model. The likelihood distributions for the four main parameters are shown figure 5.7. The most likely solution indicated by these distributions is cold (~ 10 K), dense ($\sim 10^5$ cm⁻³), optically thick gas filling about 1% of the beam. However, very hot (> 200 K) and very dense ($> 10^7$ cm⁻³) solutions are not excluded.

The two-dimensional likelihood distributions shown in the contour plots of figure 5.8 indicate two groups of likely solutions: ones with low temperature and high density or ones with high temperature and lower density. The column density and filling factor distributions are not significantly separated into two groups and are therefore more strongly constrained. The diagonal lines in the contour plots show that the high-temperature, low-density solutions fall roughly in a range of constant gas pressure ($P \propto T_{kin} n_{H_2}$) while the other group of solutions have a relatively flat distribution in pressure. The beam-averaged column density, $\langle N_{HCO^+} \rangle$, is fairly well constrained. The distributions for core

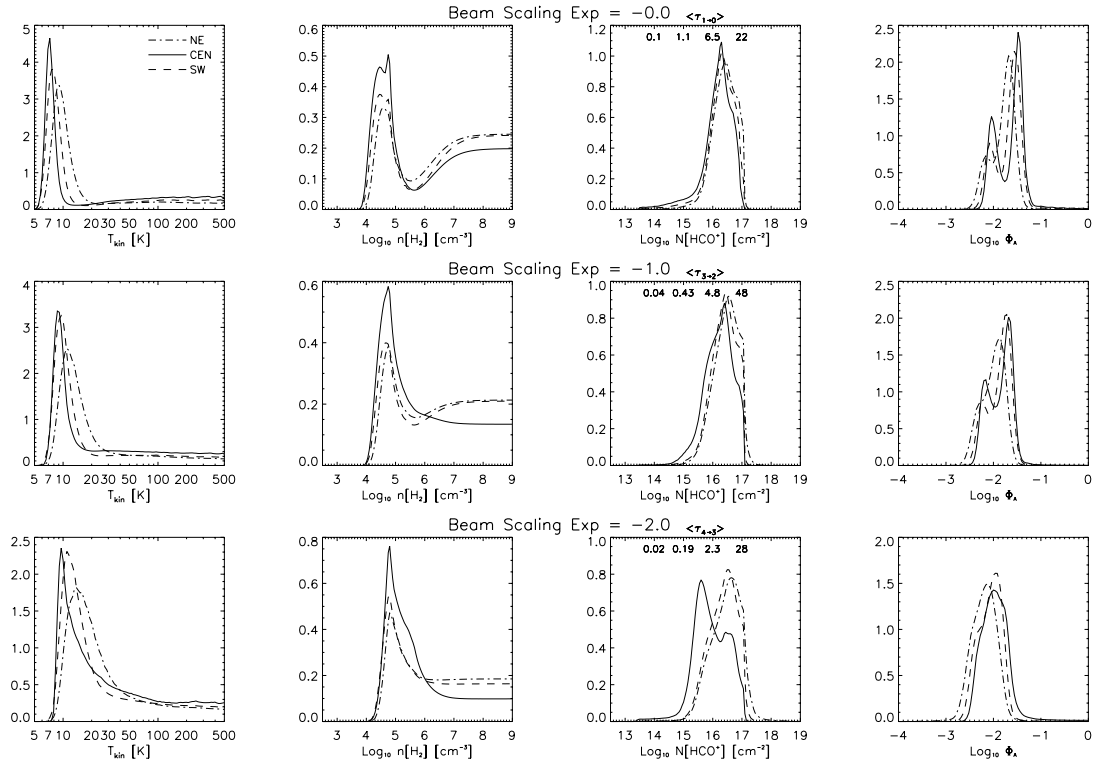


Figure 5.7. These plots show the likelihood distributions for the four parameters of the radiative transfer modeling for the species HCO^+ . The three rows of plots are for three different choices of the beam scaling exponent: 0, -1 , and -2 from top to bottom. In addition, the distributions for each pointing are indicated by dash-dotted, solid and dashed lines for the NE, CEN, and SW pointings, respectively. The plots show the full range covered by the radiative transfer simulations for all four parameters. The top axis on the column density plots shows the optical depth of the three observed transitions averaged over all solutions at the corresponding column density. As expected, the optical depth is roughly proportional to the column density.

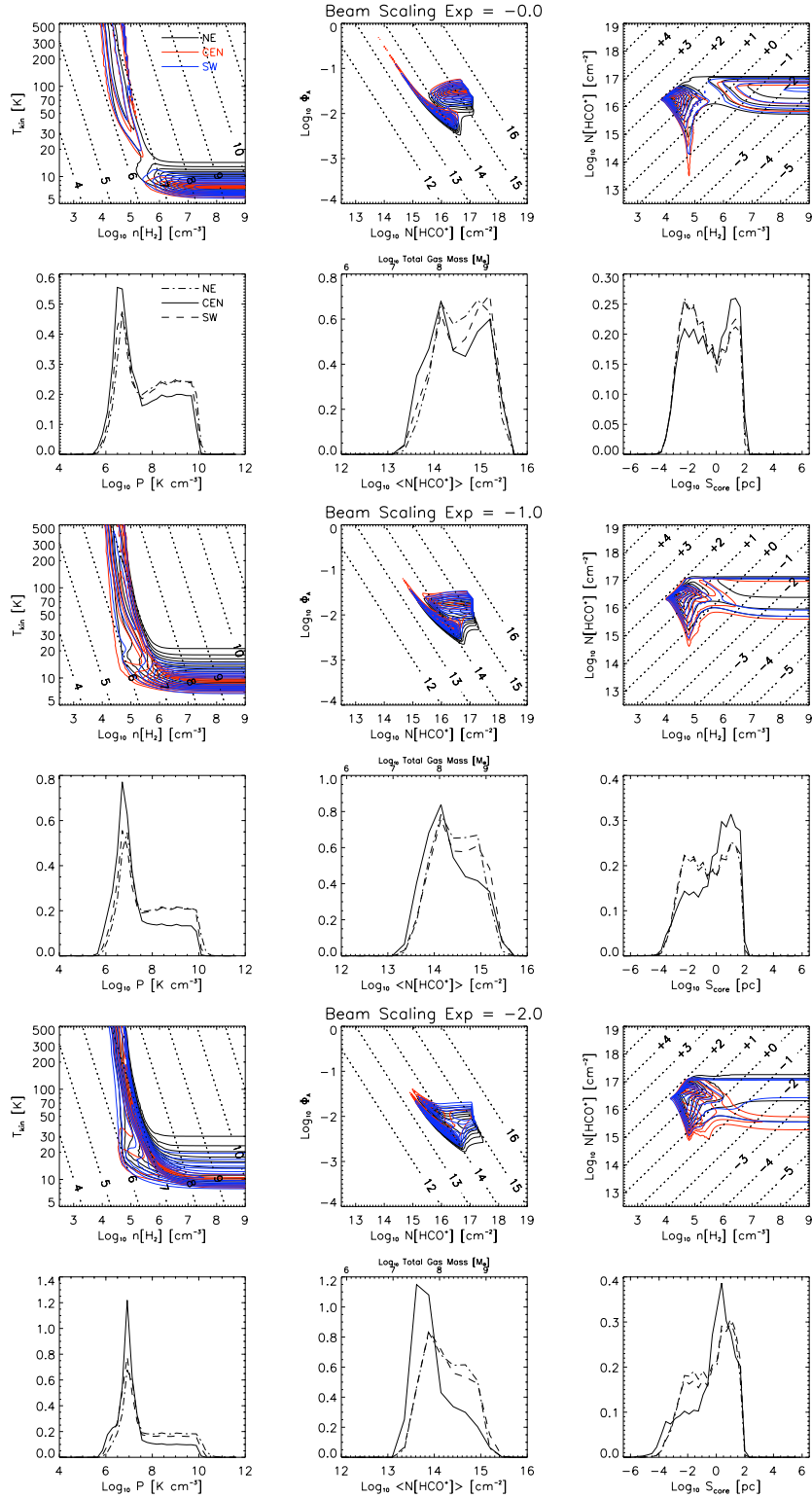


Figure 5.8. This figure shows two-dimensional likelihood distributions for HCO^+ for three beam scaling factors. The diagonal lines in the contour plots show how the auxiliary distributions for P , $\langle N_{\text{HCO}^+} \rangle$ and S_{core} are calculated. Distributions for these parameters are also shown.

Table 5.5. HCO⁺ radiative transfer results

| | NE Pointing | | CEN Pointing | | SW Pointing | |
|------------------------------------|-------------|-------------------------|--------------|-------------------------|-------------|-------------------------|
| | Median | Range | Median | Range | Median | Range |
| Beam Scaling Exponent = -0.0 | | | | | | |
| T_{kin} | 10 | > 6 | 8 | > 5 | 8 | > 5 |
| n_{H_2} | $10^{6.9}$ | $> 10^{4.2}$ | $10^{6.2}$ | $> 10^{4.1}$ | $10^{6.8}$ | $> 10^{4.1}$ |
| N_{HCO^+} | $10^{16.4}$ | $10^{15.4} - 10^{17.0}$ | $10^{16.2}$ | $10^{14.5} - 10^{16.9}$ | $10^{16.3}$ | $10^{14.9} - 10^{17.0}$ |
| Φ_{A} | $10^{-1.8}$ | $10^{-2.4} - 10^{-1.4}$ | $10^{-1.6}$ | $10^{-2.2} - 10^{-1.0}$ | $10^{-1.6}$ | $10^{-2.3} - 10^{-1.3}$ |
| $T_{\text{kin}} n_{\text{H}_2}$ | $10^{7.8}$ | $10^{6.0} - 10^{9.9}$ | $10^{7.2}$ | $10^{5.8} - 10^{9.7}$ | $10^{7.7}$ | $10^{6.0} - 10^{9.8}$ |
| $\langle N_{\text{HCO}^+} \rangle$ | $10^{14.5}$ | $10^{13.4} - 10^{15.3}$ | $10^{14.4}$ | $10^{13.3} - 10^{15.4}$ | $10^{14.5}$ | $10^{13.3} - 10^{15.4}$ |
| S_{core} | $10^{-1.0}$ | $10^{-3.4} - 10^{1.7}$ | $10^{-0.6}$ | $10^{-3.4} - 10^{1.8}$ | $10^{-1.0}$ | $10^{-3.4} - 10^{1.7}$ |
| Beam Scaling Exponent = -1.0 | | | | | | |
| T_{kin} | 13 | > 7 | 11 | > 7 | 10 | > 7 |
| n_{H_2} | $10^{6.6}$ | $> 10^{4.4}$ | $10^{5.5}$ | $> 10^{4.2}$ | $10^{6.6}$ | $> 10^{4.3}$ |
| N_{HCO^+} | $10^{16.5}$ | $10^{15.5} - 10^{17.1}$ | $10^{16.2}$ | $10^{15.0} - 10^{17.0}$ | $10^{16.4}$ | $10^{15.4} - 10^{17.0}$ |
| Φ_{A} | $10^{-2.0}$ | $10^{-2.5} - 10^{-1.6}$ | $10^{-1.8}$ | $10^{-2.3} - 10^{-1.5}$ | $10^{-1.9}$ | $10^{-2.4} - 10^{-1.5}$ |
| $T_{\text{kin}} n_{\text{H}_2}$ | $10^{7.6}$ | $10^{6.1} - 10^{9.9}$ | $10^{6.9}$ | $10^{5.8} - 10^{9.7}$ | $10^{7.5}$ | $10^{6.0} - 10^{9.9}$ |
| $\langle N_{\text{HCO}^+} \rangle$ | $10^{14.3}$ | $10^{13.4} - 10^{15.2}$ | $10^{14.2}$ | $10^{13.3} - 10^{15.3}$ | $10^{14.3}$ | $10^{13.4} - 10^{15.3}$ |
| S_{core} | $10^{-0.7}$ | $10^{-3.4} - 10^{1.7}$ | $10^{-0.1}$ | $10^{-3.5} - 10^{1.7}$ | $10^{-0.7}$ | $10^{-3.4} - 10^{1.7}$ |
| Beam Scaling Exponent = -2.0 | | | | | | |
| T_{kin} | 19 | > 9 | 18 | > 8 | 15 | > 8 |
| n_{H_2} | $10^{6.3}$ | $> 10^{4.5}$ | $10^{5.4}$ | $> 10^{4.5}$ | $10^{6.0}$ | $> 10^{4.4}$ |
| N_{HCO^+} | $10^{16.5}$ | $10^{15.4} - 10^{17.3}$ | $10^{15.9}$ | $10^{14.7} - 10^{16.9}$ | $10^{16.4}$ | $10^{15.3} - 10^{17.1}$ |
| Φ_{A} | $10^{-2.2}$ | $10^{-2.7} - 10^{-1.7}$ | $10^{-2.0}$ | $10^{-2.5} - 10^{-1.3}$ | $10^{-2.1}$ | $10^{-2.6} - 10^{-1.7}$ |
| $T_{\text{kin}} n_{\text{H}_2}$ | $10^{7.4}$ | $10^{6.2} - 10^{10.1}$ | $10^{6.9}$ | $10^{5.9} - 10^{9.7}$ | $10^{7.2}$ | $10^{6.0} - 10^{9.9}$ |
| $\langle N_{\text{HCO}^+} \rangle$ | $10^{14.1}$ | $10^{13.3} - 10^{15.0}$ | $10^{13.7}$ | $10^{13.2} - 10^{15.0}$ | $10^{14.1}$ | $10^{13.3} - 10^{15.1}$ |
| S_{core} | $10^{-0.4}$ | $10^{-3.5} - 10^{1.6}$ | $10^{-0.1}$ | $10^{-4.0} - 10^{1.7}$ | $10^{-0.2}$ | $10^{-3.5} - 10^{1.7}$ |

Note. — These are the results of comparing radiative transfer calculations to the measurements of three transitions of HCO⁺ given in table 5.4. A 20% calibration error is added in quadrature to the 4-3 transition's statistical error. The measurements are scaled to match the 27'' beam of Z-Spec using three different scaling exponents. The median and 95% confidence range are derived from the cumulative distributions for the four primary radiative transfer parameters. Lower limits are given for T_{kin} and n_{H_2} because the distributions are not constrained at the upper end of the parameter ranges. In addition to the four primary parameters, median values and 95% confidence ranges for three auxiliary parameters, pressure, beam-averaged column density and core size, are also given in the table. The units for T_{kin} , n_{H_2} , N_{HCO^+} , $T_{\text{kin}} n_{\text{H}_2}$, $\langle N_{\text{HCO}^+} \rangle$ and S_{core} are [K], [cm^{-3}], [cm^{-2}], [K cm^{-3}], [cm^{-2}] and [pc], respectively.

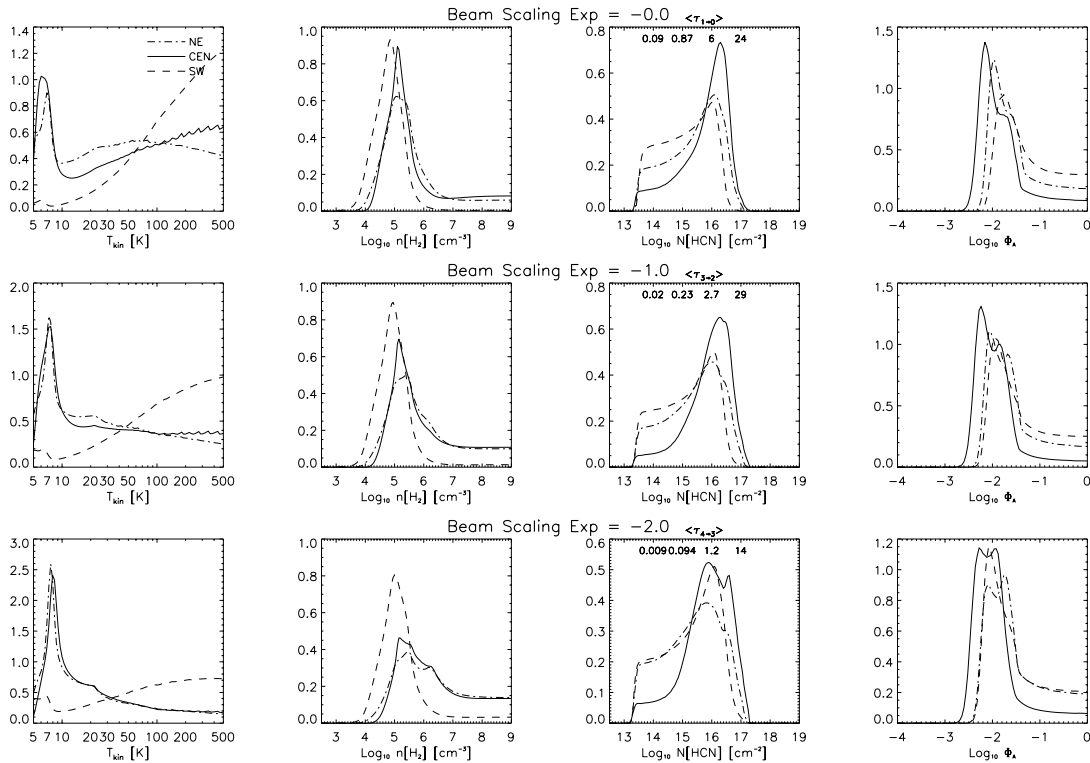


Figure 5.9. These are the calculated likelihood distributions for the four parameters of the radiative transfer model for HCN. See figure 5.7 for more information.

size, $S_{\text{core}} = N_{\text{HCO}^+}/(X_{\text{mol}} n_{\text{H}_2})$, are generally flat over a very wide range. If some of the radiative transfer models with the very smallest core sizes were excluded, the column density distribution would not be significantly affected while some of the low-temperature, high-density solutions would be eliminated. The median values and 95% confidence ranges for the radiative transfer modeling of HCO^+ are given in table 5.5.

The HCN measurements do not constrain the radiative transfer parameters as effectively as the HCO^+ measurements do (see figures 5.9 and 5.10 and table 5.6), which is not surprising given the lower signal-to-noise detection of these lines. However, the general features in the distributions are similar. Two of the three pointings have a peak in the temperature distributions at low temperatures and the two-dimensional distributions point to two groups of solutions, low temperature and high density or high temperature and low density. The column density and filling factor distributions are more extended for HCN than for HCO^+ . The plateaus seen in these two parameters' distributions correspond to a constant beam-averaged column density, which is the most well constrained parameter for HCN. In general, the most likely model has characteristics similar to that of HCO^+ : cold, dense, optically-thick gas filling about 1% of the beam.

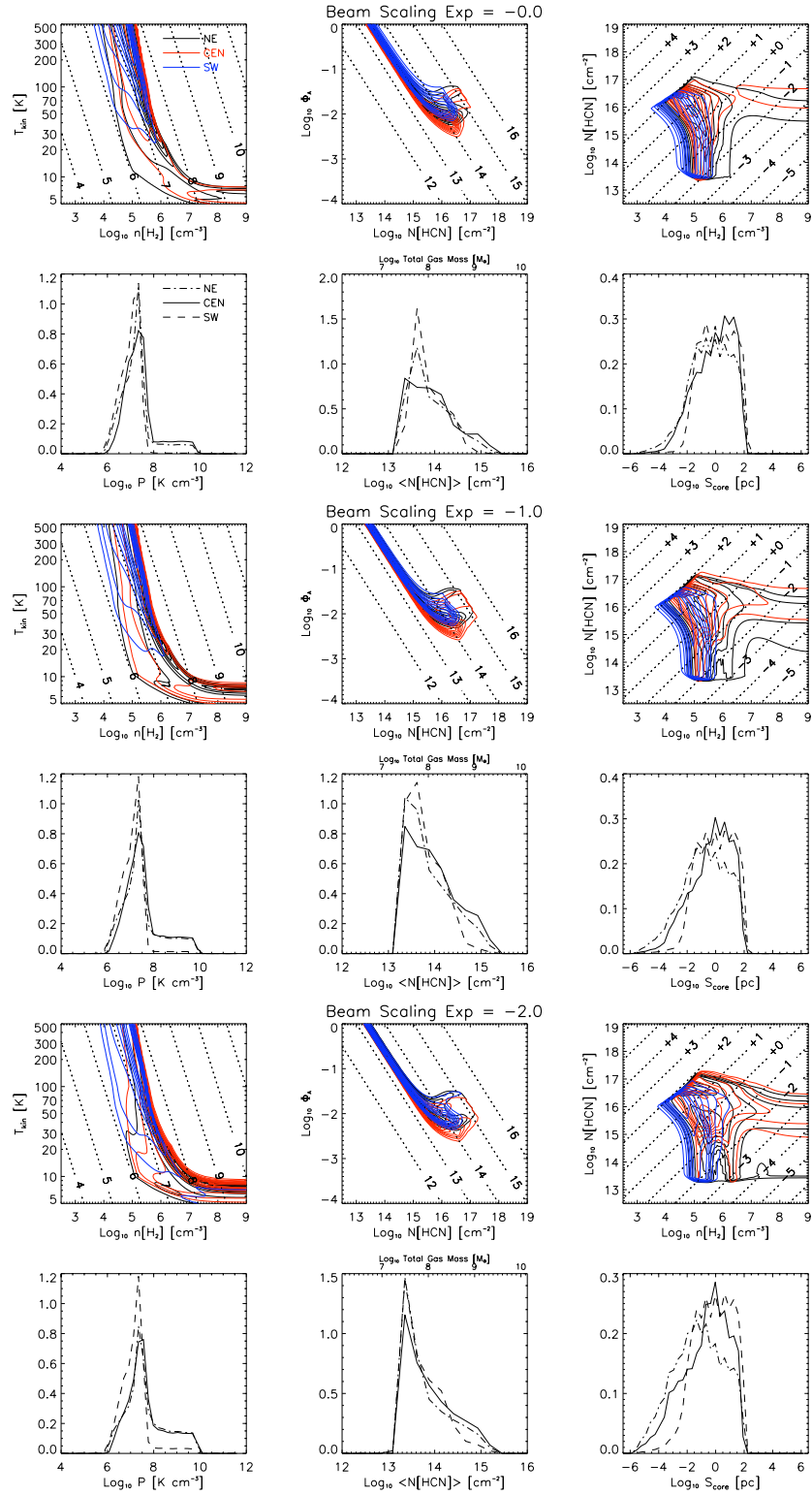


Figure 5.10. These plots show some two-dimensional and projected auxiliary likelihood distributions based on the radiative transfer modeling of HCN. See figure 5.8 for more details.

Table 5.6. HCN radiative transfer results

| | NE Pointing | | CEN Pointing | | SW Pointing | |
|----------------------------------|-------------|-------------------------|--------------|-------------------------|-------------|-------------------------|
| | Median | Range | Median | Range | Median | Range |
| Beam Scaling Exponent = -0.0 | | | | | | |
| T_{kin} | 48 | > 5 | 65 | > 5 | 172 | > 11 |
| n_{H_2} | $10^{5.3}$ | $> 10^{4.2}$ | $10^{5.2}$ | $> 10^{4.4}$ | $10^{4.8}$ | $10^{3.8} - 10^{5.9}$ |
| N_{HCN} | $10^{15.5}$ | $10^{13.6} - 10^{16.7}$ | $10^{15.9}$ | $10^{13.6} - 10^{16.8}$ | $10^{15.2}$ | $10^{13.6} - 10^{16.4}$ |
| Φ_{A} | $10^{-1.7}$ | $10^{-2.2} - 10^{-0.1}$ | $10^{-2.0}$ | $10^{-2.4} - 10^{-0.3}$ | $10^{-1.4}$ | $10^{-2.1} - 10^{-0.1}$ |
| $T_{\text{kin}} n_{\text{H}_2}$ | $10^{7.1}$ | $10^{6.0} - 10^{9.3}$ | $10^{7.2}$ | $10^{6.2} - 10^{9.4}$ | $10^{6.9}$ | $10^{5.9} - 10^{7.6}$ |
| $\langle N_{\text{HCN}} \rangle$ | $10^{13.7}$ | $10^{13.1} - 10^{14.9}$ | $10^{13.7}$ | $10^{13.1} - 10^{15.0}$ | $10^{13.7}$ | $10^{13.2} - 10^{14.5}$ |
| S_{core} | $10^{-0.5}$ | $10^{-3.8} - 10^{1.8}$ | $10^{-0.1}$ | $10^{-3.2} - 10^{1.7}$ | $10^{-0.0}$ | $10^{-2.3} - 10^{2.0}$ |
| Beam Scaling Exponent = -1.0 | | | | | | |
| T_{kin} | 22 | > 5 | 24 | > 5 | 138 | > 6 |
| n_{H_2} | $10^{5.6}$ | $> 10^{4.3}$ | $10^{5.6}$ | $> 10^{4.5}$ | $10^{4.9}$ | $10^{4.0} - 10^{7.3}$ |
| N_{HCN} | $10^{15.5}$ | $10^{13.5} - 10^{16.8}$ | $10^{16.0}$ | $10^{13.7} - 10^{16.9}$ | $10^{15.3}$ | $10^{13.5} - 10^{16.5}$ |
| Φ_{A} | $10^{-1.7}$ | $10^{-2.2} - 10^{-0.1}$ | $10^{-2.0}$ | $10^{-2.5} - 10^{-0.4}$ | $10^{-1.6}$ | $10^{-2.2} - 10^{-0.1}$ |
| $T_{\text{kin}} n_{\text{H}_2}$ | $10^{7.2}$ | $10^{6.0} - 10^{9.5}$ | $10^{7.3}$ | $10^{6.2} - 10^{9.5}$ | $10^{7.0}$ | $10^{6.0} - 10^{8.0}$ |
| $\langle N_{\text{HCN}} \rangle$ | $10^{13.6}$ | $10^{13.1} - 10^{14.9}$ | $10^{13.8}$ | $10^{13.0} - 10^{15.0}$ | $10^{13.6}$ | $10^{13.1} - 10^{14.5}$ |
| S_{core} | $10^{-0.9}$ | $10^{-4.4} - 10^{1.7}$ | $10^{-0.3}$ | $10^{-3.7} - 10^{1.7}$ | $10^{-0.1}$ | $10^{-2.6} - 10^{1.9}$ |
| Beam Scaling Exponent = -2.0 | | | | | | |
| T_{kin} | 13 | > 5 | 13 | > 5 | 95 | > 5 |
| n_{H_2} | $10^{6.1}$ | $> 10^{4.5}$ | $10^{6.0}$ | $> 10^{4.7}$ | $10^{5.1}$ | $> 10^{4.1}$ |
| N_{HCN} | $10^{15.4}$ | $10^{13.5} - 10^{16.9}$ | $10^{15.9}$ | $10^{13.6} - 10^{17.0}$ | $10^{15.4}$ | $10^{13.4} - 10^{16.6}$ |
| Φ_{A} | $10^{-1.7}$ | $10^{-2.3} - 10^{-0.1}$ | $10^{-2.0}$ | $10^{-2.5} - 10^{-0.4}$ | $10^{-1.7}$ | $10^{-2.3} - 10^{-0.1}$ |
| $T_{\text{kin}} n_{\text{H}_2}$ | $10^{7.4}$ | $10^{6.1} - 10^{9.6}$ | $10^{7.4}$ | $10^{6.2} - 10^{9.6}$ | $10^{7.1}$ | $10^{6.0} - 10^{9.0}$ |
| $\langle N_{\text{HCN}} \rangle$ | $10^{13.5}$ | $10^{13.0} - 10^{14.9}$ | $10^{13.6}$ | $10^{13.0} - 10^{15.0}$ | $10^{13.5}$ | $10^{13.0} - 10^{14.7}$ |
| S_{core} | $10^{-1.3}$ | $10^{-4.9} - 10^{1.6}$ | $10^{-0.6}$ | $10^{-4.5} - 10^{1.6}$ | $10^{-0.3}$ | $10^{-3.2} - 10^{1.8}$ |

Note. — These are the results of comparing radiative transfer calculations to the measurements of three transitions of HCN given in table 5.4, including an extra 20% calibration error on the 4–3 transition. See table 5.5 for more information.

Table 5.7. HNC transition data

| Transition | Freq. [GHz] | E_{upper} [K] | Beam Size | NE Flux | CEN Flux | SW Flux |
|------------|-------------|------------------------|-----------|----------------|----------------|----------------|
| 1–0 | 90.663 | 4.35 | 25'' | 10.7 ± 2.1 | 13.4 ± 0.8 | 12.3 ± 3.0 |
| 3–2 | 271.981 | 26.11 | 26'' | 1.5 ± 1.2 | 5.0 ± 0.6 | 4.4 ± 1.0 |

Note. — This table lists the line intensities (in K km/s) for the two detected transitions of HNC. The 1–0 intensities are sums of the fluxes quoted by Huettemeister et al. [1995] for two velocity separated components. The marginal detection of the 3–2 transition in the NE pointing is somewhat affected by poor baselining and could be as much as double the reported value.

5.4.2 HNC

Hydrogen isocyanide (HNC) has a transition ladder like HCO^+ and HCN but is much less abundant; therefore, its transitions are weaker. Its 1–0 transition at 90.663 GHz had been detected in M82 by Huettemeister et al. [1995]. Our detections of the 3–2 transition in the CEN and SW pointings are the first higher-order transitions seen for this molecule. These two transitions (listed in table 5.7) were used to interpret radiative transfer calculations using the method outlined above. The two measurements were made with very similar beam sizes, 25'' for 1–0 and 26'' for 3–2, so that beam scaling uncertainties play very little role in interpreting the results.

With only two detected transitions, the constraints on the four parameters of the radiative transfer model are marginal at best. The results shown in figures 5.11 and 5.12 and summarized in table 5.6 suggest the most likely solution is similar to that for HCO^+ and HCN, suggesting that all three species are tracing similar regions in M82. The best-constrained parameter is the beam-averaged column density whose 95% confidence range spans only 1.5 orders of magnitude, while the filling factor and clump column density span 2.5 to 3 orders of magnitude.

5.4.3 CS

Carbon monosulfide (CS) is an ideal molecule for study with Z-Spec because three of its transitions fall within the instrument’s bandpass. Unfortunately, for the M82 data, the sensitivity at the edges of the band is much worse than in the center and we are unable to detect the CS 4–3 (195.954 GHz) and CS 6–5 (293.912 GHz) transitions, which are also undetected in the literature. The previously detected CS 5–4 transition is seen in all three pointings, most strongly in the CEN pointing. In addition, the 2–1 and 3–2 transitions have also been detected [Mauersberger and Henkel 1989; Nguyen-Q-Rieu, Nakai, and Jackson 1989]. However, the detections have been made over a wide range in beam size from 16'' to 29'' complicating the comparisons and emphasizing pointing mismatches, particularly in the 3–2 measurements. Radiative transfer models for CS have been calculated and compared with the transition data given in table 5.9. The radiative transfer calculations use recently recomputed collisional rate coefficients for CS from Lique, Spielfiedel, and Cernicharo [2006] ($T_{\text{kin}} < 300$ K) and Lique and Spielfiedel [2007] ($T_{\text{kin}} \geq 300$ K). These calculations

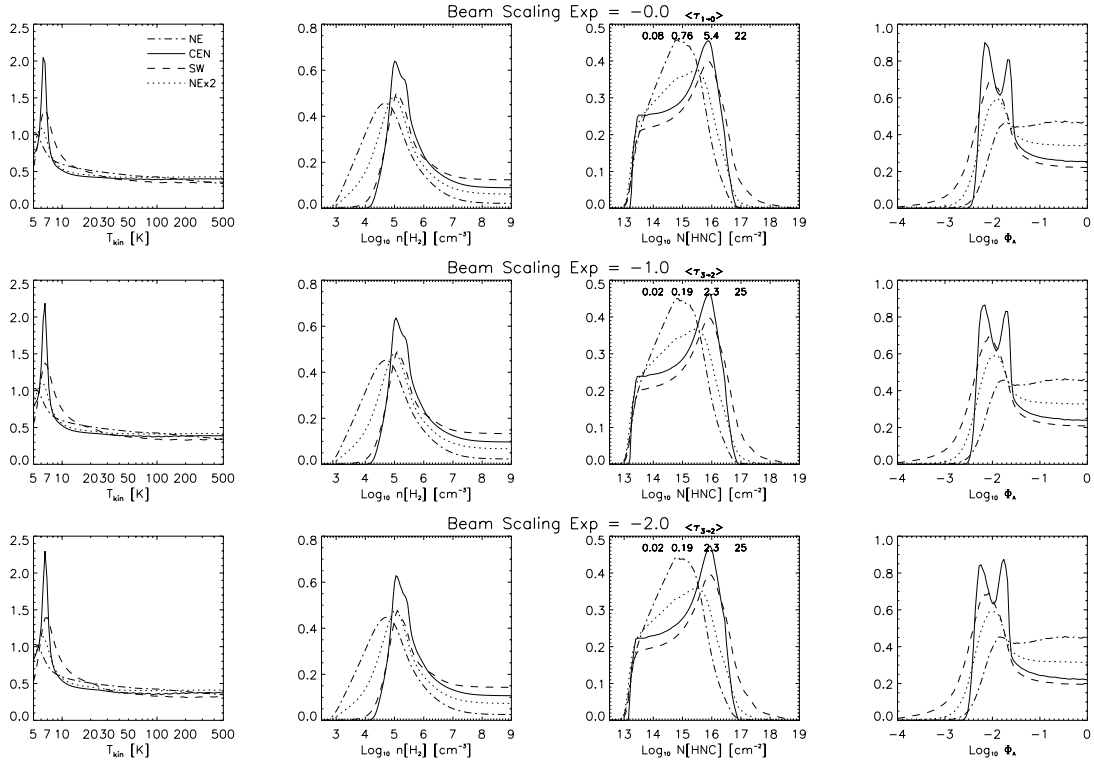


Figure 5.11. These plots show the likelihood distributions for the four parameters of the HNC radiative transfer calculations. See figure 5.7 for more information. One additional distribution is plotted in dotted lines which corresponds to using twice the measured flux in the 3–2 transition of the NE pointing. No additional calibration uncertainty is included because it is smaller than the statistical uncertainty and would not effect the distributions.

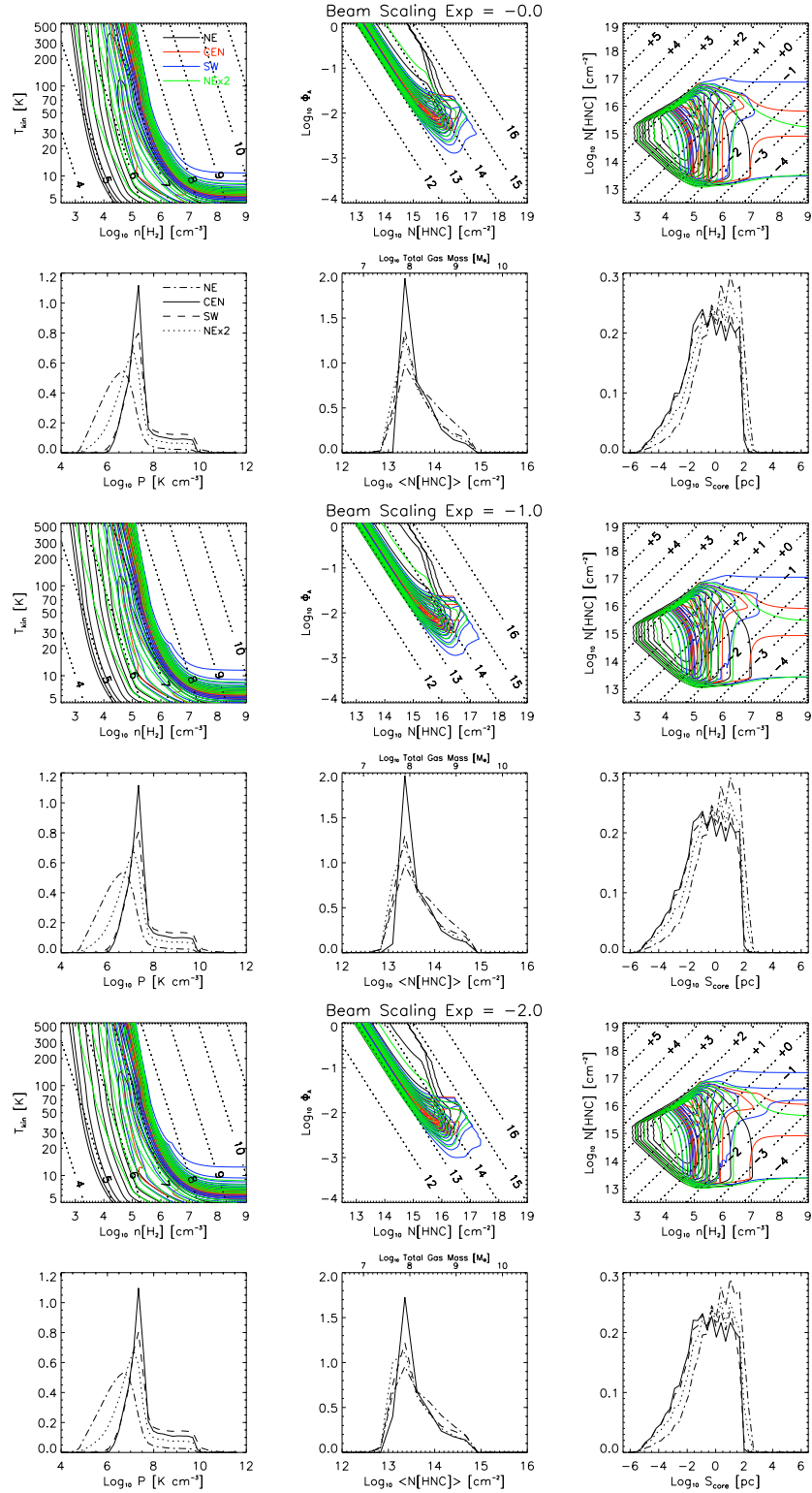


Figure 5.12. This figure shows some two-dimensional and projected auxiliary likelihood distributions based on the radiative transfer modeling of HNC. See figure 5.8 for more details. Additional distributions are plotted for the NE pointing using twice the measured flux of the 3–2 transition.

Table 5.8. HNC radiative transfer results

| | NE Pointing | | CEN Pointing | | SW Pointing | |
|----------------------------------|-------------|-------------------------|--------------|-------------------------|-------------|-------------------------|
| | Median | Range | Median | Range | Median | Range |
| Beam Scaling Exponent = -0.0 | | | | | | |
| T_{kin} | 29 | > 5 | 27 | > 5 | 22 | > 5 |
| n_{H_2} | $10^{4.8}$ | $> 10^{3.3}$ | $10^{5.5}$ | $> 10^{4.5}$ | $10^{5.7}$ | $> 10^{4.3}$ |
| N_{HNC} | $10^{14.8}$ | $10^{13.3} - 10^{16.3}$ | $10^{15.2}$ | $10^{13.4} - 10^{16.5}$ | $10^{15.3}$ | $10^{13.3} - 10^{17.2}$ |
| Φ_{A} | $10^{-1.1}$ | $10^{-2.3} - 10^{-0.0}$ | $10^{-1.7}$ | $10^{-2.3} - 10^{-0.1}$ | $10^{-1.8}$ | $10^{-3.1} - 10^{-0.1}$ |
| $T_{\text{kin}} n_{\text{H}_2}$ | $10^{6.4}$ | $10^{5.0} - 10^{8.7}$ | $10^{7.2}$ | $10^{6.2} - 10^{9.4}$ | $10^{7.2}$ | $10^{6.1} - 10^{9.7}$ |
| $\langle N_{\text{HNC}} \rangle$ | $10^{13.5}$ | $10^{12.8} - 10^{14.6}$ | $10^{13.4}$ | $10^{13.0} - 10^{14.5}$ | $10^{13.4}$ | $10^{12.8} - 10^{14.5}$ |
| S_{core} | $10^{0.1}$ | $10^{-3.6} - 10^{2.1}$ | $10^{-0.7}$ | $10^{-4.3} - 10^{1.7}$ | $10^{-0.7}$ | $10^{-4.4} - 10^{1.7}$ |
| T_{kin} | 33 | > 5 | | | | |
| n_{H_2} | $10^{5.2}$ | $> 10^{3.5}$ | | | | |
| N_{HNC} | $10^{14.9}$ | $10^{13.3} - 10^{16.6}$ | | | | |
| Φ_{A} | $10^{-1.4}$ | $10^{-2.5} - 10^{-0.1}$ | | | | |
| $T_{\text{kin}} n_{\text{H}_2}$ | $10^{6.9}$ | $10^{5.3} - 10^{9.4}$ | | | | |
| $\langle N_{\text{HNC}} \rangle$ | $10^{13.4}$ | $10^{12.7} - 10^{14.5}$ | | | | |
| S_{core} | $10^{-0.3}$ | $10^{-4.2} - 10^{1.9}$ | | | | |
| Beam Scaling Exponent = -1.0 | | | | | | |
| T_{kin} | 30 | > 5 | 25 | > 5 | 20 | > 5 |
| n_{H_2} | $10^{4.8}$ | $> 10^{3.2}$ | $10^{5.6}$ | $> 10^{4.5}$ | $10^{5.8}$ | $> 10^{4.3}$ |
| N_{HNC} | $10^{14.8}$ | $10^{13.3} - 10^{16.3}$ | $10^{15.2}$ | $10^{13.3} - 10^{16.5}$ | $10^{15.4}$ | $10^{13.3} - 10^{17.3}$ |
| Φ_{A} | $10^{-1.1}$ | $10^{-2.3} - 10^{-0.0}$ | $10^{-1.7}$ | $10^{-2.4} - 10^{-0.1}$ | $10^{-1.9}$ | $10^{-3.2} - 10^{-0.1}$ |
| $T_{\text{kin}} n_{\text{H}_2}$ | $10^{6.4}$ | $10^{4.9} - 10^{8.7}$ | $10^{7.3}$ | $10^{6.3} - 10^{9.5}$ | $10^{7.3}$ | $10^{6.2} - 10^{9.8}$ |
| $\langle N_{\text{HNC}} \rangle$ | $10^{13.5}$ | $10^{12.7} - 10^{14.6}$ | $10^{13.4}$ | $10^{13.0} - 10^{14.5}$ | $10^{13.4}$ | $10^{12.7} - 10^{14.5}$ |
| S_{core} | $10^{0.1}$ | $10^{-3.7} - 10^{2.1}$ | $10^{-0.8}$ | $10^{-4.3} - 10^{1.7}$ | $10^{-0.7}$ | $10^{-4.4} - 10^{1.7}$ |
| T_{kin} | 31 | > 5 | | | | |
| n_{H_2} | $10^{5.2}$ | $> 10^{3.5}$ | | | | |
| N_{HNC} | $10^{14.9}$ | $10^{13.3} - 10^{16.6}$ | | | | |
| Φ_{A} | $10^{-1.5}$ | $10^{-2.6} - 10^{-0.1}$ | | | | |
| $T_{\text{kin}} n_{\text{H}_2}$ | $10^{6.9}$ | $10^{5.3} - 10^{9.4}$ | | | | |
| $\langle N_{\text{HNC}} \rangle$ | $10^{13.4}$ | $10^{12.7} - 10^{14.5}$ | | | | |
| S_{core} | $10^{-0.4}$ | $10^{-4.2} - 10^{1.9}$ | | | | |
| Beam Scaling Exponent = -2.0 | | | | | | |
| T_{kin} | 30 | > 5 | 22 | > 5 | 19 | > 5 |
| n_{H_2} | $10^{4.8}$ | $> 10^{3.2}$ | $10^{5.6}$ | $> 10^{4.6}$ | $10^{5.9}$ | $> 10^{4.4}$ |
| N_{HNC} | $10^{14.8}$ | $10^{13.3} - 10^{16.3}$ | $10^{15.3}$ | $10^{13.3} - 10^{16.5}$ | $10^{15.5}$ | $10^{13.3} - 10^{17.3}$ |
| Φ_{A} | $10^{-1.1}$ | $10^{-2.4} - 10^{-0.1}$ | $10^{-1.8}$ | $10^{-2.4} - 10^{-0.1}$ | $10^{-1.9}$ | $10^{-3.2} - 10^{-0.1}$ |
| $T_{\text{kin}} n_{\text{H}_2}$ | $10^{6.4}$ | $10^{4.9} - 10^{8.8}$ | $10^{7.3}$ | $10^{6.3} - 10^{9.5}$ | $10^{7.3}$ | $10^{6.2} - 10^{9.8}$ |
| $\langle N_{\text{HNC}} \rangle$ | $10^{13.5}$ | $10^{12.7} - 10^{14.6}$ | $10^{13.4}$ | $10^{12.9} - 10^{14.5}$ | $10^{13.4}$ | $10^{12.7} - 10^{14.5}$ |
| S_{core} | $10^{0.1}$ | $10^{-3.7} - 10^{2.1}$ | $10^{-0.8}$ | $10^{-4.4} - 10^{1.7}$ | $10^{-0.7}$ | $10^{-4.4} - 10^{1.7}$ |
| T_{kin} | 29 | > 5 | | | | |
| n_{H_2} | $10^{5.3}$ | $> 10^{3.5}$ | | | | |
| N_{HNC} | $10^{14.9}$ | $10^{13.2} - 10^{16.7}$ | | | | |
| Φ_{A} | $10^{-1.5}$ | $10^{-2.7} - 10^{-0.1}$ | | | | |
| $T_{\text{kin}} n_{\text{H}_2}$ | $10^{6.9}$ | $10^{5.3} - 10^{9.4}$ | | | | |
| $\langle N_{\text{HNC}} \rangle$ | $10^{13.3}$ | $10^{12.7} - 10^{14.5}$ | | | | |
| S_{core} | $10^{-0.4}$ | $10^{-4.3} - 10^{1.8}$ | | | | |

Note. — These are the results of comparing radiative transfer calculations to the measurements of two transitions of HNC given in table 5.7. See table 5.5 for more information. Two versions for the NE pointing are reported, the second uses twice the flux in the 3–2 line to assess the baseline quality.

Table 5.9. CS transition data

| Transition | Freq. [GHz] | E_{upper} [K] | Beam Size | NE Flux | CEN Flux | SW Flux |
|------------|-------------|------------------------|-----------|----------------|----------------|---------------|
| 2-1 | 97.980 | 7.05 | 25'' | 15.5 | 12.5 | 9.8 |
| 3-2 | 146.969 | 14.11 | 16'' | 11.0 ± 1.2 | 16.3 ± 2.5 | 7.6 ± 1.7 |
| 5-4 | 244.935 | 35.27 | 29'' | 3.8 ± 1.0 | 4.4 ± 0.6 | 3.0 ± 0.9 |

Note. — This table lists the line intensities (in K km/s) for the detected transitions of CS. The 2-1 intensities have been scaled up from the reported T_A^* units into T_{mb} units by dividing by the 60% main beam efficiency. No errors were given with the 2-1 detections; a fixed 2 K km/s, or approximately 15% fractional uncertainty, is used for the likelihood calculations.

are based on a new model for the potential energy surface of the interaction between CS and He. The coefficients have been scaled by 1.4 to convert to the more dominant CS-H₂ interaction. This scaling factor accounts for the smaller reduced mass and larger size of H₂ [Schöier et al. 2005].

The previous detection of the 5-4 line [Mauersberger and Henkel 1989] was made with a beam size of 11'' and would presumably measure a significantly larger flux than we do in our 29'' beam. Surprisingly, this is not the case; however, an examination of the published spectra shows significant baseline noise that may have lead to underestimates of the width (by a factor of 2-3) and the peak (by 25%). These potential corrections would give results consistent with a beam scaling exponent of -1.

As with the other molecules, the likelihood distributions for CS (figures 5.13 and 5.14) indicate a significant amount of cold, dense molecular gas that fills about 1% of the beam. The temperature is constrained within the bounds of the simulation in two of the three pointings (table 5.10). The distributions for N_{CS} and Φ_A are fairly broad but in such a way that the beam-averaged column density is fairly well constrained.

5.4.4 SO₂

Sulfur dioxide (SO₂) is the only potential detection in our spectra of M82 of a previously unseen species. Its complicated rotational energy diagram is characterized by three quantum numbers and the molecule has a large number of transitions within our band. SO₂ is a strong emitter in this frequency range; in the core of the Orion molecular cloud it accounts for roughly 28% of the total line flux [Sutton et al. 1985]. 3σ upper limits of 0.95 K km/s for lines at 104.029 and 104.239 GHz were reported by Petuchowski and Bennett [1992]. These observations were made toward the CEN pointing with a 64'' beam. We detect two lines at SO₂ transition frequencies of 221.965 (32'') and 255.958 GHz (27.8''), though the latter could be a blend of three neighboring SO₂ transitions. Two additional transitions at 235.152 and 241.616 GHz included in our spectral fits and radiative transfer calculations are detected at the 1σ level.

Unfortunately, the radiative transfer modeling for SO₂ does not support the identification of these

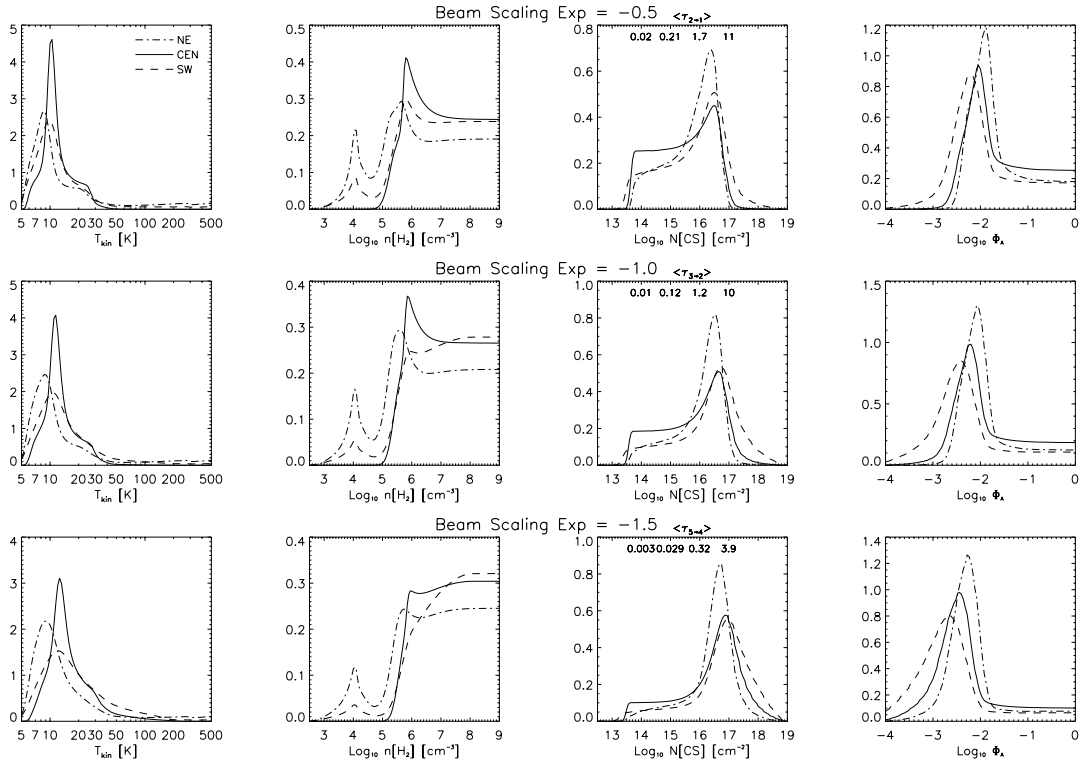


Figure 5.13. These are the likelihood distributions calculated for the four parameters of the radiative transfer model of CS. See figure 5.7 for more information. The CS measurements cover a larger range of beam sizes than the other species, so the values of beam-scaling exponent used for CS are -0.5 , -1.0 , and -1.5 .

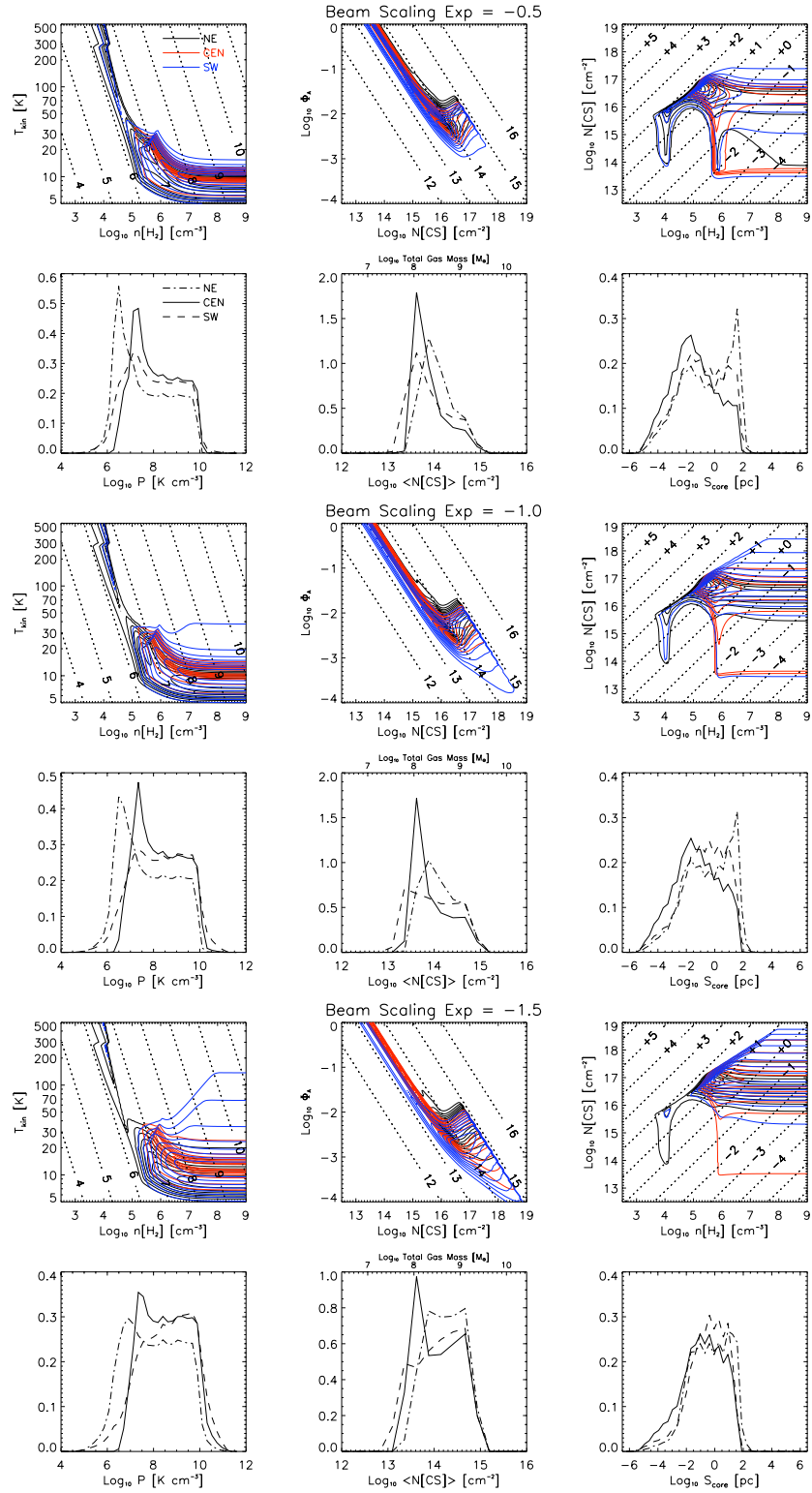


Figure 5.14. These plots show the two-dimensional and auxiliary likelihood distributions for CS. Refer to figure 5.8 for more details.

Table 5.10. CS radiative transfer results

| | NE Pointing | | CEN Pointing | | SW Pointing | |
|---------------------------------|-------------|-------------------------|--------------|-------------------------|-------------|-------------------------|
| | Median | Range | Median | Range | Median | Range |
| Beam Scaling Exponent = -0.5 | | | | | | |
| T_{kin} | 9 | > 5 | 10 | 6 - 27 | 10 | 5 - 218 |
| n_{H_2} | $10^{6.3}$ | $> 10^{3.7}$ | $10^{7.0}$ | $> 10^{5.3}$ | $10^{6.9}$ | $> 10^{3.9}$ |
| N_{CS} | $10^{15.9}$ | $10^{13.8} - 10^{16.8}$ | $10^{15.5}$ | $10^{13.7} - 10^{16.9}$ | $10^{16.0}$ | $10^{13.6} - 10^{17.5}$ |
| Φ_{A} | $10^{-1.9}$ | $10^{-2.4} - 10^{-0.1}$ | $10^{-1.8}$ | $10^{-2.6} - 10^{-0.1}$ | $10^{-2.1}$ | $10^{-3.2} - 10^{-0.1}$ |
| $T_{\text{kin}} n_{\text{H}_2}$ | $10^{7.2}$ | $10^{5.8} - 10^{9.7}$ | $10^{7.9}$ | $10^{6.4} - 10^{9.9}$ | $10^{7.8}$ | $10^{5.9} - 10^{9.9}$ |
| $\langle N_{\text{CS}} \rangle$ | $10^{13.9}$ | $10^{13.3} - 10^{14.8}$ | $10^{13.7}$ | $10^{13.2} - 10^{14.7}$ | $10^{13.7}$ | $10^{13.0} - 10^{14.8}$ |
| S_{core} | $10^{-0.7}$ | $10^{-4.3} - 10^{1.9}$ | $10^{-1.7}$ | $10^{-4.7} - 10^{1.4}$ | $10^{-1.1}$ | $10^{-4.6} - 10^{1.7}$ |
| Beam Scaling Exponent = -1.0 | | | | | | |
| T_{kin} | 9 | > 5 | 11 | 6 - 31 | 11 | 5 - 149 |
| n_{H_2} | $10^{6.6}$ | $> 10^{3.7}$ | $10^{7.1}$ | $> 10^{5.4}$ | $10^{7.2}$ | $> 10^{4.0}$ |
| N_{CS} | $10^{16.2}$ | $10^{13.9} - 10^{17.0}$ | $10^{16.0}$ | $10^{13.6} - 10^{17.4}$ | $10^{16.5}$ | $10^{13.6} - 10^{18.1}$ |
| Φ_{A} | $10^{-2.1}$ | $10^{-2.6} - 10^{-0.2}$ | $10^{-2.1}$ | $10^{-3.0} - 10^{-0.1}$ | $10^{-2.4}$ | $10^{-3.6} - 10^{-0.2}$ |
| $T_{\text{kin}} n_{\text{H}_2}$ | $10^{7.5}$ | $10^{5.8} - 10^{9.8}$ | $10^{8.1}$ | $10^{6.6} - 10^{10.0}$ | $10^{8.2}$ | $10^{6.0} - 10^{10.2}$ |
| $\langle N_{\text{CS}} \rangle$ | $10^{13.9}$ | $10^{13.3} - 10^{14.8}$ | $10^{13.7}$ | $10^{13.2} - 10^{14.8}$ | $10^{13.8}$ | $10^{13.0} - 10^{14.8}$ |
| S_{core} | $10^{-0.5}$ | $10^{-4.1} - 10^{1.7}$ | $10^{-1.5}$ | $10^{-4.6} - 10^{1.4}$ | $10^{-0.8}$ | $10^{-4.4} - 10^{1.6}$ |
| Beam Scaling Exponent = -1.5 | | | | | | |
| T_{kin} | 10 | 5 - 276 | 13 | 7 - 66 | 14 | 5 - 132 |
| n_{H_2} | $10^{6.9}$ | $> 10^{3.7}$ | $10^{7.4}$ | $> 10^{5.6}$ | $10^{7.4}$ | $> 10^{4.1}$ |
| N_{CS} | $10^{16.5}$ | $10^{14.0} - 10^{17.7}$ | $10^{16.6}$ | $10^{13.7} - 10^{18.1}$ | $10^{16.9}$ | $10^{13.7} - 10^{18.3}$ |
| Φ_{A} | $10^{-2.3}$ | $10^{-3.1} - 10^{-0.3}$ | $10^{-2.5}$ | $10^{-3.5} - 10^{-0.2}$ | $10^{-2.7}$ | $10^{-3.8} - 10^{-0.4}$ |
| $T_{\text{kin}} n_{\text{H}_2}$ | $10^{7.9}$ | $10^{5.8} - 10^{10.0}$ | $10^{8.4}$ | $10^{6.7} - 10^{10.2}$ | $10^{8.6}$ | $10^{6.1} - 10^{10.4}$ |
| $\langle N_{\text{CS}} \rangle$ | $10^{14.1}$ | $10^{13.3} - 10^{14.8}$ | $10^{13.9}$ | $10^{13.1} - 10^{14.8}$ | $10^{14.0}$ | $10^{13.0} - 10^{14.8}$ |
| S_{core} | $10^{-0.4}$ | $10^{-3.5} - 10^{1.7}$ | $10^{-0.9}$ | $10^{-4.4} - 10^{1.3}$ | $10^{-0.5}$ | $10^{-4.1} - 10^{1.4}$ |

Note. — These are the results of comparing radiative transfer calculations to the measurements of three transitions of CS given in table 5.9. See table 5.5 for more details. A 30% uncertainty is added in quadrature to the 3–2 detections’ measurement uncertainty to account for pointing offsets, calibration uncertainty and line-width variation.

lines. The deviations between line fluxes predicted by the most likely radiative transfer model and the Z-Spec measurements are much larger than the statistical uncertainty in the tentative detections. The strongest feature associated with SO_2 is the 3σ feature at 222 GHz. The centroid of that feature, particularly in the center pointing, matches well with the SO_2 $11_{1,11}-10_{0,10}$ transition. However, the high excitation energy of that transition coupled with the weak to nonexistent detections of lower energy transitions suggest that either there is a flaw in the radiative transfer calculation or the identification of the 222 GHz feature is incorrect. Without higher-spectral-resolution follow-up observations of this region of our spectra, we must conclude that the bump at 222 GHz is unidentified.

5.5 Multiple Species Model

The single species models presented in the previous section are significantly limited by the fact that the number of parameters of the model is larger than the number of measurements used to constrain the model. However, the modeling for HCO^+ , HCN, HNC and CS suggest that all of these molecules are tracing gas with similar physical conditions. Multiple species observations within our galaxy of star-forming regions indicate a fair level of similarity between the intensity distributions and line shapes of these four species [Brand et al. 2001; Nikolić et al. 2003]. High spatial resolution maps of the galactic circumnuclear disk [Christopher et al. 2005] and of the starburst galaxy NGC 253 [Knudsen et al. 2007] in HCO^+ and HCN indicate strong similarity, in general, between the emission of these two molecules.

A sensible model for the emission of these high-density regions would be clumps of gas with specific physical conditions described by four parameters, T_{kin} , n_{H_2} , N_{H_2} and Φ_{A} , and four abundance ratios, X_{mol} , for each of the four modeled species. Such a model is degenerate because the single species radiative transfer calculations only depend on the species column density, $N_{\text{mol}} = X_{\text{mol}} N_{\text{H}_2}$. A better set of parameters is T_{kin} , n_{H_2} and Φ_{A} and four column densities, one for each species. The seven parameters of this model should be properly constrained by the eleven transitions of HCO^+ , HCN, HNC and CS that have been measured.

Likelihood distributions for several parameters of the multiple species radiative transfer modeling are shown in figures 5.15 – 5.18 for the three different pointings observed in M82. The line intensities and uncertainties used for the multiple species model are the same as described in the previous section. These intensities and uncertainties are scaled to a beam size of $27''$ assuming a beam scaling exponent of -1.0 , which is the most reasonable value from the continuum emission fitting and the single species modeling. The median and 95% confidence ranges for the seven primary and several derived parameters of the model are given in table 5.11. All parameters are well constrained within the simulation limits.

The model points to a significant amount of 20 K molecular gas with a density of $4 \times 10^5 \text{ cm}^{-3}$

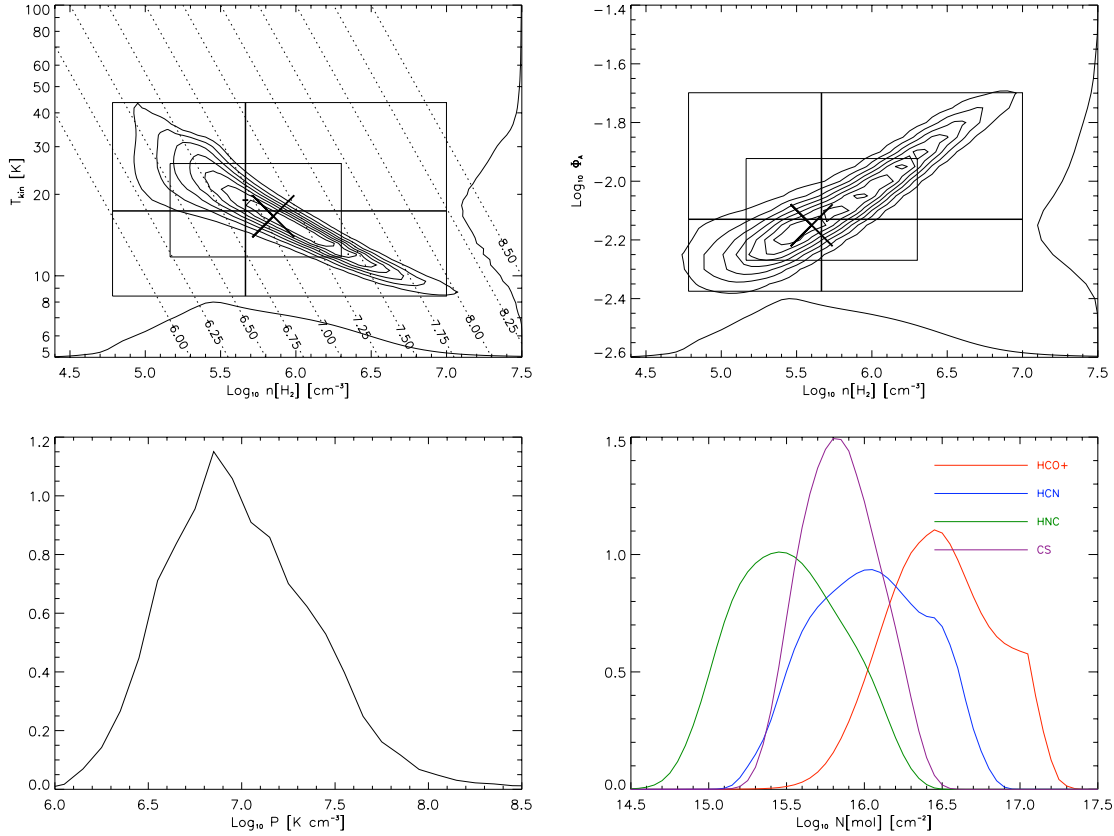


Figure 5.15. This figure shows various likelihood distributions for the multiple species radiative transfer modeling for the NE pointing of M82. The top two panels show two-dimensional distributions in the $T_{\text{kin}}-n_{\text{H}_2}$ and $\Phi_{\text{A}}-n_{\text{H}_2}$ planes. The one-dimensional projections of these distributions onto their respective axes are also shown. The boxes indicate the 68% (1σ) and 95% (2σ) confidence ranges determined from the one-dimensional distributions. The cross hairs show the median values. The large X marks the spot of maximum likelihood of the two-dimensional distribution. The diagonal lines in the $T_{\text{kin}}-n_{\text{H}_2}$ plot are loci of constant pressure labeled in logarithmic units of $[\text{K cm}^{-3}]$. The pressure distribution is shown in the lower left plot. The lower right plot has the likelihood distributions for the four column densities. A legend indicates which color corresponds to which species.

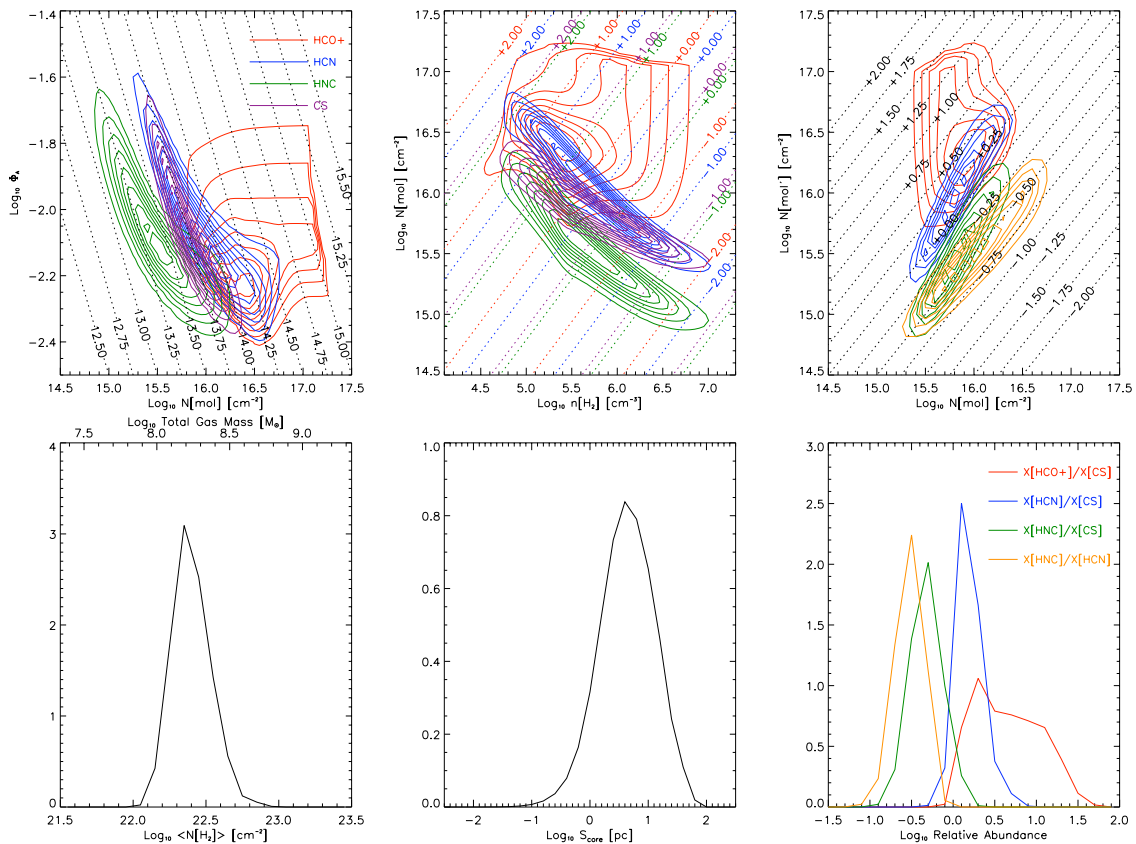


Figure 5.16. These are plots of various likelihood distributions for the multiple species radiative transfer model of the NE pointing. The top row of contour plots shows two-dimensional species distributions in the Φ_A - N_{mol} , N_{mol} - n_{H_2} and N_{mol} - N_{mol} planes, respectively, from left to right. These distributions are used to create the projected distributions in the bottom row.

The Φ_A - N_{mol} plot in the top left corner shows four distributions, one for each species, labeled by color and identified by the legend in the upper left corner. Dashed lines of constant beam-averaged column density are also included and labeled with their associated value in logarithmic units of $[\text{cm}^{-2}]$. The two-dimensional distributions can be used to create beam-averaged column density distributions but because the filling factor is the same for all species, the $\langle N_{\text{mol}} \rangle$ distributions look very similar to the clump column density distributions shown in the lower left plot of figure 5.15. However, using the derived abundance ratios from table 5.12, a species-averaged distribution for $\langle N_{\text{H}_2} \rangle$ can be calculated. This distribution is shown in the lower left and includes an alternative horizontal axis reflecting the conversion to total molecular mass in the galaxy using equation (5.6).

The top center plot of the N_{mol} - n_{H_2} likelihood distributions use the same color legend as the top left figure. This plot also shows color-coded dashed lines of constant $\log_{10} S_{\text{core}}$ in [pc] for each of the four species at values of -2.0 , -1.0 , 0.0 , 1.0 and 2.0 . A species-averaged distribution for S_{core} is plotted in the bottom center.

The N_{mol} - N_{mol} plot in the top right corner is used to create the relative abundance ratio plot on the bottom left. The color coding legend is indicated in the upper right of the abundance distribution plot. The contour plot includes dashed lines of constant abundance ratio in logarithmic units. These lines are labeled with their associated values.

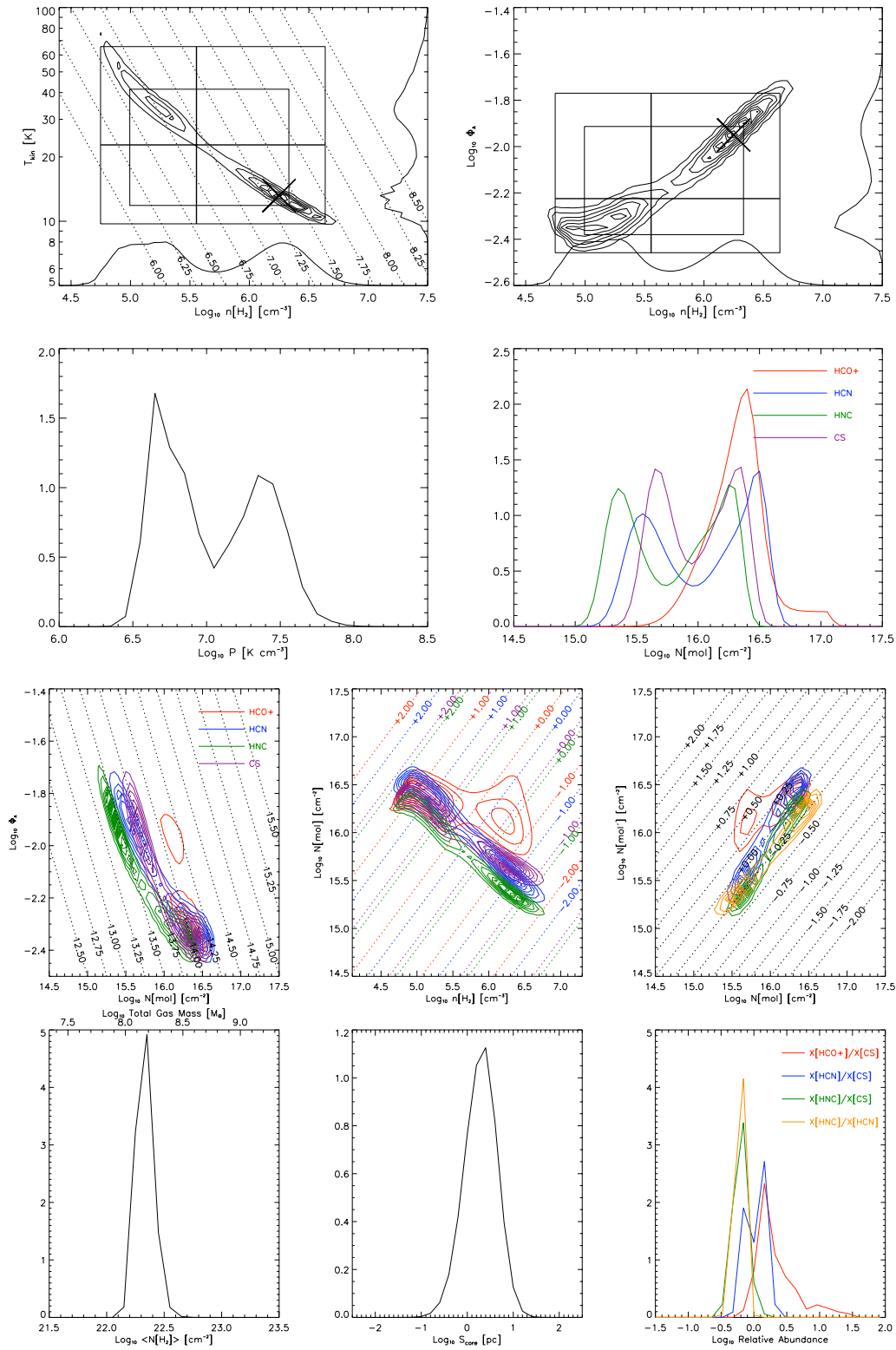


Figure 5.17. This figure shows likelihood distributions for the parameters of the multiple species radiative transfer model for the CEN pointing. See figures 5.15 and 5.16 for further details.

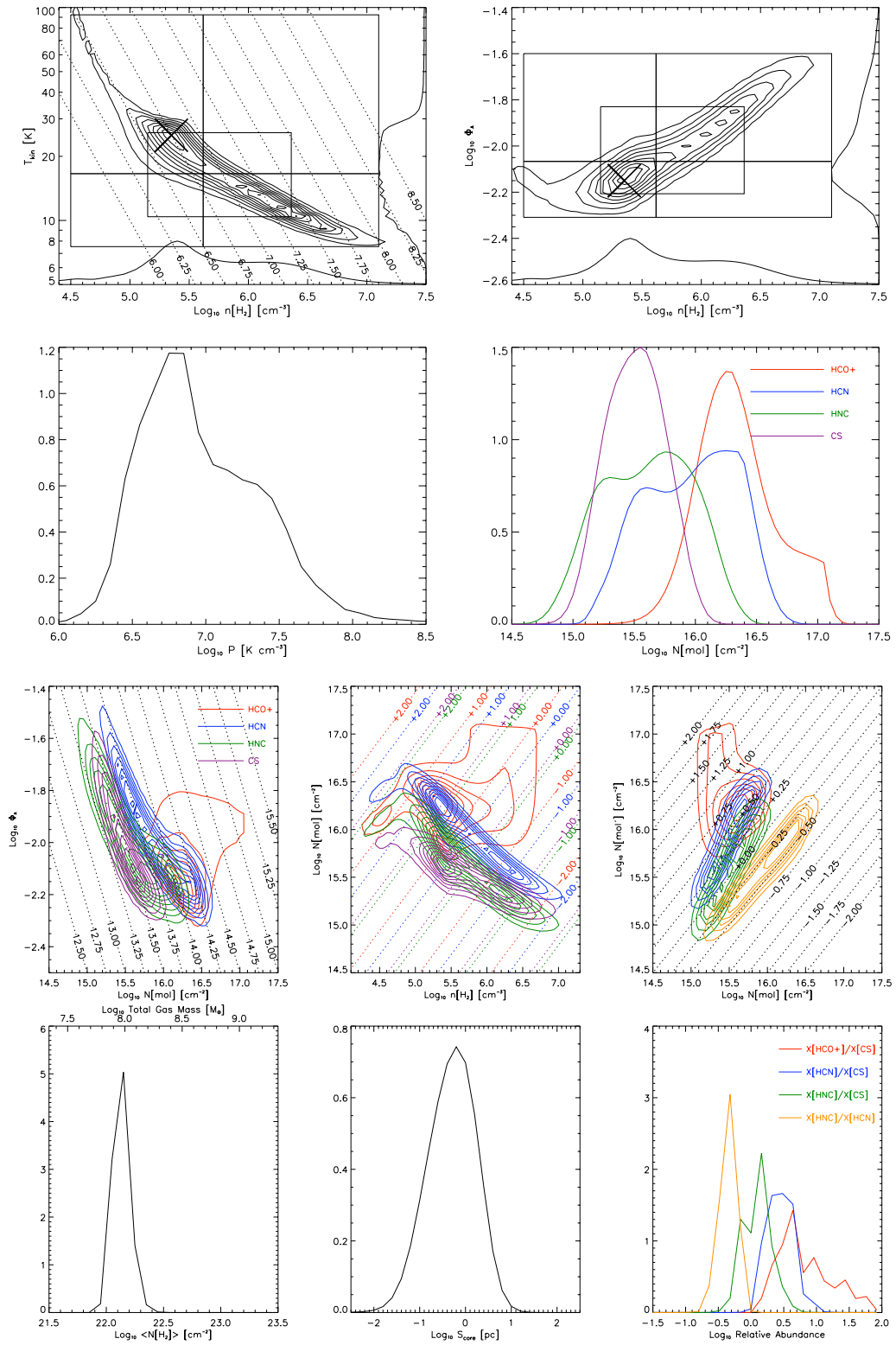


Figure 5.18. These plots show likelihood distributions for the parameters of the multiple species radiative transfer model for the SW pointing. See figures 5.15 and 5.16 for more information.

Table 5.11. Multiple species modeling results

| | NE Pointing | | CEN Pointing | | SW Pointing | |
|---|-------------|-------------------------|--------------|-------------------------|-------------|-------------------------|
| | Median | Range | Median | Range | Median | Range |
| Primary Model Parameters | | | | | | |
| T_{kin} | 17 | 8 - 44 | 23 | 10 - 66 | 17 | 8 - 92 |
| n_{H_2} | $10^{5.7}$ | $10^{4.8} - 10^{7.0}$ | $10^{5.6}$ | $10^{4.7} - 10^{6.6}$ | $10^{5.6}$ | $10^{4.5} - 10^{7.1}$ |
| Φ_{A} | $10^{-2.1}$ | $10^{-2.4} - 10^{-1.7}$ | $10^{-2.2}$ | $10^{-2.5} - 10^{-1.8}$ | $10^{-2.1}$ | $10^{-2.3} - 10^{-1.6}$ |
| N_{HCO^+} | $10^{16.5}$ | $10^{15.8} - 10^{17.1}$ | $10^{16.3}$ | $10^{15.8} - 10^{16.9}$ | $10^{16.3}$ | $10^{15.7} - 10^{17.0}$ |
| N_{HCN} | $10^{16.0}$ | $10^{15.3} - 10^{16.7}$ | $10^{16.0}$ | $10^{15.3} - 10^{16.6}$ | $10^{16.0}$ | $10^{15.2} - 10^{16.6}$ |
| N_{HNC} | $10^{15.5}$ | $10^{14.8} - 10^{16.2}$ | $10^{15.8}$ | $10^{15.2} - 10^{16.4}$ | $10^{15.6}$ | $10^{14.9} - 10^{16.2}$ |
| N_{CS} | $10^{15.8}$ | $10^{15.4} - 10^{16.3}$ | $10^{16.0}$ | $10^{15.5} - 10^{16.4}$ | $10^{15.5}$ | $10^{15.0} - 10^{16.0}$ |
| Projected Parameters – Core Properties | | | | | | |
| $P \propto T_{\text{kin}} n_{\text{H}_2}$ | $10^{6.9}$ | $10^{6.2} - 10^{7.9}$ | $10^{6.9}$ | $10^{6.4} - 10^{7.6}$ | $10^{6.9}$ | $10^{6.3} - 10^{7.9}$ |
| $\langle N_{\text{H}_2} \rangle$ | $10^{22.3}$ | $10^{22.1} - 10^{22.7}$ | $10^{22.3}$ | $10^{22.1} - 10^{22.5}$ | $10^{22.1}$ | $10^{21.9} - 10^{22.3}$ |
| S_{core} | $10^{0.5}$ | $10^{-0.5} - 10^{1.5}$ | $10^{0.2}$ | $10^{-0.6} - 10^{0.9}$ | $10^{-0.4}$ | $10^{-1.5} - 10^{0.6}$ |
| Relative Abundance Ratios | | | | | | |
| $X_{\text{HCO}^+}/X_{\text{CS}}$ | $10^{0.7}$ | $10^{1.6} - 10^{0.0}$ | $10^{0.3}$ | $10^{1.3} - 10^{-0.1}$ | $10^{0.8}$ | $10^{1.8} - 10^{0.2}$ |
| $X_{\text{HCN}}/X_{\text{CS}}$ | $10^{0.3}$ | $10^{0.8} - 10^{-0.1}$ | $10^{0.1}$ | $10^{0.4} - 10^{-0.2}$ | $10^{0.5}$ | $10^{1.0} - 10^{0.1}$ |
| $X_{\text{HNC}}/X_{\text{CS}}$ | $10^{-0.2}$ | $10^{0.3} - 10^{-0.7}$ | $10^{-0.1}$ | $10^{0.2} - 10^{-0.4}$ | $10^{0.2}$ | $10^{0.7} - 10^{-0.2}$ |
| $X_{\text{HNC}}/X_{\text{HCN}}$ | $10^{-0.6}$ | $10^{-1.1} - 10^{-0.2}$ | $10^{-0.3}$ | $10^{-0.5} - 10^{-0.1}$ | $10^{-0.4}$ | $10^{-0.8} - 10^{-0.1}$ |

Note. — This table summarizes the results obtained from the multiple species radiative transfer modeling of the lines of HCO⁺, HCN, HNC and CS. The median and 95% confidence ranges are obtained from the likelihood distributions shown in figures 5.15 – 5.18. The seven primary parameters are all well constrained within the radiative transfer simulation limits and several projected parameters of interest are also well constrained. The units for T_{kin} , n_{H_2} , P and S_{core} are [K], [cm^{-3}], [K cm^{-3}] and [pc], respectively. All column densities are given in units of [cm^{-2}].

Table 5.12. Selected molecular abundance ratios for M82

| Species | HCO ⁺ | HCN | HNC | CS |
|-----------------------------|------------------|------|------|------|
| $\log_{10}(X_{\text{mol}})$ | -8.05 | -8.3 | -8.7 | -8.6 |

Note. — This table gives the abundance ratios (with respect to H₂) used for the radiative transfer modeling. They are derived from the multiple species modeling results for the abundance of HCO⁺, HCN and HNC relative to CS and the abundance for CS relative to H₂ from Mauersberger and Henkel [1989].

that fills about 0.7% of the 27'' beam. The column densities indicate that observed transitions are somewhat optically thick with typical optical depths in the 1-10 range. The quality of the fit of the median values for the model parameters can be assessed by comparing the scaled, measured intensities to the modeled intensities, relative to the error in the measurements. The reduced χ^2 values for eleven measurements and seven free parameters are 5.2, 5.2 and 3.7 for the NE, CEN and SW pointings, respectively. These reduced χ^2 values do not achieve the ideal value of unity but are fairly reasonable given that the model is certainly a simplification of the actual physical conditions present in M82. All of the measurements contribute fairly equally to χ^2 except for the CS 5-4 transition, which the model indicates should be smaller by more than 2σ .

The distributions for the projected quantities indicate that certain parameters and combinations are better constrained than others. The pressure, $P \propto T_{\text{kin}} n_{\text{H}_2}$, is constrained by the model to a range of 1.5 orders of magnitude but does not represent the principle axis of the T_{kin} versus n_{H_2} likelihood distribution. The quantity that is most well constrained in that plane is approximately $T_{\text{kin}}^3 n_{\text{H}_2}$ or $P T_{\text{kin}}^2$. Conversely, the beam averaged column density and the relative abundance ratios, particularly for the neutral species, do represent the principle constraint axis in the $\Phi_{\text{A}}-N_{\text{mol}}$ and $N_{\text{mol}'}-N_{\text{mol}}$ planes, respectively. The distribution for the core size, $S_{\text{core}} = N_{\text{mol}}/(X_{\text{mol}} n_{\text{H}_2})$, is fairly broad, spanning almost 2 orders of magnitude, because it appears to be perpendicular to the principle axes of the likelihood distributions in the $N_{\text{mol}}-n_{\text{H}_2}$ plane. From those distributions, the best constrained parameter, at least for the neutral species, is the product $N_{\text{mol}} n_{\text{H}_2}$ rather than the quotient.

The relative abundance ratios are computed with respect to the abundance of CS because its column density distribution is the most strongly peaked. These abundance ratios are plotted with respect to T_{kin} in figure 5.19. The abundance of HNC versus HCN is also plotted in that figure and compared with results from OMC-1 [Schilke et al. 1992]. A slight downward trend with respect to temperature is seen in the relative abundances of HCO⁺ and HCN with respect to CS but the error bars are too large to make a definitive claim. The OMC-1 results for HNC abundance relative to HCN also show a downward trend with increasing temperature. The ratios obtained for the three pointings of M82 are consistent with the OMC-1 results though the M82 results only cover a very small range in temperature compared to the Orion data. Because the error bars on the abundances

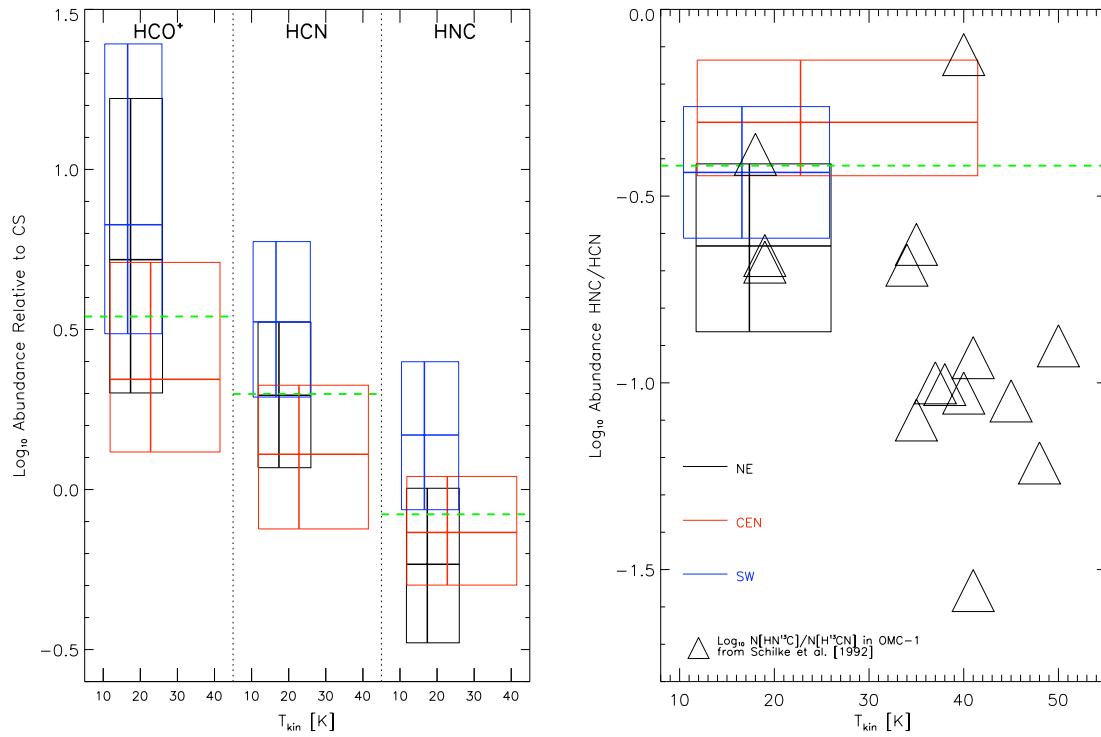


Figure 5.19. These plots show some of the relative abundance ratios obtained from the multiple species radiative transfer modeling. The panel on the left shows the abundances relative to CS versus T_{kin} for the three pointings, NE, CEN and SW, which are indicated by black, red and blue boxes, respectively. The panel on the right shows $X_{\text{HNC}}/X_{\text{HCN}}$ versus T_{kin} for the M82 pointings (boxes) and for the Orion molecular cloud from Schilke et al. [1992] (triangles). The edges of the boxes indicate the 1σ or 68% confidence range for the plotted parameters and the cross hairs show the median values. The dashed green lines show the weighted average of the three pointings where the weights are given by $1/\sigma^2$. These average values are used to estimate the abundances relative to H_2 given in table 5.12.

are fairly large, a weighted average is calculated to estimate the abundance ratio within the entire galaxy. Using the abundance of CS relative to H_2 derived in Mauersberger and Henkel [1989], the standard abundances of the three other species in the multiple species model can be calculated and are given in table 5.12. These are the abundances used for calculating the radiative transfer parameter limits for both the single species and multiple species models and to convert from N_{mol} to N_{H_2} , when required.

The total mass of molecular gas can be calculated from the beam-averaged column density using

$$M_{\text{tot}} = \frac{\langle N_{\text{mol}} \rangle}{X_{\text{mol}}} \times m_{H_2} \times A \times 1.6, \quad (5.6)$$

where m_{H_2} is the mass of a hydrogen molecule, A is an area and the factor of 1.6 accounts for the additional mass of He and dust in the molecular clouds. The choice of A is somewhat arbitrary; a reasonable choice would be the area of the beam at a distance of 3.9 Mpc. However, typical mass estimates from the literature are given for the entire galaxy so I chose an area of $15'' \times 50''$. A plot of M_{tot} versus n_{H_2} is shown in figure 5.20.

The total mass plot indicates that the high-density tracer molecules of HCO^+ , HCN, HNC and CS are emitted from regions with 100 times higher density than CO-emitting regions but that the mass distribution over this range in density is fairly constant. The multiple species models, based on the distribution for $\langle N_{H_2} \rangle$, are obviously much better constrained than the single species models and they indicate a half an order of magnitude drop in total mass from densities of 10^3 to $10^{5.5} \text{ cm}^{-3}$. A study of the mass versus density distribution for two starburst galaxies and two normal galaxies found that the starburst galaxies' distributions are fairly flat while the distributions for the normal galaxies show a stronger downward trend [Paglione, Jackson, and Ishizuki 1997]. This is consistent with our results for M82.

5.6 Summary Discussion

The three-pointing study of the nucleus of the starburst galaxy M82 reveals that this region contains large quantities of high density molecular gas capable of exciting transitions in several molecules. Fits to the continuum baseline are consistent with the 48 K average dust temperature for the entire galaxy and the galaxy's spatial distribution at our beam size. However, the molecular gas traced by the emission from HCO^+ , HCN, HNC and CS is a somewhat cooler 20 K. This low temperature combined with the high density suggests a connection to the cores of cold dark clouds. Cold dark clouds are dusty patches of the Milky Way that appear blank at optical wavelengths, completely blocking the light from background stars [Bergin and Tafalla 2007]. The cores of these objects are strongly associated with star formation and are likely to be sites of low-mass star formation. These

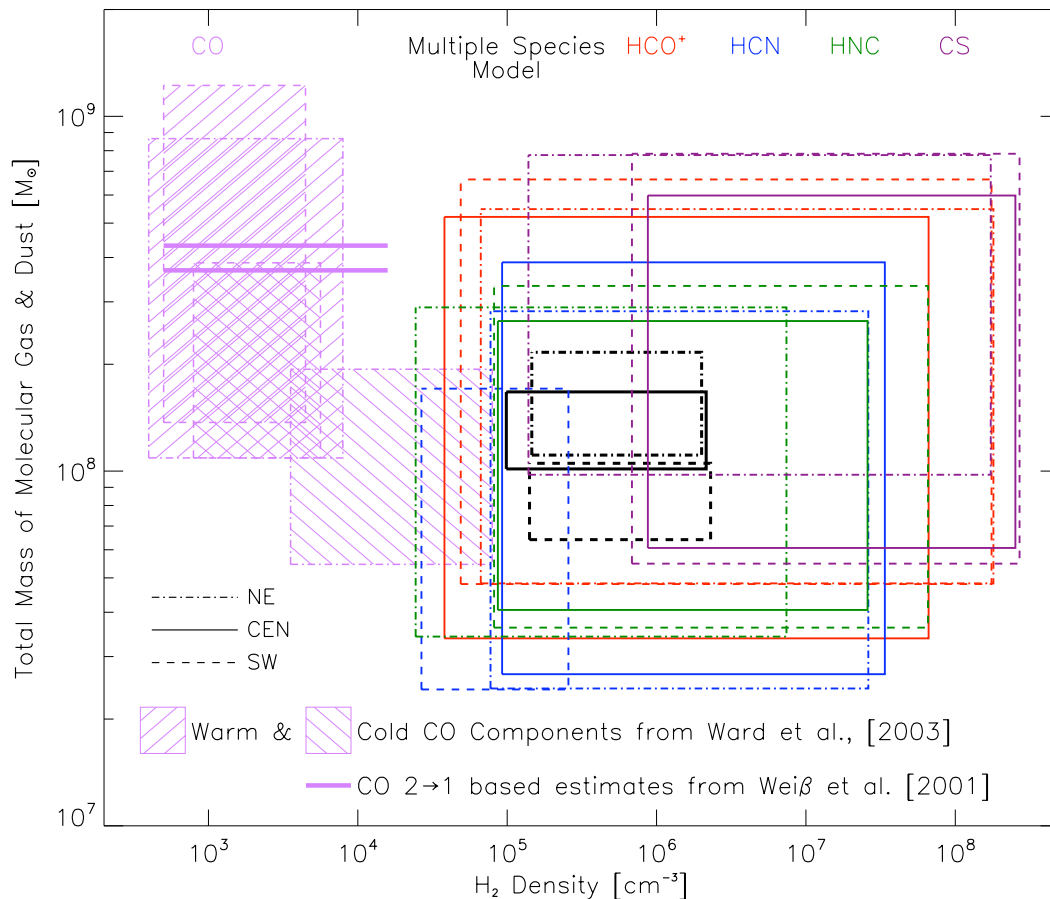


Figure 5.20. This plot shows the total molecular gas mass traced by some of the species seen in M82. Different species are indicated using different colored boxes, one for each pointing with the multiple species model shown in black. The pointings are distinguished by line style: dash-dot, solid and dash for NE, CEN and SW, respectively. The boxes show the 1σ or 68% confidence range for the plotted parameters using the θ^{-1} beam scaling factor results. In addition to the species analyzed in this work, some estimates based on CO observations are also included. The thick horizontal lines come from two radiative transfer models to describe a CO 2–1 map of M82 [Weiß et al. 2001]. The higher mass estimate is based on a local thermodynamic equilibrium model while the lower is based on a large velocity gradient calculation. The horizontal extent of these lines comes from the density ranges found with the radiative transfer modeling. The boxes with diagonal hashing come from the warm and cold components of the CO radiative transfer model of Ward et al. [2003] assuming a $X_{CO} = 2 \times 10^{-5}$, as indicated by the modeling of Weiß et al. [2001].

cores are small (~ 0.1 pc), cold (10-20 K) [Ladd et al. 1994] and have a flat central density profile of a few times 10^5 cm^{-3} [Bacmann et al. 2000].

More recent observations have revealed a population of infrared dark clouds which appears to be associated with high-mass and clustered star formation. A study of the cores of infrared dark clouds [Pillai et al. 2006] indicates that the temperature is similar to that in cold dark cloud cores but that they contain 20-100 times more mass. The high star formation rate present in M82 requires a large amount of pre-stellar material ready to be converted into stars. The radiative transfer modeling of the emission of the high-density tracer molecules HCO^+ , HCN , HNC and CS presented here indicates a significant quantity of molecular gas with physical conditions similar to those found in star-forming regions in our galaxy. In spite of the extreme starburst currently underway in M82, there appears to be some commonality between the star-producing material in it and that in the Milky Way, with quantity being perhaps the most significant difference.

Chapter 6

Future of Waveguide Spectrometers

In addition to being a powerful and unique millimeter-wave spectrometer, Z-Spec is the proving ground for a new architecture for low-background submillimeter and far-infrared spectroscopy. Z-Spec is primarily limited by its resolution which was constrained by the desire to make the instrument reasonably sized. However, as the wavelength of operation is reduced, the resolution scales up for a module of the same physical size. In addition, as the operating frequency increases, the noise penalty paid by heterodyne spectrometers becomes larger and larger compared to the intrinsic photon noise, particularly in the case of an actively cooled telescope in space. Some of the solutions to technical problems worked out during the design of Z-Spec would not be suitable to a higher-resolution, shorter-wavelength version, but Z-Spec has proven the viability of this new spectrometer architecture.

Moreover, the large instantaneous coverage afforded by this spectrometer architecture opens a new door for spectral surveys. The first blind molecular line survey of a galaxy outside our own took at least 50 hours of integration time obtained over the course of three years [Martín et al. 2006]. Of the 25 species identified in that survey, nearly a third were previously undetected outside the Milky Way. Unbiased extra-galactic line surveys will turn up unexpected results because the targets for such surveys are very different than our own galaxy. Instantaneous broadband coverage enables a new kind of study of the interstellar medium of external galaxies and strongly complements currently available spectrometers. The future is bright for large-bandwidth, high-sensitivity spectroscopy at long wavelengths, and waveguide grating spectrometers like Z-Spec can help develop this evolving discipline.

Appendix A

Propagation of Guided Waves

A.1 Electromagnetic Plane Waves

A.1.1 Maxwell's Equations

All phenomena of electromagnetism can be described by Maxwell's four equations. The differential form of Maxwell's equations can be written in terms of the electric, \vec{E} , and magnetic, \vec{B} , vector fields, the electric current density, \vec{J} , vector field and the electric charge density, ρ . In MKS units, the four equations are

$$\nabla \cdot \vec{E} = \frac{1}{\epsilon_0} \rho, \quad (\text{A.1})$$

$$\nabla \times \vec{E} = -\frac{\partial \vec{B}}{\partial t}, \quad (\text{A.2})$$

$$\nabla \cdot \vec{B} = 0, \quad (\text{A.3})$$

$$\nabla \times \vec{B} = \mu_0 \vec{J} + \mu_0 \epsilon_0 \frac{\partial \vec{E}}{\partial t}, \quad (\text{A.4})$$

where the permittivity of free space $\epsilon_0 = 8.85 \times 10^{-12} \text{ coul}^2/\text{Nm}^2$ and the permeability of free space $\mu_0 = 4\pi \times 10^{-7} \text{ N/A}^2$. The first equation describes how electric charge creates electric fields while the second shows how electric fields will wrap around time-varying magnetic fields. The magnetic field equations demonstrate that there is no direct source of magnetic fields but that they will form around electric currents and changing electric fields.

A.1.2 Solving the Wave Equation

Electric and magnetic fields are connected to each other such that even in a region of empty space with no electric charge or currents, the fields can be present in the form of electromagnetic waves. The curl ($\nabla \times$) of equations (A.2) and (A.4) produces wave equations for the electric and magnetic fields in a source-free region ($\rho = 0; \vec{J} = 0$). These equations can be solved separately for the time

and space dependence. The electric field can be written as $\vec{E}(x, y, z, t) = \bar{E}(x, y, z)e^{-j\omega t}$ which gives

$$\begin{aligned}\nabla^2 \bar{E} + k_0^2 \bar{E} &= 0, \\ \text{where } k_0 &\equiv \omega\sqrt{\mu_0\epsilon_0}.\end{aligned}\tag{A.5}$$

The same transformation can be applied to the magnetic field wave equation and both can be solved for the space dependence by separation of variables. This gives traveling-wave solutions

$$\vec{E} = \vec{E}_0 e^{j(\vec{k}\cdot\vec{r}-\omega t)} \quad \text{and} \quad \vec{B} = \vec{B}_0 e^{j(\vec{k}\cdot\vec{r}-\omega t)},\tag{A.6}$$

where $\vec{k} = k_x\hat{x} + k_y\hat{y} + k_z\hat{z}$ and $\vec{r} = x\hat{x} + y\hat{y} + z\hat{z}$.

A.1.3 Wave Definitions and Constraints

In order for the solutions in (A.6) to fully satisfy Maxwell's equations, there are additional constraints on the amplitudes of the electric and magnetic waves. In vacuum, equation (A.1) gives

$$\vec{k} \cdot \vec{E}_0 = 0.\tag{A.7}$$

This relationship demonstrates that the electric field vector points in the plane perpendicular to the propagation direction. Equation (A.3) produces a similar requirement of \vec{B}_0 . Furthermore, from (A.2),

$$\vec{B}_0 = \frac{\vec{k} \times \vec{E}}{\omega} = \sqrt{\mu_0\epsilon_0} \hat{k} \times \vec{E}_0 = \frac{1}{\eta_0} \hat{k} \times \vec{E}_0, \quad \text{where } \hat{k} \equiv \frac{\vec{k}}{|\vec{k}|}\tag{A.8}$$

and $\eta_0 = 377\Omega$ is the free space impedance. The magnetic field of a plane wave is perpendicular to both the direction of propagation and the electric field, and the amplitude is proportional to the electric field amplitude. The vectors $(\vec{E}_0, \vec{B}_0, \vec{k})$ form a right-handed cartesian coordinate system.

A.2 Wave Propagation in Media

A.2.1 Auxiliary Fields

While equations (A.1)-(A.4) are valid in all cases, it is convenient to introduce additional fields when working in media other than empty space. Materials have both free and bound charges that contribute to the electric and magnetic fields in and around them. Maxwell's equations can be recast in terms of the free charges ρ_f and currents \vec{J}_f by introducing the permittivity ϵ and permeability μ of the media in question. These are proportionality constants between the electric and magnetic fields and their respective auxiliary fields that are defined by the constitutive relations $\vec{D} = \epsilon\vec{E}$ and

$\vec{B} = \mu\vec{H}$. Maxwell's equations in media are

$$\nabla \cdot \vec{D} = \rho_f, \quad (\text{A.9})$$

$$\nabla \times \vec{E} = -\frac{\partial \vec{B}}{\partial t}, \quad (\text{A.10})$$

$$\nabla \cdot \vec{B} = 0, \quad (\text{A.11})$$

$$\nabla \times \vec{H} = \vec{J}_f + \frac{\partial \vec{D}}{\partial t}. \quad (\text{A.12})$$

The solution for plane wave propagation in a linear medium can simply be obtained by comparison of the above equations to the free-space Maxwell's equations in the source-free case. The two sets of equations are identical except for the permittivity and permeability. Therefore, the solutions will be the same except for the substitutions $\mu_0 \rightarrow \mu$ and $\epsilon_0 \rightarrow \epsilon$.

A.2.2 Conducting Media

A medium with conductivity σ will allow electromagnetic waves to penetrate its surface but the electric field will cause a current to flow which will decrease the strength of the excitation as it propagates into the material. That current is proportional to the electric field $\vec{J} = \sigma\vec{E}$ and modifies equation (A.12) to be

$$\nabla \times \vec{B} = \mu\sigma\vec{E} + \mu\epsilon\frac{\partial \vec{E}}{\partial t}.$$

This extra term leads to modified wave equations and solutions that look exactly like (A.6) except that $k \equiv |\vec{k}|$ is a complex number given by

$$k^2 = \mu\epsilon\omega^2 + j\mu\sigma\omega.$$

The real and imaginary parts of k can be obtained by taking the proper square root of the above equation

$$k = k_+ + jk_-, \quad \text{where} \quad k_{\pm} = \omega\sqrt{\frac{\mu\epsilon}{2}} \left[\sqrt{1 + \left(\frac{\sigma}{\epsilon\omega}\right)^2} \pm 1 \right]^{1/2}. \quad (\text{A.13})$$

The solutions to the modified wave equations are

$$\vec{E} = \vec{E}_0 e^{-k_- \hat{k} \cdot \vec{r}} e^{j(k_+ \hat{k} \cdot \vec{r} - \omega t)}, \quad \text{and} \quad \vec{B} = \vec{B}_0 e^{-k_- \hat{k} \cdot \vec{r}} e^{j(k_+ \hat{k} \cdot \vec{r} - \omega t)}. \quad (\text{A.14})$$

Clearly, the fields will attenuate as they propagate through the conductor depending on the size of the imaginary part of k . A convenient characterization of the scale of attenuation is called the skin depth δ_s , which is the distance of propagation required to decrease the amplitude by a factor of $1/e$.

From (A.14),

$$\delta_s = \frac{1}{k_-}. \quad (\text{A.15})$$

The real part of k determines the wavelength and phase velocity as in the nonconducting case.

A convenient approximation is the limit of large, but not infinite, conductivity. A good conductor with $\sigma \gg \omega\epsilon$ will attenuate waves very quickly as k_+ and k_- are approximately equal ($k_+ \simeq k_- \simeq \sqrt{\frac{\omega\sigma\mu}{2}}$). The wave decays rapidly compared to its wavelength in the conductor, λ_c , as the skin depth is

$$\delta_s \simeq \sqrt{\frac{2}{\omega\sigma\mu}} \simeq \frac{\lambda_c}{2\pi}. \quad (\text{A.16})$$

A.3 Guided Waves

A.3.1 Waveguide Basics

Electromagnetic energy can be transmitted in uniform space in the form of plane waves, but can also be delivered using tubular structures called waveguides. Waveguides are structures made from conductors that have uniform cross sections that extend many wavelengths. In general they can be made with a single conductor such as a hollow pipe or with two or more conductors as in a coaxial cable. The fields in plane waves are transverse; that is, they are perpendicular to the direction of propagation. However, in waveguide, the fields cannot in general be fully transverse. Single conductor waveguides can support both transverse electric (TE) and transverse magnetic (TM) waves which have zero transverse electric and magnetic fields, respectively. TE waves are also called H-waves while TM waves are referred to as E-waves, reflecting the nonzero transverse component of the wave. Waveguides with multiple conductors can also support TEM (transverse electric and magnetic) waves which are fully transverse to the direction of propagation.

Imagine an arbitrary waveguide extending infinitely in the \hat{z} direction filled with a linear, nonconducting medium with permittivity ϵ and permeability μ . Assuming the standard time dependence ($e^{-j\omega t}$) and propagation along the waveguide in the \hat{z} direction ($e^{j\beta z}$), the transverse fields can be written in terms of E_z and B_z ,

$$E_x = \frac{j}{k_c^2} \left(\beta \frac{\partial E_z}{\partial x} + \omega \frac{\partial B_z}{\partial y} \right), \quad (\text{A.17})$$

$$E_y = \frac{j}{k_c^2} \left(\beta \frac{\partial E_z}{\partial y} - \omega \frac{\partial B_z}{\partial x} \right), \quad (\text{A.18})$$

$$B_x = \frac{j}{k_c^2} \left(\beta \frac{\partial B_z}{\partial x} - \omega\mu\epsilon \frac{\partial E_z}{\partial y} \right), \quad (\text{A.19})$$

$$B_y = \frac{j}{k_c^2} \left(\beta \frac{\partial B_z}{\partial y} + \omega\mu\epsilon \frac{\partial E_z}{\partial x} \right), \quad (\text{A.20})$$

where $k_c^2 = k^2 - \beta^2$ and $k^2 = \omega^2\mu\epsilon$. The transverse (x and y) dependence of the longitudinal fields

are subject to reduced wave equations

$$\left(\frac{\partial^2}{\partial x^2} + \frac{\partial^2}{\partial y^2} + k_c^2\right) E_z = 0, \quad (\text{A.21})$$

$$\left(\frac{\partial^2}{\partial x^2} + \frac{\partial^2}{\partial y^2} + k_c^2\right) B_z = 0, \quad (\text{A.22})$$

which are consistent with the general wave equations from section A.1.2 and the \hat{z} propagation assumption. The fields for TE and TM waves can be obtained using the above equations and the proper boundary conditions for the particular waveguide, which will generally give restrictions of the value of k_c . For TEM waves, the above formulae for the transverse components give all zeros, except if $k_c = 0$ which makes the equations indeterminate. Therefore, for TEM waves, $\beta = k$ and the transverse components can be shown to be subject to two-dimensional Laplace equations. They therefore can be described by the gradient of a scalar potential and can be solved by the techniques of electro- and magnetostatics.

A.3.2 Parallel-Plate Waveguide

A parallel-plate waveguide consists of two large conducting plates separated by a constant distance d . In principle, the plates should be perfectly flat and infinite in extent, but are typically rough (at scales much smaller than a wavelength) and finite, though large compared to λ and d . This type of waveguide can support all three classes of waves. Assume the plates are perfectly conducting and parallel to the x - z plane, the boundaries lie at $y = 0$ and $y = d$ and the gap between the plates is filled with a nonconducting material with permittivity ϵ and permeability μ . A perfect conductor is a lossless material with infinite conductivity; charges flow instantly to counteract any electric field that penetrates its surface. The continuity requirements at material boundaries show that at $y = 0$ and $y = d$, $E_x = E_z = 0$ and $B_y = 0$ for the perfectly conducting parallel-plate waveguide. Since the choice of \hat{z} propagation is somewhat arbitrary when considering parallel plate waveguide (\hat{x} would have been just as good), the solutions obtained below will be somewhat less than general. For clarity, the analysis will proceed with the \hat{z} assumption and will be extended to propagation in any direction in the x - z plane. The \hat{z} propagation and the symmetry along the x -axis mean that there will not be any variation with respect to x in the various components and thus all terms with $\frac{\partial}{\partial x}$ can be dropped.

A.3.2.1 TE Modes

These modes are characterized by $E_z = 0$. The general solution to the reduced wave equation of B_z is a sum of sine and cosine of $k_c y$ with arbitrary amplitude. The boundary condition $E_x = 0$ at $y = 0, d$ shows that E_x can only have $\sin(k_c y)$ dependence and furthermore $k_c = \frac{m\pi}{d}$ where

$m = 1, 2, 3$, etc. The complete solution for the TE modes can be obtained from equations (A.17) - (A.22),

$$\vec{E}(x, y, z, t; m) = B_m e^{j(\beta_m z - \omega t)} \left[\frac{-j\omega d}{m\pi} \sin\left(\frac{m\pi y}{d}\right) \right] \hat{x}, \quad (\text{A.23})$$

$$\vec{B}(x, y, z, t; m) = B_m e^{j(\beta_m z - \omega t)} \left[\frac{-j\beta_m d}{m\pi} \sin\left(\frac{m\pi y}{d}\right) \hat{y} + \cos\left(\frac{m\pi y}{d}\right) \hat{z} \right], \quad (\text{A.24})$$

where $\beta_m = \sqrt{k^2 - \left(\frac{m\pi}{d}\right)^2}$. If the frequency of the wave is low enough, such that $k < \frac{m\pi}{d}$, β_m will be imaginary and the wave in that mode will be evanescent. The cutoff frequency for the m^{th} mode is defined by

$$f_c = \frac{m}{2d\sqrt{\mu\epsilon}}, \quad (\text{A.25})$$

such that only frequencies greater than the cutoff frequency will propagate in the waveguide in that mode.

The above solutions assume the wave is propagating in the $+\hat{z}$ direction but parallel-plate waveguide can support waves traveling in any direction in the x - z plane. If the wave propagates at an angle θ away from the z -axis, the fields are

$$\vec{E}(x, y, z, t; m) = B_m e^{j(\vec{\beta}_m \cdot \vec{\rho} - \omega t)} \left[\frac{-j\omega d}{m\pi} \sin\left(\frac{m\pi y}{d}\right) \right] (\hat{y} \times \hat{\beta}_m), \quad (\text{A.26})$$

$$\vec{B}(x, y, z, t; m) = B_m e^{j(\vec{\beta}_m \cdot \vec{\rho} - \omega t)} \left[\frac{-j\beta_m d}{m\pi} \sin\left(\frac{m\pi y}{d}\right) \hat{y} + \cos\left(\frac{m\pi y}{d}\right) \hat{\beta}_m \right], \quad (\text{A.27})$$

where $\vec{\beta}_m = \beta_m [\sin(\theta)\hat{x} + \cos(\theta)\hat{z}]$, $\vec{\rho} = x\hat{x} + z\hat{z}$ and $\hat{\beta}_m = \vec{\beta}_m/\beta_m$.

A.3.2.2 TM and TEM Modes

The field profiles for the TM modes can be derived in much the same way as in the previous section. The reduced wave equation for the E_z component is solved in general by a sum of sine and cosine of $k_c y$. The boundary requirement that $E_z = 0$ at $y = 0, d$ implies that only the sine term is acceptable and that $k_c = \frac{m\pi}{d}$ where $m = 1, 2, 3$, etc. The general solutions are

$$\vec{E}(x, y, z, t; m) = E_m e^{j(\vec{\beta}_m \cdot \vec{\rho} - \omega t)} \left[\frac{j\beta_m d}{m\pi} \cos\left(\frac{m\pi y}{d}\right) \hat{y} + \sin\left(\frac{m\pi y}{d}\right) \hat{\beta}_m \right], \quad (\text{A.28})$$

$$\vec{B}(x, y, z, t; m) = E_m e^{j(\vec{\beta}_m \cdot \vec{\rho} - \omega t)} \left[\frac{-j\omega\mu\epsilon d}{m\pi} \sin\left(\frac{m\pi y}{d}\right) \right] (\hat{y} \times \hat{\beta}_m), \quad (\text{A.29})$$

using the same definitions as above for $\vec{\beta}_m$ and $\vec{\rho}$. Clearly, the TM modes will be cut off like the TE modes at frequencies below f_c , as given in equation (A.25), and not able to propagate in the waveguide.

The derivation of the field solutions for the TEM mode is done differently than for the TE and

Table A.1. Rectangular waveguide fields

| | TE _{<i>mn</i>} Mode | TM _{<i>mn</i>} Mode |
|--|--|---|
| E_x | $-\frac{j\omega m\pi}{k_c^2 a} B_{mn} \cos\left(\frac{n\pi x}{b}\right) \sin\left(\frac{m\pi y}{a}\right)$ | $\frac{j\beta n\pi}{k_c^2 b} E_{mn} \cos\left(\frac{n\pi x}{b}\right) \sin\left(\frac{m\pi y}{a}\right)$ |
| E_y | $\frac{j\omega n\pi}{k_c^2 b} B_{mn} \sin\left(\frac{n\pi x}{b}\right) \cos\left(\frac{m\pi y}{a}\right)$ | $\frac{j\beta m\pi}{k_c^2 a} E_{mn} \sin\left(\frac{n\pi x}{b}\right) \cos\left(\frac{m\pi y}{a}\right)$ |
| E_z | 0 | $E_{mn} \sin\left(\frac{n\pi x}{b}\right) \sin\left(\frac{m\pi y}{a}\right)$ |
| B_x | $-\frac{j\beta n\pi}{k_c^2 b} B_{mn} \sin\left(\frac{n\pi x}{b}\right) \cos\left(\frac{m\pi y}{a}\right)$ | $-\frac{j\omega\mu\epsilon m\pi}{k_c^2 a} E_{mn} \sin\left(\frac{n\pi x}{b}\right) \cos\left(\frac{m\pi y}{a}\right)$ |
| B_y | $-\frac{j\beta m\pi}{k_c^2 a} B_{mn} \cos\left(\frac{n\pi x}{b}\right) \sin\left(\frac{m\pi y}{a}\right)$ | $\frac{j\omega\mu\epsilon n\pi}{k_c^2 b} E_{mn} \cos\left(\frac{n\pi x}{b}\right) \sin\left(\frac{m\pi y}{a}\right)$ |
| B_z | $B_{mn} \cos\left(\frac{n\pi x}{b}\right) \cos\left(\frac{m\pi y}{a}\right)$ | 0 |
| $\beta = \sqrt{k^2 - k_c^2}; \quad k_c = \sqrt{\left(\frac{m\pi}{a}\right)^2 + \left(\frac{n\pi}{b}\right)^2}$ | | |

Note. — Electric and magnetic fields for TE and TM modes in rectangular waveguide. All components also include the \hat{z} propagation and time variation terms, $e^{j(\beta z - \omega t)}$.

TM modes, but it turns out that the result is similar to what can be obtained by setting $m = 0$ in equations (A.28) and (A.29),

$$\vec{E}(x, y, z, t) = \frac{V_0}{d} e^{j(\vec{k} \cdot \vec{\rho} - \omega t)} \hat{y}, \quad (\text{A.30})$$

$$\vec{B}(x, y, z, t) = -\frac{V_0 \sqrt{\mu\epsilon}}{d} e^{j(\vec{k} \cdot \vec{\rho} - \omega t)} (\hat{y} \times \hat{k}), \quad (\text{A.31})$$

where $\vec{k} = k[\sin(\theta)\hat{x} + \cos(\theta)\hat{z}]$ and V_0 is an arbitrary constant that relates to the power in this mode. In particular, it represents the potential difference assumed to be present between the two plates in the setup of the problem.

A.3.3 Rectangular Waveguide

A hollow pipe with rectangular cross-section can support TE and TM waves, but not TEM waves. Let the rectangle's sides have lengths a and b with the longer a side parallel to the y -axis while the shorter b side is parallel to the x -axis. If the pipe is made from a perfectly conducting material, then the boundary conditions yield $E_x = E_z = 0$ at $y = 0, a$ and $E_y = E_z = 0$ at $x = 0, b$. The wave equations for the longitudinal components are separable and thus solved in general by $[A \sin(k_x x) + B \cos(k_x x)][C \sin(k_y y) + D \cos(k_y y)]$ where $k_c^2 = k_x^2 + k_y^2$. By applying equations (A.17) - (A.20) to either B_z or E_z (for TE and TM modes, respectively) and using the boundary conditions

above, it can be shown that $k_x = \frac{n\pi}{b}$ where $n = 1, 2, 3$, etc. and $k_y = \frac{m\pi}{a}$ where $m = 1, 2, 3$, etc. The field components for TE and TM modes are given in table A.1. From these fields, it is clear that for TE modes at least n or m must be greater than zero while for TM modes both n and m must be greater than zero. Only waves traveling at frequencies above the cutoff frequency

$$f_{c_{mn}} = \frac{1}{2\sqrt{\mu\epsilon}} \sqrt{\left(\frac{m\pi}{a}\right)^2 + \left(\frac{n\pi}{b}\right)^2} \quad (\text{A.32})$$

will propagate in a particular mode. Modes can be sorted by the cutoff frequency into orders. The lowest order mode (also called the dominant or fundamental) is the TE_{10} mode because $a > b$. The size of rectangular waveguide is often chosen such that $a = 2b$. In this case, the second and third order modes (TE_{20} and TE_{01}) begin to propagate at twice the fundamental cutoff and the TE_{11} and TM_{11} modes appear at frequencies above $\sqrt{5}f_{c_{10}}$.

A.4 Waveguide Power Flow and Loss

Conservation of energy and momentum are fundamental concepts in mechanics but when charged particles interact, it is necessary to include the momentum and energy stored in the fields they create to properly conserve those quantities. Power flow in an electromagnetic system is described by the Poynting vector,

$$\vec{S} \equiv \vec{E} \times \vec{H}^*,$$

where \vec{H}^* is the complex conjugate of \vec{H} . The units of \vec{S} are watts per square meter such that the integral of it over any surface gives the power that flows through that surface. In general, the Poynting vector may be complex and the time-averaged power flowing through a surface S is given by

$$P_S = \frac{1}{2} \Re \left(\int_S \vec{S} \cdot d\vec{s} \right). \quad (\text{A.33})$$

The Poynting vector for plane waves is parallel to the direction of propagation since the electric and magnetic fields are perpendicular to each other and to \hat{k} . The Poynting vector can be used to show that the power absorbed by a good conductor is simply related to the tangential magnetic field at the surface of the material

$$P_t = \frac{R_s}{2} \int_S |\vec{H}_t|^2 ds, \quad (\text{A.34})$$

where $R_s = \frac{1}{\sigma\delta_s} = \sqrt{\frac{\omega\mu}{2\sigma}}$.

Waveguides have two primary sources of power loss: conductor losses in the walls of the guide and dielectric losses in the medium that fills the guide. The power lost can be characterized by an

exponential decay of the transmitted power along the direction of propagation

$$P(z) = P_0 e^{-2\alpha z},$$

where $\alpha = \alpha_d + \alpha_c$ and α_d and α_c are the characterization parameters for dielectric and conduction loss, respectively. The dielectric loss can be parameterized in terms of the loss tangent of the material

$$\tan \delta = \frac{\omega \Im(\epsilon) + \sigma}{\omega \Re(\epsilon)},$$

where ϵ is the complex permittivity and σ is the conductivity. If the loss tangent is small, the dielectric loss is independent of the shape of the waveguide and given by

$$\alpha_d = \frac{k^2 \tan \delta}{2\beta} \quad (\text{TE or TM waves}) \quad (\text{A.35})$$

$$= \frac{k \tan \delta}{2} \quad (\text{TEM waves}). \quad (\text{A.36})$$

In these equations k is calculated assuming the material is lossless ($\Im(\epsilon) = 0$) such that $k^2 = \omega^2 \mu \Re(\epsilon)$ and $\beta^2 = k^2 - k_c^2$.

The conduction loss can be calculated from the power carried down the guide, P_0 , and the power absorbed per unit length in the conducting walls of the guide, P_l using

$$\alpha_c = \frac{P_l}{2P_0}. \quad (\text{A.37})$$

Both of these quantities will depend on the specific field profiles and must therefore be calculated on a mode-by-mode basis. If the loss is small, or equivalently if the conductivity in the walls is high, the power flow and loss can be calculated using the field profiles assuming no loss. The power flow is obtained by integrating the Poynting vector over the cross-sectional area of the guide (or a cross section of a certain finite width for parallel-plate guide). The conduction loss per unit length in the walls can be calculated using equation (A.34). The results for the various modes of parallel-plate and rectangular waveguide are given in table A.2.

The conduction loss in a waveguide is proportional to surface resistance of the wall material. Calculation of the surface resistance at cryogenic temperatures for a thin film, such as a gold-plated surface, is complicated [Pippard 1947; Reuter and Sondheimer 1948; Bin 1997]. The complication comes from the fact that the mean free path of a conduction electron scattering off of thermal phonons increases with decreasing temperature. As the temperature is lowered, the mean free path, l , will become comparable to the skin depth, δ_s , entering the anomalous skin effect regime.

The cryogenic surface resistance can be estimated using the fact that the product of the resistivity, ρ , and the mean free path is independent of temperature. At room temperature, the gold plating

Table A.2. Power transmitted and conduction losses in waveguide

| | | P_0 | α_c |
|---|----------------------------------|---|---|
| Parallel-Plate Waveguide integrated over width w | TEM | $\frac{V_0^2 w}{2\eta d}$ | $\frac{R_s/\eta}{d}$ |
| | TE $_m$ | $\frac{wd}{4} \frac{\omega \Re(\beta)}{\mu k_c^2} B_m ^2$ | $\frac{2k_c^2 R_s}{dk\beta\eta}$ |
| | TM $_m$ | $\frac{wd}{4} \frac{k \Re(\beta)}{\eta k_c^2} E_m ^2$ | $\frac{2k R_s}{d\beta\eta}$ |
| | TE $_1$ | $\frac{wd^3}{4\pi^2} \frac{\omega \Re(\beta)}{\mu} B_1 ^2$ | $\frac{2\pi^2 R_s}{d^3 k\beta\eta}$ |
| Rectangular Waveguide | TE $_{m0}$ $m > 0$ | $\frac{\omega \Re(\beta) ab}{4k_c^2 \mu} B_{m0} ^2$ | $\frac{2k_c^2 R_s}{k\beta ab\eta} \left(\frac{ \beta ^2 a}{2k_c^2} + \frac{a}{2} + b \right)$ |
| | TE $_{0n}$ $n > 0$ | $\frac{\omega \Re(\beta) ab}{4k_c^2 \mu} B_{0n} ^2$ | $\frac{2k_c^2 R_s}{k\beta ab\eta} \left(\frac{ \beta ^2 b}{2k_c^2} + \frac{b}{2} + a \right)$ |
| | TE $_{mn}$ $m > 0$ $n > 0$ | $\frac{\omega \Re(\beta) ab}{8\mu k_c^2} B_{mn} ^2$ | $\frac{4k_c^2 R_s}{k\beta ab\eta} \left[\frac{ \beta ^2}{2k_c^4} \left(\frac{m^2 \pi^2}{a} + \frac{n^2 \pi^2}{b} \right) + \frac{a}{2} + \frac{b}{2} \right]$ |
| | TM $_{mn}$ $m > 0$ $n > 0$ | $\frac{k \Re(\beta) ab}{8\eta k_c^2} E_{mn} ^2$ | $\frac{4k R_s}{ab\beta k_c^2 \eta} \left[\left(\frac{m\pi}{a} \right)^2 b + \left(\frac{n\pi}{b} \right)^2 a \right]$ |
| | TE $_{10}$ | $\frac{\omega \Re(\beta) a^3 b}{4\pi^2 \mu} B_{10} ^2$ | $\frac{2\pi^2 R_s}{k\beta a^3 b\eta} \left(\frac{ \beta ^2 a^3}{2\pi^2} + \frac{a}{2} + b \right)$ |

Note. — Power carried by and conduction loss coefficient for the various possible modes in parallel-plate and rectangular waveguide. The parallel-plate waveguide formulas for the power transmitted consider a transverse area that extends from the bottom to the top plate and has a width w . The waveguides are assumed to be filled with a material with parameters ϵ and μ , and that the walls have a surface resistance R_s . The formulas also use the electromagnetic impedance of the wall material $\eta \equiv \sqrt{\mu/\epsilon}$. The impedance of free space ($\sqrt{\mu_0/\epsilon_0}$) is 377 Ω .

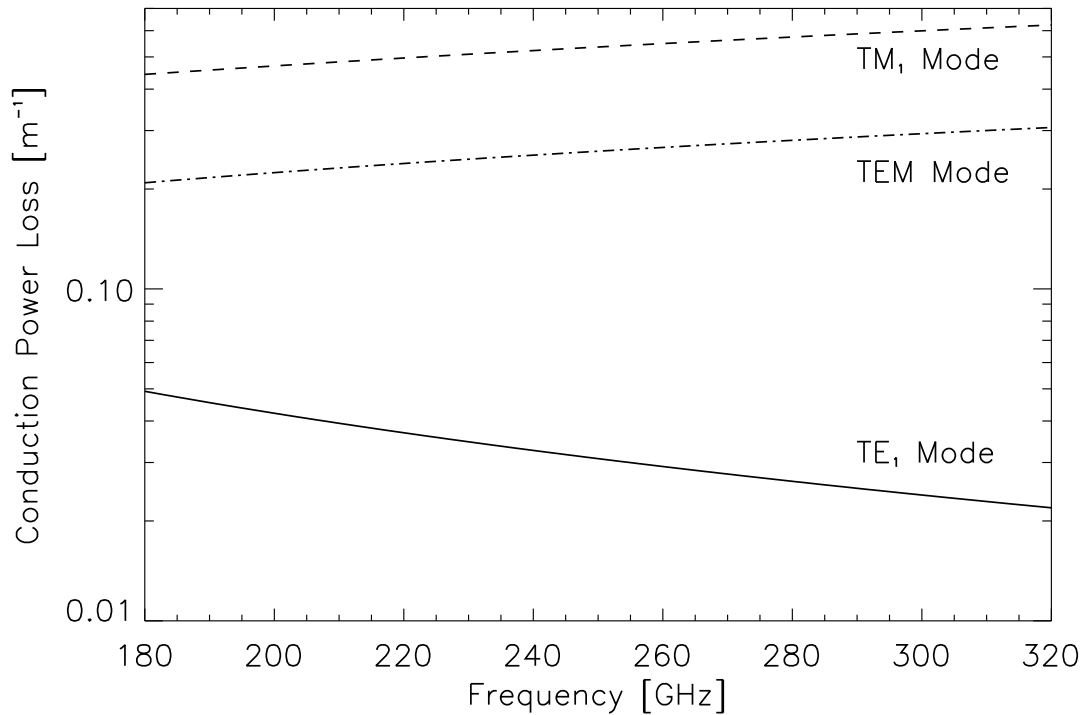


Figure A.1. This plot shows the estimated conduction power loss per meter of the TE₁, TM₁ and TEM modes in a cryogenic, gold-plated, parallel-plate waveguide with a plate separation of 2.5 mm. The calculation uses the power-loss formulae given in table A.2 and the upper-limit estimate for the cryogenic surface resistance from (A.40). The TE₁ mode is used by Z-Spec because of its small conduction losses compared to the other possible modes. A typical propagation length in the parallel-plate waveguide of Z-Spec is approximately one meter, therefore we expect the conduction losses to contribute less than 5% loss for the lowest frequency channels and about half that for the highest frequency channels. The plate separation of Z-Spec gives an overmoded parallel-plate waveguide to take advantage of the strong d^{-3} dependence of the conduction loss on the plate separation d in the TE₁ mode. The power loss of the TM and TEM modes depends much less strongly on the plate separation and clearly gives unacceptable losses over the 1 m propagation length.

on the parallel-plate waveguide walls have $\rho_{300\text{ K}} = 2.04\ \mu\Omega\ \text{cm}$ and $l_{300\text{ K}} = 40.9\ \text{nm}$. These values imply that $\Lambda \equiv \rho \times l = 834\ \mu\Omega\ \mu\text{m}^2$ for all temperatures [Ashcroft and Mermin 1976]. Setting $l = \delta_s$ and substituting in the temperature independent Λ gives

$$l = \delta_s = \sqrt{\frac{2\rho}{\mu\omega}} = \sqrt{\frac{2\Lambda}{\mu\omega l}}.$$

Solving this equation for l gives an estimate of the mean free path in the anomalous skin effect regime

$$l^* = \left[\frac{2\Lambda}{\mu\omega} \right]^{1/3}. \quad (\text{A.38})$$

This equation estimates the mean free path to be 95 nm at 250 GHz. This is more than an order of magnitude smaller than the thickness of Z-Spec's gold plating, which is 1.3 μm . The actual low-temperature mean free path is probably larger than this estimate but the surface resistance varies quite slowly with mean free path in the anomalous limit so that using this estimate in the classical formula for surface resistance should give a reasonable upper limit,

$$R_s^* = \frac{\rho}{\delta_s} = \frac{\Lambda}{(l^*)^2} = \Lambda^{1/3} \left(\frac{\omega\mu}{2} \right)^{2/3}. \quad (\text{A.39})$$

For the gold plating in Z-Spec at frequencies around 250 GHz, this equation can be written

$$R_s^* = \left[\frac{\nu}{250\text{GHz}} \right]^{2/3} 93.3\ \text{m}\Omega. \quad (\text{A.40})$$

The estimated power loss in the parallel-plate waveguide section of Z-Spec using (A.40) is shown in figure A.1. The losses of two other modes not used in Z-Spec are also shown in that figure. These plots demonstrate the low loss advantage of the TE_1 mode that comes from the overmoded configuration of Z-Spec's parallel-plate waveguide.

A.5 Waveguide Horns

A problem of particular interest for this project is how rectangular waveguide horns excite waves in parallel-plate waveguide. If the sizes of the guides are chosen such that $a = d$, then it is clear from equations (A.23) and (A.24) and table A.1 that the TE_{10} rectangular waveguide mode has the same field profiles as the TE_1 parallel-plate waveguide mode. In addition, the y dependence of these fields is constant throughout the confined region and is therefore uninteresting. By recasting the three-dimensional vector fields in terms of a two-dimensional scalar field that retains all the information about the boundary conditions present, the beam pattern of a simple horn can be modeled and the crosstalk between two horns connected by a large parallel-plate region can be estimated.

A.5.1 2D Scalar Field Representation

The inherent symmetry of parallel-plate waveguide implies that the electric and magnetic fields can be described by a set of parameters that depends only on x , z and t . In particular, the fields of the TE₁ mode can be written in terms of a scalar field ψ which is a solution to the two-dimensional wave equation

$$\left(\nabla_{xz}^2 + \mu\epsilon \frac{\partial^2}{\partial t^2} \right) \psi(x, z, t) = 0, \quad (\text{A.41})$$

where $\vec{\nabla}_{xz} = \frac{\partial}{\partial x} \hat{x} + \frac{\partial}{\partial z} \hat{z}$. The solution to this equation is a superposition of plane waves of the form $\psi(x, z, t) = \psi_0 e^{(j\vec{\beta} \cdot \vec{r} - j\omega t)}$ where $\vec{\beta} = \vec{\beta}_1$ from equation (A.27). The three-dimensional vector fields can be reconstructed from ψ using

$$\vec{E}(x, y, z, t) = \sin\left(\frac{\pi y}{d}\right) \hat{y} \times \vec{\nabla}_{xz} \psi(x, z, t), \quad (\text{A.42})$$

$$\vec{B}(x, y, z, t) = \frac{j}{\omega} \left[\beta^2 \sin\left(\frac{\pi y}{d}\right) \hat{y} \psi(x, z, t) - \frac{\pi}{d} \cos\left(\frac{\pi y}{d}\right) \vec{\nabla}_{xz} \psi(x, z, t) \right], \quad (\text{A.43})$$

which imply that $\psi_0 = -\frac{\omega d}{\pi \beta} B_1$. Using these relations and integrating over the uninteresting y dependence, a two-dimensional Poynting vector \vec{S} can be worked out in terms of ψ ,

$$\vec{S}(x, z, t) = -\frac{j\beta^2 d}{2\mu\omega} \psi^*(x, z, t) \vec{\nabla}_{xz} \psi(x, z, t). \quad (\text{A.44})$$

This vector can be integrated over a curve in the x - z plane as in equation (A.33) to give the time-averaged power flowing across the curve. For example, the power carried by a plane wave traveling in the \hat{z} direction across a width w extending in the \hat{x} direction is

$$P = \frac{\beta^2 dw}{4\mu\omega} \Re(\beta) |\phi_0|^2 = \frac{dw}{4} \frac{\omega \Re(\beta)}{\mu \left(\frac{\pi}{d}\right)^2} |B_1|^2, \quad (\text{A.45})$$

which is identical to the result given in table A.2.

A.5.2 Waveguide Horn Beam Pattern

The complicated three-dimensional problem of a rectangular waveguide feedhorn of height a and width w connected to a large volume of parallel plate waveguide can be reduced to a much simpler two-dimensional one as long as the plate separation $d = a$. If the rectangular waveguide is excited in the TE₁₀ mode and it is placed such that the propagation axis points in the \hat{z} direction, the wave amplitude at the mouth of the horn is given by

$$\psi(x, z = 0, t) = e^{-j\omega t} \left\{ \begin{array}{l} \phi_0, \quad |x| \leq \frac{w}{2} \\ 0, \quad \text{otherwise} \end{array} \right\}.$$

The solution for $z > 0$ must be a linear combination of plane waves. This combination can be determined by Fourier transforming the problem into k -space. The Fourier transform of the $z = 0$ boundary condition determines the k_x -space spectrum and the relation $\beta^2 = k_x^2 + k_z^2$ connects the k_x and k_z spectra. Leaving off the uninteresting $e^{-j\omega t}$ dependence, $\psi(x, z)$ can be written in terms of $\hat{\psi}(k_x)$, the Fourier transform of the top-hat boundary condition:

$$\begin{aligned}\psi(x, z) &= \int \hat{\psi}(k_x) e^{jk_x x} e^{jk_z z} dk_x \\ &= \frac{\psi_0 \beta w}{2\pi} \int_{-\pi/2}^{\pi/2} \text{sinc} \left[\frac{\beta w \sin \theta'}{2} \right] e^{j\vec{\beta} \cdot \vec{\rho}} \cos \theta' d\theta',\end{aligned}$$

where $\text{sinc}(x) \equiv \sin(x)/x$ and the integration variable has been changed using the relation $k_x = \beta \sin \theta'$. Converting to polar coordinates (ρ, θ) gives $\vec{\beta} \cdot \vec{\rho} = \beta \rho \cos(\theta' - \theta)$. In the far-field limit where $\beta \rho \gg 1$, the exponential in the integral will oscillate rapidly when $\theta' \neq \theta$ and will not contribute to the total integral. Changing variables to $\theta'' = \theta' - \theta$ and Taylor expanding the exponent around $\theta'' = 0$ gives

$$\psi(\rho, \theta) = \frac{\psi_0 \beta w}{2\pi} \cos \theta \text{sinc} \left[\frac{\beta w \sin \theta}{2} \right] e^{j\beta \rho} \int_{-\pi/2-\theta}^{\pi/2-\theta} e^{-j\beta \rho \theta''^2/2} d\theta''. \quad (\text{A.46})$$

The remaining integral can be evaluated by extending the limits to $\pm\infty$. This is reasonable because the integrand is a peaked Gaussian function, so only the small neighborhood around $\theta'' = 0$ will contribute to the result. The only problem with this extension is when $|\theta| = \pi/2$, but the $\cos \theta$ term ensures $\psi = 0$ for those values of theta. The far field pattern is thus given by

$$\psi(\rho, \theta) = \frac{\psi_0 \beta w}{2\pi} \cos \theta \text{sinc} \left[\frac{\beta w \sin \theta}{2} \right] e^{j\beta \rho} \sqrt{\frac{\pi}{\beta \rho}} (1 - j). \quad (\text{A.47})$$

This beam pattern can be turned into the power pattern via the two-dimensional Poynting vector, \mathbf{S} . If this is integrated over a half circle with radius ρ , the total power radiated by the horn can be calculated. The integral over θ of the $\hat{\rho}$ projection of \mathbf{S} is impossible to solve analytically, but the trivial relationship $P_{rad} = \int d\theta \frac{dP}{d\theta}$ shows that

$$\begin{aligned}\frac{dP}{d\theta} &= \frac{1}{2} \Re [\mathbf{S}_\rho(\rho, \theta)] \\ &= \Re \left[-\frac{j\beta^2 d}{4\mu\omega} \psi^*(\rho, \theta) \frac{\partial \psi(\rho, \theta)}{\partial \rho} \right] \\ &= \frac{\beta^4 d w^2 |\psi_0|^2}{8\pi\mu\omega} \left\{ \cos \theta \text{sinc} \left[\frac{\beta w \sin \theta}{2} \right] \right\}^2,\end{aligned} \quad (\text{A.48})$$

where β is assumed to be real.

A.5.3 Scattering Matrix Theory

Transmission line circuits can be accurately analyzed using scattering matrix theory, a method that can be applied more generally to problems of electromagnetic power transmission. Consider, for example, a transmission line feedhorn connected to a two-dimensional medium. At the mouth of the horn it is common to talk about the wave amplitude traveling from the line into the horn, a_l , and the amplitude traveling down the line away from the horn, b_l . One can also describe the wave amplitudes entering and exiting the horn from the two-dimensional medium. These amplitudes will be functions of their direction of propagation in the medium which can be parameterized by the angle between the propagation direction and the normal to the aperture of the horn, θ . Using the typical convention, the outgoing waves can be described by $b_r(\theta)$ and the incoming by $a_r(\theta)$. The outgoing wave amplitudes can be written down in terms of the incoming waves by using a type of scattering matrix:

$$\begin{aligned} b_l &= S_{ll}a_l + \int d\theta S_{lr}(\theta)a_r(\theta), \\ b_r(\theta) &= S_{rl}(\theta)a_l + \int d\theta' S_{rr}(\theta, \theta')a_r(\theta'). \end{aligned} \quad (\text{A.49})$$

Reciprocity says that the transmission beam pattern $S_{rl}(\theta)$ and the receiving beam pattern $S_{lr}(\theta)$ are equal. Furthermore, if the wave amplitudes are normalized such that the power carried in a particular direction is given by the square of the wave amplitude then the normalization of the beam pattern is determined by

$$\int d\theta |S_{lr}(\theta)|^2 = 1 - |S_{ll}|^2. \quad (\text{A.50})$$

In addition, a real field quantity at some point \vec{r} away from the horn can be written as

$$\Psi(\vec{r}) = C_\Psi \int d\theta b_r(\theta) e^{jk\hat{n}(\theta)\cdot\vec{r}}, \quad \text{or} \quad \Psi(\vec{r}) = C_\Psi \int d\theta a_r(\theta) e^{-jk\hat{n}(\theta)\cdot\vec{r}}, \quad (\text{A.51})$$

where $\Psi(\vec{r})$ is the field variable of interest, C_Ψ is a normalization constant which depends on the chosen variable, k is the wave number and \hat{n} is the direction of propagation. These integrals assume a $e^{-j\omega t}$ time dependence.

For example, this method can be used to characterize the results from the previous section. The wave amplitudes are defined such that $P_{rad} = \int d\theta |b_r(\theta)|^2$ and $P_{in} = |a_l|^2$. These imply that $|b_r(\theta)|^2 = \frac{dP}{d\theta}$ and, for the waveguide feedhorn problem, $|a_l|^2 = \frac{\beta^3 dw}{4\mu\omega} |\phi_0|^2$, from equation (A.45), assuming β is real. Assuming that the horn has small S_{rr} , then it is clear from (A.49) that $|b_r(\theta)|^2 = |S_{rl}(\theta)a_l|^2$. This result combined with the power pattern for the rectangular waveguide

horn given in equation (A.48) gives

$$S_{rl}(\theta) = \sqrt{\frac{\beta w}{2\pi}} \cos \theta \operatorname{sinc} \left[\frac{\beta w \sin \theta}{2} \right], \quad (\text{A.52})$$

which is the scattering matrix representation of the beam pattern of a horn excited with the TE₁₀ mode radiating into a parallel plate region, correct up to a phase factor.

A.5.4 2D Friis Transmission Formula

The Friis transmission formula is a standard way to calculate the power transmitted from one antenna to another. It is explicitly derived for a three-dimensional propagation medium. To work out an equivalent mechanism in a two-dimensional medium, imagine two feedhorns communicating through such a medium separated by a distance d . Let horns one and two be the transmitting and receiving horns respectively. The transmission lines connected to the feedhorns have incoming and outgoing wave amplitudes $a_i^{(1)}$, $b_i^{(1)}$, $a_i^{(2)}$ and $b_i^{(2)}$. We wish to calculate S_{21} , which connects an incoming wave on the line feeding horn one to an outgoing wave on the line leaving horn two, such that $b_i^{(2)} = S_{21}a_i^{(1)}$. There are also the wave amplitudes within the two-dimensional transmission medium, $a_r^{(1)}(\theta)$, $b_r^{(1)}(\theta)$, $a_r^{(2)}(\theta')$ and $b_r^{(2)}(\theta')$, which are connected via each horn's scattering matrix to the line wave amplitudes. Assuming $a_i^{(2)} = 0$ and $S_{rr}^{(1)}$ is small, then the definition of the scattering matrix (A.49) gives

$$b_r^{(1)}(\theta_1) = S_{rl}^{(1)}(\theta_1)a_i^{(1)}, \quad (\text{A.53})$$

$$b_i^{(2)} = \int d\theta_2 S_{rl}^{(2)}(\theta_2)a_r^{(2)}(\theta_2), \quad (\text{A.54})$$

where θ_1 and θ_2 are defined in the coordinate systems of horn one and horn two, respectively. Connecting $b_r^{(1)}$ and $a_r^{(2)}$ will enable calculating S_{21} .

The two-dimensional medium contains electric and magnetic fields created by the incoming and outgoing waves of the two horns. At some point \mathbf{P} in the medium, the electric or magnetic field is a specific quantity which can be described in terms of either horn's incoming and outgoing wave amplitudes. If \mathbf{P} is a distance \vec{r}_1 away from horn one and \vec{r}_2 away from horn two then, from (A.51), any field quantity at point \mathbf{P} can be written in two ways:

$$\begin{aligned} \Psi(\mathbf{P}) &= \Psi(\vec{r}_1) = C_\Psi \int d\theta_1 b_r^{(1)}(\theta_1) e^{jk\hat{n}_1(\theta_1) \cdot \vec{r}_1}, \\ &= \Psi(\vec{r}_2) = C_\Psi \int d\theta_2 a_r^{(2)}(\theta_2) e^{-jk\hat{n}_2(\theta_2) \cdot \vec{r}_2}. \end{aligned} \quad (\text{A.55})$$

If \vec{d} is a vector that points from horn one to two, then clearly $\vec{r}_1 = \vec{r}_2 + \vec{d}$, which implies that

$$a_r^{(2)}(\theta_2) = b_r^{(1)}(\theta_1(\theta_2))e^{-jk\hat{n}_2(\theta_2)\cdot\vec{d}}, \quad (\text{A.56})$$

where the geometrical requirement that $\hat{n}_2(\theta_2) = -\hat{n}_1(\theta_1)$ defines the relationship between θ_1 and θ_2 .

Combining equations (A.54) and (A.56) leads to an equation for $b_l^{(2)}$ in terms of $b_r^{(1)}$ involving the beam pattern of the receiving horn,

$$b_l^{(2)} = \int_{-\pi/2}^{\pi/2} d\theta_2 S_{rl}^{(2)}(\theta_2) b_r^{(1)}(\theta_1(\theta_2)) e^{-jk\hat{n}_2(\theta_2)\cdot\vec{d}}.$$

Let Φ be the angle of the vector that points from horn two to horn one ($-\vec{d}$) in the coordinate system of horn two. Then $\hat{n}_2(\theta_2) \cdot \vec{d} = -d \cos(\theta_2 - \Phi)$ and in the far-field limit, where $kd \gg 1$, the only contribution to the integral will occur when \hat{n}_2 is antiparallel to \vec{d} , or $\theta_2 = \Phi$. Changing integration variables to $\Theta = \theta_2 - \Phi$ and Taylor expanding the exponent in the integrand around $\Theta = 0$ gives the result

$$b_l^{(2)} = S_{rl}^{(2)}(-\hat{d}) b_r^{(1)}(\hat{d}) e^{jkd} \int_{-\pi/2-\Phi}^{\pi/2-\Phi} d\Theta e^{-jk d \Theta^2/2}.$$

As with the integral in equation (A.46), the only contribution is in the neighborhood of $\Theta = 0$ and the integral can be performed by extending the limits to $\pm\infty$. The important region will be fully covered as long as $|\Phi| < \pi/2$, which is not strictly enforced, but the reception of the horn to waves traveling across its aperture should be negligible. Extending the integration limits gives the result

$$b_l^{(2)} = S_{rl}^{(2)}(-\hat{d}) b_r^{(1)}(\hat{d}) e^{jkd} \sqrt{\frac{\pi}{kd}} (1 - j).$$

The definition of S_{21} and (A.53) give the final result that

$$S_{21} = S_{rl}^{(1)}(\hat{d}) S_{rl}^{(2)}(-\hat{d}) \sqrt{\frac{\lambda}{d}} e^{j(kd - \pi/4)}. \quad (\text{A.57})$$

This is the wave amplitude version of the two-dimensional Friis transmission formula and it has all the expected elements. The product of the transmitting and receiving beam patterns is evaluated only along the direction that connects the two horns. There is an exponential factor that comes from propagating the waves from one horn to the other. The most interesting factor is the $\sqrt{\lambda/d}$ term which comes from the amplitude decay with distance for a circular (two-dimensional) wave. This two-dimensional result is fully analogous to the standard Friis transmission formula and can be expressed in terms of power by calculating $|S_{21}|^2$.

Appendix B

Thermometry Monitoring and Control

B.1 LabVIEW Programming

The thermometry readout and control software for Z-Spec is written in the LabVIEW programming environment. LabVIEW is based on a graphical programming language developed by National Instruments, a company that also makes generic data acquisition hardware. LabVIEW is particularly capable in the area of data recording and processing. Many lab equipment companies supply LabVIEW drivers for their products to enable communication between the device and a host computer.

Z-Spec uses several different pieces of equipment to measure and control the cryogenic systems in the dewar. LabVIEW is used to record the data from these different devices and uses those measurements to control various elements of the cooling system. The software is written to abstract the measurement devices from the reading and control they provide. Most of the communication between the computer running the LabVIEW code and the individual instruments is done via GPIB, a short-range parallel bus designed for instrument automation. Most of the instruments have vendor-provided drivers and a suitable driver has been created for those which do not.

LabVIEW programs are called virtual instruments (VIs) and they can contain subroutines, called subVIs. The front panel of a VI indicates the interface to that routine, both inputs and outputs. The processing of the inputs and production of outputs is written in the block diagram, which is wired together like a virtual electrical circuit. SubVIs are called in the block diagram by including an icon that represents the routine and has connections for the inputs and outputs. An instrument driver is a suite of subVIs that sends instructions to, and sometimes receives information from, the associated machine. The sequence of execution of a LabVIEW program starts with the inputs to the routine and travels down the connections in the block diagram. When a subVI is encountered on one of these connections, program control travels into that subroutine and does not return until the subroutine has completed its task. There are several program control elements available in

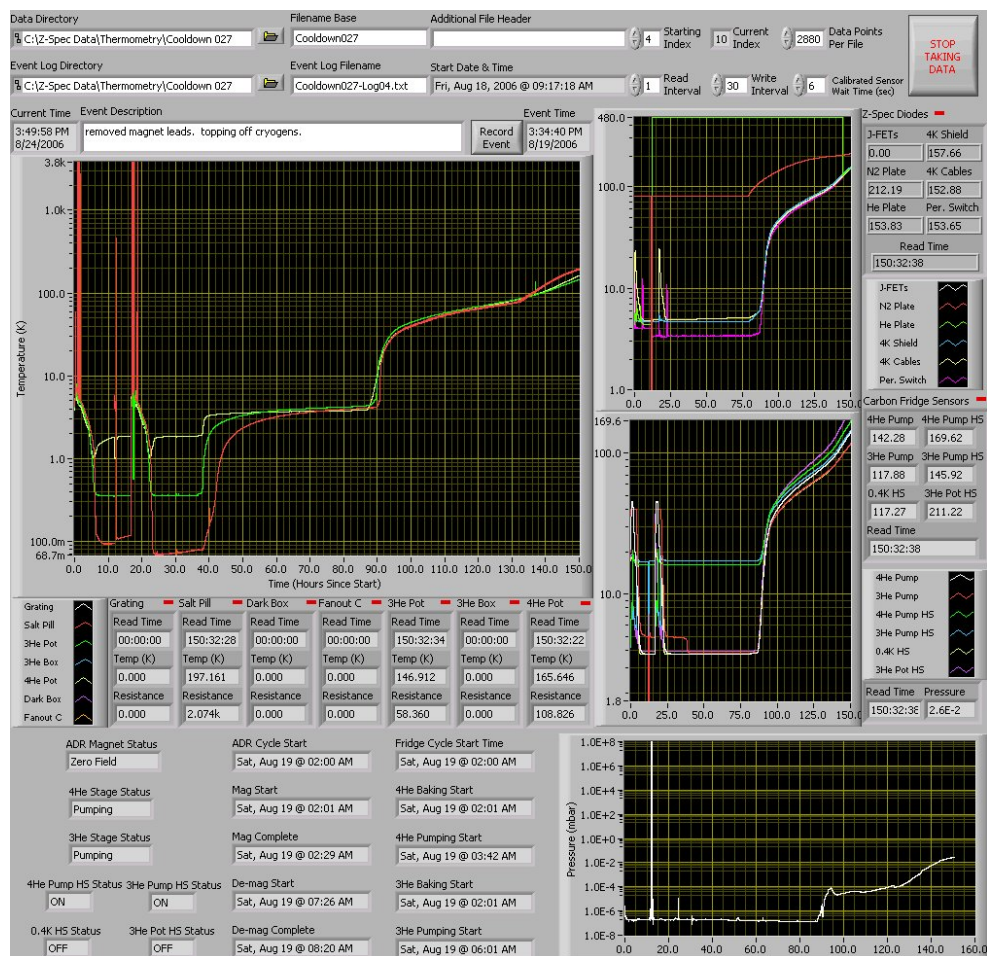


Figure B.1. This screen dump of the front panel of the Z-Spec Thermometry Readout program shows the numerical displays and four plots for different types of sensors: cold stage temperatures on the left, diode temperature sensors which are placed at various locations in the dewar on the top right, temperature sensors at various locations on the $^3\text{He}/^4\text{He}$ sorption cooler (called the “fridge” in the thermometry software) on the middle right, and a plot of the dewar pressure on the bottom right. This screen dump was produced as the dewar warmed to room temperature.

LabVIEW, such as conditional and looping structures. Cooperative multi-threaded applications are simple to write by using several program control structures in parallel; for example, two separate loops will automatically run simultaneously. Loops typically contain wait statements to adjust their execution frequency and help render the cooperative multi-threading more harmonious.

The subsequent sections give descriptions of the readout and control programs used by Z-Spec. The concluding section is a reference guide for the subroutines used by these programs to interface with different aspects of the cryogenic system.

B.2 Readout Program

The main readout program for the Z-Spec cryostat is called “Z-Spec Thermometry Readout.vi”. Its primary purpose is to issue queries to the temperature sensor readout devices and to plot, record and store those values. It also records data from a pressure sensor. The data is displayed on-screen in the front panel of the application by numerical indicators and several plots (shown in figure B.1). It has several inputs which control where and how often data is taken and written to disk. It creates an event log that can be used by the operator, and is used by several of the other routines to record various pieces of time-stamped information. And finally it has several indicators to show the status of the components of the cryogenic and cycling system.

The readout and control programs use several sets of global variables to store and share information. There is a set of variables to store temperatures of various stages and others for cryogenic status indicators. Global variables are used for communication between simultaneously running programs. For example, in the readout program, there are loops that take the temperature and pressure readings and a separate loop that updates the plots and writes data to files. These loops must run asynchronously because of the different time it takes to read out different sensors. The temperatures are read out and stored in the global variables. The plot and write loop reads the values of the global variables that it needs. The global variable system of communication works well as long as the programmer takes care to limit the ways the global variables are updated. The temperature and pressure sensor readings are stored in their respective global variables in only one place in the code.

B.3 Cycling and Control Programs

B.3.1 Automated Cycles

The program that runs the fully automatic cryogenic cycle has the unfortunate name “Z-Spec Cycle ADR & Fridge-CURRENT.vi”. It executes the cycle procedure outlined in section 3.4.1. It has various controls for tuning the performance of the cycle and can be set to run a cycle at an arbitrary time in the future. It is designed to run in parallel with the readout program as it uses the temperatures that are measured and stored in the global temperature variables discussed in the previous section. It uses additional global variables to communicate between different simultaneously running loops. These global variables are used to trigger certain cycle events such as pumping on the ^3He stage based on either the salt pill getting sufficiently cold or the ^4He liquid running out. The front panel image of this routine can be seen in figure B.2.

Start Time & Date
 10:00 PM
 5/10/2005

Cycle will start in -00:00:30 **Elapsed Cycle Time** 06:07:37

Magnetizing Parameters
 Programmed Current (A) 20.00
 Ramp Up Rate (A/sec) 0.015
 Stability Wait (sec) 20
 Close PSwitch Wait (sec) 55
 Ramp Down Rate (A/sec) 0.100

Mag PSwitch Params
 Firing Voltage 2.50
 Fire Time (s) 25.00
 Quiescent Voltage 1.25

Demagnetizing Parameters
 Ramp Up Rate (A/sec) 0.10
 Stability Wait (sec) 20
 Ramp Down Rate (A/sec) 0.007
 Completion Wait (sec) 0
 Close PSwitch Wait (sec) 0

Demag PSwitch Params
 Firing Voltage 2.50
 Fire Time (s) 25.00
 Quiescent Voltage 1.25

Baking Parameters
 4He Bake Temp (K) 45.00
 4He Baking Time (min) 60.00
 Initial 3He Bake Temp (K) 40.00
 Final 3He Bake Temp (K) 40.00

4He Pump Temp Reg Scaling Parameters
 Scale Factor [volts/kelvin] 1.00
 Look-Ahead Time (sec) 40.00

3He Pump Temp Reg Scaling Parameters
 Scale Factor [volts/kelvin] 1.00
 Look-Ahead Time (sec) 50.00

Salt Pill Temp Threshold (K) 1.80
Salt Pill Cooling Time (min) 0

Figure B.2. This is the front panel of the automatic cycling program. Across the top are a control to set when the cycle should start, a countdown timer indicator and a count-up timer that measures the total cycle time. The middle row of controls specify certain ADR cycle parameters. As discussed in section 3.4.2, the ramp-down rate setting in the demagnetizing parameters has a strong influence on the achieved base temperature. The $^3\text{He}/^4\text{He}$ sorption cooler controls are at the bottom left and are explained in more detail in the following reference section. The bottom-right controls specify how cold the salt pill should get before the demagnetization should begin and how long the grating and salt pill should remain connected to the ^3He stage after pumping on it begins, even if the salt pill has crossed the threshold value.

B.3.2 Cryogenic Controls

It is sometimes useful to have more direct access to the individual elements of the cryogenic system for testing purposes. The program “Z-Spec Manual Controls.vi” provides control to certain elements of the sorption cooler and the persistence switch. Beyond testing, these manual controls are also necessary for cooling the grating from room temperature to 4.2 K. After a few days of pre-cooling with liquid nitrogen in both cryogen tanks, the helium tank is evacuated and liquid helium is transferred. This rapidly cools the heat switches in the sorption cooler to below their transition temperature and they thermally isolate the grating from the helium bath. The heat switches between the grating and the ^3He pot, and the ^3He pot and the helium bath have to be switched on to properly cool the grating initially. In addition to these heat switches (HS 3 and 4), having gas in the ^3He and ^4He

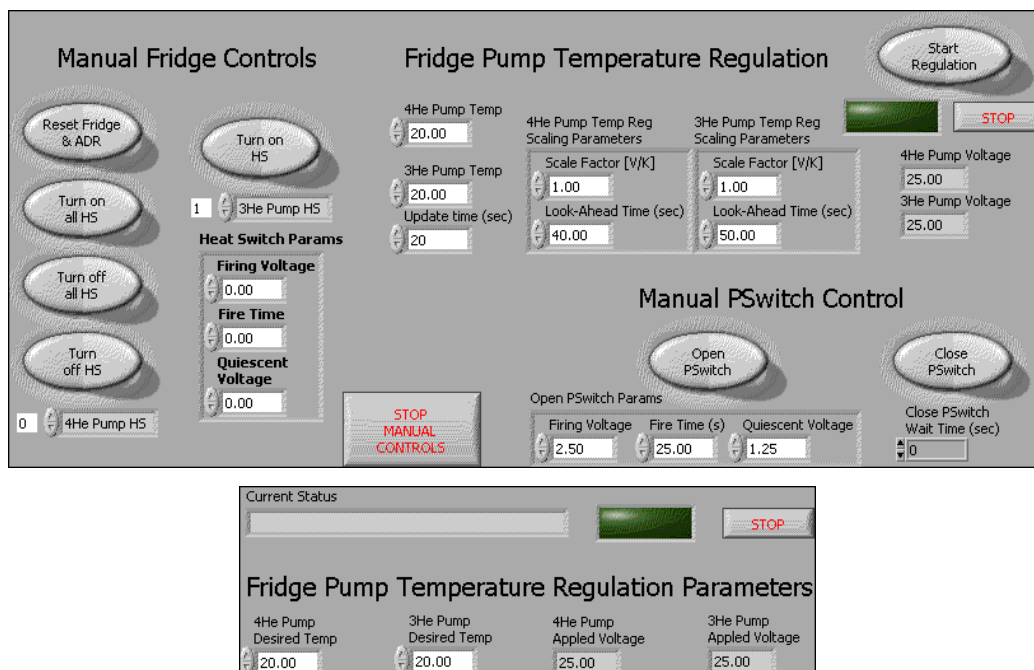


Figure B.3. The upper image shows the front panel of “Z-Spec Manual Controls.vi”. Most of the functionality is for controlling various pieces of the $^3\text{He}/^4\text{He}$ sorption cooler (called the “fridge” in the thermometry software). The heat switches can be turned on or off using the default or user-specified parameters. Regulation of the pump temperatures can be tested using the controls in the upper-right section. This program also allows manual control of the persistence switch. The second image shows “Z-Spec Inital He Cooldown.vi” which is to be used during the first helium transfers to properly cool the grating to 4.2 K. It uses default values for turning on the appropriate heat switches and regulating the pump temperatures to the level specified in the “desired temp” fields.

pump tube during this initial cooldown phase improves the cooling of the grating by about 25%. The program “Z-Spec Inital He Cooldown.vi” sets up all of these elements and can be run just before or after the first helium transfer. Like the cycling program described in the previous section, these two programs must be run in parallel with the readout program. The interfaces to these two functions are reproduced in figure B.3.

B.4 SubVI Reference

The main programs described in the previous sections rely heavily on subroutines for much of their functionality. A hierarchy diagram for the automatic cycling programs is shown in figure B.4. The subVIs described below have been separated into categories and are individually documented with their connector pane and a textual description. The connector pane is the icon that represents the subroutine in a block diagram along with labeled inputs and outputs. In general, inputs go in on the left side of the square (or sometimes rectangular) icon while outputs come out on the left. Sometimes a routine has too many inputs to fit on one side so that either the top or bottom or both will be

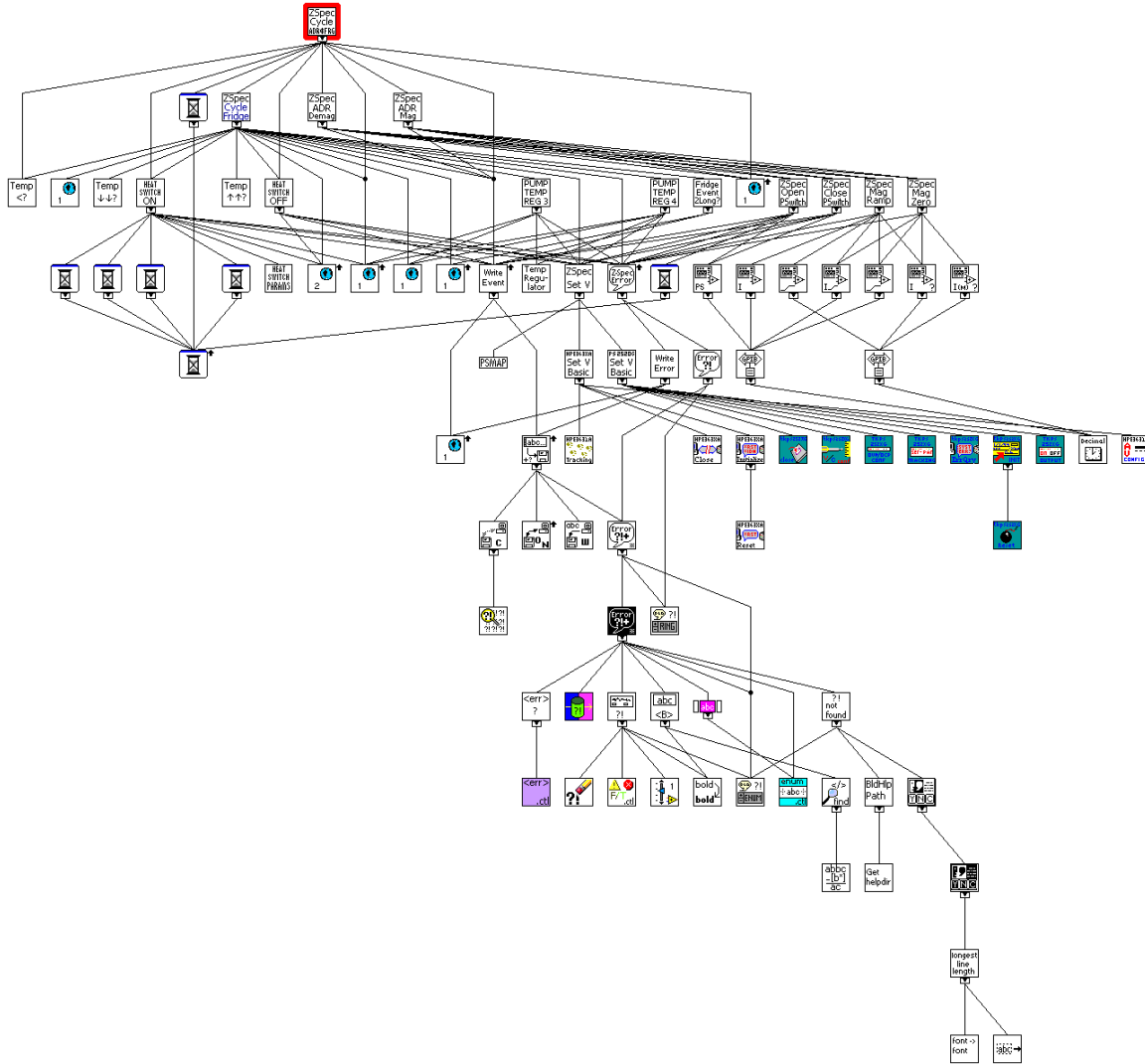


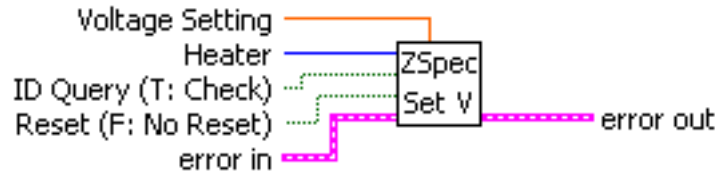
Figure B.4. This figure represents the software hierarchy for the automated cycling program. Its icon at the top of the graph is connected to the subVIs that it directly calls. Those subVIs are connected to the routines they call and so on down the graph.

used for additional inputs. The descriptions will discuss the inputs, outputs and results of executing each subVI.

B.4.1 Instrument Interface Functions

B.4.1.1 Power Supplies

Z-Spec Set Voltage.vi



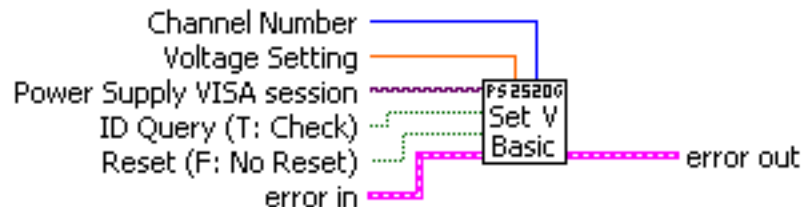
This function is a generic voltage setting routine. Specify a heater (pump, heat switch, persistence switch) and a voltage setting and this routine sends the appropriate power supply the proper commands.

Z-Spec Power Supply Map.vi



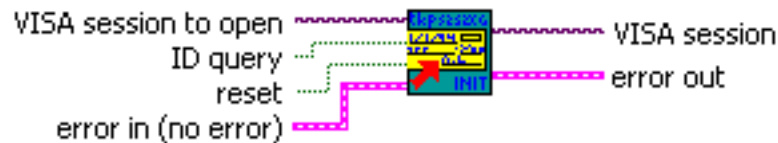
This routine specifies the connections between heaters and power supply channels.

Textronics PS2520G Set Voltage.vi



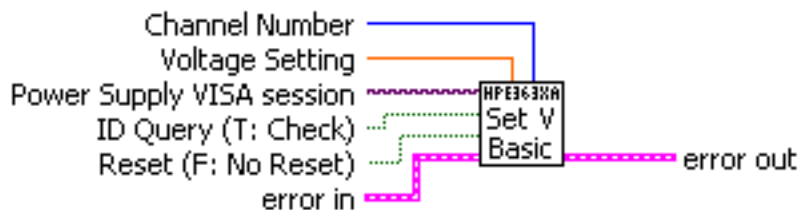
This function opens a communication channel to a Tektronix PS2520G, sets the voltage to the given setting on the given channel and then closes the communication session.

TKPS252XG Initialize - Mod.vi



This function was slightly modified from the original instrument driver distribution.

HPE3631A Set Voltage.vi



This is another instrument specific voltage setting routine that is called by Z-Spec Set Voltage.

HPE363xA Initialize-Mod.vi



This routine was slightly modified from the original version from Agilent.

B.4.1.2 Resistance Bridge

Z-Spec uses an AC resistance bridge from Linear Research (model LR-750) to read out several sensors in the cryostat. The LR-750 does have a GPIB interface, but the company does not provide a LabVIEW driver.

Z-Spec Get Cal Sensor Value - Fixed Wait Time.vi



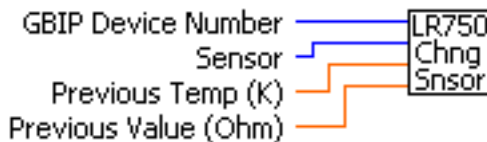
This routine abstracts away the actual device used for the sensor measurement. The sensor is specified by a list of names (3HePot, SaltPill, etc.). The Previous Sensor Data input, which contains the read time, resistance and calculated temperature is used to preset the resistance bridge, which enables faster readouts. The Wait Time input specifies how long to wait for a reading after all the setup commands have been issued to the bridge.

Z-Spec Calibrated Sensor Map.vi



This function specifies the mapping between sensor names and the channels on the bridge into which they are plugged.

LR-750 Change Sensor.vi



This routine issues a series of GPIB commands to the bridge to change the channel, adjust the scale and offset based on the previous resistance, and adjust the excitation level based on the previous temperature. The bridge does not automatically adjust the scale, and setting the offset to the previous reading reduces the settling time. Adjusting the excitation level based on temperature is necessary so that the bridge does not over-excite the sensors on the cold stages.

LR-750 Compute Scale.vi



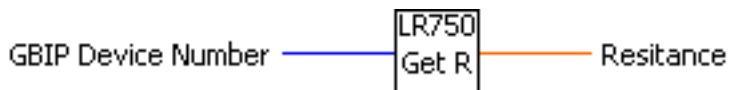
This function calculates the appropriate scale (or range) and offset to use based on the previous reading. Each scale on the LR-750 tops out at 200,000 counts, so this function switches ranges when the reading gets to 170,000 counts. The counts are equal to some power of ten times an ohm, depending on the scale setting.

LR-750 Select Excitation.vi



This function selects an appropriate excitation range based on the information from the sensor manufacturer (Lake Shore Cryotronics) and empirical testing of readout noise levels versus thermal loading at various levels of excitation.

LR-750 Get R.vi



This routine issues GPIB queries to get the resistance measurement from the LR-750 bridge.

B.4.1.3 Temperature Monitors

Z-Spec Read Carbon Sensors.vi



This function is an abstract routine to get the temperature readings from the sensors on the $^3\text{He}/^4\text{He}$ sorption cooler. Except for the ^3He pot, all the thermometers are $102\ \Omega$ carbon resistors, whose resistance rises as their temperature decreases. Their resistance is about $1000\ \Omega$ at $4.2\ \text{K}$.

Z-Spec Carbon Sensor Map.vi



This routine maps between named temperature stages (3HePump, 4HePumpHS, etc.) and the associated readout channel.

Z-Spec Read Diodes.vi



Similar to “Z-Spec Read Carbon Sensors”, this routine is an abstract function to read out the various diode temperature sensors installed at various places in the dewar.

Z-Spec Diode Map.vi



This function maps between diode location and channel number.

B.4.1.4 Other Instruments

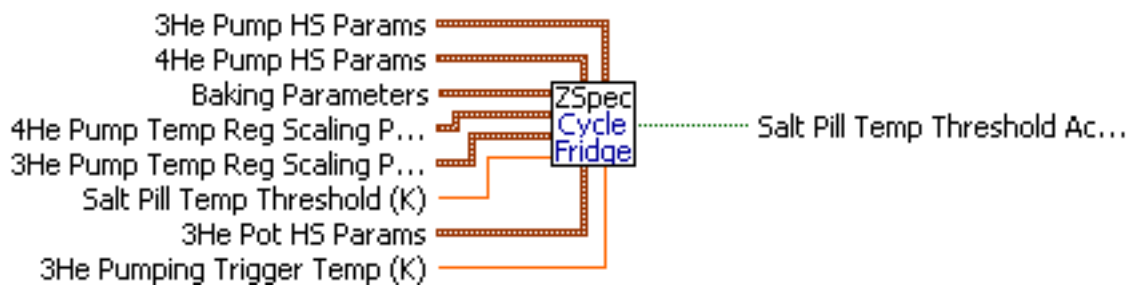
Get Pressure.vi



This routine uses a serial bus communication protocol to get the pressure reading from our BOC Edwards Wide Range Gauge pressure transducer and TIC instrument controller.

B.4.2 Helium-3/Helium-4 Sorption Cooler Controls

Z-Spec Cycle Fridge - No Heating.vi



The sorption cooler is called the “fridge” throughout the thermometry software and this routine handles all aspects of its cycle. During the course of that cycle it turns on three heat switches and can use non-standard parameters for turning on those switches if desired (3He Pump, 4He Pump and 3He Pot HS params, HS 2, HS 1 and HS 3 respectively). These inputs are optional and default values will be used if they are not connected. It also accepts the parameters of the pump temperature regulation feedback loop (4He Pump and 3He Pump Temp Reg Scaling Params). The Baking Parameters are comprised of four values: the desired ⁴He pump baking temperature and baking time and two baking temperature levels for the ³He pump. The initial ³He baking temperature is set during the time when the ⁴He stage is heating up to its set temperature. Once the ⁴He pump reaches its set point, its countdown begins and the final ³He baking temperature is set. This two phase heating of the ³He pump is generally unused by setting the initial and final temperatures equal, as seen in figure B.2. The 3He Pumping Trigger Temp triggers the ³He pumping. If this is set to zero or unconnected, then ³He pumping will be triggered by either the ⁴He liquid running out (which can be observed based on what the ⁴He pot temperature does after ⁴He pumping begins) or the salt pill achieving the Salt Pill Temp Threshold, whichever comes first. This is the standard cycling method. If the 3He Pumping Trigger Temp is not zero, then ³He pumping begins when the ³He pot gets below the given temperature. The only output of this routine indicates whether or not the salt pill achieved the given temperature threshold.

Z-Spec Heat Switch On.vi



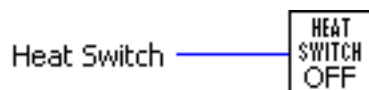
This abstract function switches on a given heat switch. HS 1 - 4 are named 4He Pump HS, 3He Pump HS, 3He Pot HS, and 0.4K HS, respectively, in the software. Heat Switch Params are composed of three values: the firing voltage, firing time and quiescent voltage. Turning on a heat switch is done by applying the firing voltage for the firing time (if the heat switch temperature is below 20K and in the off state) and then setting the quiescent voltage. If that voltage is set to zero or the Heat Switch Params is unconnected, default parameters are used for the given heat switch.

Z-Spec Heat Switch Default Params.vi



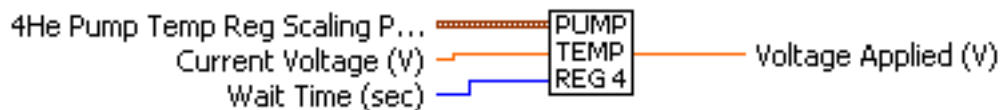
This routine returns the default parameters for turning on the given heat switch. These empirically determined values allow the switches to be turned on as quickly as possible without overheating them.

Z-Spec Heat Switch Off.vi



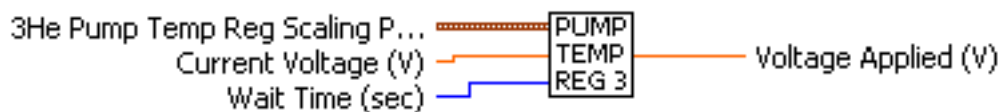
This function turns off the given heat switch by setting the voltage applied to its heater to zero.

Regulated 4He Pump Baking.vi



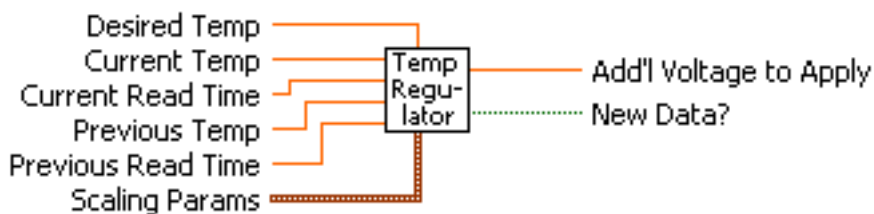
This routine controls regulated baking of the 4He pump. The feedback loop adjusts the voltage applied to the heater based on the temperature value and the change in temperature over the number of seconds specified in Wait Time. The function computes an expected temperature error which it converts to a needed voltage correction which is added to Current Voltage. The new voltage is set and returned in Voltage Applied. If the temperature reading is not updated while this function executes, it sets the voltage to zero to avoid runaway heating of the pump. This function uses the global temperature variables and an additional global variable which contains the pump temperature set point.

Regulated ^3He Pump Baking.vi



This function is the same as the previous subVI except that it regulates baking of the ^3He pump.

Generic Temp Regulator.vi



This routine does the math that drives the pump temperature regulation. It returns the calculated voltage correction and a boolean value, “New Data,” that depends on whether the Current Read Time and Previous Read Time are equal or not.

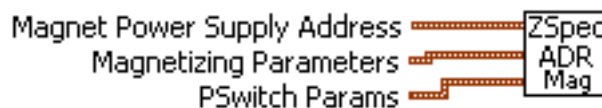
Z-Spec Fridge Event Too Long.vi



This fail-safe function ensures that the cycle does not take too long. It checks the event time associated with the given Fridge Process (e.g. ^3He baking) to see if it occurred more or less than Time Limit hours before the current time. If it is over the time limit, then the returned boolean is true; otherwise, false.

B.4.3 ADR Controls

Z-Spec ADR Magnetize.vi



This function communicates with the magnet power supply (a GPIB enabled Model 420 Controller from American Magnetics) and the persistence switch heater power supply to magnetize the ADR. It opens the persistence switch, sets and slowly ramps up the current on the magnet supply. When

the set current has been reached it waits for a few seconds for things to stabilize then closes the persistence switch, waits again for it too cool off and return to the superconducting state and then quickly ramps down the current on the supply to zero. The set current, ramp rates and wait times can be adjusted via the elements of Magnetizing Parameters while the activation parameters of the persistence switch are controlled by PSwitch Params.

Z-Spec ADR Demagnetize.vi



This function is similar to the previous subroutine except that it demagnetizes the ADR. It quickly ramps up the magnet power supply current then waits for a few seconds to stabilize. Then it turns the persistence switch on (using the given parameters) and it slowly ramps the current to zero. After the current is zeroed and a few seconds of waiting, the persistence switch is turned off.

Z-Spec Ramp Up Current.vi



This function ramps up the current of the magnet power supply at the given Ramp Rate. It can also set the current to Programmed Current if that input is not equal to zero. It exits when the ramping is complete as identified by the magnet power supply.

Z-Spec Zeroing Current.vi



This routine zeros the current of the magnet power supply at the given Ramp Rate. Exits when the current reading from the magnet power supply is less than 5 mA.

Z-Spec Open Persistent Switch.vi



Voltage is applied to the persistence switch (called “persistent” switch in the thermometry software) heater by this subVI. The persistence switch heater and the heat switches on the sorption cooler are turned on in the same way: a large voltage is applied for a short time to quickly warm the superconductor past the transition temperature, then a smaller voltage to maintain that temperature is applied. While the magnet power supply has the ability to heat the persistence switch itself, we use an external power supply for refined control.

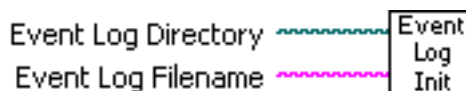
Z-Spec Close Persistent Switch.vi



This function turns off the voltage to the persistence switch heater and waits a few seconds before exiting.

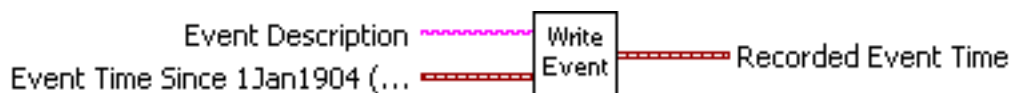
B.4.4 File I/O

Initialize Event Log.vi



This routine sets the two global variables associated with the electronic event log available to all routines. It stores the full path to the log file (directory + filename) and resets the event log counter.

Write Event.vi



This function writes an event to the event log using the global variables set by the initialization function above. Each event is numbered and time and date stamped. The optional input Event Time provides the time and date stamp for the event. If it is not present then the current time and date are used. The subVI also increments the event log counter global variable.

Write Error.vi



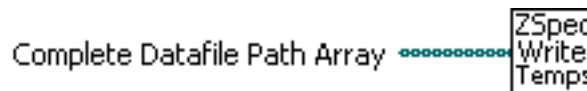
This function uses the same directory as the configured event log but writes or appends descriptions of errors to a file called ERROR.txt. This is generally used by the Z-Spec Error Handler subVI to deal with GPIB communication errors which sometimes occur randomly and always occur when someone forgets to turn on the magnet power supply (or any other piece of equipment).

Data Path & Header.vi



This sets up the data recording files for the readout program. It creates several paths that point to files in Data Directory using Filename Base and Filename Index to create the full file names. It also creates headers which contain the File Header Info and the Start Time along with column labels for each element of data to be stored in the files.

Write Temperature Data.vi



This takes the file path output from the function above and reads from the temperature global variables to write temperature and other data to the given files.

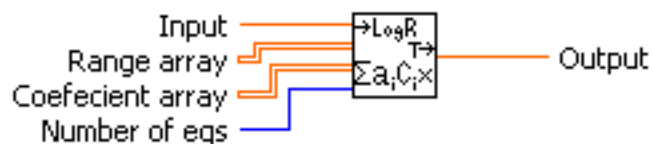
B.4.5 Sensor Calibration

Carbon Sensor R to T.vi



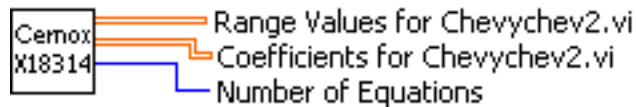
This routine applies the generic calibration for the carbon resistor temperature sensors on the $^3\text{He}/^4\text{He}$ sorption cooler.

Chebychev2.vi



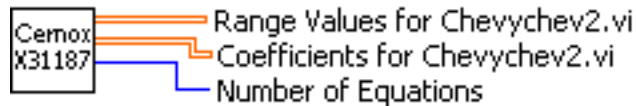
This subVI implements the calibration system used by Lake Shore Cryotronics for their calibrated sensors. It is based on a Chebychev polynomial expansion of the base-ten logarithm of the resistance (Input). For enhanced accuracy, this expansion is usually applied in several temperature blocks which are specified by the Range array. The coefficients of the expansions are given in Coefecient array and Number of eqs is the number of temperature ranges used. The Output is the calculated temperature.

CernoxX18314.vi



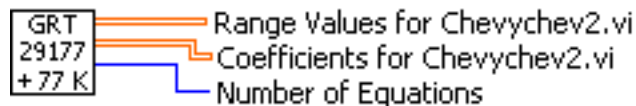
Z-Spec uses several calibrated sensors at different locations in the dewar. This and the following 5 subVIs store the calibration data for individual sensors in the format used by Chebychev2. This is a Cernox sensor which is calibrated from 300 mK to 300K.

CernoxX31187.vi

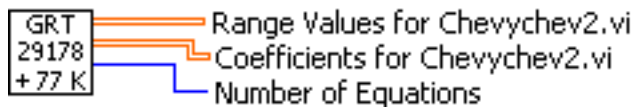


This is another Cernox sensor calibrated from 300 mK to 300K. The Cernox sensors are used on the ^3He pot and ^3He radiation shield.

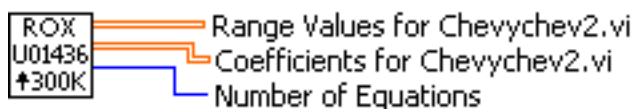
GRT29177 + 77K.vi



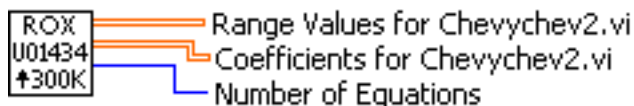
Germanium resistance temperature (GRT) sensors can be tuned to be the most sensitive thermometer at any given temperature but they are limited to about 2 orders of magnitude in range. This GRT is calibrated from 50 mK to 5 K and the fit has been linearly extended to include 77 K. It cannot be extended further because the sensors resistance is not monotonic between 77 K and 300 K and that cannot be handled by the calibration system. Experience has shown that the extended fit is fairly inaccurate particularly at temperatures slightly above 5 K.

GRT29178 + 77K.vi

This routine is another GRT sensor calibrated from 50 mK to 5 K and linearly extended to 77 K. These GRTs are installed on the grating and are now recorded by the readout electronics rather than the LR-750 bridge.

ROXU01436 + 300K.vi

Ruthenium oxide temperature (RuOx) sensors are almost as sensitive as GRTs and can be calibrated over a larger range. Their resistance is monotonic all the way up to room temperature so this sensor's calibration from 50 mK to 40 K has been linearly extended to 77 K and then to 300 K.

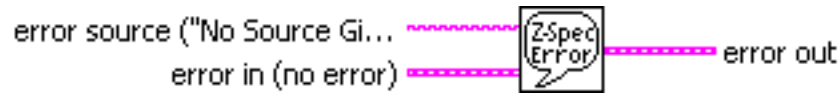
ROXU01434 + 300K.vi

As with the previous RuOx sensor, this 50 mK to 40 K calibration is extended in two linear steps to 77K and 300K. These sensors are used on the salt pill and grating to track their progress during the initial cooldown and the salt pill's sensor is also used to control the ADR/sorption cooler cycle.

B.4.6 Miscellaneous**Z-Spec Reset Fridge & ADR.vi**

This routine resets the cycling system. It sets all the heater voltages to zero, all cycling global variables to suitable reset values and closes the persistence switch.

Z-Spec Error Handler.vi



Some LabVIEW routines use an error structure to indicate success or failure. This subVI can intercept these errors and print an error report using Write Error.

Append Cal Sensor Data for Plot Arrays.vi



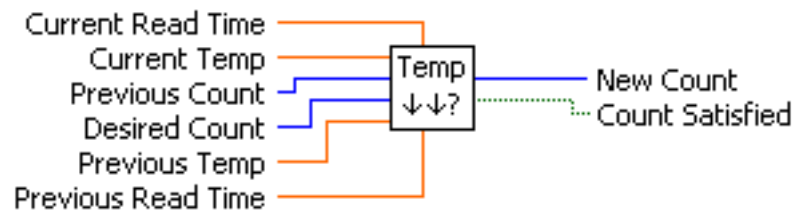
The plots in the readout program accept arrays in a certain format for proper plotting. This routine takes the calibrated sensor reading format (read time, resistance, temperature) and appends the appropriate elements to the plot arrays.

Append Sensor Data for Plot Arrays.vi



This function is similar to the previous function except it is intended for use with the sensors measured by the temperature monitors.

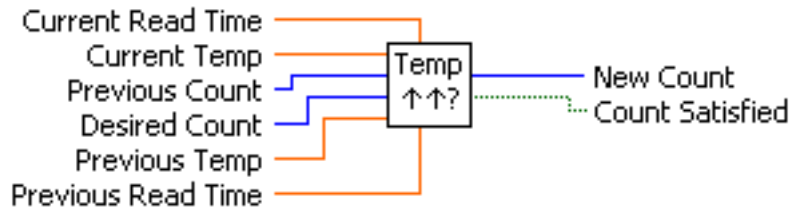
Temperature Decreasing.vi



The following three subroutines perform mathematical comparisons on temperature readings which enable conditions based on the asynchronous and sometimes glitchy measurement system to be checked safely. This function checks if the temperature given in Current Temp is less than Previous Temp and increments Previous Count by one if it is. This is returned in New Count which is checked with respect to Desired Count and sets Count Satisfied to true if New Count is greater than or equal to Desired Count. If the given temperature readings are not different, as indicated by Current and

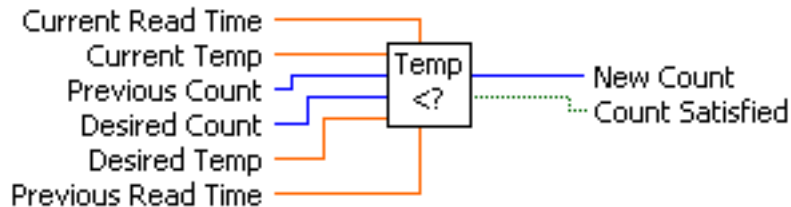
Previous Read Times being equal, then Previous Count is passed directly to New Count without increment. If Current Temp is greater than or equal to Previous Temp then New Count is reset to 0.

Temperature Increasing.vi



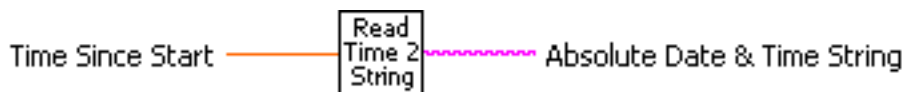
This routine is similar to Temperature Decreasing but instead checks if Current Temp is greater than Previous Temp.

Temperature Less Than.vi



This function works exactly like Temperature Decreasing except that one of the inputs has a different name and is intended to check a temperature reading with respect to a constant value Desired Temp. There is a similar but unused function Temperature Greater Than that works like Temperature Increasing. This subVI could have been, but was not, implemented as a wrapper to Temperature Decreasing.

Read Time to Excel Date&Time String.vi



This helper subroutine converts the Time Since Start input, which is in seconds, to a string that is easily interpreted by Microsoft Excel as a date and time. It accesses the global variable Start Time which is set when the readout program starts.

Pad Decimal with Zeros.vi



This function takes an integer, Value, and appends to Initial String a string that contains the integer plus a number of preceding zeros to make the added string Width long. For example, if Initial String = 'filename', Value = 5 and Width = 3 then Output String = 'filename005'.

B.4.7 Global Variables

The connector panes for global variables are uninteresting, so the front panels are shown instead.

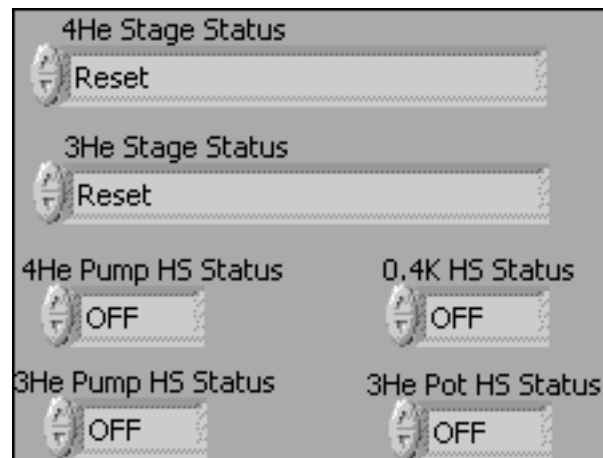
Temperatures.gbl.vi

| Section | Variable | Value | |
|-----------------|----------------------------|----------------------------|----------|
| Z-Spec Diodes | Read Time Since Start(sec) | 39807.20 | |
| | J-FETs (K) | 0.0000 | |
| | N2 Cold Plate (K) | 93.2630 | |
| | He Cold Plate (K) | 1.0000 | |
| | 4K Cable Heat Sink (K) | 187.1900 | |
| | 4K Cables (K) | 87.6920 | |
| | Persistence Switch (K) | 89.4960 | |
| | Carbon Fridge Sensors | Read Time Since Start(sec) | 39807.20 |
| | | 4He Pump (K) | 79.2821 |
| | | 3He Pump (K) | 69.7294 |
| 4He Pump HS (K) | | 94.5043 | |
| 3He Pump HS (K) | | 82.8524 | |
| 0.4K HS (K) | | 70.6273 | |
| 3He Pot HS (K) | | 108.2395 | |
| 4He Pot | Read Time Since Start(sec) | 39801.40600 | |
| | Temp (K) | 81.8670 | |
| 3He Pot | Read Time Since Start(sec) | 39795.28100 | |
| | Temp (K) | 82.5982 | |
| Pressure | Read Time Since Start(sec) | 39807.21900 | |
| | Pressure (mbar) | 0.0011 | |
| GRT 29177 | Read Time Since Start(sec) | 0.00000 | |
| | Temp (K) | 0.0000 | |
| | Resistance (Ohm) | 0.0000 | |
| GRT 29178 | Read Time Since Start(sec) | 0.00000 | |
| | Temp (K) | 0.0000 | |
| | Resistance (Ohm) | 0.0000 | |
| 3He Box | Read Time Since Start(sec) | 0.00000 | |
| | Temp (K) | 0.0000 | |
| | Resistance (Ohm) | 0.0000 | |
| Salt Pill | Read Time Since Start(sec) | 39789.17200 | |
| | Temp (K) | 76.0184 | |
| | Resistance (Ohm) | 2156.6000 | |
| Grating | Read Time Since Start(sec) | 0.00000 | |
| | Temp (K) | 0.0000 | |
| | Resistance (Ohm) | 0.0000 | |

This large collection of global variables contains all the temperature readings and the pressure reading. The temperatures measured by the temperature monitors are grouped together into Diodes and Carbon Fridge Sensors. The seven sensors read out by the LR-750 bridge have individual

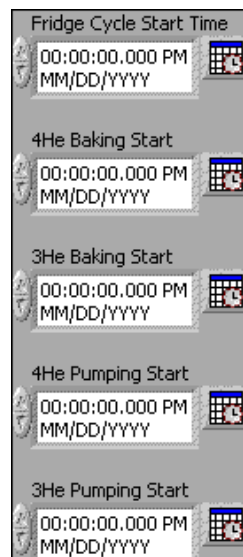
structures with the read time, temperature and resistance. The pressure reading is also separate with its value and read time grouped together. It also includes the Start Time which indicates when temperature reading began. The Start Time is a time type variable; this type was introduced part way into the development of this software with LabVIEW version 7. All sensor readings are associated with a decimal value of the number of seconds since the start time. When the new time type was introduced, development of the software had progressed too far to change these elapsed time measurements over to the new type.

Fridge Status.gbl.vi



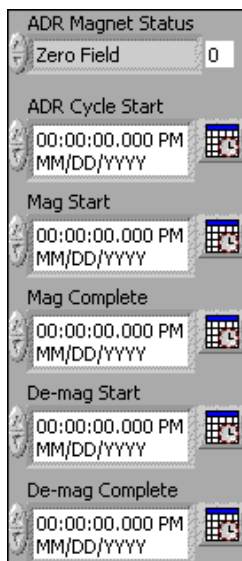
These globals contain the status of certain stages of the sorption cooler. The ^4He and ^3He stage status can be either Reset, Baking or Pumping and the heat switches can be either ON or OFF.

Fridge Times.gbl.vi



These globals store the start times for various $^3\text{He}/^4\text{He}$ sorption cooler events.

ADR Status & Times.gbl.vi



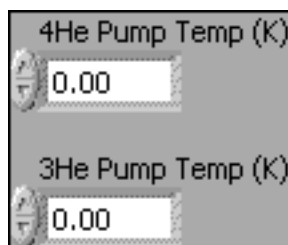
The ADR status can be either Zero Field, Magnetizing, Magnetized, or Demagnetizing. The times of certain ADR cycle events are also included in this file.

Fridge Triggers.gbl.vi



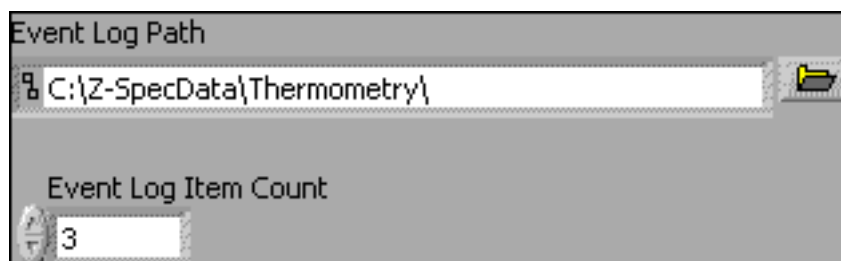
These two booleans are used to trigger pumping of the ^4He and ^3He stages.

Fridge Pump Temps.gbl.vi



These two values are the set temperatures used by the pump temperature regulating subroutines.

Event Log.gbl.vi



These two globals store the path to the event log file and the event counter which increments when an event is recorded.

Appendix C

Bolometer Readout Roll Off

C.1 Circuit Model

The readout electronics designed for the Z-Spec instrument are based on a dual-phase lock-in amplifier (LIA) which provides both the sine and cosine components of the lock-in signal. This enables investigation of possible readout roll off caused by reactive elements in the readout circuit. A parametric plot of a few hours of the two outputs from an LIA indicates that the roll off can be significant. Combining the LIA outputs in quadrature is one method for extracting a signal but doing so can decrease the signal to noise ratio. A simple electrical model of the readout circuit can be used to create an optimal linear combination of the sine and cosine components which does not boost the noise in the output signal. This appendix explains the model and how it is used in the data processing pipeline.

The circuit diagram used for the roll off model is shown in figure C.1. In AC mode, the bias voltage can be written as a complex phasor $\mathcal{V}_{\text{bias}} = V_{\text{bias}} e^{j\omega t}$, where ω is the bias frequency, and V_{bias} is the bias amplitude. The capacitance in the readout lines and at the inputs to the J-FET followers can be modeled as a lumped element called C_ℓ . At some time t the bolometer will have a resistance R_B which is determined by the incident optical power, the current bath temperature and the electrical dissipation in the device. The voltage across the bolometer is given by the voltage divider equation

$$\mathcal{V}_{\text{bolo}} = \frac{V_{\text{bias}} \mathcal{Z}_{BC}}{\mathcal{Z}_{BC} + R_{L1} + R_{L2}},$$

where $\mathcal{Z}_{BC} = \frac{R_B}{1 + j\omega R_B C_\ell}$, the complex impedance of the parallel combination of R_B and C_ℓ at the bias frequency. The time dependence has been dropped and the only frequency component under consideration is at the bias frequency. The above equation can be simplified by introducing some alternative dimensionless variables. Let $y = 1 + \frac{R_L}{R_B}$ and $q = \frac{\omega}{\omega_L}$, where $R_L = R_{L1} + R_{L2}$ and $\omega_L = \frac{1}{R_L C_\ell}$, which gives

$$\mathcal{V}_{\text{bolo}} = \frac{(y - jq) V_{\text{bias}}}{y^2 + q^2}. \quad (\text{C.1})$$

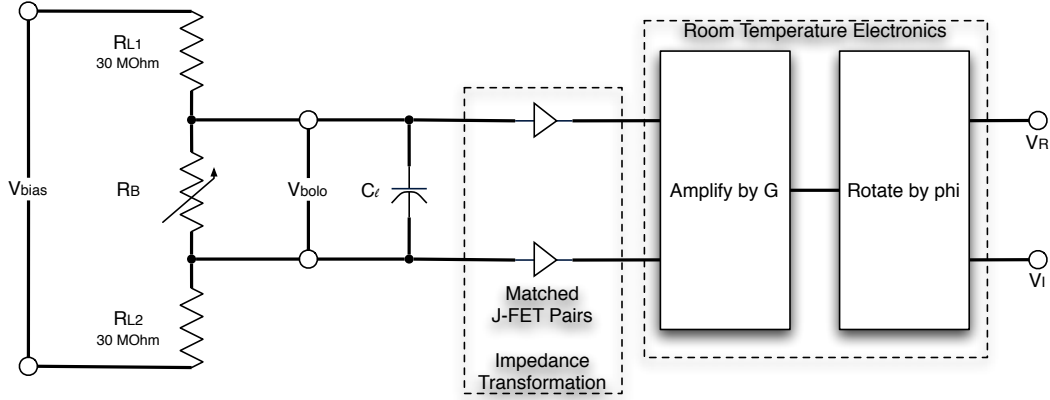


Figure C.1. This diagram represents the AC-biased bolometer readout circuit. The symmetric load resistor arrangement converts the voltage bias into a current bias. If $C_\ell = 0$ then all the current goes through R_B and no roll off occurs, but since $C_\ell > 0$, some of the bias current goes through it, rolling off the bolometer readout. After the J-FET impedance transformation, the signals are much less susceptible to line capacitance. The RTE's differential preamps and low-pass filters amplify their inputs by $G \sim 140$ for AC signals. The lock-in amplifiers impart a phase shift between the real and imaginary demodulations, and measuring this phase shift is crucial to constructing the optimum signal projection.

The J-FETs do not amplify the bolometer signal. The complex voltage above is the input to the room temperature electronics (RTE). There could be some line capacitance between the J-FETs and the RTE but it is negligible because of the impedance transformation provided by the J-FET followers. The RTE contains a preamp with a gain of $G \sim 140$ in AC mode. The LIA system locks into the reference signal at a particular sample of that signal. Since the phase of the lock point can change between power cycles of the RTE, this causes a rotation of the outputs of the LIA by an angle ϕ . The two components of the LIA output are the real and imaginary parts of the amplified and rotated input signal, $\mathcal{V}_{\text{bolo}}$,

$$\mathcal{V}_{\text{out}} = G \mathcal{V}_{\text{bolo}} e^{j\phi}.$$

The LIA outputs can be written in terms of the circuit parameters by plugging $\mathcal{V}_{\text{bolo}}$ into the above equation and taking the real and imaginary parts.

$$V_R = \Re(\mathcal{V}_{\text{out}}) = \frac{GV_{\text{bias}}}{y^2 + q^2} (y \cos \phi + q \sin \phi), \quad (\text{C.2})$$

$$V_I = \Im(\mathcal{V}_{\text{out}}) = \frac{GV_{\text{bias}}}{y^2 + q^2} (-q \cos \phi + y \sin \phi). \quad (\text{C.3})$$

V_R and V_I are the quantities actually measured by the data acquisition computer and the equations above give a parametric model of these outputs based on R_B (through the variable y) and the parameters of the readout system. The quantity of interest is the slope of the roll off curve $m = \frac{dV_I}{dV_R}$

which can be calculated by taking the derivative of the equations above with respect to R_B .

$$\begin{aligned}\frac{dV_R}{dR_B} &= \frac{G V_{\text{bias}} R_L}{R_B^2 (y^2 + q^2)^2} (y^2 \cos \phi + 2yq \sin \phi - q^2 \cos \phi), \\ \frac{dV_I}{dR_B} &= \frac{G V_{\text{bias}} R_L}{R_B^2 (y^2 + q^2)^2} (y^2 \sin \phi - 2yq \cos \phi - q^2 \sin \phi),\end{aligned}$$

which imply that

$$m = \frac{dV_R/dR_B}{dV_I/dR_B} = \frac{y^2 \sin \phi - 2yq \cos \phi - q^2 \sin \phi}{y^2 \cos \phi + 2yq \sin \phi - q^2 \cos \phi}.$$

This equation can be solved in terms of V_R and V_I by identifying the relationship between y and q implied by the equations (C.2) and (C.3):

$$\frac{y}{q} = \frac{V_R \cos \phi + V_I \sin \phi}{V_R \sin \phi - V_I \cos \phi}.$$

Plugging this into the above equation for m gives the result that the slope of the roll off curve depends only on the measured V_R and V_I plus the rotation of the roll off curve in the complex plane, ϕ .

$$m = \frac{V_I^2 \sin \phi + 2V_R V_I \cos \phi - V_R^2 \sin \phi}{V_R^2 \cos \phi + 2V_R V_I \sin \phi - V_I^2 \cos \phi}. \quad (\text{C.4})$$

The optimum signal V_{opt} is a projection onto an axis rotated by an angle $\theta = \tan^{-1}(m)$ in the complex plane.

$$V_{\text{opt}} = V_R \cos \theta + V_I \sin \theta, \quad (\text{C.5})$$

$$V_{\text{err}} = -V_R \sin \theta + V_I \cos \theta, \quad (\text{C.6})$$

where V_{err} is perpendicular to V_{opt} and should only contain electronics noise if the projection is performed properly.

C.2 Parameter Fitting

As shown in the previous section, the only model parameter needed for calculating the optimum signal is ϕ , the rotation of the roll off figure in the complex plane. Proper determination of this parameter, however, requires knowledge of the other circuit parameters. The bias voltage and frequency, the preamp gain and the load resistance can all be measured separately, but a fit must be used to determine C_ℓ . The line capacitance affects the overall curvature of the roll off figure and therefore a large range in R_B values must be covered to get enough data to accurately measure C_ℓ . One typical observation is not enough, particularly when the observation is of a faint source where this correction is most useful. Several nights of data are needed for a proper fit.

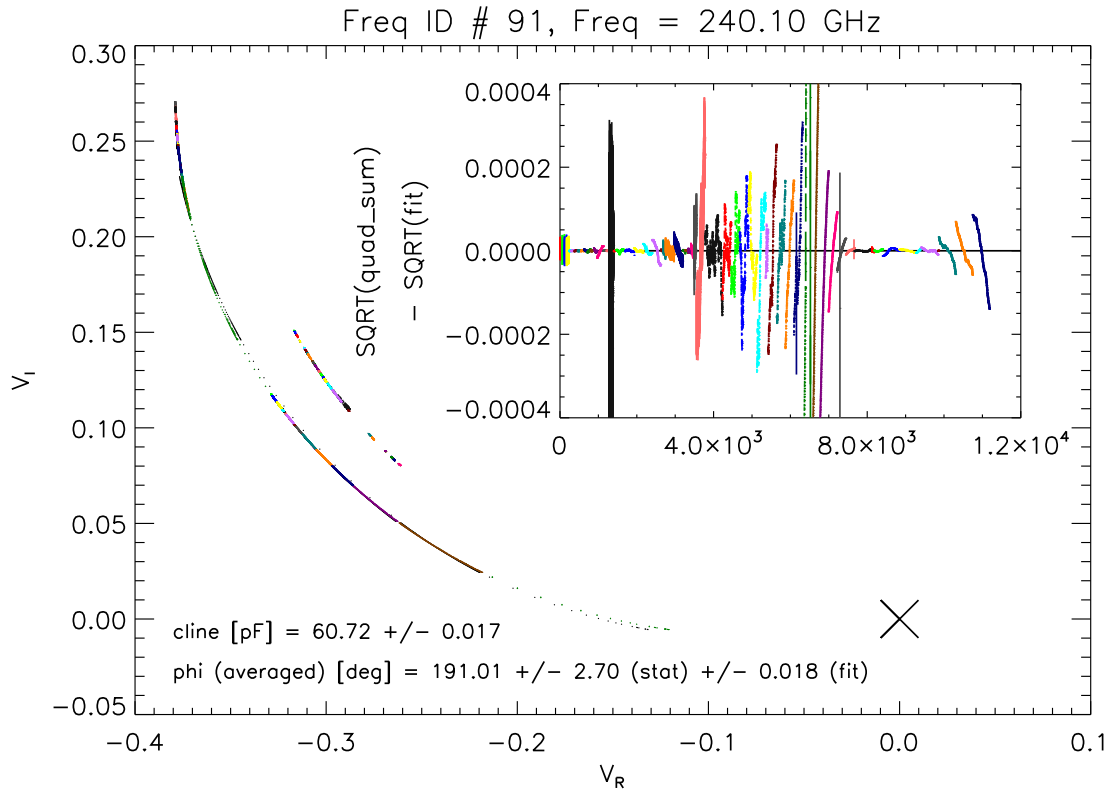


Figure C.2. This plot shows the roll off curve for frequency ID # 91 of data gathered on April 12–16, 2006 at a bias of 10 mV. Each point corresponds to an average of 5 seconds of data. The origin is indicated by the large X. The different colors correspond to different observations while the black points are the fit results. The occasional phi shift is clearly visible. The inset difference plot is plotted with respect to an index which counts the number of points included in the fit (over 10,000). As described in the text, the dependent variable of the fit is the quadrature sum of V_R and V_I , the square root of which is compared to the square root of the fit result in the inset.

Furthermore, a method for fitting must be developed. By eliminating R_B from equations (C.2) and (C.3), we find that

$$V_R^2 + V_I^2 = \frac{G V_{\text{bias}}}{q} (V_R \sin \phi - V_I \cos \phi). \quad (\text{C.7})$$

A standard fitting method would use the quadratic equation to solve for V_R in terms of V_I or vice versa and use one measured quantity to fit to the other. This method was problematic and an alternative method had to be found. An effective solution is to use both measured quantities as the independent variable and the quadrature sum as the dependent variable. The right side of the equation may then be used to calculate the dependent variable based on the model parameters. The drawback of this method is that it can only fit for two separate quantities, ϕ and $\frac{G V_{\text{bias}}}{q} = \frac{G V_{\text{bias}}}{\omega R_L C_\ell}$. The only unknown quantity in the latter coefficient is C_ℓ . An example of these fit results can be seen in figure C.2. Since ϕ can change if the RTE is power cycled, the measurement of C_ℓ from the fit of several nights' data is used to fit for ϕ when a particular observation is processed.

Appendix D

Data Reduction Pipeline

Many levels of artificial signal modulation and demodulation are applied to extract the weak astronomical signal from the data. In addition to the AC biasing of the detectors and lock-in amplifiers used in the readout electronics, the secondary mirror of the telescope is constantly chopping at about 1 Hz and the primary dish is nodded to the left or right once every twenty seconds. A single observation macro consists of several nod cycles, each of which includes a left-nod, right-nod pair followed by a right-nod, left-nod pair. The four chunks of a nod cycle are called the four nod positions. The symmetric $\pm 30''$ chopping creates two beams on the sky, and symmetric nodding by the same offset alternates the source from one beam to the other. The chopping creates a 1 Hz modulation of the bolometer signal, and the beam switching causes a 180° phase shift in this modulation. Each nod position is demodulated with respect to the chopper and then the four nod positions are differenced so that the measurement of the source spectrum for a particular channel for a particular nod is given by $(NP_1 - NP_2) - (NP_3 - NP_4)$, where NP_1 and NP_4 are left beams and NP_2 and NP_3 are right beams.

The data reduction pipeline is illustrated in figure D.1 and described in detail below. The chopper modulated bolometer timestreams are time-stamped and recorded by the data acquisition computer (DAC) which receives the data from the readout electronics via an ethernet connection. This data is called BZE (BICEP and Z-Spec Electronics) data. The DAC has an additional ethernet connection which is used to communicate with the CSO antenna computer. The DAC gets two sets of signals from the antenna computer, one that updates at a rate similar to the 50 Hz rate of the readout electronics and another that updates about once every second. The fast data from the antenna computer is called PLOG data and it contains pointing information and several logic signals that are used to determine when an observation starts and ends, when the nods within that observation start and end, and when the nod position switches occur within each nod. The slow antenna computer data, called RPC data, contains more detailed information, such as pointing offsets and optical depth values. The RPC data were not always recorded during the April 2006 run.

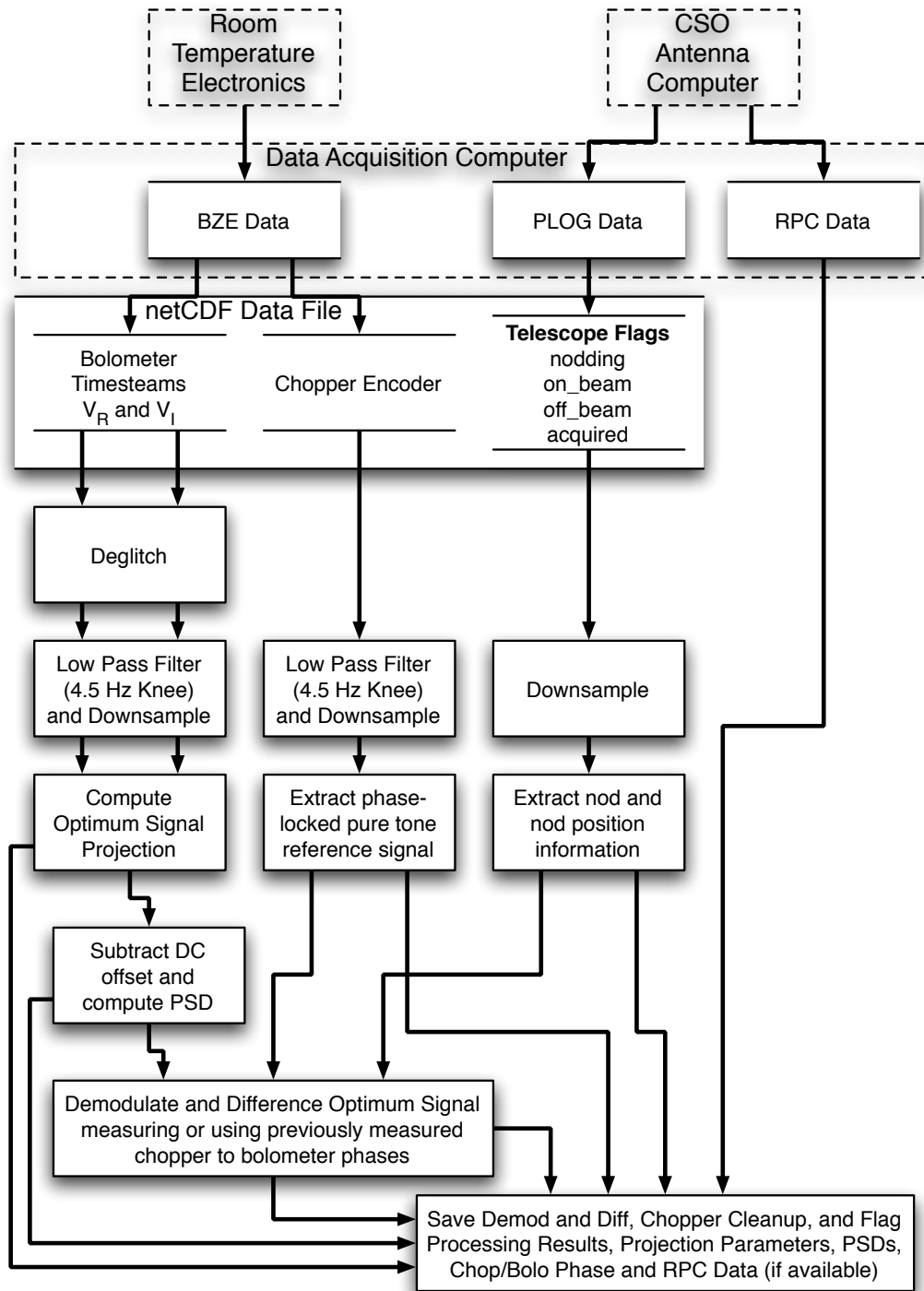


Figure D.1. This diagram indicates how the data gathered by the Data Acquisition Computer is reduced to a set of demodulated and differenced spectra. See the main text for a complete description of the data processing pipeline.

The BZE, PLOG and RPC data (if gathered) are recorded for an entire observation and then the BZE and PLOG data are trimmed and merged into a netCDF data format for processing. The time-stamped BZE and PLOG are synchronized before merging. The processing of an observation starts by deglitching, low-pass filtering and downsampling the bolometer timestreams. The deglitch pass is based on a recursive algorithm to calculate the moving average and moving standard deviation and toss out points that are too many standard deviations away from the mean. The low-pass filter is applied in the time domain by convolving the timestream with a set of coefficients generated using the Kaiser window function [Kaiser and Schafer 1980]. The pole of the low-pass filter is set to 4.5 Hz.

The next step of the data reduction pipeline is interpreting some of the logic signals from the PLOG data which are also downsampled. The nodding flag, which should reset and then set every time a nod ends and then starts again, is evaluated to determine how many nods are present in the given observation and to determine when they start and end. Then the left-beam, right-beam and acquired logic signals are analyzed to identify the starts and ends of the four nod positions. The left- and right-beam flags are high when the respective beam is selected, and the acquired flag is true when the alignment between the requested position and the actual position of the primary dish is within some telescope-defined threshold.

The chopping secondary on the CSO has an encoder on it to measure its position and that timestream is fed into Z-Spec's room-temperature electronics. The chopper switches beams at a very regular rate but sometimes experiences some irregularity. The chopper encoder signal is low-pass filtered, downsampled and then further processed to determine the period of the chopper and identify any chopper errors. An artificial pure tone, phased locked with the chopper encoder signal is created for the purposes of demodulating the bolometer timestreams. These chopper processing steps are all performed in the time domain without using the Fourier transform.

Once the pure-tone chopper signal is created, the nod positions are trimmed so that each contains exactly an integral number of chops (the same number for all nod positions). The periodic chopper waveform can only be an orthogonal basis vector when using a whole number of periods. The chopper demodulation is how the sky subtraction is implemented; if an extra fraction of a period of the chopper is included, then the sky signal will not cancel.

The pipeline returns to processing the bolometer timestreams to evaluate the roll off parameters for the given observation and calculate the optimum signal projection (see appendix C). After a linear offset is subtracted from the timestream for each bolometer for each nod position, the timestreams are ready for demodulation. Before demodulation can proceed, the phase shift between the chopper and bolometers must be evaluated. For strong sources, this is easy; simply demodulate with the pure-tone chopper and then demodulate using a pure-tone chopper that has been phase shifted by 90° . The arctangent of the ratio between these two demodulations is the chopper-to-bolometer phase for

that particular channel. If the source is weak, then this measurement will be polluted by noise and it is better to use reference chopper-to-bolometer phases determined using a separate observation. Once these phases have been obtained, the final demodulation and nod-position differencing can proceed. These results are saved for the observation being processed.

The demodulation results are in units of volts, which is related to the chopper modulated optical power landing on the detector by the bolometer responsivity, S_{ac} . While this quantity can be derived in terms of the bolometer parameters and the readout roll off parameters in theory; in practice, it is much easier to use an observation of a source of known brightness as a calibrator. This method is limited because S_{ac} depends strongly on the bolometer bath temperature and the total optical loading. The adiabatic demagnetization refrigerator in Z-Spec (see chapter 3) provides a bath temperature that slowly but constantly increases during a night of observing. The optical loading on the detectors can change as the zenith optical depth changes and as sources rise and set resulting in less or more line-of-sight optical depth, respectively. Fortunately for the observations of M82, the calibration observations of Mars occurred immediately prior to the source observations at similar bath temperatures, τ_{225} and zenith angle. A more sophisticated and flexible calibration scheme is being developed for observations of other sources based on the change in the DC level of the bolometer timestream. The DC level will track changes in bath temperature and optical loading and should be related to the responsivity. The current results indicate that for a fractional change of Δ in the DC level, the responsivity will change by $2 \times \Delta$. For the M82 observations, this indicates a calibration uncertainty of up to 10%.

Using Mars as a calibrator starts with the assumption that Mars is a black body with temperature $T_{\text{mars}} = 220$ K. An ephemeris calculator is used to determine Mars's angular size on the night in question which then can be used to calculate the beam smeared temperature each of Z-Spec's channels would see, taking into account the FTS response profiles (see section 2.4). The beam temperature can be simply converted into flux density units using the standard conversion factor $[Jy] = 2kT_{\text{beam}}/A_{\text{tel}}/10^{-26}$ which is only valid in the Rayleigh-Jeans limit. Using this flux density model for Mars and the demodulation results for a Mars observation, the conversion from volts to Jy is determined. One then divides the source demodulation by that of Mars and multiplies by the Mars flux model to obtain the source spectrum in proper units.

Since observations contain several nods, each channel produces several measurements of the flux density at that channel's frequency. Those multiple measurements must be averaged to produce a final spectrum. An estimate of the (statistical) accuracy of that average value is also necessary. A simple method would be to calculate the arithmetic mean and standard deviation of the mean of the set of nods to estimate the true value and its uncertainty. We found that it was better to use a weighted average where the weights were based on the variance estimated in the power spectral density (PSD). A PSD for each channel for each nod can be calculated by taking the Fourier

Transforms of the four nod positions' timestreams and averaging the resultant PSDs. The variance can be estimated by looking at the white-noise level around (but not including) the chop frequency. The median of ten nods' PSD variance estimate is used to weight the average (the weights are the inverse of the variance) which sensibly gives more weight to measurements with lower uncertainty. The uncertainty in the weighted mean can be calculated from the weights, though a recent paper [Zhang 2006] has indicated that the standard formula of one over the sum of the weights is typically an underestimate. Zhang [2006] proposes two alternatives, and we use the second, more conservative one that gives the estimated variance in a weighted mean as

$$\widehat{Var}_2(\bar{X}_{GD}) = \frac{(n-1)/(n-3)}{\sum_{i=1}^k 1/S_i'^2} \left[1 + \frac{2}{n-1} \sum_{i=1}^k \hat{w}_i(1-\hat{w}_i) \right], \quad (\text{D.1})$$

where $n = 10$, $S_i'^2 = S_i^2/n$, S_i^2 is the estimated sample variance (using the median of n PSD variance estimators), k is the number of groups of n nods being averaged and $\hat{w}_i = \frac{1/S_i'^2}{\sum_{i=1}^k 1/S_i'^2}$ are the normalized weights. For completeness, the weighted mean $\bar{X}_{GD} = \sum_{i=1}^k \hat{w}_i \bar{X}_i$, where \bar{X}_i is the arithmetic mean of n nods.

Appendix E

Warm Optics for the Caltech Submillimeter Observatory

The Caltech Submillimeter Observatory (CSO) is a telescope facility near the summit of Mauna Kea, Hawaii; a site nearly 14,000 feet above sea level. It is based on a compact optical design conceived by Robert Leighton. The fast $f/0.4$ beam of the 10.4 m primary dish (M1) is re-imaged to $f/12$ by a chopping secondary mirror (M2) [Leighton 1978; Serabyn 1992]. Z-Spec shares the right Nasmyth port with the submillimeter camera SHARC-II. The optical design for Z-Spec was created by Lieko Earle of the University of Colorado at Boulder and driven by the requirement that the SHARC-II dewar would remain in place on the alidade platform while Z-Spec observes. SHARC-II has an optics box that directly receives the telescope beam, folded out through the elevation bearing by the flat M3.

We attach a flat mirror on a sliding rail to fold the beam down and away from the telescope. This mirror (M4) can slide in and out of the telescope beam to enable weather multiplexed observing with both SHARC-II and Z-Spec. When observing with Z-Spec, M4 is positioned 80 cm from the Cassegrain focus in the elevation tube. The final optical element is a re-imaging ellipsoidal mirror (M5) which re-focuses the $f/12$ telescope beam to match the $f/2.7$ beam of Z-Spec's feedhorn. The distance from M4 to M5 is 190.5 cm and from M5 to the feedhorn is another 63.5 cm. The reflection angles off of M4 and M5 have been chosen so that the beam enters the dewar horizontally. M4 and M5 are significantly oversized so that the spillover efficiency is limited by the size of the secondary and should be about 89-91% across Z-Spec's bandpass. Both mirrors and dewars can be seen in figure E.1.



Figure E.1. This photograph shows the M4 and M5 mirrors of the relay optics used by Z-Spec at the CSO. They were designed by Lieko Earle from the University of Colorado at Boulder who also designed the mounting system for the dewar and optics. The back of M5 can be seen in the bottom of the image, in the foreground. It is a light-weighted ellipsoidal mirror that re-focuses the expanding $f/12$ telescope back down to $f/2.7$. The Z-Spec dewar can be seen on the right of the image, with most of the white Zotefoam window visible over the edge of M5. The SHARC-II dewar is behind Z-Spec and the flat folding M4 can be seen in the upper left background mounted to the SHARC-II optics box. M4 is mounted on rails that allow it to slide into and out of the beam of the telescope so that switching between SHARC-II and Z-Spec takes only a few minutes.

Bibliography

- Aguirre, J. E., 2003. Properties of astrophysical submillimeter emission near the South Celestial Pole from the TopHat telescope. Ph.D. thesis, The University of Chicago.
- Alloin, D., Guilloteau, S., Barvainis, R., Antonucci, R., and Tacconi, L., 1997. The gravitational lensing nature of the Cloverleaf unveiled in CO (7-6) line emission. *Astronomy and Astrophysics*, 321:24–28.
- Andreani, P., Cimatti, A., Loinard, L., and Röttgering, H., 2000. CO detection of the extremely red galaxy HR10. *Astronomy and Astrophysics*, 354:L1–L5.
- Ashcroft, N. W. and Mermin, N. D., 1976. *Solid State Physics*. Philadelphia: Saunders College.
- Bacmann, A., André, P., Puget, J.-L., Abergel, A., Bontemps, S., and Ward-Thompson, D., 2000. An ISOCAM absorption survey of the structure of pre-stellar cloud cores. *Astronomy and Astrophysics*, 361:555–580.
- Baugh, C. M., Lacey, C. G., Frenk, C. S., Granato, G. L., Silva, L., Bressan, A., Benson, A. J., and Cole, S., 2005. Can the faint submillimetre galaxies be explained in the Λ cold dark matter model? *Monthly Notices of the Royal Astronomical Society*, 356:1191–1200. doi:10.1111/j.1365-2966.2004.08553.x.
- Benford, D. J., Hunter, T. R., and Phillips, T. G., 1998. Noise equivalent power of background limited thermal detectors at submillimeter wavelengths. *International Journal of Infrared and Millimeter Waves*, 19(7):931–938.
- Bergin, E. A. and Tafalla, M., 2007. Cold dark clouds: The initial conditions for star formation. *Annual Review of Astronomy and Astrophysics*, 45:339–396. doi:10.1146/annurev.astro.45.071206.100404.
- Bertoldi, F., Carilli, C. L., Menten, K. M., Owen, F., Dey, A., Gueth, F., Graham, J. R., Kreysa, E., Ledlow, M., Liu, M. C., Motte, F., Reichertz, L., Schilke, P., and Zylka, R., 2000. Three high-redshift millimeter sources and their radio and near-infrared identifications. *Astronomy and Astrophysics*, 360:92–98.

- Bin, M., 1997. Low-noise THz niobium SIS mixers. Ph.D. thesis, California Institute of Technology.
- Blain, A. W., Smail, I., Ivison, R. J., Kneib, J.-P., and Frayer, D. T., 2002. Submillimeter galaxies. *Physics Reports*, 369:111–176.
- Blake, G. A., Masson, C. R., Phillips, T. G., and Sutton, E. C., 1986. The rotational emission-line spectrum of Orion A between 247 and 263 GHz. *Astrophysical Journal Supplement Series*, 60:357–374. doi:10.1086/191090.
- Brand, J., Cesaroni, R., Palla, F., and Molinari, S., 2001. A molecular-line study of clumps with embedded high-mass protostar candidates. *Astronomy and Astrophysics*, 370:230–264. doi:10.1051/0004-6361:20010190.
- Carlstrom, J. E. and Kronberg, P. P., 1991. H II regions in M82: High-resolution millimeter continuum observations. *Astrophysical Journal*, 366:422–431. doi:10.1086/169576.
- Chapman, S. C., Blain, A. W., Smail, I., and Ivison, R. J., 2005. A redshift survey of the submillimeter galaxy population. *Astrophysical Journal*, 622:772–796. doi:10.1086/428082.
- Christopher, M. H., Scoville, N. Z., Stolovy, S. R., and Yun, M. S., 2005. HCN and HCO⁺ observations of the galactic circumnuclear disk. *Astrophysical Journal*, 622:346–365. doi:10.1086/427911.
- Colbert, J. W., Malkan, M. A., Clegg, P. E., Cox, P., Fischer, J., Lord, S. D., Luhman, M., Satyapal, S., Smith, H. A., Spinoglio, L., Stacey, G., and Unger, S. J., 1999. ISO LWS Spectroscopy of M82: A unified evolutionary model. *Astrophysical Journal*, 511:721–729. doi:10.1086/306711.
- van Dishoeck, E. F. and Blake, G. A., 1998. Chemical evolution of star-forming regions. *Annual Review of Astronomy and Astrophysics*, 36(1):317–368. doi:10.1146/annurev.astro.36.1.317.
- Dole, H., Le Floch, E., Pérez-González, P. G., Papovich, C., Egami, E., Lagache, G., Alonso-Herrero, A., Engelbracht, C. W., Gordon, K. D., Hines, D. C., Krause, O., Misselt, K. A., Morrison, J. E., Rieke, G. H., Rieke, M. J., Rigby, J. R., Young, E. T., Bai, L., Blaylock, M., Neugebauer, G., Beichman, C. A., Frayer, D. T., Mould, J. R., and Richards, P. L., 2004. Far-infrared source counts at 70 and 160 microns in Spitzer deep surveys. *Astrophysical Journal Supplement Series*, 154:87–92. doi:10.1086/422472.
- Downes, D., Neri, R., Wiklind, T., Wilner, D. J., and Shaver, P. A., 1999. Detection of CO (4-3), CO (9-8), and dust emission in the broad absorption line quasar APM 08279+5255 at a redshift of 3.9. *Astrophysical Journal Letters*, 513:L1–L4. doi:10.1086/311896.
- Downes, D. and Solomon, P. M., 2003. Molecular gas and dust at $z=2.6$ in SMM J14011+0252: A strongly lensed ultraluminous galaxy, not a huge massive disk. *Astrophysical Journal*, 582:37–48. doi:10.1086/344594.

- Duband, L., 2000. Double stage helium sorption coolers. In *Cryocoolers 11*, edited by R. G. Ross Jr., Proceedings of the 11th International Cryocooler Conference, pp. 561–566. New York: Kluwer Academic/Plenum Publishers.
- Fixsen, D. J., Dwek, E., Mather, J. C., Bennett, C. L., and Shafer, R. A., 1998. The spectrum of the extragalactic far-infrared background from the COBE FIRAS observations. *Astrophysical Journal*, 508:123–128. doi:10.1086/306383.
- Fuente, A., García-Burillo, S., Gerin, M., Teyssier, D., Usero, A., Rizzo, J. R., and de Vicente, P., 2005. Photon-dominated chemistry in the nucleus of M82: Widespread HOC⁺ emission in the inner 650 parsec disk. *Astrophysical Journal Letters*, 619:L155–L158. doi:10.1086/427990.
- Garwin, R. L., 1956. Calculation of heat flow in a medium the conductivity of which varies with temperature. *Review of Scientific Instruments*, 27(10):826–828. doi:10.1063/1.1715385.
- Greaves, J. S. and White, G. J., 1991. A 257–273 GHz spectral survey of the OMC1 cloud core. *Astronomy and Astrophysics, Supplement Series*, 91:237–258.
- Halpern, M., Gush, H. P., Wishnow, E., and de Cosmo, V., 1986. Far infrared transmission of dielectrics at cryogenic and room temperatures: Glass, Fluorogold, Eccosorb, Stycast, and various plastics. *Applied Optics*, 25:565–570.
- Hanbury Brown, R. and Twiss, R. Q., 1956. Correlation between photons in two coherent beams of light. *Nature*, 177(4497):27–29.
- Hauser, M. G., Arendt, R. G., Kelsall, T., Dwek, E., Odegard, N., Weiland, J. L., Freudenreich, H. T., Reach, W. T., Silverberg, R. F., Moseley, S. H., Pei, Y. C., Lubin, P., Mather, J. C., Shafer, R. A., Smoot, G. F., Weiss, R., Wilkinson, D. T., and Wright, E. L., 1998. The COBE diffuse infrared background experiment search for the cosmic infrared background. I. limits and detections. *Astrophysical Journal*, 508:25–43. doi:10.1086/306379.
- Henkel, C., Schilke, P., and Mauersberger, R., 1988. Molecules in external galaxies: The detection of CN, C₂H, and HNC, and the tentative detection of HC₃N. *Astronomy and Astrophysics*, 201:L23–L26.
- Holland, W. S., Robson, E. I., Gear, W. K., Cunningham, C. R., Lightfoot, J. F., Jenness, T., Ivison, R. J., Stevens, J. A., Ade, P. A. R., Griffin, M. J., Duncan, W. D., Murphy, J. A., and Naylor, D. A., 1999. SCUBA: A common-user submillimetre camera operating on the James Clerk Maxwell Telescope. *Monthly Notices of the Royal Astronomical Society*, 303(4):659–672. doi:10.1046/j.1365-8711.1999.02111.x.

- Hollenbach, D. J. and Tielens, A. G. G. M., 1997. Dense photodissociation regions (PDRs). *Annual Review of Astronomy and Astrophysics*, 35(1):179–215. doi:10.1146/annurev.astro.35.1.179.
- Huettemeister, S., Henkel, C., Mauersberger, R., Brouillet, N., Wiklind, T., and Millar, T. J., 1995. Dense gas in nearby galaxies. IX. A survey for HNC. *Astronomy and Astrophysics*, 295:571–584.
- Hughes, D. H., Gear, W. K., and Robson, E. I., 1994. The submillimetre structure of the starburst nucleus in M82: A diffraction-limited 450-micron map. *Monthly Notices of the Royal Astronomical Society*, 270:641–649.
- Kaiser, J. F. and Schafer, R. W., 1980. On the use of the I_0 -sinh window for spectrum analysis. *IEEE Transactions on Acoustics, Speech, and Signal Processing* [see also *IEEE Transactions on Signal Processing*], 28(1):105–107.
- Knudsen, K. K., Walter, F., Weiss, A., Bolatto, A., Riechers, D. A., and Menten, K., 2007. New insights on the dense molecular gas in NGC 253 as traced by HCN and HCO⁺. *Astrophysical Journal*, 666:156–164. doi:10.1086/519761.
- Ladd, E. F., Myers, P. C., and Goodman, A. A., 1994. Dense cores in dark clouds. X: Ammonia emission in the perseus molecular cloud complex. *Astrophysical Journal*, 433:117–130. doi:10.1086/174629.
- Laurent, G. T., Aguirre, J. E., Glenn, J., Ade, P. A. R., Bock, J. J., Edgington, S. F., Goldin, A., Golwala, S. R., Haig, D., Lange, A. E., Maloney, P. R., Maukopf, P. D., Nguyen, H., Rossinot, P., Sayers, J., and Stover, P., 2005. The Bolocam Lockman Hole millimeter-wave galaxy survey: Galaxy candidates and number counts. *Astrophysical Journal*, 623:742–762. doi:10.1086/428823.
- Laurent, G. T., Glenn, J., Egami, E., Rieke, G. H., Ivison, R. J., Yun, M. S., Aguirre, J. E., Maloney, P. R., and Haig, D., 2006. The Bolocam 1.1 mm Lockman Hole galaxy survey: SHARC II 350 μ m photometry and implications for spectral models, dust temperatures, and redshift estimation. *Astrophysical Journal*, 643:38–58. doi:10.1086/502625.
- Leighton, R. B., 1978. A 10-meter telescope for millimeter and sub-millimeter astronomy. Final Technical Report for NSF Grant 73-04908, California Institute of Technology.
- Lique, F. and Spielfiedel, A., 2007. Ro-vibrational excitation of CS by He. *Astronomy and Astrophysics*, 462:1179–1185. doi:10.1051/0004-6361:20066422.
- Lique, F., Spielfiedel, A., and Cernicharo, J., 2006. Rotational excitation of carbon monosulfide by collisions with helium. *Astronomy and Astrophysics*, 451:1125–1132. doi:10.1051/0004-6361:20054363.

- Loewen, E. G. and Popov, E., 1997. *Diffraction Gratings and Applications, Optical Science and Engineering*, volume 58. New York: Marcel Dekker, Inc. ISBN 0-8247-9923-2.
- Lord, S. D., Hollenbach, D. J., Haas, M. R., Rubin, R. H., Colgan, S. W. J., and Erickson, E. F., 1996. Interstellar properties of a dual nuclear starburst: Far-infrared spectroscopy of M82. *Astrophysical Journal*, 465:703–716. doi:10.1086/177455.
- Mao, R. Q., Henkel, C., Schulz, A., Zielinsky, M., Mauersberger, R., Störzer, H., Wilson, T. L., and Gensheimer, P., 2000. Dense gas in nearby galaxies. XIII. CO submillimeter line emission from the starburst galaxy M 82. *Astronomy and Astrophysics*, 358:433–450.
- Martín, S., Mauersberger, R., Martín-Pintado, J., Henkel, C., and García-Burillo, S., 2006. A 2 millimeter spectral line survey of the starburst galaxy NGC 253. *Astrophysical Journal Supplement Series*, 164:450–476. doi:10.1086/503297.
- Marz, R. and Cremer, C., 1992. On the theory of planar spectrographs. *Journal of Lightwave Technology*, 10(12):2017–2022. ISSN 0733-8724. doi:10.1109/50.202814.
- Mauersberger, R. and Henkel, C., 1989. Dense gas in nearby galaxies. I. Distribution, kinematics and multilevel studies of CS. *Astronomy and Astrophysics*, 223:79–88.
- Mauskopf, P. D., Bock, J. J., del Castillo, H., Holzapfel, W. L., and Lange, A. E., 1997. Composite infrared bolometers with Si₃N₄ micromesh absorbers. *Applied Optics*, 36:765–771.
- McGreer, K. A., 1995. Diffraction from concave gratings in planar waveguides. *IEEE Photonics Technology Letters*, 7(3):324–326.
- Nguyen-Q-Rieu, Nakai, N., and Jackson, J. M., 1989. Dense molecular gas in galaxies: HCN, HCO(+), and CS in M 82 and NGC 253. *Astronomy and Astrophysics*, 220:57–64.
- Nikolić, S., Johansson, L. E. B., and Harju, J., 2003. Star forming cores in L 1251: Maps and molecular abundances. *Astronomy and Astrophysics*, 409:941–951. doi:10.1051/0004-6361:20031102.
- Nummelin, A., Bergman, P., Hjalmarson, A., Friberg, P., Irvine, W. M., Millar, T. J., Ohishi, M., and Saito, S., 1998. A three-position spectral line survey of Sagittarius B2 between 218 and 263 GHz. I. The observational data. *Astrophysical Journal Supplement Series*, 117:427–529. doi:10.1086/313126.
- Paglione, T. A. D., Jackson, J. M., and Ishizuki, S., 1997. The average properties of the dense molecular gas in galaxies. *Astrophysical Journal*, 484:656–663. doi:10.1086/304356.
- Papovich, C., Dole, H., Egami, E., Le Floch, E., Pérez-González, P. G., Alonso-Herrero, A., Bai, L., Beichman, C. A., Blaylock, M., Engelbracht, C. W., Gordon, K. D., Hines, D. C., Misselt,

- K. A., Morrison, J. E., Mould, J., Muzerolle, J., Neugebauer, G., Richards, P. L., Rieke, G. H., Rieke, M. J., Rigby, J. R., Su, K. Y. L., and Young, E. T., 2004. The 24 micron source counts in deep Spitzer Space Telescope surveys. *Astrophysical Journal Supplement Series*, 154:70–74. doi:10.1086/422880.
- Petuchowski, S. J. and Bennett, C. L., 1992. SO in starburst galaxies. *Astrophysical Journal*, 391:137–140. doi:10.1086/171330.
- Pillai, T., Wyrowski, F., Carey, S. J., and Menten, K. M., 2006. Ammonia in infrared dark clouds. *Astronomy and Astrophysics*, 450:569–583. doi:10.1051/0004-6361:20054128.
- Pippard, A. B., 1947. The surface impedance of superconductors and normal metals at high frequencies. II. The anomalous skin effect in normal metals. *Royal Society of London Proceedings Series A*, 191:385–399.
- Puget, J.-L., Abergel, A., Bernard, J.-P., Boulanger, F., Burton, W. B., Desert, F.-X., and Hartmann, D., 1996. Tentative detection of a cosmic far-infrared background with COBE. *Astronomy and Astrophysics*, 308:L5–L8.
- Reuter, G. E. H. and Sondheimer, E. H., 1948. The theory of the anomalous skin effect in metals. *Royal Society of London Proceedings Series A*, 195:336–364.
- Rice, F., Sumner, M., Zmuidzinas, J., Hu, R., LeDuc, H. G., Harris, A. I., and Miller, D., 2003. SIS mixer design for a broadband millimeter spectrometer suitable for rapid line surveys and redshift determinations. In *Millimeter and Submillimeter Detectors for Astronomy*, edited by T. G. Phillips and J. Zmuidzinas, *Proceedings of the SPIE*, volume 4855, pp. 301–311.
- Richards, P. L., 1994. Bolometers for infrared and millimeter waves. *Journal of Applied Physics*, 76:1–24.
- Rowland, H. A., 1883. On concave gratings for optical purposes. *Philosophical Magazine*, 16:197–210.
- Sakai, S. and Madore, B. F., 1999. Detection of the red giant branch stars in M82 using the Hubble Space Telescope. *Astrophysical Journal*, 526:599–606. doi:10.1086/308032.
- Sanders, D. B., Mazzarella, J. M., Kim, D.-C., Surace, J. A., and Soifer, B. T., 2003. The IRAS revised bright galaxy sample. *Astronomical Journal*, 126:1607–1664. doi:10.1086/376841.
- Scalo, J. and Elmegreen, B. G., 2004. Interstellar turbulence II: Implications and effects. *Annual Review of Astronomy and Astrophysics*, 42(1):275–316. doi:10.1146/annurev.astro.42.120403.143327.
- Schilke, P., Walmsley, C. M., Pineau Des Forets, G., Roueff, E., Flower, D. R., and Guilloteau, S., 1992. A study of HCN, HNC and their isotopomers in OMC-1. I - abundances and chemistry. *Astronomy and Astrophysics*, 256:595–612.

- Schöier, F. L., van der Tak, F. F. S., van Dishoeck, E. F., and Black, J. H., 2005. An atomic and molecular database for analysis of submillimetre line observations. *Astronomy and Astrophysics*, 432:369–379. doi:10.1051/0004-6361:20041729.
- Seaquist, E. R. and Frayer, D. T., 2000. The distribution of HCO⁺ J=4-3 and HCN J=4-3 in the nuclear region of M82. *Astrophysical Journal*, 540:765–770. doi:10.1086/309378.
- Serabyn, E., 1992. CSO chopping secondary motion requirements. CSO Optics Memo 1, California Institute of Technology, Pasadena, CA.
- Solomon, P. M., Downes, D., and Radford, S. J. E., 1992. Warm molecular gas in the primeval galaxy IRAS 10214 + 4724. *Astrophysical Journal Letters*, 398:L29–L32. doi:10.1086/186569.
- Sutton, E. C., Blake, G. A., Masson, C. R., and Phillips, T. G., 1985. Molecular line survey of Orion A from 215 to 247 GHz. *Astrophysical Journal Supplement Series*, 58:341–378. doi:10.1086/191045.
- van der Tak, F. F. S., Black, J. H., Schöier, F. L., Jansen, D. J., and van Dishoeck, E. F., 2007. A computer program for fast non-LTE analysis of interstellar line spectra: With diagnostic plots to interpret observed line intensity ratios. *Astronomy and Astrophysics*, 468:627–635. doi:10.1051/0004-6361:20066820.
- Thuma, G., Neininger, N., Klein, U., and Wielebinski, R., 2000. Cold dust in the starburst galaxy M 82. *Astronomy and Astrophysics*, 358:65–71.
- Turner, A. D., Bock, J. J., Beeman, J. W., Glenn, J., Hargrave, P. C., Hristov, V. V., Nguyen, H. T., Rahman, F., Sethuraman, S., and Woodcraft, A. L., 2001. Silicon nitride micromesh bolometer array for submillimeter astrophysics. *Applied Optics*, 40(28):4921–4932.
- Ward, J. S., 2002. Observations of carbon monoxide in the starburst galaxy M82 with a 690 GHz wide spectral bandwidth receiver. Ph.D. thesis, California Institute of Technology.
- Ward, J. S., Zmuidzinas, J., Harris, A. I., and Isaak, K. G., 2003. A ¹²CO J=6–5 map of M82: The significance of warm molecular gas. *Astrophysical Journal*, 587:171–185. doi:10.1086/368175.
- Weiß, A., Neininger, N., Hüttemeister, S., and Klein, U., 2001. The effect of violent star formation on the state of the molecular gas in M82. *Astronomy and Astrophysics*, 365:571–587. doi:10.1051/0004-6361:20000145.
- Wild, W., Harris, A. I., Eckart, A., Genzel, R., Graf, U. U., Jackson, J. M., Russell, A. P. G., and Stutzki, J., 1992. A multi-line study of the molecular interstellar medium in M82's starburst nucleus. *Astronomy and Astrophysics*, 265:447–464.

- Yun, M. S., Ho, P. T. P., and Lo, K. Y., 1994. A high-resolution image of atomic hydrogen in the M81 group of galaxies. *Nature*, 372:530–532. doi:10.1038/372530a0.
- Zhang, N. F., 2006. The uncertainty associated with the weighted mean of measurement data. *Metrologia*, 43:195–204. doi:10.1088/0026-1394/43/3/002.
- Zhang, X., 1993. Design of conical corrugated feed horns for wide-band high-frequency applications. *IEEE Transactions on Microwave Theory and Techniques*, 41(8):1263–1274.
- Zmuidzinas, J., 2003. Thermal noise and correlations in photon detection. *Applied Optics*, 42:4989–5008.